

Novel microtubule-targeting agents: synthesis and structural determination of their interactions

Inauguraldissertation

zur

Erlangung der Würde eines Doktors der Philosophie
vorgelegt der
Philosophisch-Naturwissenschaftlichen Fakultät
der Universität Basel

und der Universität Mailand

von

Zlata Boiarska

2024

Originaldokument gespeichert auf dem Dokumentenserver der Universität Basel

<https://edoc.unibas.ch>

Genehmigt von der Philosophisch-Naturwissenschaftlichen Fakultät auf
Antrag von

Erstbetreuende: Prof. Dr. Michel Steinmetz
Dr. Andrea E. Prota
Prof. Dr. Daniele Passarella (Universität Milano)

Zweitbetreuende: Prof. Dr. Jan Pieter Abrahams
Prof. Dr. Stefano Pieraccini (Universität Milano)

externer Experte: Dr. Juan Ignacio Padrón Peña

Basel, den 25. April 2023

Prof. Dr. Marcel Mayor, Dekan



The research presented in this PhD thesis was performed under the Marie Skłodowska – Curie Actions, at the Università degli studi di Milano, Italy and via the co-tutelle agreement, at the Paul Scherrer Institut and University of Basel, Switzerland. It was financially supported by the European Union’s Framework Programme for Research and Innovation Horizon H2020-MSCA-ITN-European Joint Doctorate “Tuning Tubulin Dynamics and Interactions to Face Neurotoxicity: a Multidisciplinary Approach for Training and Research”, named with the acronym TubInTrain, Grant agreement n°: 860070.

www.tubintrain.eu



Table of Contents

OUTLINE OF THE THESIS	9
CHAPTER I	13
1.1 THE CYTOSKELETON.....	15
1.2 MICROTUBULES AND THEIR DYNAMICS.....	16
1.3 MICROTUBULE-TARGETING AGENTS (MTAs) AND THEIR BINDING SITES ON TUBULIN.....	18
1.3.1 General overview of MTAs and ligand binding sites on tubulin	18
1.3.2 Microtubule-stabilizing agents.....	22
1.3.3 Microtubule-destabilizing agents.....	27
1.4 THERAPEUTIC APPLICATIONS OF MICROTUBULE-TARGETING AGENTS.....	38
1.4.1 MTAs as chemotherapeutics.....	38
1.4.2 MTAs as antiparasitic and antifungal drugs	40
1.4.3 MTAs in neurodegeneration	41
1.5 AIM OF THE THESIS	51
1.6 REFERENCES.....	53
CHAPTER 2	59
2.1 MAYTANSINOL FUNCTIONALIZATION: TOWARDS NEW TUBULIN BINDERS AND CHEMICAL PROBES.....	63
2.1.1 INTRODUCTION.....	65
2.1.2 AIM OF THE PROJECT	66
2.1.3 RESULTS AND DISCUSSION.....	67
2.1.4 CONCLUSIONS AND FUTURE DIRECTIONS	89
2.1.5 EXPERIMENTAL PART	91
2.1.6 REFERENCES.....	108
2.2 SYNTHETIC EFFORTS TOWARDS THE TOTAL SYNTHESIS OF A NATURAL PRODUCT GLYCYBRIDIN B.....	111
2.2.1 INTRODUCTION.....	112
2.2.2 AIM OF THE PROJECT	113
2.2.3 RESULTS AND DISCUSSION.....	113
2.2.4 EXPERIMENTAL PART	123

2.2.5	REFERENCES.....	131
2.3	SYNTHESIS OF SIMPLIFIED BIOTINYLATED PIRONETIN ANALOGUES.....	133
2.3.1	INTRODUCTION.....	134
2.3.2	AIM OF THE PROJECT.....	135
2.3.3	RESULTS AND DISCUSSION.....	136
2.3.4	EXPERIMENTAL PART.....	143
2.3.5	REFERENCES.....	154
2.4	RATIONALLY DESIGNED NOVEL TODALAM ANALOGUES: TOWARDS SITE_SPECIFIC CYSTEINE TARGETING (synthetic part).....	155
2.4.1	INTRODUCTION.....	156
2.4.2	AIM OF THE PROJECT.....	157
2.4.3	RESULTS AND DISCUSSION.....	159
2.4.4	EXPERIMENTAL PART.....	175
2.4.5	REFERENCES.....	186
CHAPTER 3	187
3.1	DETERMINING PROTEIN-LIGAND INTERACTIONS BY X-RAY CRYSTALLOGRAPHY 189	
3.1.1	General introduction on structural biology.....	189
3.1.2	Foundation of X-ray crystallography.....	190
3.1.3	X-ray crystallographic studies of protein-ligand interactions.....	192
3.1.4	Other methods to study protein-ligand interactions: comparisons with X-ray crystallography.....	194
3.2	TUBULIN CRYSTALLIZATION.....	198
3.2.1	INTRODUCTION.....	198
3.2.2	MATERIALS AND METHODS.....	200
3.2.3	REFERENCES.....	212
3.3	X-RAY CRYSTALLOGRAPHY STRUCTURE DETERMINATION OF TUBULIN-MTAs COMPLEXES.....	215
3.3.1	SuFEX SULFONATE MIMICS COMBRETASTATIN-A4.....	217
3.3.2	STILBENE_DERIVED COLCHICINE SITE BINDERS.....	225
3.3.3	CHALCONE 251 SELECTIVELY TARGETING β III TUBULIN ISOTYPE.....	233

3.3.1	REFERENCES.....	241
3.3.2	RATIONALLY DESIGNED NOVEL TODALAM ANALOGUES: TOWARDS SITE_SPECIFIC CYSTEINE TARGETING (structural part).....	243
3.3.1	REFERENCES.....	254
	CONCLUSIONS AND FUTURE PERSPECTIVES	255
	ACKNOWLEDGEMENTS.....	257

OUTLINE OF THE THESIS

This thesis, performed within the EU-funded Innovative Training Network - European Joint Doctorate TubInTrain, via the cotutelle agreement for a double degree between University of Milan and University of Basel, is focused on the microtubules dynamics and its breakdown associated to neurodegenerative diseases.

Microtubule-targeting agents constitute a large group of chemically diverse molecules that bind tubulin and perturb the stability and functions of microtubules. While microtubule-targeting agents constitute a successful class of cancer drugs, the way in which tubulin binders can face neurodegeneration and neurotoxicity has yet to be determined. We aimed to develop a set of tubulin binders acting as chemical probes to explore different ligand-tubulin interactions modes and to potentially study how they affect the behaviour of microtubules in cell free systems. The chosen compounds are further studied in neuronal models, in order to clarify how small molecules affect microtubule dynamics in neurons. In **Chapter I**, the introduction on microtubules, their structure, and functions, and in particular the microtubule-targeting agents is described. The chemical structures of the representative tubulin binders, their respective bindings sites and therapeutic applications are addressed. Furthermore, the aims and objectives of the thesis are discussed.

Within the workflow, the main objectives of my project included the synthesis of new tubulin binders, performed at the University of Milan. This was complemented by the X-ray crystallography structure determination of individual tubulin-compound complexes, which was performed in the course of my one-year secondment period at the Paul Scherrer Institute. Based on that, **Chapter II** covers the synthetic part of the work, while **Chapter III** covers structural determination of ligands-tubulin complexes.

More precisely, **Chapter II** includes four different projects. Section **2.1** focuses on the functionalization of a natural product maytansinol. Maytansinoids represent a successful class of natural and semisynthetic tubulin binders, known for their potent cytotoxic activity. Their wider application as cytotoxins and chemical probes to study tubulin dynamics was set back due to the complexity of natural product chemistry and lack of SAR studies. Natural product maytansinol is a valuable precursor for the preparation of maytansine derivatives. Thus, one of the main objectives was to establish synthetic routes for the functionalization of maytansinol and to synthesize a set of maytansine analogues with different side chain substituents in C3-position, in order to investigate the effect of bulky substituents in the C3-position on the binding mode and activity of maytansinoids. Design, synthesis and biological evaluation of short-chain, long-chain and maytansinoid conjugates is described.

Section **2.2** focuses on the synthetic efforts towards the total synthesis of a natural product glycybridin B. We aimed to identify and synthesize new maytansine site binders, structurally less complex than the family of maytansinoids. A natural product glycybridin B, isolated for the first time in 2017 from the herbal medicine *Glycyrrhiza glabra*, has been chosen for

synthesis based on the computational screening. It attracted our interest due to the following factors: a) its total synthesis has not yet been reported in literature; b) different biological studies attribute it a variety of biological activities; c) it has been predicted to bind to maytansine site in computational studies. Therefore, synthetic efforts to synthesize the desired glycybridin B are described.

Section **2.3** and **2.4** both focus on the covalent-targeting strategy to target tubulin. Covalent probes are characterized by prolonged duration of action, improved potency, and exquisite selectivity. Moreover, they could be used e.g., to immobilize the protein of interest, tubulin. In Section **2.3**, the synthesis of simplified biotinylated pironetin analogues is described. Pironetin, a natural product that covalently binds α -tubulin, and the possibility of its biotinylation to use then biotin capturing on streptavidin for protein immobilization. Taking into consideration the low availability and time-consuming synthesis of natural pironetin, we designed and synthesized its simpler biotinylated analogues. In its turn, Section **2.4** comprises Todalam site ligands. Todalam targets the most recently discovered eighth small molecule binding site on tubulin and displays a unique molecular mechanism of action. Using the time- and cost-efficient synthetic approaches, we intended to develop novel, different from Todalam scaffolds and then, based on the structural data, rationally optimize them with the idea of site-specific covalent targeting. I was involved both in the chemistry and structural biology aspects of this project. I aimed to obtain and characterize the crystal structures of todalam analogues synthesized in our laboratory in complex with tubulin, to then design (in collaboration with the computational groups) and synthesize a library of optimized warhead-bearing ligands for the covalent targeting. Section **2.4** covers the synthetic work performed on this project, while the structural work including the obtain crystal structures of the developed todalam site ligands in complex with tubulin is described in detail in Section **3.3.5**.

Chapter III contains the introduction to the methods used to determine protein-ligand interactions, with particular focus on X-ray crystallography, discussed in Section **3.1**. In the following Section **3.2**, tubulin crystallization systems and the experimental data regarding the used tubulin crystallization system T₂R-TTL is described. Finally, the determined tubulin-ligands crystal structures are discussed in detail in Section **3.3**. Two training projects, which allowed to acquire skills in protein expression and purification; crystallization, crystal harvesting and cryo-cooling, data collection at synchrotron, model building and refinement, are contained in Sections **3.3.1** and **3.3.2**. Both training projects focus on the colchicine site ligands: the analogues of combretastatin A4 and the stilbene-derived derivatives.

Section **3.3.3** addresses the results of the crystallographic screening of other sixty-eight compounds derived from synthesis or virtual screening of Enamine libraries. As a result of the screening campaign, we managed to identify another colchicine site ligand, specifically binding to β 3 isotype of tubulin. Isotype-specific ligands present an advantage as they can target certain isotypes, overexpressed in specific cells and therefore can be selectively used

for certain types of diseases (e.g. β 3 tubulin present mostly in neurons). The relevant results and the successfully obtained crystal structure of the hit are described in this Section.

CHAPTER I

INTRODUCTION AND SCOPE OF THE THESIS

1.1 THE CYTOSKELETON

As early as 1930 the existence of “an organised network of protein molecules, forming a three-dimensional mosaic extending throughout the cell” has been proposed by a biochemist Rudolph Peters.^[1] The hypothesis was then elaborated by Paul Wintrebert, who was the first to introduce the term “cytoskeleton” one year later.^[2] Further studies, strongly depended on the development of electron microscopy techniques (EM), revealed an increasingly complicated cytoskeletal network in cells, composed of actin filaments, microtubules and intermediate filaments (Figure 1), as well as their numerous crosslinkers and associated proteins.^[3–8] Nowadays, the cytoskeleton is known as a dynamic network of intracellular protein filaments, which complex interplay provides the framework for nearly all cellular processes, including maintenance of the cell shape, motility, endocytosis, cell division and intracellular transport of cargo.^[9]

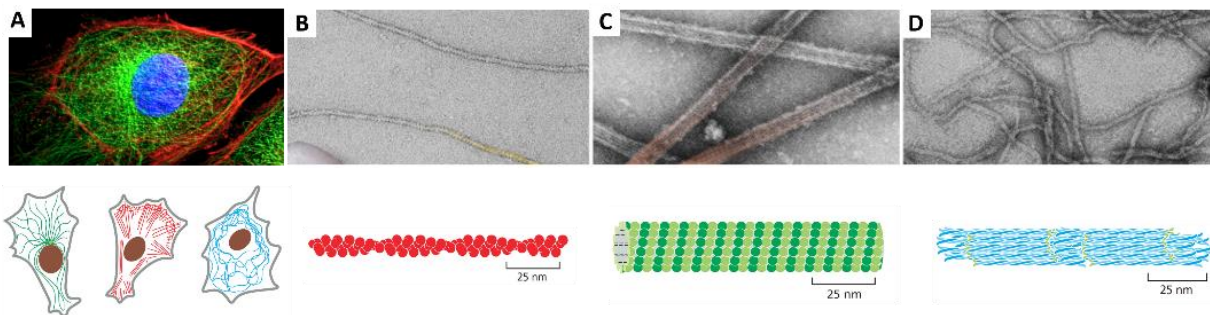


Figure 1-1. Main components of the cytoskeleton

(A) Top panel: Cell with fluorescently labelled cytoskeleton components: microtubules in green, actin filaments in red and the nucleus in blue. Bottom panel: A schematic localization of the cytoskeleton components within the cell (B) Microfilaments, (C) Microtubules, and (D) Intermediate filaments. For (B)-(D), the top panel shows a negative stain electron microscopy image of the corresponding filament, the bottom panel a schematic representation of its structure. Figure modified from¹⁰.

The cytoskeletal filaments can be distinguished on the bases of their diameter, their mechanical stiffness, polarity, type of subunit as well as its arrangement and dynamics.^[10] Actin filaments, also called microfilaments, are 8–9 nm in diameter which makes them the thinnest filaments of the cytoskeleton (Figure 1-1B). The actin cytoskeleton is continually assembled and disassembled under physiological conditions. It elongates steadily in the presence of ATP-bound monomers (G-actin), forming a twisted filamentous two-stranded structure (F-actin). Upon the formation of the stable filaments, the bound ATP hydrolyses with the subsequent phosphate release.^[11] In cells, actin filaments serve as tracks for molecular motors of the large family of myosin proteins, provide cells with mechanical support and driving forces for locomotion and are involved in cell division and endocytosis.^[12,13]

Intermediate filaments, 10-11 nm in diameter, are composed of numerous different but homologous proteins, encoded by over 70 genes (Figure 1-1C). While localization and

function of the IF proteins differ, many of them share a similar structure made of two-stranded coiled coils and a common polymerization mechanism. An average of eight tetramers join laterally to form unit-length filaments (ULFs), which then assemble end-to-end to constitute a filament. The latter then compacts the classical filament observed in cells. Some prominent examples of intermediate filaments proteins are the keratins, vimentin, desmin, peripherin, nestin, synemin and lamins.^[14] Intermediate filaments integrate the components of the cytoskeleton and are crucial for the functional organization of structural elements and tissue construction. They play a pivotal role in cell plasticity, provide mechanical strength to cells and tissues and maintain their integrity, while their mutations are associated a wide range of diverse diseases.^[15,16]

Microtubules are the third and largest components of the cell cytoskeleton, with a diameter of 25 nm. They are also the stiffest of three polymers and are known to have the most complex assembly and disassembly dynamics.^[10] Since the work of this thesis is focused on the small molecules targeting tubulin and microtubules, their structure, functions and properties are introduced in more detail in the following section.

1.2 MICROTUBULES AND THEIR DYNAMICS

Microtubules were first described in 1954 as long filaments in cilia and termed “microtubules” due to their tubular structure.^[6,17] They play fundamental roles in diverse cellular functions, including cell division, maintenance of cell shape, migration and intracellular transport. Of particular interest to this thesis is the role of microtubules in the nervous system. Due to their polarized structure, they are crucial for such processes as neuronal morphology, migration, differentiation as well as establishing and maintenance of neuronal polarity.^[18,19] Moreover, they maintain axonal integrity and serve as cytoskeletal “highways” for axonal transport.^[20]

Microtubules are formed by polymerization of α - and β -tubulin heterodimers, aligned longitudinally into protofilaments which then laterally assemble in a helical fashion (Figure 1-2).^[21] In cells, they typically comprise 13 parallel protofilaments, while *in vitro* the number of filaments varies from 10 to 15 with the majority consisting of 14.^[22,23] Since tubulin dimers assemble in a head-to-tail fashion, microtubules are polar structures with two distinct ends: the fast-growing plus end with the exposed β -subunit and a slow-growing minus end with the exposed α -subunit.^[24] Furthermore, the microtubule lattice presents a discontinuity in the microtubule wall, termed the “seam”.^[25,26] At this site the α - β and β - α lateral contacts are made instead of the usual α - α and β - β lateral contacts, and it is often speculated to be the weakest point of microtubule, however the functional relevance of it is not yet understood. Recently, the atomic resolution structures of microtubules have been

determined by cryo-electron microscopy, clearly showing the seam and the lateral contacts between protofilaments.^[27–29]

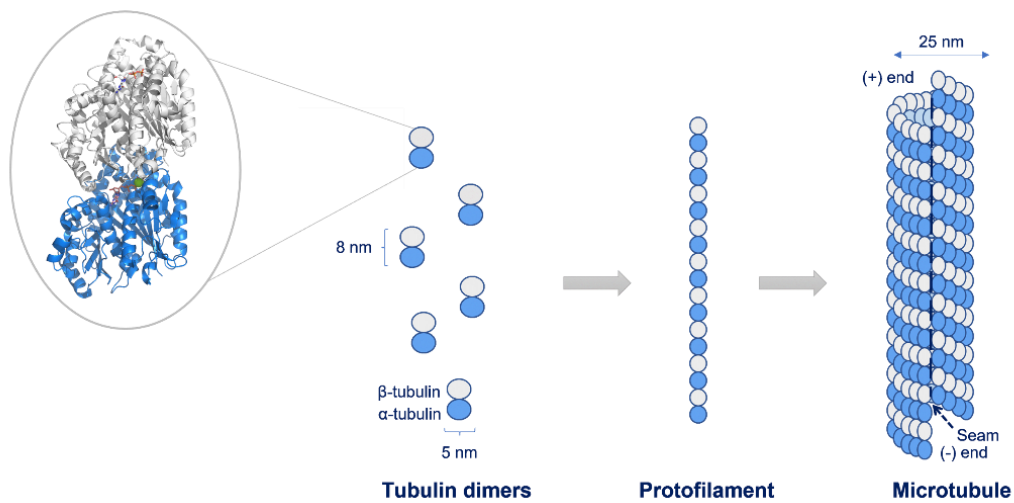


Figure 1-2. Schematic representation of microtubule structure and organization.

The α - and β -tubulin exist in multiple isoforms, capable of forming heterodimers and assembling into microtubules. Overall, the α - and β -tubulin subunits share high sequence identity and structural similarities and can be both generally divided into three main domains (Figure 1-3A). This includes the N-terminal domain that contains the guanine nucleotide-binding site, the intermediate domain that contains the M-loop which contributes to the lateral interaction between protofilaments, and the C-terminal domain.^[30] Each α - and β -tubulin contain a GTP binding site located at the longitudinal interface. However, the α -tubulin site is buried at the intradimer interface where it rather plays a structural role (N-site, non-exchangeable). On the other hand, the β -tubulin GTP is exposed in the unassembled dimer, making it susceptible to exchange and hydrolysis (E-site, exchangeable). Both N- and E-sites of tubulin also fit a magnesium ion that is critical for microtubule assembly and GTPase activity.^[31] In the presence of GTP, free soluble tubulin–GTP dimers assume a “curved” conformation. As they incorporate into the growing microtubule lattice, their conformation changes towards a more rigid, “straight” structure (curved-to-straight transition) (Figure 1-3B). This is needed to establish lateral tubulin contacts between microtubule protofilaments. Tubulin incorporation induces β -tubulin GTP hydrolysis, which, however, occurs with a delay in respect to microtubule growth, allowing growing microtubule ends to maintain an extended region of added GTP-tubulin, known as a GTP cap. It is generally accepted that the GTP-cap has stabilizing properties, whereas the body of a microtubule is composed mainly of GDP-tubulin and is intrinsically unstable. The stochastic loss of the GTP cap leads to rapid depolymerization of a microtubule, characterized by protofilaments peeling off and dissociating into tubulin–GDP dimers and small curved oligomers. The change from the growing phase to the shrinkage phase is called a “catastrophe”; the reverse process is called a “rescue”. The physiological state of MTs is

known as “dynamic instability” as they undergo polymerization and depolymerization of tubulin heterodimers, stochastically switching between growing and shrinking phases.^[24]

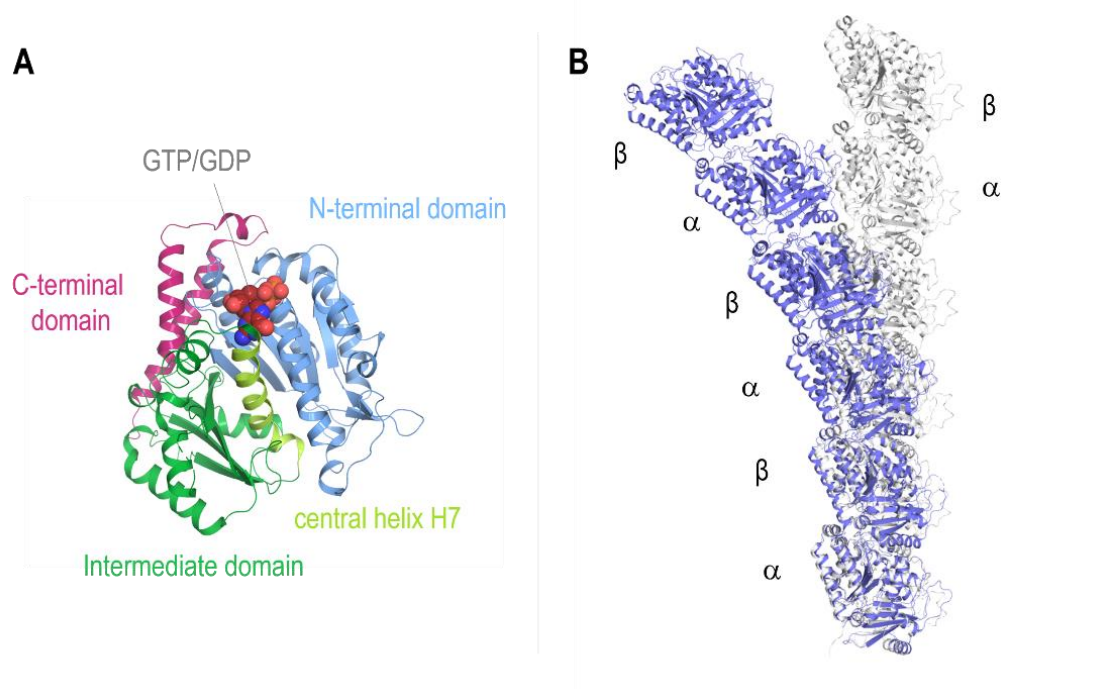


Figure 1-3. (A) Structural features of the tubulin. (B) Tubulin conformational changes associated with microtubule assembly. A “straight” microtubular protofilament is shown in ribbon presentation in light grey (PDB ID 7SJ7). A protofilament constituted of tubulin in a curved conformation is shown in blue (from PDB ID 5LXT), modified from¹⁷⁶.

The balance between growing and shrinking microtubules is essential for normal functioning of the MT cytoskeleton, whereas the shift from one to another might result in dramatic abnormalities. Since the initial concept of dynamic instability, it has been established that this equilibrium is strongly affected by a family of stabilizing MT-associated proteins (MAPs), destabilizing tubulin-binding proteins (e.g., stathmin) and tubulin post-translational modifications (PTMs) that can shift MTs into ‘rescue’ or ‘catastrophe’ depending on their qualities and/or and/or pathologies.^[28,32] The changes in microtubule dynamics can also be influenced and restored by a variety of tubulin-binding small molecules, which compose a large group of chemically diverse compounds generally referred to as microtubule-targeting agents, MTAs.

1.3 MICROTUBULE-TARGETING AGENTS (MTAs) AND THEIR BINDING SITES ON TUBULIN

1.3.1 General overview of MTAs and ligand binding sites on tubulin

Microtubule-targeting agents, MTAs, are a group of chemically diverse molecules, that bind to tubulin and affect its properties and functions. Depending on their effect, tubulin binders can be generally divided into microtubule-stabilizing agents (MSAs) and microtubule-

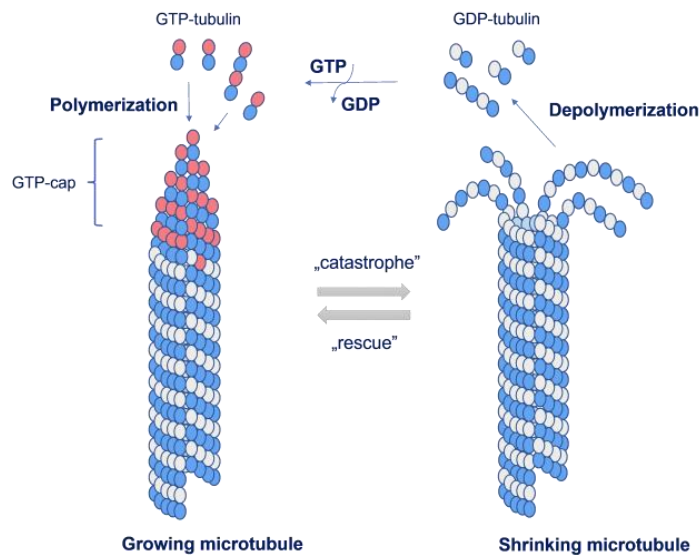


Figure 1-4. Schematic representation of Microtubule Dynamic Instability

destabilizing agents (MDAs). MSAs promote microtubule polymerization, by strengthening lateral and/or longitudinal tubulin contacts in microtubule lattice. MDAs destabilize microtubules by either by inhibiting the formation of native tubulin contacts or preventing the curved-to-straight conformational change (Figure 1-5).

Interestingly, at very low concentrations, MDAs can also “kinetically stabilize” microtubules and induce effects similar to those of MSAs.^[33]

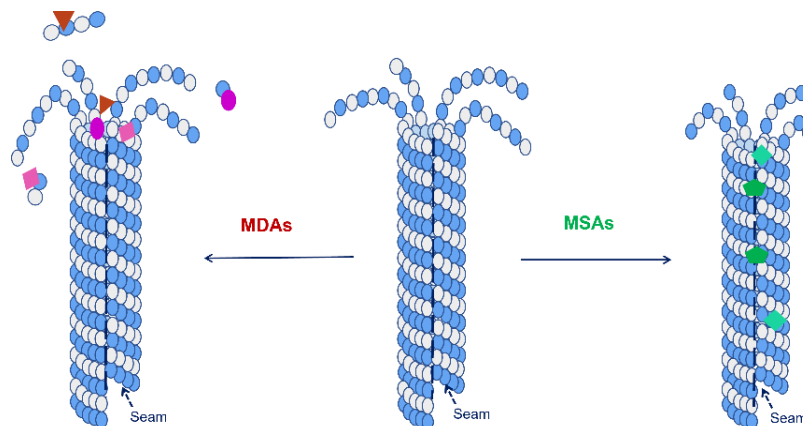


Figure 1-5. Schematic representation of the MSAs and MDAs effects. MDAs are represented as red, pink and violet shapes. MSAs are represented in darker and lighter green shapes.

Up-to-date, dozens of MTAs have been identified and characterized, binding to eight distinct sites on tubulin. This includes vinca, taxane, laulimalide/peloruside, colchicine, maytansine and gatorbulin sites on β -tubulin, pironetin site on α -tubulin and Todalam site at the β - α interdimer interface (Figure 1-6). This impressive list emerged over the decades of research, with the first tubulin binder, colchicine, identified over 50 years ago^[34] and the newest, Todalam, described only last year.^[35] The binding sites are named after their most prominent members, which chemical structures are depicted in Figure 1-6. As shown, they are represented mainly by natural products originating from plants, marine sponges or bacteria and their synthetic derivatives, often possessing macrocyclic structures and multiple stereogenic centers. The only exception constitutes Todalam, a fully synthetic molecule with a less complicated chemical structure. This can be easily explained by the story of its

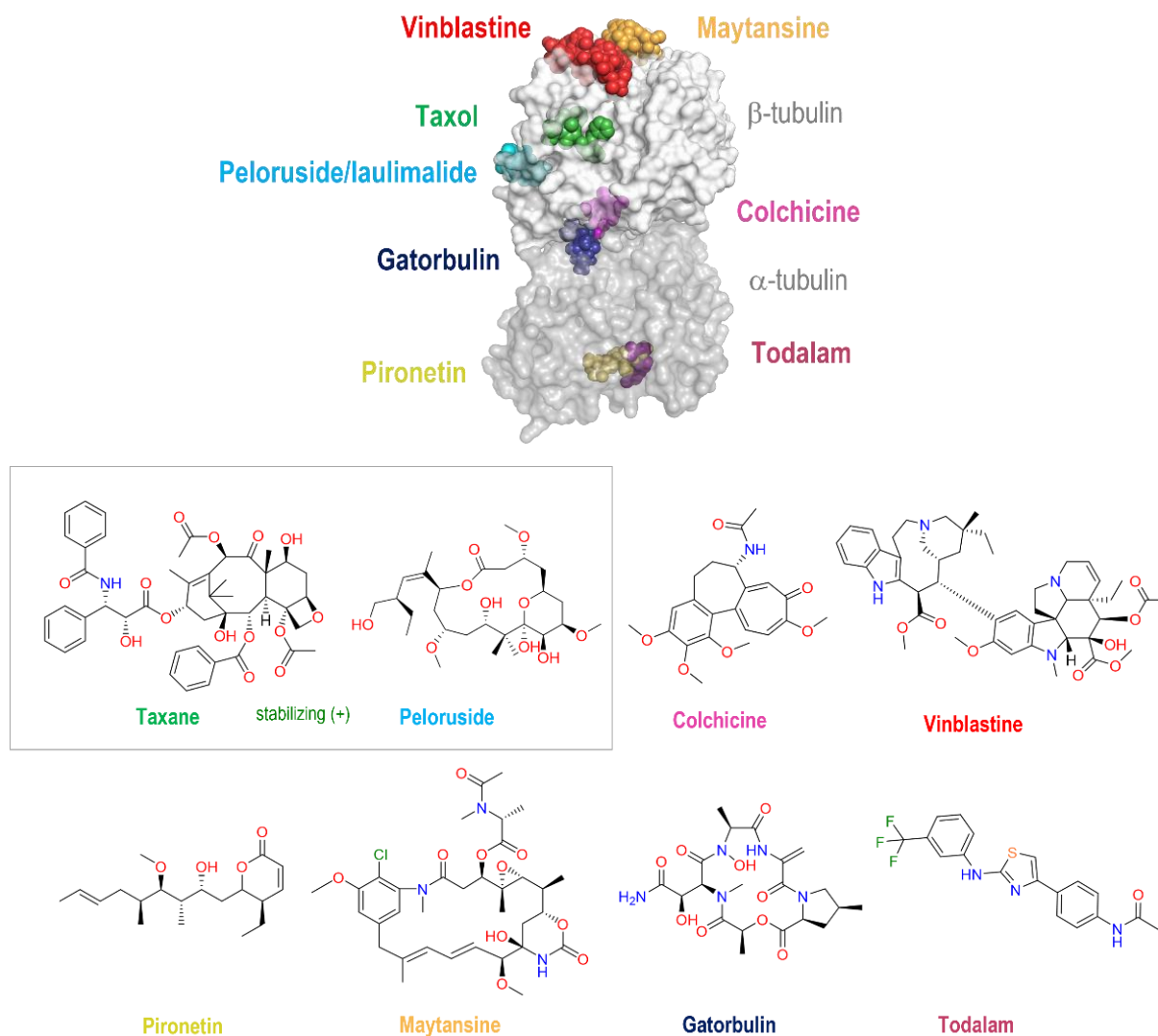


Figure 1-6. Microtubule-targeting agents (MTAs) binding sites on tubulin and the chemical structures of the representative MTAs for each of the known binding sites.

development. Unlike the natural products, it has been rationally designed based on the small inactive fragments able to bind tubulin (reviewed in Section 1.3.3).

In fact, the eight MTAs binding sites described relate only to the fully active molecules, able of inducing the polymerizing or destabilizing effect on tubulin. Apart from that, six additional tubulin binding sites occupied by small inactive fragments were described in 2021 by Mühlethaler and co-workers. They were discovered in a result of a combined computational and crystallographic screening, performed by the groups of Prof. Steinmetz and Prof. Cavalli.

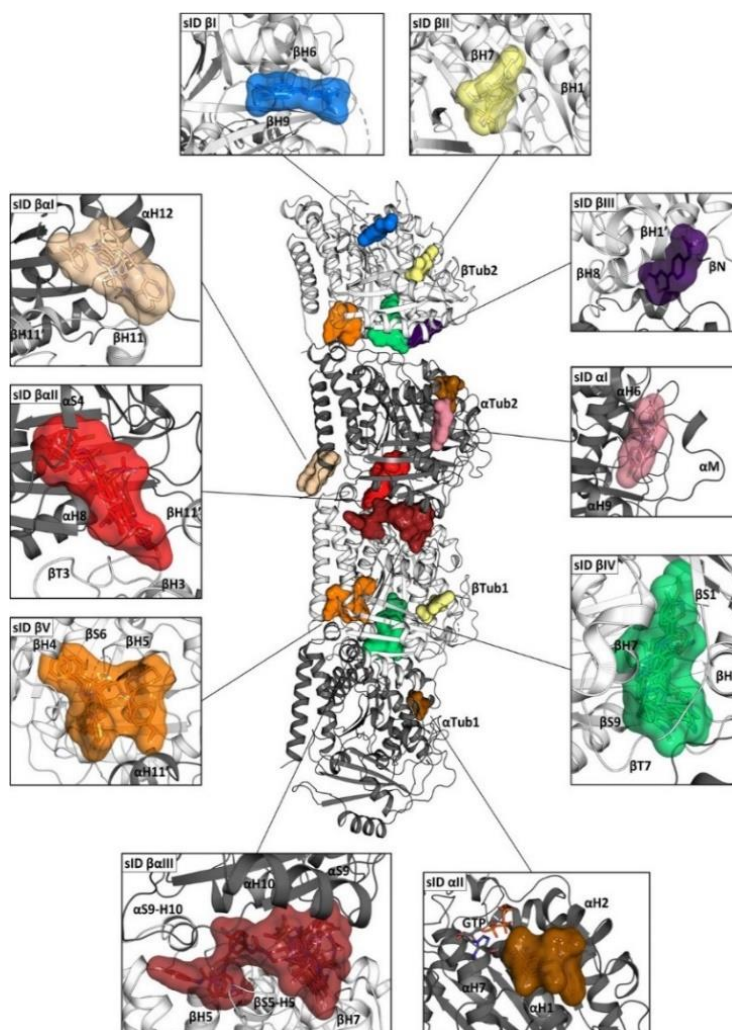


Figure 1-7. Fragment-binding sites in tubulin determined by X-ray crystallography. In the center of the figure, the structure of the two tubulin heterodimers α Tub1- β Tub1 and α Tub2- β Tub2 are depicted as they are observed in the T2R-TTL tubulin crystallization complex. The α - and β -tubulin monomers are shown in dark and light gray ribbon representation, respectively. The 56 fragments bound to 10 different binding sites (highlighted in colors), of which 6 were novel (adapted from³⁷).

More precisely, they identified fifty-six chemically diverse fragments that bound to ten distinct tubulin sites, six of which were novel (Figure 1-7).^[36]

1.3.2 Microtubule-stabilizing agents

Taxane-site ligands

Paclitaxel, commonly known under the name “taxol”, is the first and best-known microtubule stabilizing agent described in the literature. It is a natural plant alkaloid, first discovered and isolated from the bark of the Pacific yew tree (*Taxus brevifolia*) in 1971 by Monroe Wall and Mansukh Wani.^[37] Its ability to stabilize microtubules both *in vitro* and in cells, and subsequently disrupt cell cycle progression and induce apoptosis, prompted its development as a successful chemotherapeutic.^[38–40] In 1992, Taxol was FDA-approved for the treatment of ovarian cancer, and, 2 years later, for the use against breast cancer. Over the years, the list of its applications got extended to non–small cell lung cancer, esophageal cancer, lung cancer, cervical cancer, pancreatic cancer, and Kaposi's sarcoma.^[41]

Despite the successful use of Taxol® in cancer therapy, a great effort has been made to produce its synthetic and semisynthetic analogues, to improve its pharmacokinetic properties and water solubility. Structurally, paclitaxel is a diterpene composed of a taxane ring fused with a four-membered oxetane ring, a benzoyl side chain at the C2 position and an ester side chains at C13 (Figure 1-8). Due to the structural complexity of this molecule, its total synthesis took chemists over a decade.^[42,43] Docetaxel and cabazitaxel have emerged as more potent semisynthetic derivatives. Both drugs have found their application in clinics for the treatment of breast cancer (Taxotere®) and prostate cancer (Jevtana®), respectively. Among the newer taxane derivatives, one could distinguish a TPI-287, a brain-penetrant abeotaxane, investigated for brain metastases of the cancers and some neurodegenerative disorders.^[44,45] It is worth noting that regardless of these efforts, the use of taxanes is still limited due to their low solubility, toxicity, drug resistance and serious side effects, such as peripheral neurotoxicity.^[46]

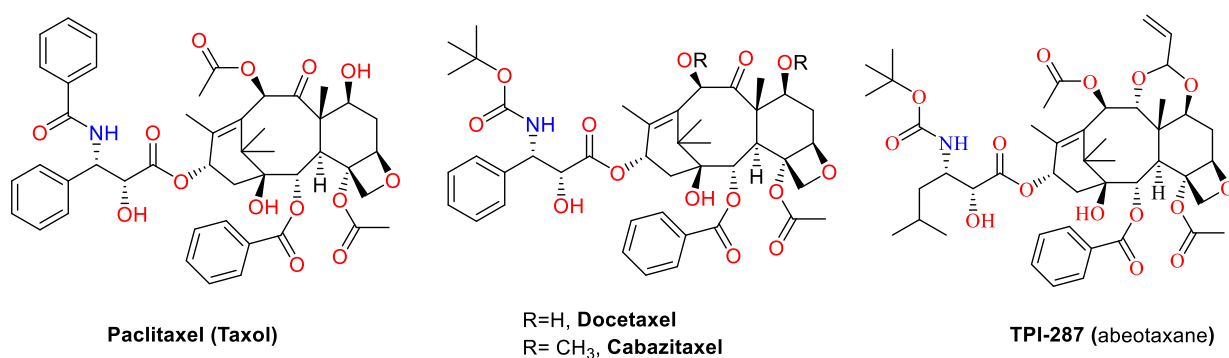


Figure 1-8. Chemical structures of taxanes.

Another large family of taxane-site binders is constituted by epothilones, characterized by a better water solubility and brain permeability compared to taxanes. Originally discovered in 1987 by Höfle and Reichenbach during a screen for antifungal agents, epothilones are 16-membered macrocyclic lactones (Figure 1-9), isolated from the soil myxobacterium *Sporangium cellulosum*.^[47] They were shown to bind to β -tubulin and induce tubulin polymerization in a manner similar to taxol.^[47,48] Interestingly, the name epothilone reflects the basic structural features of the originally identified compounds, epothilone A and B, such as an epoxide moiety, a thiazole-containing side chain and a ketone function in the macrolide ring. However, later it came to light that epoxide does not belong to the pharmacophore and new epothilones, in which an alkene-cored structure replaced the epoxide, were identified. Hence, epothilones can be divided into two classes based on the functional group at C12-C13 position: epoxide epothilones (A, B, E, F) and olefin epothilones (C, D). Generally, the chemical structures of epothilones are simpler in comparison to taxanes, leading to easier chemical modifications. Similarly to taxanes, they have found application as chemotherapeutics, and have been evaluated in multiple clinical trials for the treatment of various cancers. Importantly, ixabepilone (Ixempra™, azaepothilone B) was the first epothilone approved by FDA for the treatment of aggressive metastatic or locally advanced breast cancer.^[49]

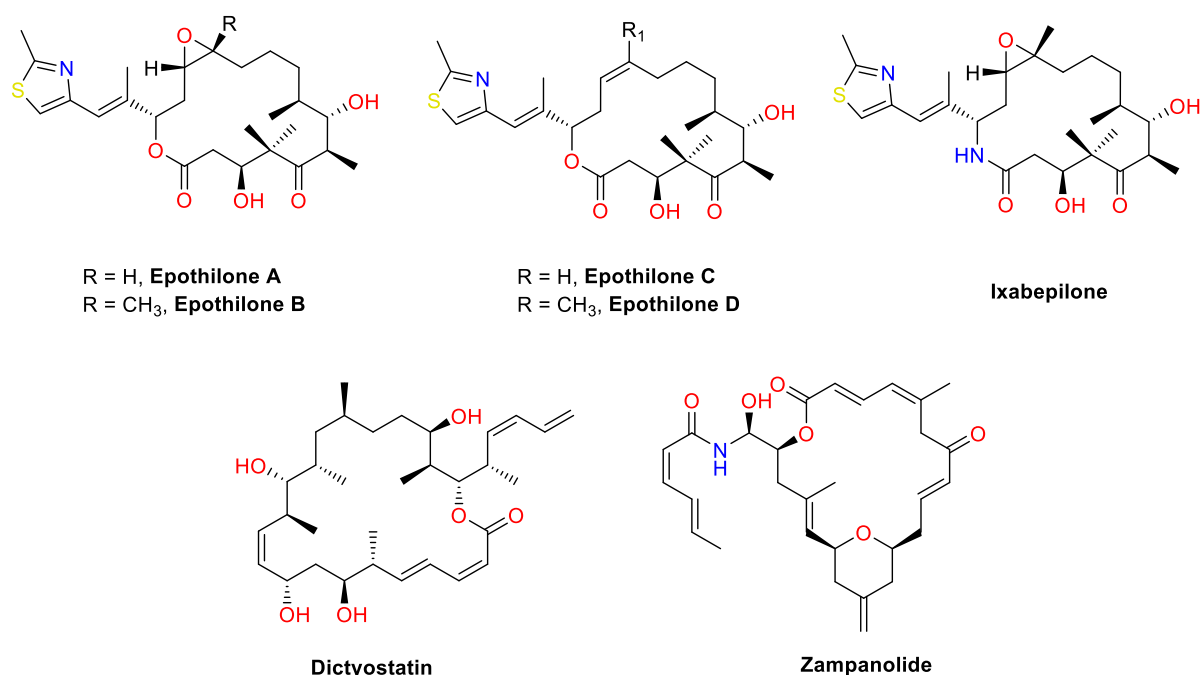


Figure 1-9. Chemical structures of epothilones, dictyostatin and zampanolide.

Other known members of the taxane-site ligands are i.a. dictyostatin and zampanolide, represented in Figure 1-9. Dictyostatin is a polyketide of marine origin, initially isolated in 1994 from the sponge of the genus *Spongia sp.* and *Lithistida sponge*.^[50,51] Structurally, dictyostatin is a 22-membered macrocyclic lactone, featuring 11 stereogenic centers, an

endocyclic (2Z,4E)-dienoate moiety, a (Z)-olefin and a terminal (Z)-diene. The growing interest in this compound is due to its potent microtubule stabilizing properties and the ability to overcome P-gp-mediated drug resistance mechanisms.^[52,53]

Zampanolide is a potent microtubule-stabilizing agent, isolated from the marine sponge *Fasciospongia rimosa*.^[54] It is a 20-membered macrolide with a largely unsaturated ring and an *N*-acyl hemiaminal side chain. It is characterized by the presence of only 4 stereogenic centers, which makes it more amenable for large-scale synthesis. Zampanolide was shown to covalently bind to β -tubulin at the taxane site, to circumvent taxane resistance *in vitro* and demonstrate potent antitumor efficacy when delivered intratumorally *in vivo*.^[55–57]

Compounds binding at the taxane site of tubulin or at a close proximity to it are not limited to those described here. More compounds have been identified and characterized, including e.g. discodermolide, taccalonolides and cyclostreptin.^[33]

Despite the discovery of numerous taxane site ligands and successful application of some of them as chemotherapeutics, their molecular mechanism of action has remained elusive for a long time. In 1998, when paclitaxel was already in clinical use, its structure bound to tubulin was solved based on electron crystallography. Notably, it was the first structure of a tubulin-bound drug. Over the last two decades, several tubulin and microtubules structures in complex with taxane-site ligands have been solved by X-ray crystallography and cryo-EM, providing the structural basis to elucidate the MSAs mechanism of action.

A taxane site is a pocket of β -tubulin on the luminal side of microtubules, predominantly formed by hydrophobic residues of helix H7, strand S7, and loops H6–H7, S7–H9 (the M-loop), and S9–S10 of β -tubulin (Figure 10A). All taxane-site ligands establish hydrophobic and polar contacts with those secondary structural elements, while zampanolide, cyclostreptin and taccalonolide AJ additionally target covalently His229 and Asp226, respectively.

Initially, it was suggested that taxanes strengthen the longitudinal tubulin contacts via an allosteric regulation.^[58,59] However, more recently it has been described that, by partially stabilizing the β M-loop conformation by its interaction with β R278, paclitaxel is involved in establishing the lateral contact between protofilaments.^[60] Furthermore, the analysis of two X-ray structures of structurally different zampanolide and epothilone suggested the mechanism which involves the structuring of the otherwise disordered M-loop into a short helix, which then promotes tubulin assembly into a microtubule (Figure 10B).^[61] Similarly, dictyostatin and discodermolide were also proposed to stabilize the M-loop conformation, although no helical structure was observed.^[53,62] Notably, zampanolide and epothilone A have a side-chain which allows them to interact with the M-loop directly, in contrast to taxol, taccalonolide or discodermolide. Altogether, this suggests that although one could propose a general mechanism of action, true for most taxane-site ligands, due to the great structural

differences each class of taxane-site ligands has unique effects on the microtubule lattice structure.

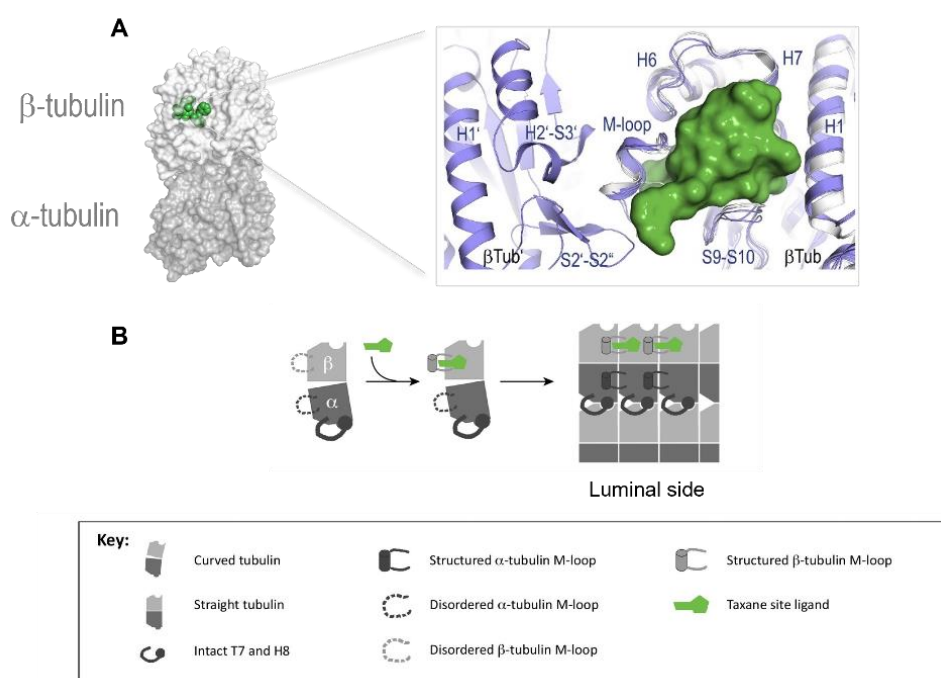


Figure 1-10. (A) Left: localization of taxane site on tubulin. Paclitaxel is depicted in green sphere representation, α - and β -tubulin in grey and white ribbon representation, respectively. Right: close-up view of the taxane site, superimposed in the curved and straight tubulin conformational states. β Tub and β Tub' indicate β -tubulin subunits that belong to two neighboring protofilaments (B) Schematic representation of the general mechanism of action of taxane-site MSAs (adapted from ³⁴).

Laulimalide/peloruside-site ligands

Laulimalide and peloruside A (commonly known as peloruside) are both marine natural products with potent microtubule-stabilizing properties, isolated from the marine sponges *Cacospongia mycofijiensis* and *Mycale hentscheli*, respectively. Structurally, laulimalide is an 18-membered macrocyclic lactone, characterized by the presence of two dihydropyran rings and a trans-disubstituted epoxide, while peloruside A is a polyoxygenated, pyranose ring containing 16-membered macrolide (Figure 1-11). Similarly to taxanes, both compounds

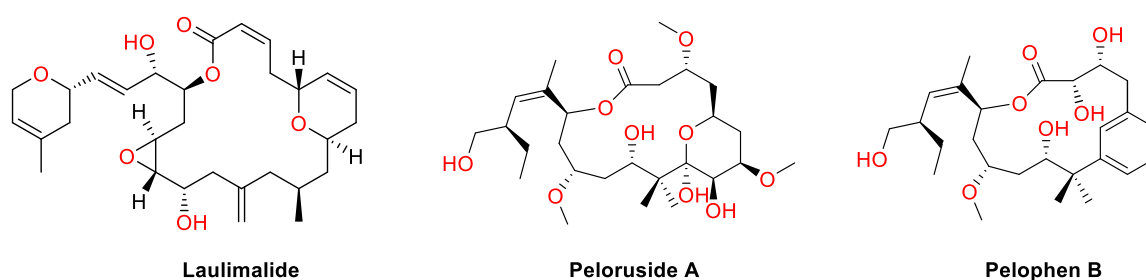


Figure 1-11. Chemical structures of laulimalide/peloruside-site ligands.

were shown to stabilize microtubules, to promote mitotic arrest at G2/M and to cause apoptosis.^[63–65]

Both laulimalide and peloruside have shown activity in multidrug-resistant cell lines which overexpress P-glycoprotein.^[66] However, laulimalide showed low antitumor potency and severe toxicity *in vivo*, thereby limiting the interest in further preclinical studies of this compound.^[67] In its turn, peloruside has demonstrated a more favourable therapeutic profile, with higher antitumor activity and lower toxicity, and has been subsequently tested in various *in vitro* and *in vivo* models of cancer, neurodegeneration, and autoimmune disease. One of the major challenges of the further evaluation of this compound is its scarce natural supply as well as the difficulty and low yields of the total synthesis.^[68] Nowadays, a range of its natural (pelorusides B-E), semisynthetic and synthetic analogues has been described, including monocyclic, deoxygenated or stereoisomeric derivatives, some of which were found moderately active.^[69] One of the most prominent synthetic analogues is pelophen B (Figure 1-11), which is known to maintain the potent activity of the parent natural product (described in patent PCT/EP2014/075903).^[70]

The insusceptibility of laulimalide and peloruside to the resistance mutations in taxane site of β -tubulin has been the first indication of those drugs binding to another tubulin site. In 2014, this has been confirmed by the high-resolution X-ray crystal structures of laulimalide and peloruside in complex with tubulin. In contrast to the taxane site, which is located at the luminal side of the microtubule, the pocket on β -tubulin occupied by laulimalide and peloruside faces the outside of the microtubule.^[71] It is formed by hydrophobic and polar

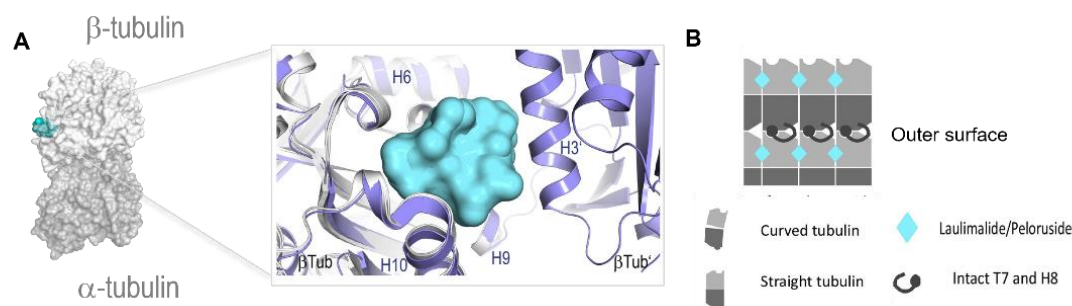


Figure 1-12. (A) Left: localization of laulimalide/peloruside site on tubulin. Laulimalide/peloruside site ligand is depicted in cyan sphere representation, α - and β -tubulin in grey and white ribbon representation, respectively. Right: close-up view of the laulimalide/peloruside site, superimposed in the curved and straight tubulin conformational states. β Tub and β Tub' indicate β -tubulin subunits that belong to two neighboring protofilaments (B) Schematic representation of the general mechanism of action of laulimalide/peloruside-site MSAs (adapted from³⁴).

residues of the H9 and H10 helices, and the loops H9–H9' and H10–S9 of β -tubulin (Figure 1-12A).

Located on the outer surface of microtubules, it is the site where the lateral contacts between protofilaments are established. In fact, it has been described that the macrocyclic cores of laulimalide and peloruside stabilize microtubules through lateral interprotofilament contacts. More precisely, the ligands are able to establish lateral contacts with

the H3 helix of the tubulin and have been compared to molecular ‘clamps’ that hold together the protofilaments.^[33] Furthermore, peloruside has been described to stabilize microtubules without inducing axial expansion, as revealed by cryo-EM studies.^[59] Previous results have also implied that laulimalide or peloruside A provide an allosteric contribution to M-loop-mediated lateral contacts in microtubules, as their binding stabilizes structural elements in the proximity of the M-loop. Recent data on laulimalide, peloruside and a series of their derivatives confirmed that these drugs stabilize microtubules only through lateral contacts, without engaging the M-loop. Furthermore, the chemotypes targeting this site did not induce microtubule lattice expansion *in vitro* and were shown to directly alter the angle between protofilaments, contributing to the formation of smaller (in case of peloruside) or larger (in case of laulimalide) microtubules. Therefore, the mechanism of action of laulimalide/peloruside site ligands is clearly different from those of taxane-binding molecules. This could suggest other potential applications of these compounds beyond cancer, e.g. Alzheimer’s disease and other neurodegenerative disorders.^[70]

1.3.3 Microtubule-destabilizing agents

Colchicine-site ligands

Colchicine is a tricyclic alkaloid (Figure 1-13) extracted from the herbaceous plant *Colchicum autumnale*. While discovery of colchicine can be tracked to 3000 years ago, the drug is known to be isolated in the 19th century and included in the pharmacopeia of the time for the treatment of gout.^[72] Since then for many years it has been known as an anti-inflammatory drug for acute gout, also used for Mediterranean family fever, paint joint, pericarditis and Behçet’s disease. Its ability to target tubulin was discovered in 1970s, making it the first compound identified as an MTA.^[34] Potent antimitotic properties, inhibition of cancer cell migration and angiogenesis could suggest the application of colchicine as an anticancer drug. However, its narrow therapeutic index, serious side effects and toxicity preclude its potential use as chemotherapeutic.^[73] However, colchicine tablets are on the market (Colctab[®]), approved for the treatment of acute gout. Since the first colchicine-tubulin crystal structure was published in 2004, many synthetic efforts have been made to investigate the SAR of colchicine alkaloids and their analogues with modified A, B, and C rings, as well as colchicine prodrugs, delivery systems and conjugates. Some of the most famous colchicine analogues include thicolchicine, cornigerine, glycoside analogs colchicoside and thicolchicoside. (reviewed in ^[74]).

Another important class of colchicine site ligands is represented by combretastatins, with combretastatin A4 (CA-4) being the most prominent. It is a natural stilbenoid with strong antimitotic activity, isolated from the African tree *Combretum caffrum*.^[75] CA-4 and its water-soluble phosphate derivative have been evaluated in multiple clinical trials as anticancer drugs.^[76] Like colchicine, CA-4 contains a trimethoxyphenyl ring, one of the most recognizable features of many colchicine site binders. Another crucial feature is its cis-trans isomerism, as the active cis-CA-4 can be isomerized into the significantly less potent trans-

CA-4 isomer. It is worth noting that only the active cis-isomer was found bound in a CA-4 crystal structure in complex with tubulin.^[77] Consequently, the synthesis of the photoswitchable trans-cis CA-4 analogues (Azo-CA4) has been recently described, opening up new possible applications for this class of colchicine site binders, e.g. as probes in the microtubule cytoskeleton research or isomerization-dependent cancer therapy.^[78,79]

Apart from colchicine alkaloids and combretastatins, a variety of chemically diverse ligands targeting the colchicine site has been discovered over the years, with some examples depicted on Figure 1-13.

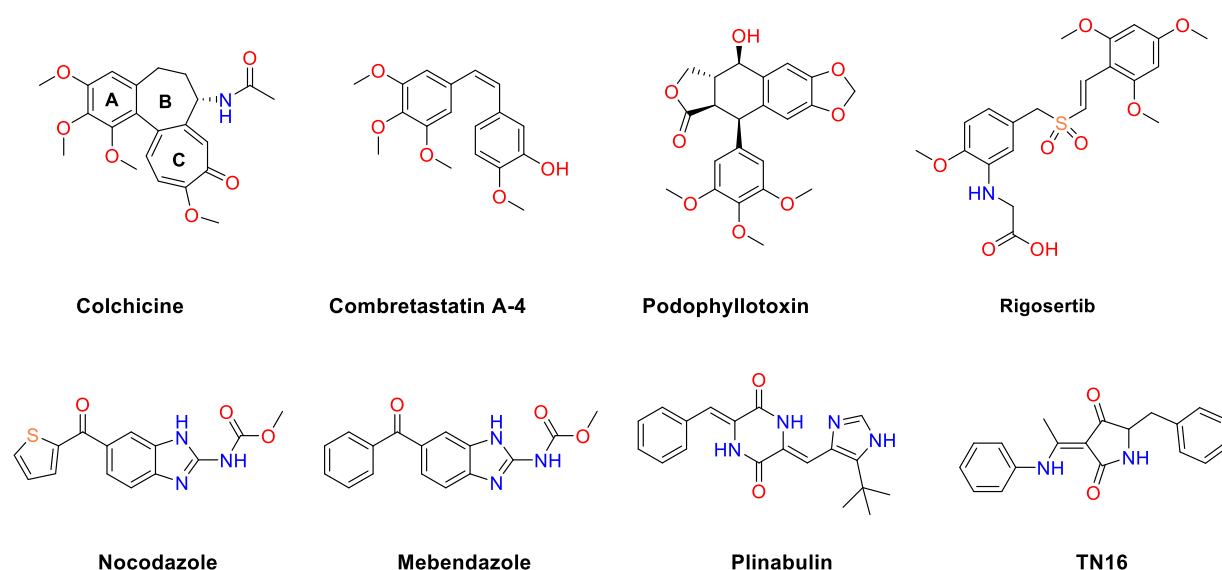


Figure 1-13. Chemical structures of representative colchicine site ligands.

Thus, podophyllotoxin is a non-alkaloid toxin lignan extracted from the roots and rhizomes of the *Podophyllum species*, commonly used to treat warts in topical ointments.^[80]

In its turn, rigosertib is an investigational drug with a potent antitumor activity, evaluated for the treatment of high-risk myelodysplastic syndrome. Interestingly, it was first believed to act as a polo-like kinase 1 (PLK1) inhibitor, and only later its activity has been attributed to microtubule destabilization.^[81]

Nocodazole and mebendazole are both benzimidazole derivatives, the only difference is the that the thiophen ring of nocodazole is replaced by a phenyl ring in mebendazole. However, nocodazole is known as an antineoplastic agent, which is often used as a tool to study microtubule functions, while mebendazole has been long used in the clinics an antihelmintic drug.^[82-84]

Plinabulin was shown to selectively inhibits the $\alpha\beta$ II isotype over $\alpha\beta$ III and is in phase 3 clinical trial for non-small cell lung cancer and chemotherapy-induced neutropenia.^[85]

Lastly, TN16 is a tenuazonic acid derivative, developed as a potential antitumor agent.^[86,87]

These molecules provide examples of the huge variety of colchicine site ligands, their diverse chemical motifs and their use and applications. However, as revealed by extensive structural studies, all of them bind to the same site on tubulin, destabilize microtubule dynamics and share a common mechanism of action.

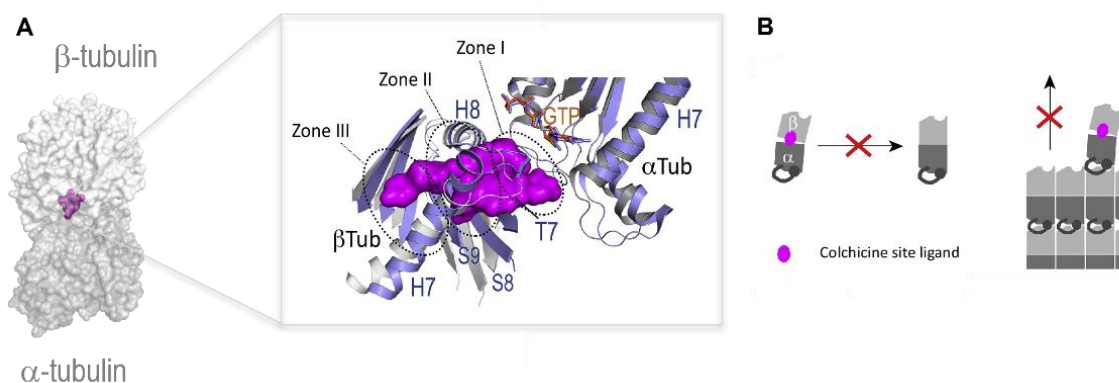


Figure 1-14. (A) Left: localization of the colchicine site on tubulin. Colchicine site ligand is depicted in violet sphere representation, α - and β -tubulin in grey and white ribbon representation, respectively. Right: close-up view of the colchicine site, superimposed in the curved and straight tubulin conformational states. (B) Schematic representation of the general mechanism of action of colchicine site MDA (adapted from ^[34]).

Colchicine site ligands bind to a deeply buried, extended pocket between the α - and β -subunits of the tubulin dimer. It is comprised mostly of hydrophobic residues by helices H7 and H8, the T7 loop, and the S8 and S9 strands of β -tubulin, and the T5 loop of α -tubulin (Figure 1-14). Due to the high structural diversity of the colchicine-site ligands, the site has been divided into three zones.^[33] The central part is known as zone II, surrounded by zone I facing α -tubulin subunit and zone III deeply buried in the β -subunit. The classical colchicine site binders e.g. colchicine and CA-4 occupy zone I and II, while more recent nonclassical compounds occupy zones II and III (e.g. plinabulin).^[88] Under physiological conditions, the ‘curved-to-straight’ conformational transition of tubulin is characterized by the movement of the α T5 loop towards the colchicine site and the flip of β T7 out of the site, eventually leading to an overall contraction of the colchicine site. Upon the ligand binding, the T7 loop switches free up the space to allow the ligand to bind, thus tubulin remains locked in its curved confirmation. Therefore, colchicine site ligands inhibit microtubule polymerization by preventing the curved-to-straight conformational change in tubulin.^[33]

Vinca-site ligands

Vinca alkaloids, originally extracted from the periwinkle plant *Catharanthus rosea* (formely *Vinca rosea*), represent one of the oldest families of tubulin binders. Out of 30 alkaloids isolated from the plant, vinblastine and vincristine were found to be the most biologically active. They are asymmetric dimeric terpenoid indole alkaloids, built from two different terpenoid indole units derived from the precursors vindoline and catharanthine (Figure 1-

15). Both compounds were proved to be effective in treatment of chorioepithelioma, Hodgkin's disease, and other lymphomas, and breast carcinoma.^[89] In the 1970s, vincristine sulfate and vinblastine sulfate were FDA approved for the treatment of Hodgkin's disease, lymphosarcoma, neuroblastoma, breast carcinoma and other types of cancers. Some of their semisynthetic derivatives such as vindesine and vinorelbine (Figure 1-15), have also entered the clinical use with similar indications.^[90]

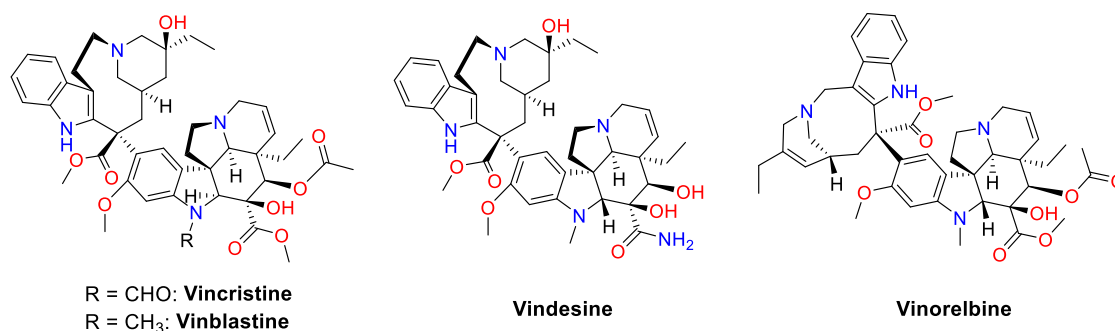


Figure 1-15. Chemical structures of vinca alkaloids.

Eventually, the potent activity of vinca was attributed to their interaction with tubulin. They were found to inhibit microtubule assembly and interfere with the formation of the mitotic spindle, thereby arresting cell growth during metaphase.^[91–93]

With time, other vinca-site targeting agents have emerged, including eribulin, dolastatins and auristatins (representative compounds shown on Figure 1-16).

Eribulin is a simplified synthetic macrocyclic ketone analogue of the natural product halichondrin B, from the marine sponge *Halichondria okada*. Even though its structure has been considered simplified in comparison to that of natural halichondrins, eribulin represents the most complex drug molecule prepared by total synthesis that is either in development or on the market. The structure features a complex ring system and 19 chiral centers, and its total synthesis comprises 62 steps.^[94] Eribulin inhibits the microtubule

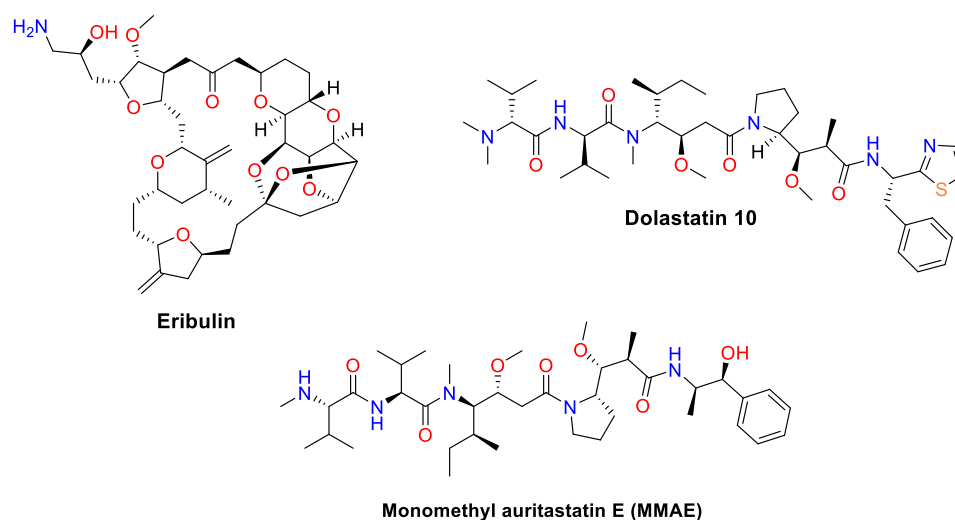


Figure 1-16. Chemical structures of eribulin, dolastatin 10 and monomethyl auristatin E.

polymerization with little or no effect on shortening and sequesters tubulin into non-productive aggregates.^[95]

It showed the potential to overcome acquired drug resistance (e.g. in case of taxane) and has been approved for the treatment of metastatic breast cancer in patients who have been previously treated with a taxane or anthracycline.^[96]

Dolastatins are peptides isolated from the marine mollusc *Dolabella Auricularia*. Initially, dolastatin 10, exhibited cytotoxicity at nanomolar concentrations and showed the most promising antiproliferative properties from the family of dolastatins.^[97] However, its clinical development was stopped due to the serious adverse effects. The synthetic derivatives of dolastatin 10, auritastatins, in particular monomethyl auritastatin E (MMAE), maintained significant potency against tumor lines. While its systemic toxicity is still too high to be used in monotherapy, it has found application as a payload for antibody-drug conjugates (ADCs). Nowadays, MMAE is the most common ADC warhead conjugated to an expanding range of antibodies for oncologic applications. Three MMAE-containing ADCs (brentuximab vedotin, polatuzumab vedotin, enfortumab vedotin) have been approved for the treatment of a number of cancers, while many others are in clinical development.^[98]

The structural basis for the mechanism of action of vinca-site ligands was first revealed by the crystal structure of a tubulin-vinblastine complex, followed by other ligands including eribulin, dolastatins and auristatins.^[33] Vinca site ligands bind to the interdimer interface between two longitudinally aligned tubulin dimers. The interface is formed by the loops T5 and H6–H7 of β -tubulin, and helix H10, sheet S9, and loop T7 of α -tubulin. The bound ligands

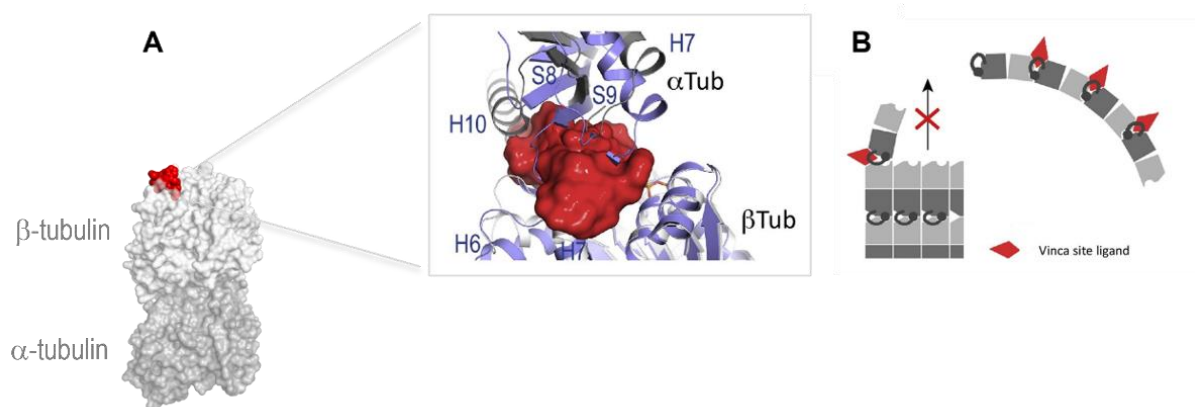


Figure 1-17. (A) Left: localization of vinblastine site on tubulin. Vinblastine site ligand is depicted in dark red sphere representation, α - and β -tubulin in grey and white ribbon representation, respectively. Right: close-up view of the vinblastine site, superimposed in the curved and straight tubulin conformational states. (B) Schematic representation of the general mechanism of action of vinca site MDAs (adapted from ³⁴).

act as a wedge between those two dimers at the tip of microtubules, thus preventing the curved-to-straight conformational change and inhibiting tubulin assembly. Furthermore, they stabilize assembly-incompetent curved tubulin oligomers. (Figure 1-17). As a result, this

leads to mitotic arrest and apoptosis and explains successful application of vinca-site ligands in cancer chemotherapy.^[33,99]

Interestingly, not all ligands binding to the vinblastine site destabilize microtubules. A small series of synthetic triazolopyrimidines was found to bind to the vinca site and stabilize microtubules by acting on longitudinal tubulin contacts. This can be explained by their compact structure and small size, due to which they are unable to act as classical vinca-site wedges.^[100]

Maytansine-site ligands

Maytansine is a natural product isolated from *Maytenus ovatus*; it has a 19-member ansamacrolide attached to a chlorinated benzene ring (Figure 1-18). Maytansine is a highly potent antimitotic agent that exerts an antiproliferative effect by inhibiting microtubule assembly upon binding to tubulin.^[101–103] Despite a promising *in vitro* profile, clinical trials with maytansine in cancer patients failed because of poor efficacy and unacceptable systemic toxicity.^[104,105] Although the narrow therapeutic window precluded further clinical development of the parent compound, maytansine, its derivatives were successfully developed as cytotoxic payloads. Two thiol-containing maytansinoids, emtansine (DM1) and ravtansine (DM4) found clinical application as ADCs. DM1-containing trastuzumab emtansine (Figure 1-18) entered the clinics for the treatment of HER2 positive breast cancer

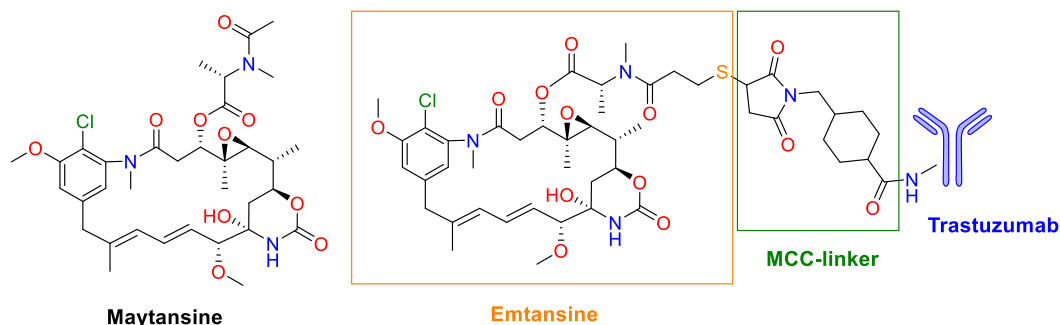


Figure 1-18. Chemical structures of maytansine and antibody-conjugated maytansinoid emtansine. DM1 is attached to trastuzumab through a non-reducible thioether linker, (4-[N-maleimidomethyl]cyclohexane-1-carboxylate, MCC).

in 2013, while DM4-containing mirvetuximab soravtansine was FDA-approved for the treatment of platinum-resistant epithelial ovarian cancer in late 2022. Initially, biophysical experiments showed maytansine competition with vincristine for binding, and for a long time it was believed to bind to the vinca site on β -tubulin.^[106] In 2014, the high-resolution

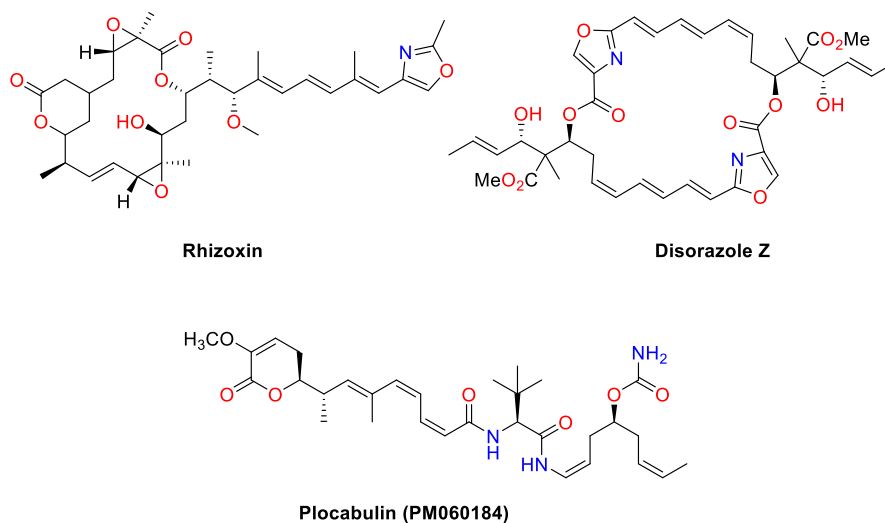


Figure 1-19. Chemical structures of maytansine-site binders rhizoxin, disorazole Z and plocabulin.

crystal structure of the tubulin-maytansine complex clarified that maytansine binds to a distinct site from the vinca domain site. Similarly, it elucidated the previously unclear binding modes of rhizoxin, a macrolide antibiotic isolated from the fungus *Rhizopus chinensis*^[107,108], and plocabulin (PM060184), isolated from the marine sponge *Lithoplocamia lithistoides* (Figure 1-19).^[109] These ligands bind to a site located on an exposed longitudinal interdimer interface of β -tubulin, closely to the nucleotide binding site. The shallow site is shaped by hydrophobic and polar residues of helices H3', H11, and H11', as well as the loops T3, T5 and H11-H11' of β -tubulin. Maytansine-site ligands bind independently of the conformational

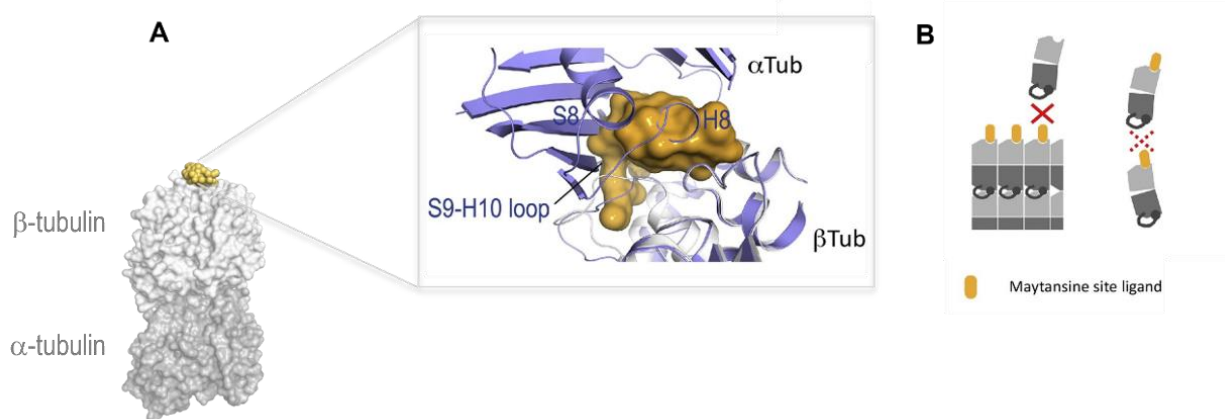


Figure 1-20. (A) Left: localization of maytansine site on tubulin. Maytansine site ligand is depicted in light orange sphere representation, α - and β -tubulin in grey and white ribbon representation, respectively. Right: close-up view of the maytansine site, superimposed in the curved and straight tubulin conformational states. (B) Schematic representation of the general mechanism of action of maytansine site MDAs (adapted from ³⁴).

state of tubulin. By binding to the plus ends of growing microtubules, they directly block the longitudinally exposed surface of β -tubulin and hinder the additions of further tubulin dimers to the microtubule end. Furthermore, at high concentrations some maytansine-site ligands can bind to unassembled tubulin subunits and form assembly incompetent tubulin–

drug complexes. Among them, Plocabulin was also shown to induce tubulin ring-like oligomers.^[33,110,111]

Interestingly, rhizoxin and plocabulin have both been investigated in clinical trials as chemotherapeutics. Although the development of rhizoxin was discontinued, plocabulin is still evaluated in phase I and II clinical trials for advanced malignancies.^[112–114]

In 2018, additional maytansine site-ligands, spongistatin-1 and disorazole Z, were identified using a fluorescence anisotropy-based assay with a fluorescent FcMaytansine probe. The authors demonstrated high affinity of maytansine-site ligands towards β -tubulin, (in the nanomolar range) and solved their crystal structures in complex with tubulin.^[115] Spongistatin-1 is a macrocyclic lactone, isolated from the marine sponges *Spirastrella spinispirulifera* and *Hyrtios erecta*; it is known as an experimental chemotherapeutic agent.^[116] Disorazole Z is a 24-membered macrocycle obtained from the myxobacteriagenus *Sorangium* with antifungal and cytotoxic activity (described in the patent EP 1743897 A1).

Pironetin-site ligand

Pironetin, initially extracted from fermentation broths of *Streptomyces* strains a growth plant regulator, is currently the only natural compound known to bind to α -tubulin.^[117] It has a unique structure, strikingly different from other known MDAs: an α/β unsaturated substituted lactone and an alkyl side chain comprising 6 stereogenic centers in total (Figure 1-21). Several total syntheses of this compound have been reported in the literature.^[118–121] By inhibiting microtubule assembly, pironetin arrests cell cycle progression in the M phase

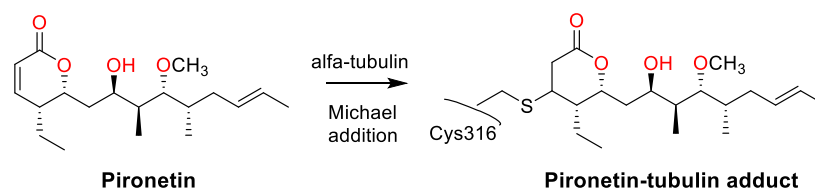


Figure 1-21. Chemical structure of pironetin and its covalently bound form to Cys316 of α -tubulin, respectively

of mitosis and exhibits antitumor activity by inducing apoptosis.^[122] The crucial property of pironetin is its ability to covalently bind to α -tubulin by Michael addition via its α,β -unsaturated δ -lactone. In 2004, the first experiments to determine the covalent binding of pironetin used biotinylated pironetin as a probe. Based on peptide sequencing of biotinylated pironetin bound to tubulin, followed by site-directed mutagenesis and molecular modelling, pironetin was reported to covalently target α Lys352.^[123] However, in 2016, two crystal structures of a pironetin-tubulin complex were solved independently, and both revealed the covalent binding of pironetin to Cys316 of α -tubulin, and not α Lys352, as previously reported. This was also confirmed by mass spectroscopy studies using the pironetin itself (Figure 1-21).^[124,125]

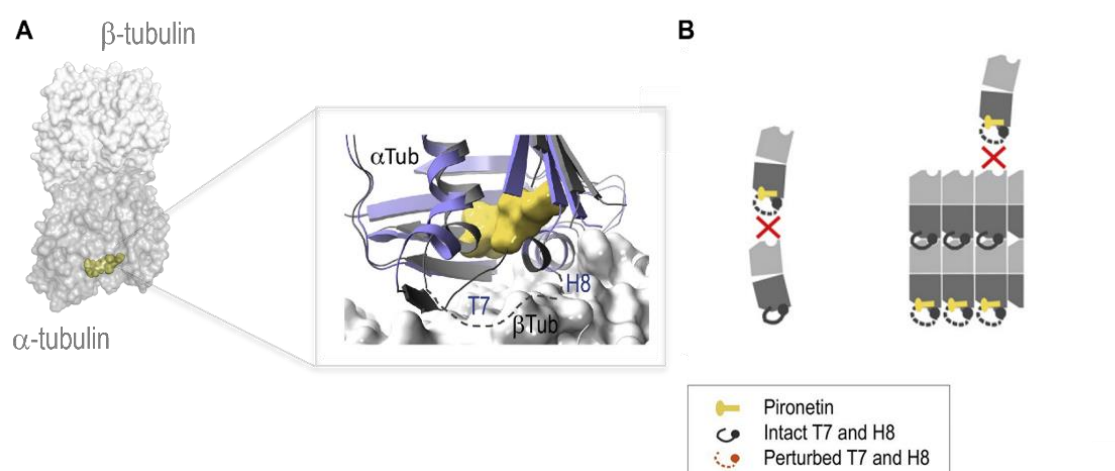


Figure 1-22. (A) Left: localization of pironetin site on tubulin. Pironetin is depicted in yellow sphere representation, α - and β -tubulin in grey and white ribbon representation, respectively. Right: close-up view of the pironetin site, superimposed in the curved and straight tubulin conformational (adapted from ³⁴). The pironetin molecule is shown in stick representation and α - and β -tubulin in ribbon. Secondary structural elements involved in protein–compound interactions are depicted in blue. (B) Schematic representation of the general mechanism of action of pironetin (adapted from ¹²⁵).

Pironetin was found to bind to an extended hydrophobic pocket on α -tubulin. Its lactone ring is surrounded by the residues of strands S8 and S10, and with helix H7, whereas the alkyl sidechain is further buried in a pocket shaped helix H7 and by strands S4, S5, and S6. The binding of pironetin perturbs both the T7 loop and helix H8 of α -tubulin, two crucial secondary structural elements for the establishment of longitudinal tubulin contacts in microtubules. In a pironetin-bound state, further tubulin dimers cannot be added to neither of the exposed plus and minus ends of microtubules. Furthermore, at high ligand concentrations pironetin can form the assembly incompetent tubulin–pironetin complexes (Figure 1-22).^[33,124]

Covalent drugs have been of high interest in drug discovery, and such a potent, covalent microtubule destabilizer as pironetin has certainly caught attention of researchers. However, its major drawback is its high cytotoxicity, and so far, multiple efforts to modify the pironetin structure in an attempt to improve its properties have resulted in failures. As of today, pironetin still remains the only compound that targets α -tubulin exclusively.

Gatorbulin-site ligand

Gatorbulin-1 is cyclodepsipeptide, isolated from a marine cyanobacteria *Lyngbya cf. confervoides* and first reported in 2021. Using an isogenic screening campaign, the Hendrik Luesch's group isolated gatorbulin-1 and determined its structure by a comprehensive NMR analysis. This pentapeptide possesses a series of unusual structural features, such as a cyclic hydroxamate moiety, C-hydroxylated, and dehydroamino acids, and a modified proline (Figure 1-23A). The authors reported its total synthesis, starting from epoxysuccinic acid, obtaining the final compound in 20 steps with an overall yield of 5.6%. Finally, to identify the biological target and a mechanism of action of gatorbulin-1, the compound was subjected

to comprehensive biochemical and structural studies. Gatorbulin-1 has demonstrated strong antiproliferative activity against HCT116 colorectal cancer cells, and induced G2/M cell cycle accumulation, characteristic for antimetabolic agents. Interestingly, its N-deoxy derivative, gatorbulin-2, lacked this activity, indicating that the hydroxamate moiety is critical for the activity.

Gatorbulin-1 was then shown to directly inhibit tubulin polymerization *in vitro* and to bind tubulin to a novel, seventh binding site on tubulin, as revealed by the gatorbulin-1-tubulin crystal structure. The gatorbulin binding site is located at the intradimer interface between

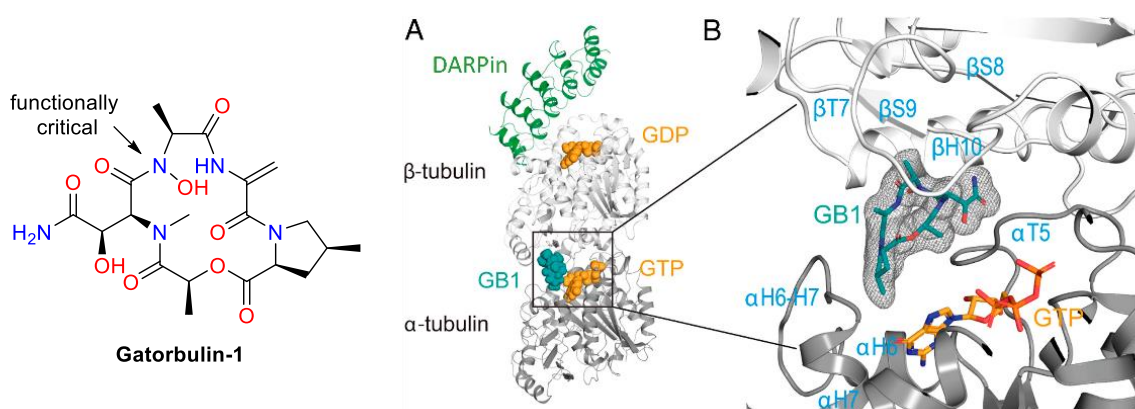


Figure 1-23. (A) Chemical structure of gatorbulin-1. (B) Crystal structure of TD1-gatorbulin complex. Left: Overall view of the TD1-GB1 complex (PDB ID: 7alr). Gatorbulin-1 and nucleotides are depicted in green and yellow sphere representation, α - and β -tubulin in grey and white ribbon representation, respectively. Right: close-up view of the gatorbulin site. The gatorbulin molecule is shown in stick representation and α - and β -tubulin in ribbon. Secondary structural elements involved in protein-compound interactions are depicted in blue.

α - and β -tubulins, closely to the colchicine site. It is shaped by the T7 loop, helix H10, and S9 strand of β -tubulin, and by T5, H6-H7 loops of α -tubulin (Figure 1-23B). Interestingly, gatorbulin-1 and colchicine cannot bind tubulin simultaneously, as they share some of the interactions. However, in comparison to colchicine site ligands, gatorbulin-1 was shown to establish more extensive interactions with α -tubulin. The mechanism of action underlying the microtubule destabilization of gatorbulin-1 is similar to that of vinblastine: it introduces a wedge inhibiting the longitudinal interactions between tubulin dimers and thus preventing further addition of tubulin subunits to a microtubule.

Todalum site ligands

Todalum binds to the eighth, the newest small molecule binding site characterized on tubulin.^[35] In contrast to other MTAs, most of which are natural products or their derivatives, Todalum is the first rationally designed small molecule MTA. The design of Todalum and its analogues was based on a previously performed crystallographic fragment screen, which allowed to identify 56 chemically diverse fragments that bound a total of 10 distinct sites in tubulin, six of which were novel^[36] (p. 9, Figure 1-7). Based on both the structural and chemical considerations, three fragments, identified at the interdimer interface, were

chosen as a starting point for “growth” into a fully functional microtubule inhibitor. It is important to note that the selected fragments on their own are not cytotoxic and do not have any activity on tubulin polymerization. Taking into consideration the synthetic feasibility, a series of new compounds was rapidly generated via one-step Hantzsch aminothiazole synthesis. The synthesized compounds were assessed using cytotoxicity

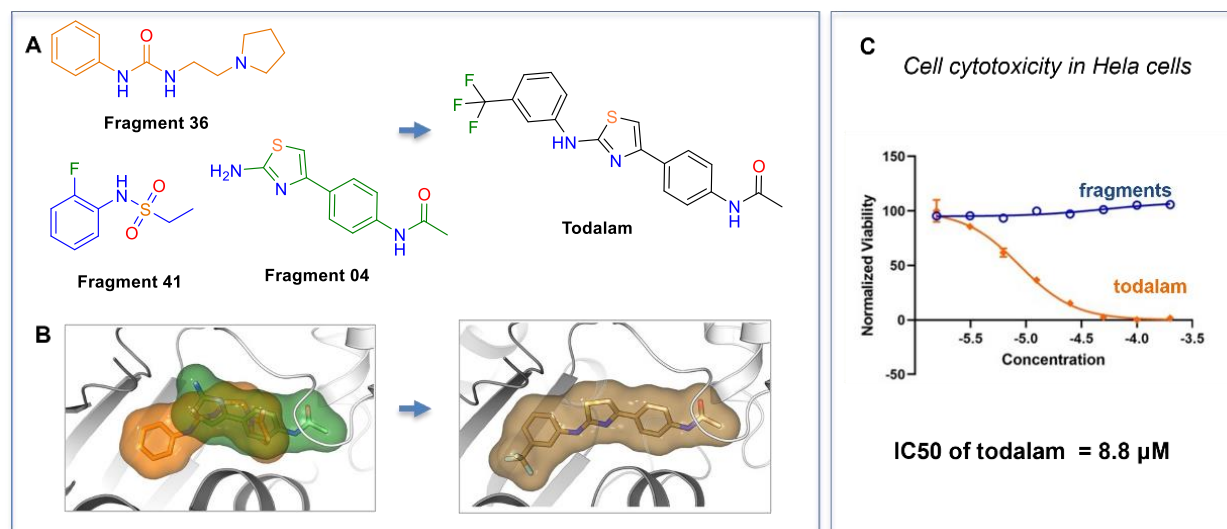


Figure 1-24. (A) The chemical structures of fragments which served as starting points for the development of Todalam and the Todalam itself. (B) The binding mode of the individual fragments and Todalam. The molecules are shown in sticks and surface representations. (C) The cell cytotoxicity graph, comparing the cell viability of fragments and Todalam in HeLa cells.

assays in HeLa cells and their ability to bind tubulin in X-ray crystallography experiments. In total, two rounds of optimization were performed, finally yielding the most active compound of the series, termed Todalam (Figure 1-24). This compound displayed an IC_{50} value of 8.8 μM . The presence of a *m*-trifluoromethyl substituted phenyl ring in its structure is most likely responsible for its activity, as its analogue without any substitutions in the phenyl ring displayed a much lower IC_{50} value of 50 μM .

Todalam binds to tubulin in between two longitudinally aligned tubulin dimers. Therefore, part of its binding site is located on α -tubulin, the other on β -tubulin. More precisely, the pocket is shaped by the sheets S4, S5 and helix H8 of α -tubulin, and the T3 loop and H11' of β -tubulin (Figure 1-25). Todalam destabilizes microtubules by acting as a “molecular plug” that sterically hinders the curved-to-straight conformational change in the α -tubulin subunit. By binding to tubulin, it blocks the shift of the α H8 helix, needed for the proper addition of the next tubulin dimer to growing microtubules. In addition, it can inhibit microtubule assembly by promoting the formation of ring-like assembly incompetent oligomers.

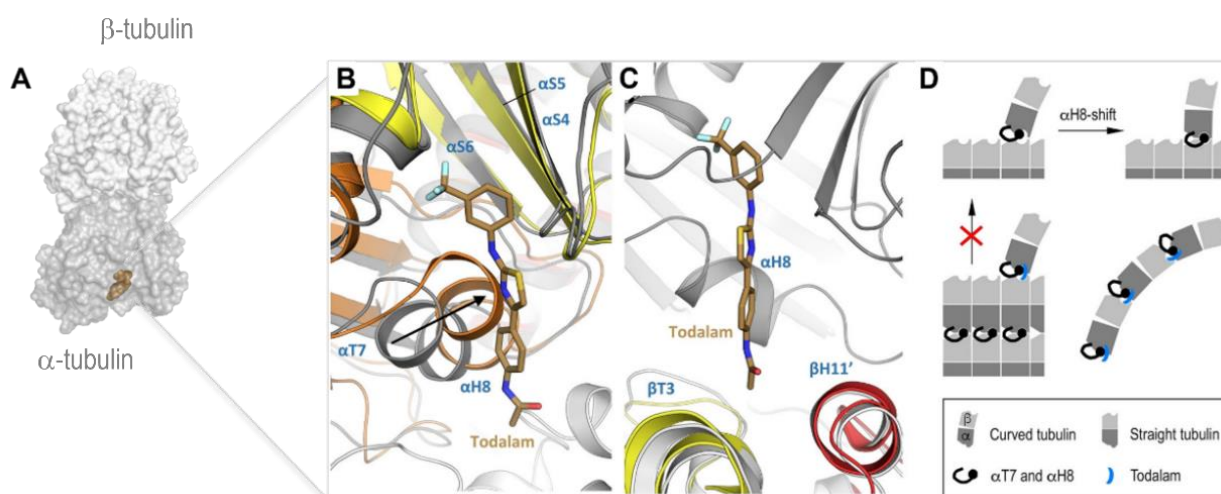


Figure 1-25. (A) Left: localization of Todalam site on tubulin. Todalam is depicted in light brown sphere representation, α - and β -tubulin in grey and white ribbon representation, respectively. (A, B) Close-up view of the Todalam site, superimposed in the curved and straight tubulin conformation. The curved conformational states of the α - and β -tubulin subunits are shown in grey and white ribbon representation, respectively. The straight states of tubulin monomer (PDB ID 6DPV) are colored accordingly: N-terminal domain in yellow, intermediate domain in orange, and C-terminal domain in red. Secondary structure elements are labelled in blue. The black arrow in panel A indicates the movement of helix α H8 during the curved-to-straight conformational transition of the tubulin dimer. (C) Schematic representation of the general mechanism of action of Todalam.

Additional experiments of Todalam were done to determine its effect on tubulin and microtubules *in vitro* and in cells. Todalam was shown to kill different type of mammalian cells, to induce G2/M arrest and to disrupt cellular microtubule networks. Moreover, it was reported to act in a synergistic manner in combination with vinblastine to inhibit cell growth.^[35] The story of Todalam has opened up new horizons in the field, showing that the use of crystallographic screening for hit discovery, structural simplicity and straightforward synthesis, are also applicable to tubulin binders.

1.4 THERAPEUTIC APPLICATIONS OF MICROTUBULE-TARGETING AGENTS

1.4.1 MTAs as chemotherapeutics

Microtubules form the mitotic spindle during mitosis; their dynamic instability to a large extent determines the shape of the mitotic spindle and is essential for the proper alignment of chromosomes. There is increasing evidence that even minor alterations of microtubule dynamics can block the progression of the cell cycle.^[126] Both MSAs and MDAs perturb microtubule dynamics by binding to microtubules and, as a result, inhibit cell proliferation, which makes them good candidates for cancer treatment. Many of them have been successfully used as chemotherapeutics, including paclitaxel (Taxol[®]), docetaxel (Taxotere[®]), eribulin (Halaven[®]) or vinca alkaloids.^[127] The overview of MTAs approved for the treatment of cancer is provided in Table 1.

Although MTAs are often effective in many types of cancers, administration of the classical tubulin binders is often connected with serious adverse effects. This can be simply explained by their mechanism of action. The cells are most vulnerable in the mitosis phase, that is why cancer cells, which divide continuously and excessively, are the most targeted. However, considering the presence of microtubules in all cell types and their multiple cellular functions chemotherapeutic agents often cannot distinguish between normal and cancer cells. Some of the serious side effects include neutropenia, because of cytotoxicity on hematopoietic precursor cells, and peripheral neuropathy, due to the critical role of microtubules in neuronal function, as well gut toxicity and alopecia. Additionally, many of the tubulin binders are often insoluble and the vehicles used for their administration can contribute to the worsening of the adverse effects. Nowadays, at the age of personalized and targeted medicines, optimization of MTAs drug delivery and distribution has become an important direction in anticancer therapy research. Some of the modern drug delivery systems include e.g. albumin nanoparticles (paclitaxel, Abraxane®), albumin bound nanoparticles (paclitaxel, Pazenir®), liposomes (vincristine, Marquibo®) and microspheres.^[128] Furthermore, many of the MTAs are nowadays used in ADCs as cytotoxic payloads, as a part of the targeted therapy for treating cancer.^[129]

Another major issue is the occurrence of resistance to MTAs. Many of the MTAs are susceptible to MDR and are pumped out of the cell by P-gp. Another important mechanism of MTAs drug resistance is the upregulation of some less-sensitive β -tubulin isotypes, e.g. β III.^[130] In consequence, the search for isotype-specific tubulin binders has become very relevant.

Table 1. MTAs used in clinics as chemotherapeutics (according to <https://www.ema.europa.eu/> and <https://www.fda.gov/>, 19/01/2023)

Drug	Indication
Paclitaxel (Taxol®), (Abraxane®), (Pazenir®)	metastatic breast cancer, advanced ovarian carcinoma, metastatic adenocarcinoma of the pancreas, non-small cell lung cancer, AIDS-related Kaposi's sarcoma
Docetaxel (Taxotere®), (Docetaxel Kabi®)	breast cancer, non-small cell lung cancer, metastatic prostate cancer, gastric adenocarcinoma
Cabazitaxel (Jevtana®), (Cabazitaxel Accord®)	metastatic resistant prostate cancer
Ixabepilone (Ixempra®),	breast cancer that is locally advanced or metastatic

*FDA approved, *EMEA withdrawn	
Vinblastine sulfate	Generalized Hodgkin's disease, lymphocytic and histiocytic lymphomas, Mycosis fungoides (advanced stages), advanced carcinoma of the testis, Kaposi's sarcoma, Letterer-Siwe disease
Vincristine sulphate (<i>Marquibo</i> ®)	Hodgkin's disease, non-Hodgkin's malignant lymphomas, rhabdomyosarcoma, neuroblastoma, Wilms' tumor, Philadelphia chromosome-negative (Ph-) acute lymphoblastic leukemia
Vinflunine (<i>Javlor</i> ®)	adults with advanced or metastatic 'transitional-cell carcinoma of the urothelial tract'
Vinorelbine (<i>Navelbine</i> ®)	In combination with cisplatin for first-line treatment of patients with locally, advanced or metastatic non-small cell lung cancer (NSCLC) As a single agent for first-line treatment of patients with metastatic NSCLC
Eribulin (<i>Halaven</i> ®)	locally advanced or metastatic breast cancer which has continued to spread after at least one previous treatment for advanced cancer, adults with advanced or metastatic liposarcoma
brentuximab vedotin (<i>Adcetris</i> ®)	Hodgkin's lymphoma, systemic anaplastic large cell lymphoma, cutaneous T-cell lymphoma
polatuzumab vedotin (<i>Polivy</i> ®)	adults with non-responsive diffuse large B-cell lymphoma (DLBCL)
Trastuzumab emtansine (<i>Kadcyla</i> ®)	advanced or metastatic breast cancer in adults who previously received trastuzumab and a taxane
Mirvetuximab Soravtansine-gynx (<i>Elahere</i> ®)	positive, platinum-resistant epithelial ovarian, fallopian tube, or peritoneal cancer
*FDA approved in November 2022	

1.4.2 MTAs as antiparasitic and antifungal drugs

The antimetabolic activities of tubulin binders can also be applied to arrest parasite replication. The crucial requirement is the specificity so that the antifungal or antiparasitic drug should not disturb the healthy cells of human or animal host.

Benzimidazoles such as albendazole and mebendazole are known as anthelmintic and antifungal tubulin binders. They bind to the colchicine site and inhibit the tubulin polymerization of parasite cells at much lower concentration than that of mammalian cells. They are in clinical use for a wide range of parasite infections, including ascariasis, giardia, pinworm infection, hookworm infection etc.^[131,132] Moreover, as shown by a recent study, mebendazole and albendazole also show activity for viral infections of DNA and RNA viruses, including SARS-CoV-2.^[84]

Other selective tubulin binders are represented by dinitroanilines and griseofulvin. Dinitroanilines efficiently bind to the tubulins of plant or protozoan origin but have little to

no effect on the mammalian or fungal tubulin. In its turn, griseofulvin is a widely used oral antifungal agent, it strongly inhibits the growth of fungal cells and weakly of mammalian cells.^[133]

Recently, an anti-tubulin drug specifically targeting the Apicomplexa parasites (causing malaria, toxoplasmosis, and cryptosporidiosis), has also been described. Based on X-ray

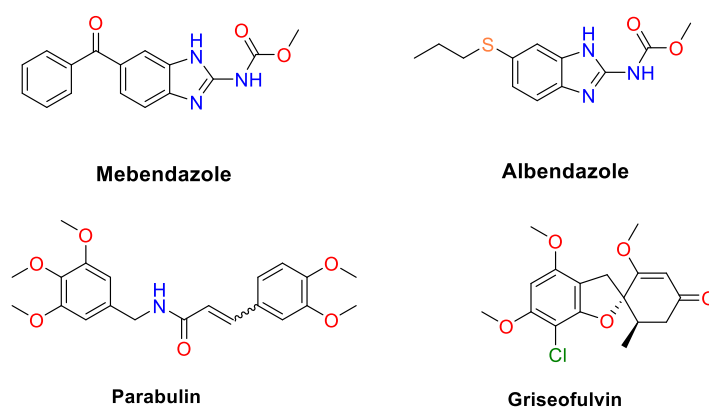


Figure 1-26. Chemical structures of antiparasitic (mebendazole, albendazole, parabulin) and antifungal (griseofulvin) MTAs.

crystallography and cryo-electron microscopy, the authors analyzed the structure of *T. thermophila* tubulin, structurally similar to Apicomplexa, and compared it to the known ligand binding sites of the mammalian tubulin. This allowed to identify significant differences in the colchicine site and rationally design of a species-specific tubulin inhibitor, parabulin. The drug binds to the colchicine site of parasite tubulin. It specifically inhibits the growth of protozoan parasites and blocks the microtubule formation in vitro, while displaying no effects on human cells.^[134]

1.4.3 MTAs in neurodegeneration

*This subchapter is a part of the publication:

Microtubule-Targeting Agents and Neurodegeneration. Z. Bojarska, D. Passarella. *Drug Discovery Today*, 2020, 26, 604-615

Dysregulation of microtubule (MT) dynamics has been observed in a range of neurodegenerative diseases. It is reflected in the defects of microtubule-dependent neuronal functions, especially notable by the worsening of axonal transport i.e. in Alzheimer's disease, Parkinson's disease, Amyotrophic Lateral Sclerosis (ALS), Huntington's disease (HD) and Hereditary spastic paraplegia (HSP).^[135] Microtubule disruption was one of the first detectable changes occurring in Wallerian degeneration and was shown to accompany axonal retraction.^[136] Moreover, MT dysfunction preceded transport impairment and mitochondria damage in methyl-4-phenylpyridinium (MPP⁺)-induced neurodegeneration.^[137] Other data suggest that dynamic microtubules take part in the

regulation of synaptic plasticity and dendritic spine morphology.^[138] Importantly, consistent results were obtained in patient-derived cells. Microtubule destabilization, represented by reduced MT mass, increased fraction of unpolymerized tubulin and significant changes in MT-related signaling pathways was observed both in the fibroblasts of patients with genetic and idiopathic parkinsonism.^[139] Furthermore, *in vitro* experiment demonstrated that imbalance between dynamic and stable microtubules underlies 2,5-hexanedione-induced parkinsonism. Exposure to the toxin induced significant changes in microtubule stability in PD patients fibroblasts, whereas it didn't affect healthy donor fibroblasts.^[140] Another study detected microtubule defects in mesenchymal stromal cells in patients with Progressive Supranuclear Palsy, PSP. Alterations included significantly decreased MT mass, imbalance in α -tubulin post-translational modifications and MT stability.^[141]

The concept of microtubule-stabilizing drugs for neurodegeneration was first proposed by Lee et al. in 1994, primarily with regard to AD.^[142] Since then, several tubulin binders have been proven to be neuroprotective in various models of neurodegeneration. Although microtubule stabilization has been the leading strategy, recent findings suggest potential benefits of microtubule destabilizing agents. Interestingly, at very low concentrations MDAs “kinetically stabilize” microtubules and induce effects similar to those of MSAs.^[127,143]

So far, eight tubulin binders have been characterized in preclinical or clinical studies for the treatment of neurodegenerative disorders (Figure 1-27, Table 2).

Paclitaxel was the first tubulin binder to be investigated in animal models of neurodegeneration. Consideration of paclitaxel use in neurodegenerative disorders initially started in 1998, when it was shown to protect primary neurons against amyloid-induced toxicity^[144]. A few years later *in vivo* study demonstrated proof-of-concept for microtubule-targeting strategy, as paclitaxel reversed fast axonal transport deficits in mouse tauopathy model.^[145] More precisely, this effect was revealed in spinal axons after 12-week paclitaxel treatment, while other observations included increase in both overall number of MT as well as stable (detyrosinated) tubulins and amelioration of motor impairments. Subsequent experiments noted rescue of neurons from tau-induced hallmark cell pathologies and synaptic weakening by paclitaxel.^[146,147] It was also demonstrated that it is able to rescue degenerating neurons in okadaic acid-induced tau phosphorylation, reversing the decrease in axonal outgrowth and branching, and preventing neuronal growth cone collapse^[148]. Moreover, paclitaxel effectively reduced α -synuclein oligomer accumulation in cybrid cell lines generated from patients affected by idiopathic Parkinson's disease.^[149]

Although the results obtained from paclitaxel studies proved that microtubule stabilizing agents could be therapeutically beneficial in neurodegeneration, numerous limitations prevented further development of this compound. First of all, due to its poor brain permeability the results obtained from *in vivo* studies cannot be translated to human trials. It's worth noting that in above-described *in vivo* experiment paclitaxel presumably accessed

spinal motor neurons through uptake from the neuromuscular junction without the need to cross the blood–brain barrier, while in neurodegenerative diseases pathologies are predominantly found in the brain and therefore BBB penetration is essential. Other concerns include poorly water solubility, susceptibility to P-glycoprotein and high toxicity, resulting in serious adverse effects, such as peripheral neuropathy, anaphylaxis and severe hypersensitivity.^[150]

The search for brain-penetrant compounds with paclitaxel-like activity has led to epothilones. One of the most prominent members of the epothilone family considered for treatment of neurodegenerative diseases is epothilone D. The first attempt to define its potential for neurodegeneration was performed in 2010 by Brunden et al. They demonstrated that low concentrations of epothilone D were able to significantly improve CNS MT density, axonal integrity and cognitive deficits in Tg mouse models of tauopathy without inducing notable side-effects^[151]. In addition, this compound was found to have favorable pharmacokinetic and pharmacodynamic properties such as longer brain than plasma half-life, prolonged accumulation within the CNS and ability to elicit delayed increase in acetyl-tubulin levels at very low doses^[152]. A series of further studies confirmed beneficial effects of epothilone D on microtubule dynamics, cognitive deficits and Alzheimer-like pathology in other *in vivo* models of tauopathies^[153,154]. Importantly, EpoD has proven to affect all the key features of AD neurodegenerative triad, as demonstrated by reduction of hippocampal neuronal loss (*in vivo* models with preexisting tau pathology) and A β -mediated spine changes as well as induced dendritic simplification (*ex vivo* AD model).^[153,155,156] In 2012 the compound was taken to clinical trials by Bristol-Myers Squibb and evaluated in patients with mild Alzheimer's disease however, despite promising results in preclinical studies, the trial was discontinued (NCT01492374). Presumably frequency and severity of adverse effects were the reasons behind this outcome, but more data is needed to address the grounds for discontinuation.

Apart from Alzheimer's disease and related tauopathies, the efficacy of epoD was examined in such disorders as PD, HSP and ALS as well as neurodegeneration following spinal cord and traumatic brain injuries. Thus, the neuroprotective effect of epothilone D was observed in MPTP-induced mouse models of Parkinson's disease. The study showed that exposure to 1-methyl-4-phenyl-1,2,3,6-tetrahydropyridine (MPTP) leads to early alterations of MTs, specifically affecting MT stability in dopaminergic neurons, and that repeated daily administrations of EpoD are able to rescue those MT defects and attenuate MPTP-induced nigrostriatal degeneration^[157]. Another interesting finding was reported recently, suggesting that EpoD interferes with microglial cell migration and, as a result, inhibits microglia-mediated spread of α -synuclein aggregates^[158]. This study was initially designed for Multiple System Atrophy (MSA), however, considering that widespread α -syn aggregation is also characteristic for patients with PD, one could elaborate on its significance both for MSA and PD and further explore that matter.

More data regarding activity of epoD comes from studies on patient-derived stem cells of Hereditary Spastic Paraplegia. Low doses of the drug restored acetylated α -tubulin levels and rescued microtubule-based peroxisome trafficking deficits, caused by spastin (microtubule-severing ATPase) mutations ^[159].

Although multiple studies prove great potential of epothilone D, as described above, we must acknowledge that some results are not completely straightforward. This happens to be the case for EpoD application in Amyotrophic Lateral Sclerosis. Therapeutic administration of EpoD was found to exert both beneficial and detrimental outcomes in the mouse model ALS ^[160]. A very recent study aimed to evaluate the dose dependent impact of Epothilone D on immature and mature mouse cortical neurons *in vitro*. It demonstrated that even though low, sublethal concentrations of this compound may not affect neuronal survival and viability during short treatment periods, they could impair normal neuronal growth and alter mitochondrial transport over time. Increasing concentrations were shown to exert progressive detrimental effects ^[161].

Epothilone B is another member of taxol-site tubulin binders that has been addressed in terms of its potential for neurodegenerative diseases. Similar to epothilone D, this analogue has a favorable PK and blood-brain barrier (BBB) permeability ^[162]. Key findings regarding pharmacological activities of EpoB in CNS were reported by Ruschel et al. in 2015, demonstrating its ability to promote axon regeneration and improve motor function after spinal cord injury. It was stated that enhanced axonal growth took place as a result of induced microtubule polymerization at the axon tips, therefore highlighting the link between axonal regeneration and microtubule dynamics ^[163]. Consistent results were obtained in a model of spinal root avulsion, as administration of EpoB promoted axonal regeneration and motor functional recovery ^[164]. Further evidence of EpoB-mediated neuroprotection was found in models of Parkinson's disease, with both *in vitro* and *in vivo* data presented. The findings indicated that EpoB protected nigrostriatal dopaminergic neurons against 6-hydroxydopamine(6-OHDA)-induced neurotoxicity, restored DA level in the striatum and improved motor performance in mouse models of parkinsonism. The underlying mechanism was then investigated *in vitro*, suggesting that beneficial effect of EpoD on DA neurons occurs through attenuation of activated microglia ^[165]. Interestingly, another study described both beneficial and negative effects of epothilone B, depending not only on drug concentration, but also type and age of treated neurons. For example, picomolar concentrations of the drug markedly promoted axon growth in young DRG and cortical neurons, while inducing opposite effect in adult sensory neurons. However, micromolar concentrations exerted neurotoxicity, preventing axon growth in all types of neurons tested ^[166].

Dictyostatin was also investigated as a potential candidate for neurodegenerative diseases, in an attempt to select additional CNS-active MT-stabilizing agents that could become alternatives to EpoD. Hence, BBB permeability and PK properties of two MT-stabilizing

natural products, dictyostatin and structurally related discodermolide, were evaluated. This study demonstrated that dictyostatin, in contrast to discodermolide, effectively crosses the blood–brain barrier and exhibits prolonged brain retention, particularly desirable for the treatment of Alzheimer’s disease and other tauopathies. Moreover, a single administration of dictyostatin at relatively low doses exerted prolonged MT stabilization in wild-type mice, as revealed by significantly increased AcTub levels ^[167]. Brunden and his team then carried on to test this compound in tau Tg mouse models of tauopathy. Mice treated with low doses of dictyostatin displayed beneficial effects resembling those of EpoD, such as improved MT density, reduced axonal dystrophy and reduction of tau pathology. However, higher concentrations led to gastrointestinal (GI) complications and loss of some experimental animals, providing evidence of dose-limiting peripheral side effects (efficacy analyses for those groups weren’t conducted) ^[168].

Peloruside A was reported to significantly increase axonal length and branching in neurons treated with okadaic acid, used as a model of AD. Moreover, the drug effectively rescued neurons from growth cone collapse and restored the levels of AcTub, even though it did not have effect on tau hyperphosphorylation.^[148] In addition, a study in mouse N2a neuroblastoma cells demonstrated that PelA stabilizes microtubules independently of tau overexpression, in contrast to paclitaxel and ixabepilone, which effects are masked by the presence of extra tau in the cell. The authors suggested that a non-taxoid drug like PelA might be more suitable for treatment of conditions with high/altered tau expression.^[169] To further explore this hypothesis, they compared the effects of Ptx and PelA on mitochondrial trafficking in cortical neurons overexpressing tau. Even though both compounds were able to partially reverse the blocked mitochondrial transport, the PelA response was better than one of Ptx.^[170] Although these outcomes are encouraging, the potential application of PelA in neurodegeneration will depend on its BBB penetration, which has yet to be determined.

One of the vinca alkaloids, vinblastine, has demonstrated beneficial effects in models of Hereditary Spastic Paraplegia. Administered at a low concentration, it was shown to significantly attenuate neurodegenerative phenotypes in a *Drosophila* model of HSP. ^[171]. Subsequent studies both in mice and human neuronal models of HSP described the efficacy of vinblastine to ameliorate disease-specific axonal defects, specifically highlighting its ability to reduce axonal swellings. ^[172,173]

TPI-287, a third generation taxane developed by Tapestry Pharmaceuticals (US patents: US7879904 and US7745650), can cross the blood-brain barrier and overcome P-glycoprotein mediated resistance. Similarly to EpoD and dictyostatin, TPI-287 tends to accumulate in the brain over plasma. For what concerns its effect on MT stability, it was shown to promote microtubule polymerization with kinetics similar to or exceeding those of paclitaxel and docetaxel ^[44]. Preclinical data regarding its efficacy in neurodegenerative models was not published and therefore cannot be addressed here. The compound advanced into two parallel clinical trials, that assessed its safety, tolerability, and

pharmacodynamics in patients with AD (NCT01966666) or 4-repeat tauopathies (4RT), PSP and corticobasal syndrome (CBS) respectively (NCT02133846). A recently published update on both trials stated that development of TPI-287 for neurodegenerative diseases will not be continued. Nevertheless, the obtained results highlight the importance of basket clinical trials and contain valuable data. It has been revealed that TPI-287 exerts different therapeutic effects in patients with different tauopathies. For example, only patients with AD developed severe hypersensitivity reactions, while clinical worsening and biomarker changes were noted in those suffering from PSP and CDS. Furthermore, it must be noted that target engagement biomarker that would show TPI-287 binding to central nervous system microtubules and its effect on MT assembly was absent in those studies. Therefore,

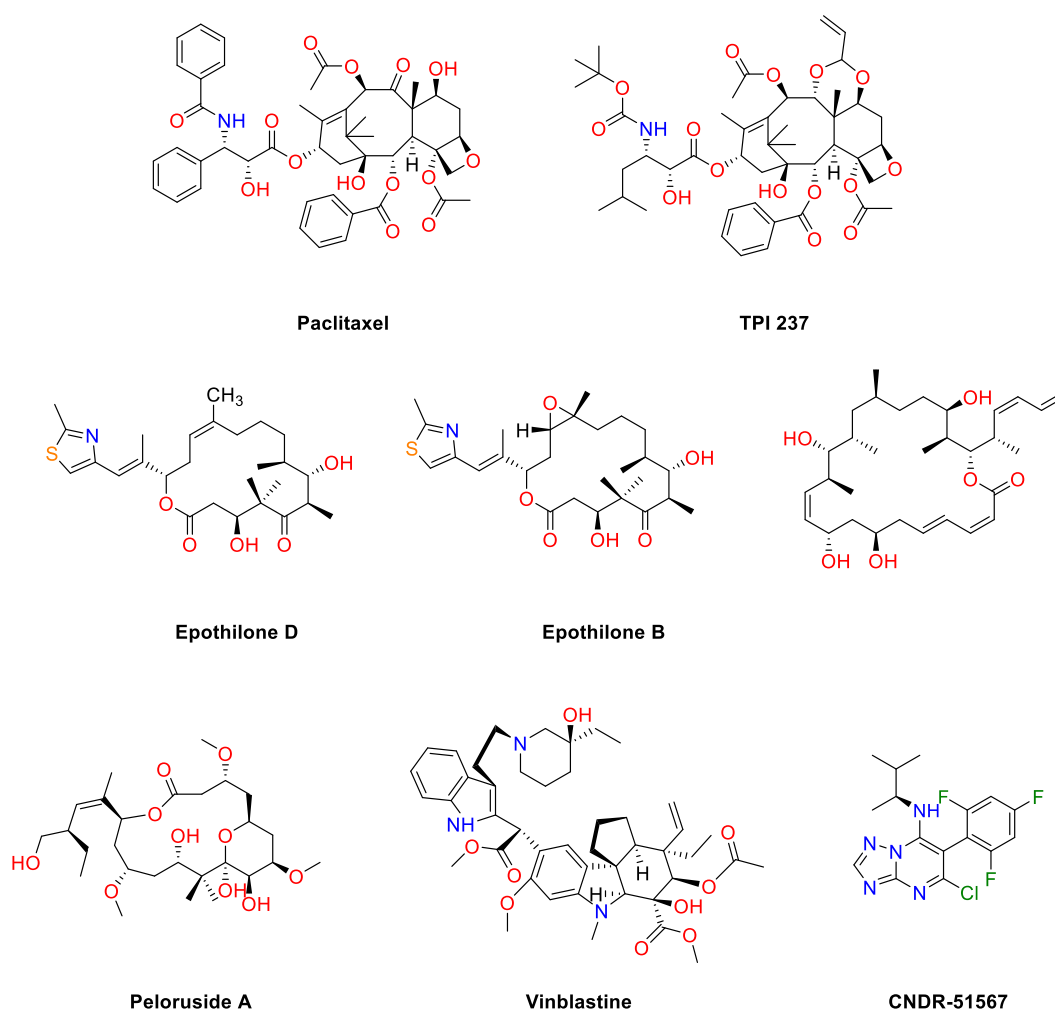


Figure 1-27. Chemical structures of MTAs evaluated in preclinical and/or clinical trials for neurodegeneration.

the potential of the drug for disease modification could not be evaluated. The authors stress that better pharmacodynamics biomarkers are needed for future clinical trials of MTAs to be successful.^[45]

In search for alternative CNS-active tubulin binders, a class of brain-penetrant, orally bioavailable triazolopyrimidines has been successfully synthesized.^[174] To determine the

potential application of triazolopyrimidines in AD and tauopathies, Kovalevich et al. characterized several brain-penetrant representatives of this group and consequently exemplified CNDR-51557 as a promising candidate. CNDR-51557 increased markers of stable MTs and MT mass in primary neurons, and alleviated MT deficits in neurons treated with okadaic acid, OA. Importantly, the compound was shown to have excellent brain exposure and increased brain AcTub in wild-type mice after single peripheral administration.^[175] A more decent data shows that CNDR-51567 enhanced microtubule-stability, reduced axonal deficits and decreased tau pathology in a mouse tauopathy model. Moreover, PK analysis performed within this study confirmed that CNDR-51567 total brain exposure exceeded that in plasma and verified the lack of interaction with P-glycoprotein.^[100]

These data proved that not only microtubule-stabilizing compounds can be applied, but that the choice of the suitable compound depends on the pathophysiology of the disorder, as some neurodegenerative diseases feature lack of dynamic MTs, while overstable MTs are characteristic for the others. The compounds described above exhibited positive pharmacological effects (improved MT dynamics, axonal regeneration, reduced tau pathology etc.) both *in vitro* and *in vivo*, while two of them, epothilone D (EpoD) and TPI 287, have reached clinical trials. Despite the promising data, the clinical trials of both compounds were discontinued, which doesn't necessarily undermine the microtubule-targeting strategy for neurodegeneration, but rather puts in evidence the subtleties that must be considered for successful execution of such studies. This concerns the active concentration and therapeutic index of the tested compound, the need for better pharmacodynamic biomarkers and specifically the necessity to test the binding to neuronal MTs. Conduction of studies concerning the above-mentioned parameters would allow to better determine the validity of microtubule-binding strategies and understand the possible limitations. Furthermore, it is important to note that out of the eight currently fully characterized binding sites on tubulin, only three of them have been evaluated in neurodegenerative models by the compounds described above. Considering the vast amount of tubulin binders identified nowadays, it seems reasonable to explore the brain penetration and pharmacological activity of other MTAs, in order to evaluate their potential for being used in the treatment of neurodegeneration and further ascertain the credibility of microtubule-targeting strategy in this field.

Table 2. Preclinical and clinical studies of tubulin binders in neurodegeneration.

NATURAL PRODUCTS					
Compound	Binding site	Study type	Conditions	Pharmacological effect	Ref.
Epothilone B	Taxane	<i>In vivo</i>	0.75 mg/kg i.p. spinal cord injury in rats	Enhanced axonal regeneration. Attenuated fibrotic scarring.	[163]
		<i>In vivo</i>	0.75 mg/kg i.p. spinal root avulsion in rats	Promoted axonal regeneration. Improved motor functional recovery.	[164]
		<i>In vivo</i>	1.5 mg/kg i.p. 6-OHDA-induced mouse model of PD	Improved behavioral deficits. Neuroprotective effects on DA Attenuated microglia activation.	[165]
Epothilone D	Taxane	<i>In vivo</i>	1 mg/kg or 3 mg/kg i.p. PS19 tau Tg mice	Improved CNS MT density, axonal integrity and cognition.	[151]
		<i>In vivo</i>	1 mg/kg or 3 mg/kg i.p. PS19 aged tau Tg Mice	Reduced axonal dysfunction, cognitive deficits, forebrain tau pathology. Increased hippocampal neuronal integrity.	[153]
		<i>In vivo</i>	1 mg/kg, rTg4510 mice	Improved MT dynamics, neuronal loss, tau pathology and cognitive deficits.	[154]
		<i>In vivo</i>	1 or 3 mg/kg, i.p. MPTP mouse model of PD	Rescued MT defects. Attenuated nigrostriatal degeneration.	[157]
		<i>In vitro</i>	0.1 nM, 1 nM, 10 nM, 100 nM YFP mice cortical neurons	Dose-dependent alterations in growth, viability, MT intracellular functions.	[161]
		<i>Clinical</i>	Safety, tolerability and effect evaluation in subjects with mild AD (Phase 1) 0.003 mg/kg, 0.01 mg/kg, 0.03 mg/kg intervention IV, once weekly, 9 weeks	Discontinued due to AEs and dose reduction. (NCT01492374)	

Dictyostatin	Taxane	<i>In vivo</i>	0.1 mg/kg PS19 tau Tg mouse model	Improved MT density. Reduced axonal dystrophy and tau pathology.	[168]
		<i>In vitro</i>	100 nM Primary neuronal cultures	Protected primary neurons against amyloid-induced toxicity.	[144]
Paclitaxel	Taxane	<i>In vivo</i>	10 or 25 mg/m ² i.p. PrP T44 tau Tg mice	Increased MT numbers and stability. Restored fast axonal transport in spinal axons.	[145]
		<i>In vitro</i>	5 nM OA-treated rat neuron cultures	Restored axonal length (177 ± 18 lm).	[148]
		<i>In vitro</i>	10 nM neuronal cell cultures	Prevented the unfolding of mt-human-tau-induced cell pathologies. Rescued mt-tau induced synaptic weakening.	[146,147]
		<i>In vitro</i>	5 nM cybrid PD cell lines	Normalized the PD tubulin ratio.	[149]
Peloruside A	Peloruside	<i>In vitro</i>	10 nM OA-treated rat neuron cultures	Restored axonal length (223 ± 6 lm) and AcTub levels. Reversed the decrease in axonal outgrowth and branching.	[148]
		<i>In vivo</i>	0.05 µM Drosophila model of HSP	Attenuated HSP-like phenotypes.	[171]
Vinblastine	Vinca	<i>In vitro</i>	10 nM SPG4 primary mouse neurons human pluripotent stem cell-based models of HSP	Significantly reduced axonal swellings. Rescued the mutant phenotype.	[172] [173]
		SYNTHETIC COMPOUNDS			
Compound	Binding site	Study type	Conditions	Pharmacological effect	Ref.

CNDR-51657	Vinca	<i>In vitro</i>	1 μ M and 10 μ M	1) Increased markers of stable MTs;	[175]
		<i>In vivo</i>	1) QBI-293 cells 2) rat primary cortical neurons 3) CD-1 wild type mice	2) Restored OA-induced neuronal MT stability; 3) Increased brain AcTub.	
		<i>In vivo</i>	3 or 10 mg/kg PS19 aged tau Tg mice	Ameliorated MT deficits, axonal dystrophy, tau pathology.	[100]
TPI 287	Taxane	<i>Clinical</i>	Two parallel, double-blind, placebo-controlled randomized clinical trials of patients with AD or 4-repeat tauopathies, CBD and PSP 2.0, 6.3, or 20.0 mg/m ² intervention, IV, once every 3 weeks for 9 weeks	Continued development not supported: Patients with different tauopathies react differently to the drug. Serious side effects. CBD/PSP group: YKL-40, inflammation marker, significantly decreased. Binding to CNS microtubules was not tested, need for better pharmacodynamics biomarkers.	[45]

Abbreviations: 6-OHDA, 6-hydroxydopamine; A β , amyloid-beta; AEs, adverse effects; APP, amyloid precursor protein; DA, dopamine; i.p., intraperitoneal injection; MT, microtubule; SPG4, Spastic paraplegia type 4; YKL-40, chitinase-3-like protein 1.

1.5 AIM OF THE THESIS

This PhD has been performed within the EU-funded Innovative Training Network TubInTrain, focused on the microtubules dynamics and its breakdown associated to neurodegenerative diseases. The TubInTrain work has been divided into three Work Packages: WP1 - Small molecules-tubulin interaction; WP2 - MAPs-microtubules interaction and WP3 – Microtubules in neurons. The work of this thesis has been a part of WP1, which ultimate goal was to understand the effects of small molecules on microtubule structure and its dynamics at the molecular level. We aimed to develop a set of tubulin binders acting as chemical probes to explore different ligand-tubulin interactions modes and to potentially study how they affect the behaviour of microtubules in cell free systems. The chosen compounds are further studied in neuronal models, in order to clarify how small molecules affect microtubule dynamics in neurons.

To fulfil this goal, we have established a workflow, based on the collaboration of five different research groups (Figure 1-28).

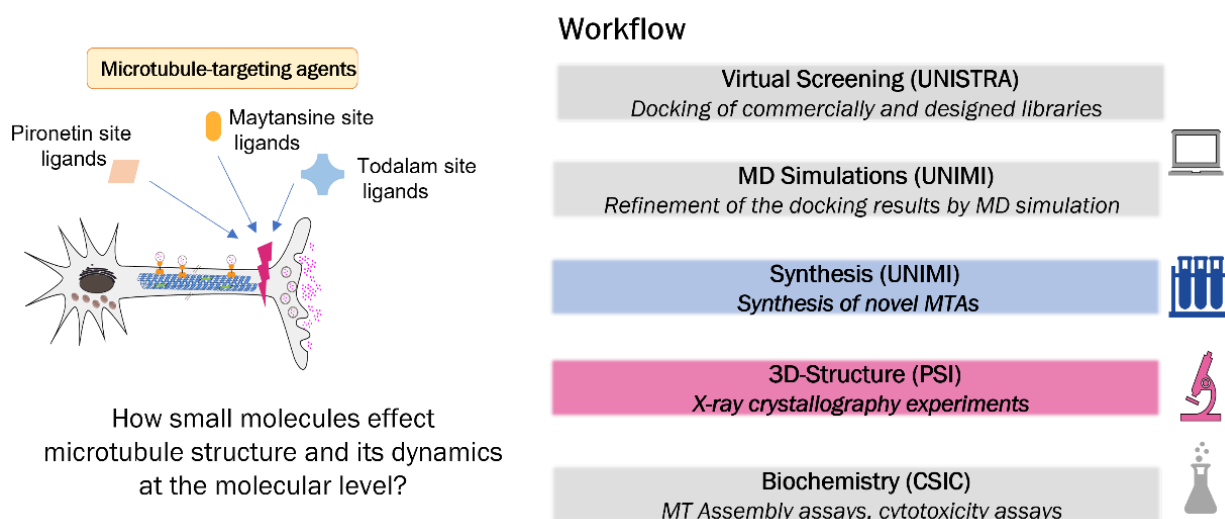


Figure 1-28. Graphical representation of the aim of the thesis and the established workflow.

Within the workflow, the main objectives of my project included the synthesis and characterization of new tubulin binders, complemented by the X-ray crystallography structure determination of individual tubulin-compound complexes, which was performed in the course of my one-year secondment period at the Paul Scherrer Institute (PSI). The focus was put on the ligands targeting some of the most recently discovered and least explored binding sites on tubulin, primarily the maytansine, the pironetin and the totalam sites.

Effortless generation of maytansine-based chemical probes is hampered by major drawbacks such as the complexity of the natural product scaffold and lack of SAR studies.

Natural product maytansinol is a valuable precursor for the preparation of maytansine derivatives. Thus, one of the main objectives was to establish the synthetic routes for the functionalization of maytansinol, to obtain a set of maytansine analogues with different side chain substituents in C3-position as well as maytansinoid conjugates (1st objective). This allowed to comprehensively evaluate whether different substituents influence their activity and the binding mode, setting the foundation for the future development of maytansine-based probes. Moreover, with an idea to provide a structurally less complex maytansine site ligand, efforts were done to synthesize a structurally simpler natural product, glycybridin B, which was predicted to bind to the maytansine site based on the computational studies performed in WP1 (2nd objective). Furthermore, we aimed to probe the covalent targeting strategy to target α -tubulin. The only compound known to covalently target α -tubulin is pironetin, a natural product of low availability. Covalent probes are characterized by prolonged duration of action, improved potency, and exquisite selectivity. Moreover, they could be used e.g., to immobilize the protein of interest, tubulin. Initially, the simplified pironetin analogues were synthesized with that goal (3rd objective). Subsequently, the discovery of the todalam site has attracted our interest. Using the time- and cost-efficient synthetic approaches, we intended to develop novel, different from Todalam scaffolds and then, based on the structural data, rationally optimize them with the idea of site-specific covalent targeting (4th objective). In this work we tackled two important questions: 1) Can other scaffolds, different from Todalam, bind to this site?; and 2) Is it possible to rationally design a small molecule that would covalently bind to the α Cys4 in the Todalam site? I was involved both in the chemistry and the structural biology aspects of this project. During the first part of the project, I aimed to obtain and characterize the crystal structures of todalam analogues in complex with tubulin, to then design (in collaboration with the computational groups) and synthesize a library of warhead-bearing ligands for the covalent targeting during the second part.

As this PhD is performed within the training network, individual goals during this PhD project included the training acquired during the one-year secondment at the Paul Scherrer Institute. This included protein expression and purification, preparation of tubulin crystallization complexes, data collection at the synchrotron, refinements, and data analysis. Two training projects comprising the X-ray crystallography structure determination of colchicine-site ligands were also included in the thesis. Another objective included the structural characterization of selected compounds emerging out of the virtual screening performed within WP1 activities (5th objective). This campaign allowed to identify a promising β 3-tubulin isotype-specific compound, described in the thesis.

1.6 REFERENCES

- [1] E. Frixione, *Cell Motil. Cytoskeleton* **2000**, 46.
- [2] F. Zampieri, M. Coen, G. Gabbiani, *Cytoskeleton* **2014**, 71.
- [3] B. Bugyi, M. Kellermayer, *J. Muscle Res. Cell Motil.* **2020**, 41.
- [4] J. V. Small, G. Isenberg, J. E. Celis, *Nature* **1978**, 272.
- [5] J. E. Heuser, M. W. Kirschner, *J. Cell Biol.* **1980**, 86.
- [6] M. C. Ledbetter, K. R. Porter, *J. Cell Biol.* **1963**, 19.
- [7] J. P. Heath, G. A. Dunn, *J. Cell Sci.* **1978**, 29.
- [8] H. Ishikawa, R. Bischoff, H. Holtzer, *J. Cell Biol.* **1968**, 38.
- [9] T. Hohmann, F. Dehghani, *Cells* **2019**, 8.
- [10] D. A. Fletcher, R. D. Mullins, *Nature* **2010**, 463.
- [11] L. Blanchoin, G. Letort, H. Ennomani, L. Gressin, M. Théry, *F1000Research* **2015**, 4.
- [12] T. D. Pollard, J. A. Cooper, *Science (80-.)*. **2009**, 326.
- [13] R. Dominguez, K. C. Holmes, *Annu. Rev. Biophys.* **2011**, 40.
- [14] G. Dutour-Provenzano, S. Etienne-Manneville, *Curr. Biol.* **2021**, 31, R522–R529.
- [15] I. Szeverenyi, A. J. Cassidy, W. C. Cheuk, B. T. K. Lee, J. E. A. Common, S. C. Ogg, H. Chen, Y. S. Shu, W. L. P. Goh, W. N. Kee, J. A. Simpson, L. C. Li, H. E. Goi, B. Li, D. P. Lunny, D. Chuon, A. Venkatesh, H. K. Kian, W. H. I. McLean, P. L. Yun, E. B. Lane, *Hum. Mutat.* **2008**, 29.
- [16] H. Herrmann, S. V. Strelkov, P. Burkhard, U. Aebi, *J. Clin. Invest.* **2009**, 119.
- [17] D. W. Fawcett, K. R. Porter, *J. Morphol.* **1954**, 94.
- [18] M. Kuijpers, C. C. Hoogenraad, *Mol. Cell. Neurosci.* **2011**, 48, 349–358.
- [19] M. T. Kelliher, H. A. Saunders, J. Wildonger, *Curr. Opin. Neurobiol.* **2019**, 57, 39–45.
- [20] S. et al. Yogev, *Neuron* **2016**, 92, 449–460.
- [21] E. Nogales, S. G. Wolf, K. H. Downing, *Nature* **1998**, 391, 199–203.
- [22] L. G. et al. Tilney, *J. Cell Biol.* **1973**, 59, 267–275.
- [23] G. B. Pierson, P. R. Burton, R. H. Himes, *J. Cell Biol.* **1978**, 76.
- [24] A. Akhmanova, M. O. Steinmetz, *Nat. Rev. Mol. Cell Biol.* **2015**, 16.
- [25] E. M. Mandelkow, R. Schultheiss, R. Rapp, M. Müller, *J. Cell Biol.* **1986**, 102.
- [26] M. Kikkawa, T. Ishikawa, T. Nakata, T. Wakabayashi, N. Hirokawa, *J. Cell Biol.* **1994**, 127.
- [27] G. M. Alushin, G. C. Lander, E. H. Kellogg, R. Zhang, D. Baker, E. Nogales, *Cell* **2014**.
- [28] R. et al. Zhang, *Cell* **2015**, 162, 849–859.
- [29] R. Zhang, B. LaFrance, E. Nogales, *Proc. Natl. Acad. Sci. U. S. A.* **2018**, 115.
- [30] J. Löwe, H. Li, K. H. Downing, E. Nogales, *J. Mol. Biol.* **2001**.
- [31] M. Menéndez, G. Rivas, J. F. Díaz, J. M. Andreu, *J. Biol. Chem.* **1998**, 273.
- [32] G. M. et al. Alushin, *Cell* **2014**, 157, 1117–1129.
- [33] M. O. Steinmetz, A. E. Prota, *Trends Cell Biol.* **2018**, 28, 776–792.
- [34] G. G. Borisy, E. W. Taylor, *J. Cell Biol.* **1967**, 34.
- [35] T. Mühlethaler, L. Milanos, J. A. Ortega, T. B. Blum, D. Gioia, B. Roy, A. E. Prota, A. Cavalli, M. O. Steinmetz, *Angew. Chemie - Int. Ed.* **2022**, 61.
- [36] T. Mühlethaler, D. Gioia, A. E. Prota, M. E. Sharpe, A. Cavalli, M. O. Steinmetz, *Angew. Chemie - Int. Ed.* **2021**, 60, 13331–13342.
- [37] M. C. et al. Wani, *J. Am. Chem. Soc.* **1971**, 93, 2325–2327.
- [38] P. B. Schiff, J. Fant, S. B. Horwitz, *Nature* **1979**, 277.
- [39] P. B. Schiff, S. B. Horwitz, *Proc. Natl. Acad. Sci. U. S. A.* **1980**, 77.
- [40] W. P. McGuire, E. K. Rowinsky, N. B. Rosenhein, F. C. Grumbine, D. S. Ettinger, D. K. Armstrong, R. C. Donehower, *Ann. Intern. Med.* **1989**, 111.
- [41] J. Gallego-Jara, G. Lozano-Terol, R. A. Sola-Martínez, M. Cánovas-Díaz, T. de D. Puente, *Molecules* **2020**, 25.
- [42] R. A. et al. Holton, *J. Am. Chem. Soc.* **1994**, 116, 1599–1600.
- [43] K. C. Nicolaou, Z. Yang, J. J. Liu, H. Ueno, P. G. Nantermet, R. K. Guy, C. F. Claiborne, J. Renaud, E. A. Couladouros, K. Paulvannan, E. J. Sorensen, *Nature* **1994**.
- [44] D. P. et al. Fitzgerald, *Mol. Cancer Ther.* **2012**, 11, 1959–1967.

- [45] R. M. et al. Tsai, *JAMA Neurol.* **2020**, *77*, 215–224.
- [46] J. Škubník, V. Pavlíčková, T. Ruml, S. Rimpelová, *Plants* **2021**, *10*.
- [47] D. M. et al. Bollag, *Cancer Res.* **1995**, *55*, 2325–2333.
- [48] J. H. et al. Nettles, *Science (80-.)*. **2004**, *305*, 866–869.
- [49] S. Forli, *Curr. Top. Med. Chem.* **2014**, *14*.
- [50] G. R. et al. Pettit, *J. Chem. Soc. Chem. Commun.* **1994**, 1111–1112.
- [51] R. M. Buey, I. Barasoain, E. Jackson, A. Meyer, P. Giannakakou, I. Paterson, S. Mooberry, J. M. Andreu, J. F. Díaz, *Chem. Biol.* **2005**, *12*, 1269–1279.
- [52] R. A. et al. Isbrucker, *Biochem. Pharmacol.* **2003**, *66*, 75–82.
- [53] C. et al. Trigili, *ACS Omega* **2016**, *1*, 1192–1204.
- [54] J. I. Tanaka, T. Higa, *Tetrahedron Lett.* **1996**, *37*.
- [55] J. J. Field, B. Pera, E. Calvo, A. Canales, D. Zurwerra, C. Trigili, J. Rodríguez-Salarichs, R. Matesanz, A. Kanakkanthara, S. J. Wakefield, A. J. Singh, J. Jiménez-Barbero, P. Northcote, J. H. Miller, J. A. López, E. Hamel, I. Barasoain, K. H. Altmann, J. F. Díaz, *Chem. Biol.* **2012**, *19*.
- [56] J. J. Field, P. T. Northcote, I. Paterson, K. H. Altmann, J. F. Díaz, J. H. Miller, *Int. J. Mol. Sci.* **2017**, *18*.
- [57] L. Takahashi-Ruiz, J. D. Morris, P. Crews, T. A. Johnson, A. L. Risinger, *Molecules* **2022**, *27*.
- [58] I. Arnal, R. H. Wade, *Curr. Biol.* **1995**, *5*.
- [59] E. H. et al. Kellogg, *J. Mol. Biol.* **2017**, *429*, 633–646.
- [60] S. W. Manka, C. A. Moores, *Nat. Struct. Mol. Biol.* **2018**, *25*.
- [61] A. E. Prota, K. Bargsten, D. Zurwerra, J. J. Field, J. F. Díaz, K. H. Altmann, M. O. Steinmetz, *Science (80-.)*. **2013**, *339*, 587–590.
- [62] A. E. Prota, K. Bargsten, M. Redondo-Horcajo, A. B. Smith, C. P. H. Yang, H. M. McDaid, I. Paterson, S. B. Horwitz, J. Fernando Díaz, M. O. Steinmetz, *ChemBioChem* **2017**, *18*, 905–909.
- [63] S. L. Mooberry, G. Tien, A. H. Hernandez, A. Plubrukarn, B. S. Davidson, *Cancer Res.* **1999**, *59*.
- [64] L. M. West, P. T. Northcote, C. N. Battershill, *J. Org. Chem.* **2000**, *65*.
- [65] K. A. Hood, L. M. West, B. Rouwé, P. T. Northcote, M. V. Berridge, S. J. Wakefield, J. H. Miller, *Cancer Res.* **2002**, *62*, 3356–3360.
- [66] T. N. Gaitanos, R. M. Buey, J. Fernando Díaz, P. T. Northcote, P. Teesdale-Spittle, J. M. Andreu, J. H. Miller, *Cancer Res.* **2004**, *64*, 5063–5067.
- [67] J. Liu, M. J. Towle, H. Cheng, P. Saxton, C. Reardon, J. Wu, E. A. Murphy, G. Kuznetsov, C. W. Johannes, M. R. Tremblay, H. Zhao, M. Pesant, F. G. Fang, M. W. Vermeulen, B. M. Gallagher, B. A. Littlefield, *Anticancer Res.* **2007**, *27*.
- [68] A. Kanakkanthara, P. T. Northcote, J. H. Miller, *Nat. Prod. Rep.* **2016**, *33*.
- [69] A. Brackovic, J. E. Harvey, *Chem. Commun.* **2015**, *51*.
- [70] J. Estévez-Gallego, B. Álvarez-Bernad, B. Pera, C. Wullschleger, O. Raes, D. Menche, J. C. Martínez, D. Lucena-Agell, A. E. Prota, F. Bonato, K. Bargsten, J. Cornelus, J. F. Giménez-Abián, P. Northcote, M. O. Steinmetz, S. Kamimura, K. H. Altmann, I. Paterson, F. Gago, J. Van der Eycken, J. F. Díaz, M. Á. Oliva, *Structure* **2023**, *31*, 88-99.e5.
- [71] A. E. Prota, K. Bargsten, P. T. Northcote, M. Marsh, K. H. Altmann, J. H. Miller, J. F. Díaz, M. O. Steinmetz, *Angew. Chemie - Int. Ed.* **2014**.
- [72] M. Karamanou, G. Tsoucalas, K. Pantos, G. Androutsos, *Curr. Pharm. Des.* **2018**, *24*, 654–658.
- [73] Y. Y. Leung, L. L. Yao Hui, V. B. Kraus, *Semin. Arthritis Rheum.* **2015**, *45*.
- [74] I. A. Gracheva, E. S. Shchegravina, H. G. Schmalz, I. P. Beletskaya, A. Y. Fedorov, *J. Med. Chem.* **2020**, *63*.
- [75] G. R. Pettit, S. B. Singh, E. Hamel, C. M. Lin, D. S. Alberts, D. Garcia-Kendal, *Experientia* **1989**, *45*.
- [76] G. Ş. Karatoprak, E. K. Akkol, Y. Genç, H. Bardakci, Ç. Yücel, E. Sobarzo-Sánchez, *Molecules* **2020**, *25*.
- [77] R. Gaspari, A. E. Prota, K. Bargsten, A. Cavalli, M. O. Steinmetz, *Chem* **2017**, *2*.
- [78] J. E. Sheldon, M. M. Dcona, C. E. Lyons, J. C. Hackett, M. C. T. Hartman, *Org. Biomol. Chem.* **2015**, *14*.
- [79] L. Gao, J. C. M. Meiring, Y. Kraus, M. Wranik, T. Weinert, S. D. Pritzl, R. Bingham, E. Ntoulidou, K. I. Jansen, N. Olieric, J. Standfuss, L. C. Kapitein, T. Lohmüller, J. Ahlfeld, A. Akhmanova, M. O. Steinmetz, O. Thorn-Seshold, *Cell Chem. Biol.* **2021**, *28*.
- [80] M. A. Jordan, D. Thrower, L. Wilson, *J. Cell Sci.* **1992**, *102*, 401–416.
- [81] M. Jost, Y. Chen, L. A. Gilbert, M. A. Horlbeck, L. Krenning, G. Menchon, A. Rai, M. Y. Cho, J. J. Stern, A. E. Prota, M. Kampmann, A. Akhmanova, M. O. Steinmetz, M. E. Tanenbaum, J. S. Weissman, *Mol. Cell* **2017**, *68*.

- [82] R. J. Vasquez, B. Howell, A. M. C. Yvon, P. Wadsworth, L. Cassimeris, *Mol. Biol. Cell* **1997**, *8*.
- [83] J. I. Sasaki, R. Ramesh, S. Chada, Y. Gomyo, J. A. Roth, T. Mukhopadhyay, *Mol. Cancer Ther.* **2002**, *1*.
- [84] M. Á. Oliva, C. Tosat-Bitrián, L. Barrado-Gil, F. Bonato, I. Galindo, U. Garaigorta, B. Álvarez-Bernad, R. París-Ogáyar, D. Lucena-Agell, J. F. Giménez-Abián, I. García-Dorival, J. Urquiza, P. Gastaminza, J. F. Díaz, V. Palomo, C. Alonso, *Int. J. Mol. Sci.* **2022**, *23*.
- [85] G. La Sala, N. Olieric, A. Sharma, F. Viti, F. de Asis Balaguer Perez, L. Huang, J. R. Tonra, G. K. Lloyd, S. Decherchi, J. F. Díaz, M. O. Steinmetz, A. Cavalli, *Chem* **2019**, *5*.
- [86] T. Arai, *FEBS Lett.* **1983**, *155*.
- [87] A. Dorléans, B. Gigant, R. B. G. Ravelli, P. Mailliet, V. Mikol, M. Knossow, *Proc. Natl. Acad. Sci. U. S. A.* **2009**.
- [88] W. Li, H. Sun, S. Xu, Z. Zhu, J. Xu, *Future Med. Chem.* **2017**, *9*, 1765–1794.
- [89] I. S. Johnson, J. G. Armstrong, M. Gorman, J. P. Burnett, *Cancer Res.* **1963**.
- [90] P. Dhyani, C. Quispe, E. Sharma, A. Bahukhandi, P. Sati, D. C. Attri, A. Szopa, J. Sharifi-Rad, A. O. Docea, I. Mardare, D. Calina, W. C. Cho, *Cancer Cell Int.* **2022**, *22*, 1–20.
- [91] R. J. Owellen, A. H. Owens, D. W. Donigian, *Biochem. Biophys. Res. Commun.* **1972**, *47*.
- [92] V. Prakash, S. N. Timasheff, *J. Biol. Chem.* **1983**, *258*.
- [93] M. A. Jordan, D. Thrower, L. Wilson, *Cancer Res.* **1991**, *51*.
- [94] A. Bauer, **2016**.
- [95] M. A. Jordan, K. Kamath, T. Manna, T. Okouneva, H. P. Miller, C. Davis, B. A. Littlefield, L. Wilson, *Mol. Cancer Ther.* **2005**, *4*.
- [96] T. K. Huyck, W. Gradishar, F. Manuguid, P. Kirkpatrick, *Nat. Rev. Drug Discov.* **2011**, *10*, 173–174.
- [97] G. R. Pettit, Y. Kamano, C. L. Herald, A. A. Tuinman, F. E. Boettner, H. Kizu, J. M. Schmidt, L. Baczynski, K. B. Tomer, R. J. Bontems, *J. Am. Chem. Soc.* **1987**, *109*.
- [98] S. B. Singh, *J. Nat. Prod.* **2022**, *85*.
- [99] B. Gigant, C. Wang, R. B. G. Ravelli, F. Roussi, M. O. Steinmetz, P. A. Curmi, A. Sobel, M. Knossow, *Nature* **2005**, *435*.
- [100] B. et al. Zhang, *Mol. Neurodegener.* **2018**, *13*, 59.
- [101] S. Remillard, L. I. Rebhun, G. A. Howie, S. M. Kupchan, *Science (80-.)*. **1975**, *189*, 1002–1005.
- [102] S. M. Kupchan, Y. Komoda, A. R. Branfman, A. T. Sneden, W. A. Court, G. J. Thomas, H. P. J. Hintz, R. M. Smith, A. Karim, G. A. Howie, A. K. Verma, Y. Nagao, R. G. Dailey, V. A. Zimmerly, W. C. Sumner, *J. Org. Chem.* **1977**, *42*, 2349–2357.
- [103] S. Ikeyama, M. Takeuchi, *Biochem. Pharmacol.* **1981**, *30*, 2421–2425.
- [104] B. F. Issell, S. T. Crooke, *Cancer Treat. Rev.* **1978**, *5*, 199–207.
- [105] J. M. Cassady, K. K. Chan, H. G. Floss, E. Leistner, *Chem. Pharm. Bull.* **2004**, *52*, 1–26.
- [106] F. Mandelbaum-Shavit, M. K. Wolpert-DeFilippes, D. G. Johns, *Biochem. Biophys. Res. Commun.* **1976**, *72*.
- [107] M. Takahashi, S. Iwasaki, H. Kobayashi, S. Okuda, T. Murai, Y. Sato, *BBA - Gen. Subj.* **1987**, *926*
- [108] E. Hamel, *Pharmacol. Ther.* **1992**, *55*.
- [109] M. J. Martín, L. Coello, R. Fernández, F. Reyes, A. Rodríguez, C. Murcia, M. Garranzo, C. Mateo, F. Sánchez-Sancho, S. Bueno, C. De Eguillor, A. Francesch, S. Munt, C. Cuevas, *J. Am. Chem. Soc.* **2013**, *135*.
- [110] A. E. Prota, K. Bargsten, J. F. Díaz, M. Marsh, C. Cuevas, M. Liniger, C. Neuhaus, J. M. Andreu, K. H. Altmann, M. O. Steinmetz, *Proc. Natl. Acad. Sci. U. S. A.* **2014**, *111*, 13817–21.
- [111] B. Pera, I. Barasoain, A. Pantazopoulou, A. Canales, R. Matesanz, J. Rodríguez-Salarichs, L. F. García-Fernandez, V. Moneo, J. Jiménez-Barbero, C. M. Galmarini, C. Cuevas, M. A. Peñalva, J. F. Díaz, J. M. Andreu, *ACS Chem. Biol.* **2013**, *8*.
- [112] A. R. Hanauske, G. Catimel, S. Aamdal, W. Ten Bokkel Huinink, R. Paridaens, N. Pavlidis, S. B. Kaye, A. Te Velde, J. Wanders, J. Verweij, *Br. J. Cancer* **1996**, *73*.
- [113] C. M. Galmarini, M. Martin, B. P. Bouchet, M. J. Guillen-Navarro, M. Martínez-Diez, J. F. Martínez-Leal, A. Akhmanova, P. Aviles, *BMC Cancer* **2018**, *18*.
- [114] P. C. Jimenez, D. V. Wilke, P. C. Branco, A. Bauermeister, P. Rezende-Teixeira, S. P. Gaudêncio, L. V. Costa-Lotufo, *Br. J. Pharmacol.* **2020**, *177*.
- [115] G. Menchon, A. E. Prota, D. Lucena-Agell, P. Bucher, R. Jansen, H. Irschik, R. Müller, I. Paterson, J. F. Díaz, K. H. Altmann, M. O. Steinmetz, *Nat. Commun.* **2018**, *9*, 2106.

- [116] L. Schyschka, A. Rudy, I. Jeremias, N. Barth, G. R. Pettit, A. M. Vollmar, *Leukemia* **2008**, *22*.
- [117] S. Kobayashi, K. Tsuchiya, T. Harada, M. Nishide, T. Kurokawa, T. Nakagawa, N. Shimada, K. Kobayashi, *J. Antibiot. (Tokyo)*. **1994**, *47*.
- [118] G. E. Keck, C. E. Knutson, S. A. Wiles, *Org. Lett.* **2001**, *3*.
- [119] X. Shen, A. S. Wasmuth, J. Zhao, C. Zhu, S. G. Nelson, *J. Am. Chem. Soc.* **2006**, *128*.
- [120] M. T. Crimmins, A. M. R. Dechert, *Org. Lett.* **2009**, *11*.
- [121] C. Bressy, J. P. Vors, S. Hillebrand, S. Arseniyadis, J. Cossy, *Angew. Chemie - Int. Ed.* **2008**, *47*.
- [122] M. Kondoh, T. Usui, S. Kobayashi, K. Tsuchiya, K. Nishikawa, T. Nishikiori, T. Mayumi, H. Osada, *Cancer Lett.* **1998**, *126*.
- [123] T. Usui, H. Watanabe, H. Nakayama, Y. Tada, N. Kanoh, M. Kondoh, T. Asao, K. Takio, H. Watanabe, K. Nishikawa, T. Kitahara, H. Osada, *Chem. Biol.* **2004**, *11*.
- [124] A. E. Prota, J. Setter, A. B. Waight, K. Bargsten, J. Murga, J. F. Diaz, M. O. Steinmetz, *J. Mol. Biol.* **2016**, *428*.
- [125] J. Yang, Y. Wang, T. Wang, J. Jiang, C. H. Botting, H. Liu, Q. Chen, J. Yang, J. H. Naismith, X. Zhu, L. Chen, *Nat. Commun.* **2016**, *7*.
- [126] E. Pasquier, M. Kavallaris, *IUBMB Life* **2008**, *60*.
- [127] C. Dumontet, M. A. Jordan, *Nat. Rev. Drug Discov.* **2010**, *9*, 790–803.
- [128] R. Visconti, D. Grieco, *Endocr. Relat. Cancer* **2017**, *24*.
- [129] P. Zhao, Y. Zhang, W. Li, C. Jeanty, G. Xiang, Y. Dong, *Acta Pharm. Sin. B* **2020**, *10*, 1589–1600.
- [130] M. Kavallaris, *Nat. Rev. Cancer* **2010**, *10*.
- [131] S. K. Katiyar, V. R. Gordon, G. L. McLaughlin, T. D. Edlind, *Antimicrob. Agents Chemother.* **1994**, *38*.
- [132] B. P. Chatterji, B. Jindal, S. Srivastava, D. Panda, *Expert Opin. Ther. Pat.* **2011**, *21*.
- [133] D. Panda, K. Rathinasamy, M. K. Santra, L. Wilson, *Proc. Natl. Acad. Sci. U. S. A.* **2005**, *102*.
- [134] N. Gaillard, A. Sharma, I. Abbaali, T. Liu, F. Shilliday, A. D. Cook, V. Ehrhard, M. Banger, A. J. Roberts, C. A. Moores, N. Morrisette, M. O. Steinmetz, *EMBO Mol. Med.* **2021**, *13*.
- [135] S. Millecamps, J. P. Julien, *Nat. Rev. Neurosci.* **2013**, *14*, 161–176.
- [136] A. et al. Ertürk, *J. Neurosci.* **2007**, *27*, 9169–9180.
- [137] D. et al. Cartelli, *J. Neurochem.* **2010**, *115*, 247–258.
- [138] J. et al. Jaworski, *Neuron* **2009**, *61*, 85–100.
- [139] D. et al. Cartelli, *PLoS One* **2012**, *7*, e37467.
- [140] F. V. M. Casagrande, E. Al., *Biochim. Biophys. Acta - Mol. Basis Dis.* **2020**, *1866*, 165581.
- [141] A. M. Calogero, E. Al., *J. Cell. Mol. Med.* **2018**, *22*, 2670–2679.
- [142] V. M. Y. Lee, R. Daughenbaugh, J. Q. Trojanowski, *Neurobiol. Aging* **1994**, *15*, 87–89.
- [143] B. T. et al. Castle, *Mol. Biol. Cell* **2017**, *28*, 1238–1257.
- [144] M. L. et al. Michaelis, *J. Neurochem.* **2002**, *70*, 1623–1627.
- [145] B. et al. Zhang, *Proc. Natl. Acad. Sci. U. S. A.* **2005**, *102*, 227–231.
- [146] O. A. Shemesh, M. E. Spira, *Neurobiol. Dis.* **2011**, *43*, 163–175.
- [147] H. Erez, O. A. Shemesh, M. E. Spira, *Front. Cell. Neurosci.* **2014**, *8*, 34.
- [148] V. Das, J. H. Miller, *Eur. J. Neurosci.* **2012**, *35*, 1705–1717.
- [149] A. R. Esteves, *Front. Aging Neurosci.* **2010**, *1*, 5.
- [150] M. et al. N.I., *Expert Opin. Drug Saf.* **2007**, *6*, 609–621.
- [151] K. R. et al. Brunden, *J. Neurosci.* **2010**, *30*, 13861–13866.
- [152] K. R. et al. Brunden, *Pharmacol. Res.* **2011**, *63*, 341–351.
- [153] B. et al. Zhang, *J. Neurosci.* **2012**, *32*, 3601–3611.
- [154] Barten D.M. et al., *J. Neurosci.* **2012**, *32*, 7137–7145.
- [155] L. et al. Penazzi, *Neuropharmacology* **2016**, *105*, 84–95.
- [156] N. et al. Golovyashkina, *Mol. Neurodegener.* **2015**, *10*, 60.
- [157] D. et al. Cartelli, *Sci. Rep.* **2013**, *3*, 1837.
- [158] D. et al. Valdinocci, *Mol. Cell. Neurosci.* **2018**, *89*, 80–94.
- [159] Y. et al. Fan, *Biol. Open* **2014**, *3*, 494–502.
- [160] J. A. et al. Clark, *Neuropathol. Appl. Neurobiol.* **2018**, *44*, 590–605.
- [161] J. A. et al. Clark, *Sci. Rep.* **2020**, *10*, 918.
- [162] T. et al. O'Reilly, *Cancer Chemother. Pharmacol.* **2008**, *62*, 1045–1054.
- [163] J. et al. Ruschel, *Science (80-.)*. **2015**, *348*, 347–352.

- [164] H. Li, W. Wu, *Eur. J. Neurosci.* **2017**, *46*, 1650–1662.
- [165] Z. et al. Yu, *Front. Cell. Neurosci.* **2018**, *12*, 324.
- [166] E. H. et al. Jang, *Neural Plast.* **2016**, *2016*, 5056418.
- [167] K. R. et al. Brunden, *ACS Med. Chem. Lett.* **2013**, *4*, 886–889.
- [168] V. et al. Makani, *Acta Neuropathol. Commun.* **2016**, *4*, 106.
- [169] V. Das, J. H. Miller, *Brain Res.* **2012**, *1489*, 121–132.
- [170] V. Das, D. A. Sim, J. H. Miller, *J. Neurosci. Res.* **2014**, *92*, 1155–1166.
- [171] G. et al. Orso, *J. Clin. Invest.* **2005**, *115*, 3026–3034.
- [172] C. et al. Fassier, *DMM Dis. Model. Mech.* **2013**, *6*, 72–83.
- [173] K. R. et al. Denton, *Stem Cells* **2014**, *32*, 414–423.
- [174] K. et al. Lou, *J. Med. Chem.* **2014**, *57*, 6116–6127.
- [175] J. et al. Kovalevich, *J. Pharmacol. Exp. Ther.* **2016**, *357*, 432–450.
- [176] H. Pérez-peña, A. Abel, M. Shevelev, A. E. Prota, **2022**, 1–47.

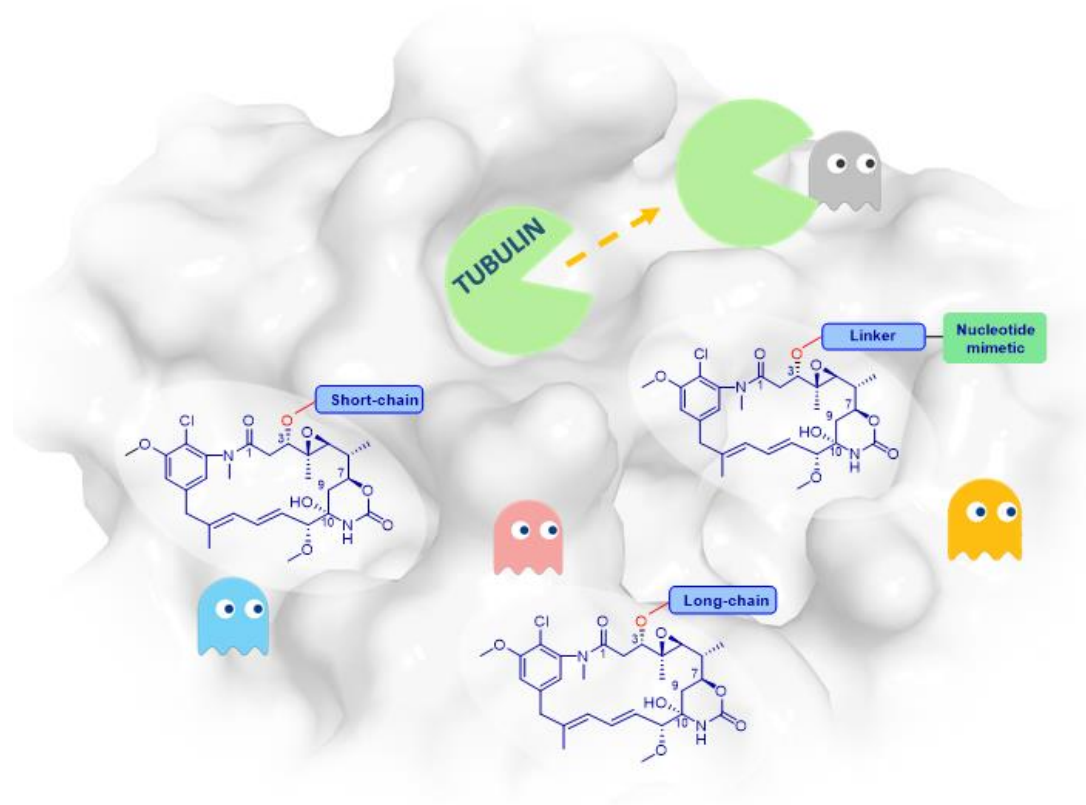
CHAPTER 2

SYNTHESIS OF NOVEL MICROTUBULE-TARGETING AGENTS

GENERAL INTRODUCTION

MTAs are a class of chemically diverse molecules, united by their abilities to bind to tubulin and exert microtubule-stabilizing or destabilizing activities. As described in Chapter 1, most MTAs are natural products, known for their structural complexity and abundant stereochemistry. As a result, their synthesis or functionalization is often a challenging task. However, natural products chemistry not only allows us to undertake synthetic challenges, but also explore the important classes of biologically active molecules providing crucial knowledge to both basic research and drug discovery. At the same time, we must acknowledge that having in hands a structurally less complex molecule can also be useful as it can be easily derivatized, optimized and turned into a probe. Hence, nowadays different chemical approaches to target tubulin can be used, based either on the natural products chemistry or time-efficient synthesis of easily accessible novel scaffolds. Both approaches, including 1) **synthesis of natural products inspired MTAs (2.1-2.3)** and 2) **synthesis of easily accessible novel scaffolds (2.4)** are further described in this Chapter. Importantly, in this work we aimed to target some of the most recently discovered and unexplored sites on tubulin, including maytansine, pironetin and todalam sites.

2.1 MAYTANSINOL FUNCTIONALIZATION: TOWARDS NEW TUBULIN BINDERS AND CHEMICAL PROBES



This work has been published.

P. Marzullo, Z. Boiarska, H. Pérez-Peña, A. Abel, B. Álvarez-Bernad, D. Lucena-Agell, F. Vasile, M. Sironi, KH. Altmann, A.E. Prota, J.F Díaz, S. Pieraccini, D. Passarella.

Chem. - A Eur. J. **2022**, *28*, e202103520

Z. Boiarska, H. Pérez-Peña, A. Abel, P. Marzullo, B. Álvarez-Bernad, F. Bonato, B. Santini, D. Horvath, D. Lucena-Agell, F. Vasile, M. Sironi, J.F Díaz, A.E. Prota, S. Pieraccini, D. Passarella.

Chem. - A Eur. J. **2023**, *29*, e2022034

Abstract: Maytansinoids represent a successful class of natural and semisynthetic tubulin binders, known for their potent cytotoxic activity. Their wider application as cytotoxins and chemical probes to study tubulin dynamics was set back due to the complexity of natural product chemistry. Maytansinol is a valuable precursor for the preparation of maytansine derivatives. Inspired by the intriguing structure of the macrocycle and the success in targeted cancer therapy of the derivatives, we explored the maytansinol acylation reaction. As a result, we were able to obtain a series of derivatives with novel modifications of the maytansine scaffold. Continuing our work, we reported the synthesis of long-chain derivatives and maytansinoid conjugates. The molecules were characterized by docking studies, a comprehensive biochemical evaluation, and determination of their crystal structures in complex with tubulin. We confirmed that bulky substituents do not impact their high activity and the scaffold's binding mode. The results shed further light on the intriguing chemical behavior of maytansinoids, confirmed the relevance of this peculiar scaffold in the scenario of tubulin binders and set a foundation for the design of new maytansine-based probes.

Declaration of contribution: This multidisciplinary project was born in our laboratory, at the group of Prof. Passarella in the University of Milan. The initial investigation of maytansinol reactivity in our group was done by Dr. Paola Marzullo, which I then continued. My work included the synthesis and analytical characterization of new maytansinol derivatives, with particular focus on the short-chain maytansinoids building blocks for further conjugation (alkene/alkyne/azide derivatives), long-chain maytansinoids and maytansinoid conjugates. I was involved in drafting of both manuscripts and finalizing them through the corrections and reviewing processes. To design the compounds for synthesis, I actively collaborated with Helena Pérez-Peña from the group of Prof. Pieraccini (University of Milan), who performed the computational studies, and Anne-Catherine Abel (Paul Scherrer Institut, Switzerland), who determined the crystal structures of the chosen hits in complex with tubulin. The biochemical characterization was done by the group of J. Fernando Díaz, Centro de Investigaciones Biológicas Margarita Salas, Madrid, Spain.

2.1.1 INTRODUCTION

Maytansine (Figure 2-1) is an ansamacrolide isolated from *Maytenus ovatus*; it is a highly potent antimitotic agent that exerts an antiproliferative effect by inhibiting microtubule assembly upon binding to tubulin.^[1-3] Despite a promising *in vitro* profile, clinical trials with maytansine in cancer patients failed because of poor efficacy and unacceptable systemic toxicity.^[4,5] Although the narrow therapeutic window precluded further clinical development of the parent compound, maytansine, its derivatives were successfully applied clinically as ADCs and thus continue to excite interest.^[6-10] This is mainly due their highly efficient mechanism of capping MT dynamics^[11] and high cytotoxicity, largely higher than those of vincristine and vinblastine.^[12] The binding site of maytansine on tubulin has been discovered relatively recently, in 2014, providing the structural basis for their high activity. Please note that more details on the maytansine site, maytansinoid-based ADCs structures and applications, as well as other maytansine site ligands are described in Chapter 1.4.

The availability of structural data and success of maytansinoid-bearing ADCs has further prompted their further development as targeted cancer therapeutics, e.g. in the form of nanoparticles^[13,14] or recently reported immune checkpoint-targeting maytansinoid conjugates.^[15] However, the high-affinity of maytansine towards β -tubulin (K_D 6.8 – 14 nM)^[16,17] not only makes it well suited as a cytotoxin, but also derivatives with a similar affinity could be used as chemical probes. As of today, effortless generation of maytansine-based molecular probes is hampered by major drawbacks such as the complexity of the natural product scaffold and lack of SAR studies, which could suggest suitable points for attachment of fluorophore tags or radionuclides.

Maytansinol (Figure 2-1) is a natural product from the maytansinoids family, first obtained by Kupchan *et al.* both by isolation from *Putterlickia verrucosa* and chemical removal of the

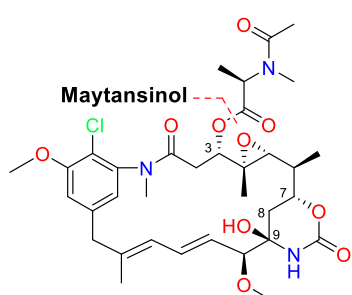


Figure 2-1. Chemical structures of maytansine and maytansinol

acyl group from the hydroxyl group at C3 position of maytansine.^[12] It showed weaker inhibitory activity on tubulin polymerization than maytansine, implying that the ester moiety at the C3 position of ansamitocins, maytansine and maytansinoids plays an important role for biological activity and cell permeability.^[18,19] In fact, it has been just recently found that the carbonyl oxygen atom of the ester moiety forms a strong intramolecular interaction with the hydroxyl at position 9, fixing the bioactive conformation.^[20] Maytansinol has been regarded as a valuable precursor, since its acylation

allows the preparation of both natural and new semisynthetic maytansinoids, differing in the ester side chain substituents.^[21,22] The acylation reaction of maytansinol is a crucial step in the preparation of maytansinoid ADCs or nanoparticles, constituting an uprising class of

targeted cancer therapeutics.^[13,14,23–25] A few attempts to conjugate maytansinoids to peptides by this reaction have also been made very recently.^[26,27]

2.1.2 AIM OF THE PROJECT

The potent biological activity of maytansinoids, the variety of possible applications, and above all the intriguing macrocyclic structure decorated by several sensitive functional groups, motivated us to investigate the chemistry of maytansinol. More precisely, we aimed to study the formation of maytansinol derivatives induced by different reaction conditions with particular attention to the acylation reaction. We prepared a series of C3-derivatized, short-chain, maytansinol derivatives (Figure 2-2). Apart from the formation of esters at C3 position, maytansinol has been discovered to undergo a range of other structural transformations not previously reported. To evaluate the potential of our maytansinoids, we submitted the obtained compounds to a) computational studies, b) experiments for evaluation of the effect on tubulin polymerization dynamics, c) evaluation of the cytotoxicity and d) structure determination by X-Ray crystallography. This served as a foundation to continue our studies on the maytansinol chemistry.

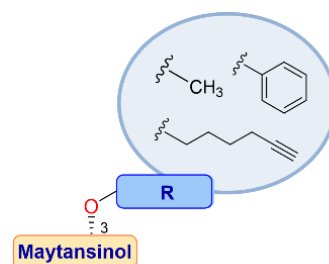


Figure 2-2. The schematic image of a short-chain maytansinoid

Taking into consideration that the maytansine binding site is one of the most recently identified and least explored on tubulin, we have considered that maytansinol functionalization may serve for the preparation of useful chemical probes to better understand the structure-activity relationships of maytansinoids or to identify new maytansine-site ligands.^[11,16] Therefore we aimed to further investigate the potential of C3-functionalized maytansinoids as chemical probes by creating novel tubulin binders. We considered two following aspects: the chemistry of maytansinol for the creation of long-chain maytansinoids and maytansinoid conjugates and the suitability of the C3-position to tolerate bulky substituents without affecting the binding mode.

The design of novel maytansinoids was led by the high-resolution X-ray crystallography structures of recently obtained maytansinoid-tubulin complexes (PDB IDs 5SB9, 5SBA and 5SBB). The maytansine binding site is located in proximity of the GDP nucleotide bound to the E-site and a GDP-coordinated Mg^{2+} . The first interesting factor that could be exploited to exert a novel effect on microtubules is the Mg^{2+} ion coordinated by the nucleotide in close proximity to the maytansine binding site. The design of long-chain maytansinoids and bivalent compounds containing maytansinol and nucleotide mimetics would a) increase the understanding of the ability of maytansinoids to accommodate in the binding site independently of the size of the substituents, and b) investigate the ability of these molecules to interact with Mg^{2+} and to displace the nucleotide from the binding site.

Tubulin inhibition by nucleotide analogues is very challenging because of GTP concentrations around 300 μM inside the cells.^[28] However, we sought to investigate whether the presence of the maytansinol moiety in a bivalent compound could favor binding of the nucleotide portion through an entropic effect. The maytansinol moiety would act as an anchor point holding the modified nucleotide portion in close proximity of the E-site through a flexible linker, thereby favoring the nucleotide exchange. Accordingly, we aimed to prepare long-chain maytansinol derivatives and maytansinoid conjugates to target either the Mg^{2+} ion or the nucleotide binding site, to further investigate the tolerance towards the introduction of bulkier groups and their impact on tubulin binding.

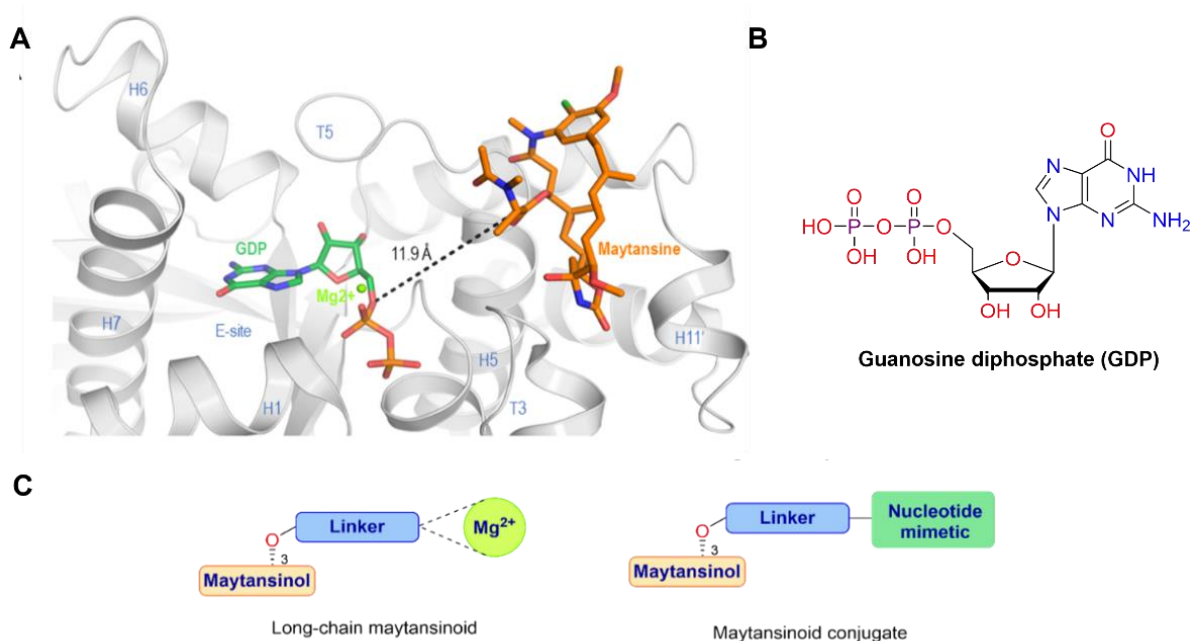


Figure 2-3. (A) Section of the crystal structure with PDB ID 4TV8 in which maytansine (orange), GDP (green), Mg^{2+} (bright green sphere), and β -tubulin (grey) are present. The black dotted line represents the distance between the C3-position of maytansine and C5-position of the GDP which is $\sim 12\text{\AA}$. (B) Chemical structure of GDP. (C) Schematic drawing of both the maytansinoids and the conjugates designed to target the nucleotide-bound Mg^{2+} or the exchangeable nucleotide site (E-site) of tubulin.

2.1.3 RESULTS AND DISCUSSION

Chemistry

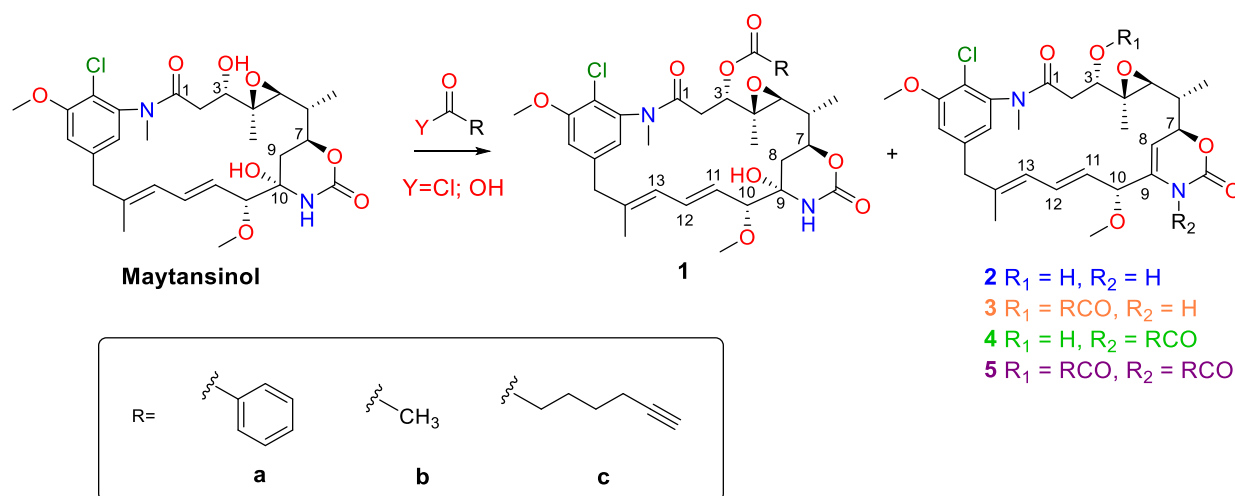
Exploring the maytansinol acylation reaction

First of all, we decided to establish the optimal reaction conditions for the acylation of maytansinol (Table 2-1). Due to the steric hindrance and the consequent poor reactivity of the maytansinol secondary alcohol, the first synthetic strategy applied in our laboratory for the acylation of maytansinol was the use of acyl chlorides. Some of the common aliphatic and aromatic acyl chlorides were studied in order to evaluate the influence of the nature of the side chain. In addition to the formation of the expected *O*-acylated product **1**, other

undescribed maytansinoids were formed (Table 2-1; **2-5**). The modifications included the formation of the new double bond in C8-C9 position, as a consequence of the dehydration of the hydroxyl group in the oxazinanone (**2, 3, 4, 5**), and the acylation of the oxazinanone nitrogen (**6, 7**). Attracted by the interesting structural transformations, we planned to monitor their formation depending on the conditions and acylating agents used. The use of benzoyl chloride as acylating agent in presence of triethylamine and 4-pyrrolidinopyridine led to a mixture of compounds **1a, 2a, 4a** and **5a** depending on the molar ratio and reaction time. Lowering the temperature (-20°C) led only to the formation of **2a** in very low yield, while the use of pyridine as solvent led to the formation of **1a** in 25% yield. Increasing the amount of benzoyl chloride shifted the composition of the reaction mixture exclusively in favor of the formation of **4a** and **5a**. In contrast, the use of aliphatic acyl chlorides, such as **b** and **c**, predominantly produced the derivative **1**, showing a weak tendency to form the corresponding dehydrated products. The common Steglich esterification procedure was applied using different coupling reagents. The use of a large excess of DCC/DMAP with a reaction time of 3-4 h gave positive results to obtain the desired C3 acylated derivatives (**1a-c**). The selectivity was improved by adding an excess of ZnCl₂, and compound **1** was preferentially obtained, although the reaction time increased. Stoichiometric amount of DCC with 4-(dimethylamino)pyridinium 4-toluenesulfonate (DPTS) as acyl transfer agent instead of DMAP did not make the reaction selective, moreover the kinetics resulted very slow. The use of excess DCC often resulted in tricky purifications of the obtained products due to the difficult removal of the DCU by-product, however this could be resolved by using the reversed-phase chromatography. Alternatively, the use of the EDC as coupling agent results in easier purifications but overall requires a longer reaction time. In summary, the use of different acylating agents, coupling reagents, reaction conditions, and reaction times showed a significant influence on the formation of diverse products, giving the possibility to shift the product formation preference (Table 2-1).

The spectroscopic characterization of the obtained derivatives required a detailed and sophisticated investigation. All compounds discussed were fully characterized using NMR data, and the complete ¹H and ¹³C NMR assignments have been determined based on 1D and 2D NMR spectra (¹H and ¹³C NMR, COSY, HSQC, and HMBC). Diagnostic NMR peaks are listed in Table 2-2. The evaluation of the main differences between maytansinol and the O-acylated derivative **1, 3, 5** shows an evident shift of H-3 signal from 3.34 to about 5 ppm as a consequence of the successfully esterification at the OH-3. It is possible to observe the shift of the H-2 signals from 2.36 and 1.91 ppm to about 2.9 and 2.2 ppm. The corresponding signals of compounds **2** and **4** did not undergo significant changes excluding an involvement of the hydroxyl group. The presence of C8-C9 double bond in compounds **2, 3-5** was

Table 2-1. Optimization studies of the maytansinol acylation



R	Y	Acyl eq	C.A.	Base	(h)	M	1	2	3	4	5
a ^a	Cl	0.5	-	TEA, A	0.5	82	-	5	-	-	-
a ^a	Cl	1	-	TEA, A	2	80	2	15	-	-	-
a	Cl	1	-	TEA, A	6	75	11	11	-	-	-
a	Cl	4	-	TEA, A	4	-	-	-	-	33	67
a ^b	Cl	6	-	Py	5	51	25	-	-	-	-
a	OH	3	DCC	DMAP	8	4	35	5	26	-	18
a	OH	6	DCC	DMAP	48	-	-	-	15	-	31
a ^c	OH	3	DCC	DMAP, ZnCl ₂	48	29	62	-	4	4	-
a ^c	OH	1	DCC	DPTS	5d	55	18	4	14	5	4
a	OH	3	EDCI	DMAP, TEA	24	21	39	8	12	-	7
a	OH	3	EDCI	DMAP, TEA	48	-	15	-	47	-	20
b	Cl	2	-	TEA, A	6	51	46	-	-	-	-
b	OH	3	DCC	DMAP	4	-	42	-	43	-	-
c ^[16]	Cl	8	-	TEA, A	7d	65	16	2	7	-	-
c	OH	3	DCC	DMAP	3	7	37	9	30	-	6
c	OH	3	EDCI	DMAP, TEA	18	17	36	4	15	-	6
a ^c	OH	3	DCC	DMAP, ZnCl ₂	48	20	66	-	5	-	-

*in standard conditions all the reactions were performed in r.t. in DCM as solvent. Exceptions: ^a Reaction performed at -20°C; ^b Reaction performed in Py; ^c Percentage determination by HPLC; M = maytansinol; DCM = dichloromethane; TEA=triethylamine; A = 4-pyrrolidinopyridine; Py = pyridine; DCC = dicyclohexylcarbodiimide; EDCI = 1-ethyl-3-(3-dimethylaminopropyl)carbodiimide; DMAP = 4-dimethylaminopyridine; DPTS = 4-(dimethylamino)pyridinium 4-toluenesulfonate

confirmed by the merge of the H-8 signals in the range of 4.5 – 5.3 ppm. Furthermore, the characteristic H-7 signal was shifted at lower field and the multiplicity changes to a *dd* for **2** and **3**, while a multiplet was observed for **4** and **5**. Similarly, it is possible to note the shift of H-10 over 4.15 ppm, moreover the olefinic protons signals H-11, H-12, and H-13 are all shifted slightly to higher fields. Finally, the disappearance of the NH signal indicates an acylation of oxazinanone and regards the compounds **4** and **5**.

Table 2-2. Diagnostic ¹H NMR spectroscopic data of the maytansinoids **2-5**.

Atom	M ^a	1 ^a	2 ^b	3 ^a	4 ^b	5 ^a
2	2.36, 2.13	2.88 – 2.79 2.26	2.32 2.14	2.91, 2.22	2.37, 2.12	2.99 – 2.87, 2.27
3	3.55	5.04 – 4.85 ^c	3.59	5.02	3.61	5.04
7	4.25	4.31 – 4.14	4.78	4.56	4.86	4.92 – 4.76 ^d
8	1.91, 1.41	1.59, 1.54 – 1.39	5.02 – 4.96	4.43	5.43 – 5.33	4.92 – 4.76 ^d
10	3.64	3.50	4.20 – 4.12	4.15	4.42	4.35
11	5.52	5.04 – 4.85 ^c	5.54	4.88	5.54	4.92 – 4.76 ^d
12	6.70	6.61	6.46	6.54	6.48	6.64
13	6.20	6.04	6.16	6.13	6.15	6.12
OH-3	4.50	-	-	-	-	-
OH-9	4.80	4.47	-	-	-	-
NH	6.42	6.33	7.08	8.03	-	-

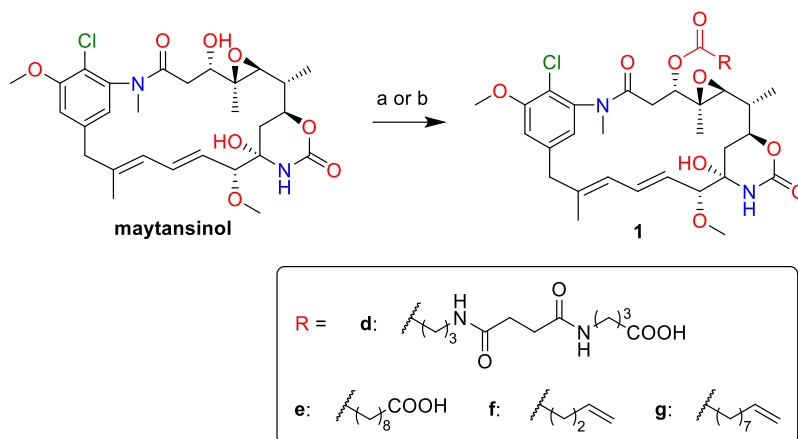
Chemical shifts (in ppm) were determined with reference to TMS; Spectra determined at 400 MHz; ^a Solvent is acetone-d₆; ^b Solvent is deuterated chloroform; ^{c-d} Chemical shifts bearing the same symbol overlap. M = maytansinol.

Long-chain maytansinoids

Having successfully established the maytansinol acylation reaction and comprehensively characterized the obtained products, we planned to obtain the long-chain maytansinoids. The designed compounds would have a terminal free carboxylic acid, for the eventual coordination of Mg²⁺ present in the site. It is worth noting that neither long-chain maytansinoids of this type nor acylation reaction of maytansinol with a dicarboxylic acid have been reported in the literature. The same procedure as in the case of short-maytansinoids was envisioned. However, initial trials to functionalize maytansinol with a prepared peptide-like linker or with sebacic acid to obtain **1d** or **1e**, using Steglich esterification, were not successful. An attempt to increase the temperature did not lead to any formation of the product either (Scheme 2-1).

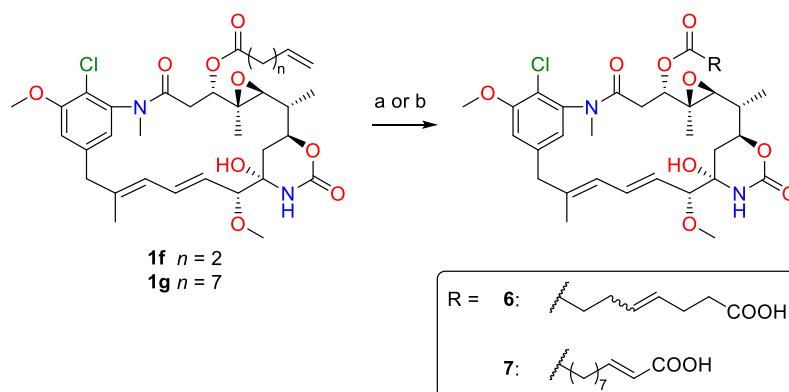
This prompted the change of the synthetic approach to a two step-synthesis: the preparation of short-chain maytansinoids with a terminal alkene, followed by a cross metathesis reaction with an unsaturated carboxylic acid. The acylation reaction of maytansinol to obtain **1f** and **1g** worked well. To check the influence of ZnCl₂ on the specificity towards the formation of a desired product, the reaction was performed both with and without the presence of ZnCl₂. The highest yields were obtained with the addition of ZnCl₂, although in both cases the yields were a bit lower for a longer-chain compound **1g**. The time prolongation had no great influence on the formation of the desired products, and only affected the ratios of different by-products obtained.

Compounds **1f** and **1g** were then used in the Ru-catalyzed olefin metathesis reaction to obtain the long-chain derivatives, using the 2nd generation Hoveyda-Grubbs catalyst. The



Scheme 2-1. Reaction conditions: a) RCOOH 3 eq, DMAP 3 eq, DCC 3.3 eq in DCM, DCM/DMF 1:1, r.t., 24-48h, **1d** n.r. (or **1e** n.r.; **1f** 45%; **1g** 39%). At 40°C: **1d** n.r. (or **1e** n.r.); b) RCOOH 3 eq, DMAP 3 eq, DCC 3.3 eq in DCM, ZnCl₂ 3 eq, DCM (+10% DMF), 48h, **1f** 68% (or **1g** 57%).

compound **1f** was reacted with 4-pentenoic acid, while compound **1g** was reacted with acrylic acid, to obtain maytansinoids **6** and **7**, respectively. The purification was found to be trickier for compound **6**, it was obtained in lower purity than 90%, while compound **7** didn't present this issue. Based on the docking studies, the preferred length of a long-chain maytansinoid was estimated at 10-11 carbon atoms. Therefore, compound **7** had a linker of an optimum length. The *trans*-isomer of compound **7** was the one detected by ¹H NMR analysis. Importantly, the docking studies showed that the E/Z isomerism did not seem to



Scheme 2-2. Reaction conditions: a) **1f** 1 eq, 4-pentenoic acid 2.25 eq, Hoveyda-Grubbs 2nd gen 20 mol%, DCM, reflux, 18h, **6** 44%; b) **1g** 1 eq, acrylic acid 2.5 eq, Hoveyda-Grubbs 2nd gen 20 mol%, DCM, reflux, 18h, **7** 46%.

influence the outcome since both stereo isomers were able to establish the same interactions with the Mg²⁺ even if the poses of the linkers slightly differed from each other. Obtaining both short-chain maytansinoids **1f** and **1g** and long-chain maytansinoids **6** and **7** allowed us to perform more studies on maytansinoids SAR based on the length and nature of the chain. Moreover, the long-chain analogue could be exploited to attach other molecules of interest. All the compounds were submitted to X-ray crystallography structure determination. Moreover, compounds **1f**, **1g** and **7** were submitted for biological evaluation.

Maytansinoid conjugates

We then moved on to establish the conditions for the conjugation of the maytansinoids with guanosine nucleotide mimetics. Guanosine itself and its 2', 3'-dideoxyguanosine analogue, acyclovir, widely known for its antiviral properties^[29,30], were chosen as nucleotide mimetics (Figure 2-4). The length of the linker was based on computational studies. Since the measured spatial distance between the two functional groups of interest was of ~ 12 Å, the desired linker lengths ranged from 12-14 atoms.

We have considered different chemical strategies, including the olefin metathesis previously used to obtain the long-chain maytansinoids and the copper-catalyzed azide-alkyne cycloaddition (CuAAC) click reaction. Initially, we tried to use a similar approach used for the

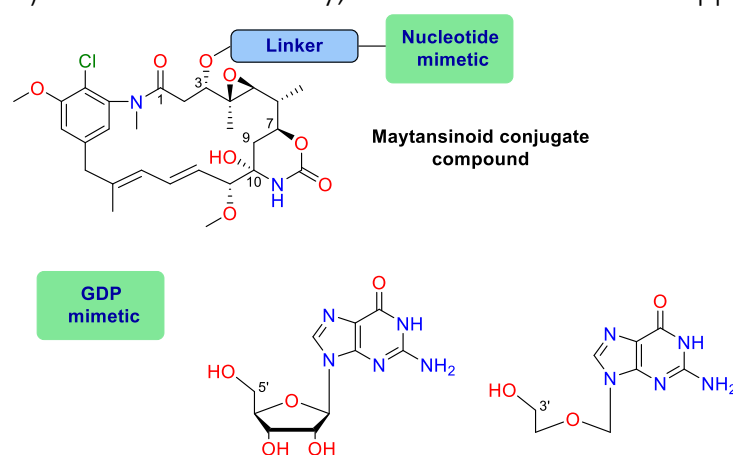
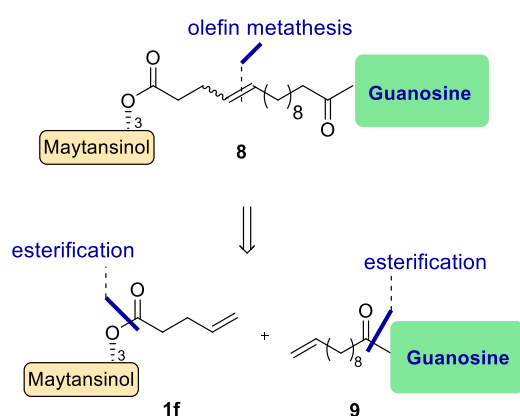


Figure 2-4. A schematic image of the maytansinoid-conjugate compounds to target maytansine and GDP binding sites.



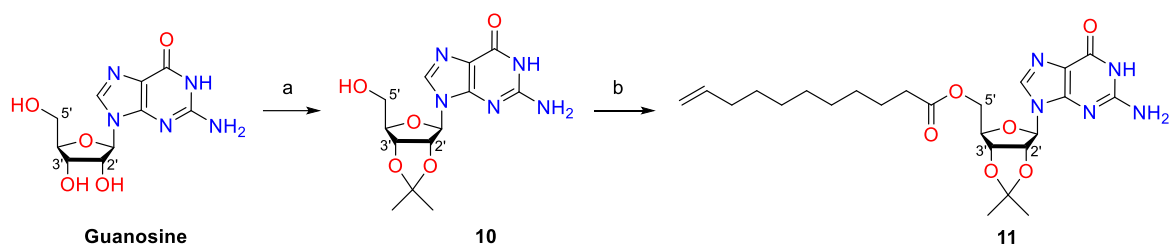
Scheme 2-3. Retrosynthetic pathway for the synthesis of maytansinoid conjugate **8**

synthesis of long-chain maytansinoids, by applying cross metathesis reaction. Compound **8** was planned to try out this route (retrosynthetic approach depicted in Scheme 2-3). The docking studies confirmed that the length and flexibility were appropriate to accommodate the maytansinoid and nucleotide mimetic, represented in this compound by guanosine. Compound **1f** was prepared as discussed above (Scheme 2-1). Similarly, guanosine fragment could be obtained through 5'-O- esterification. However, the poor solubility of guanosine in most organic solvents complicates the reactivity and the handling. In this

regard, 2',3'-diol or free amine protection of guanosine could be considered.^[31-37] The isopropylidene ketal formation on guanosine sufficiently increased the solubility, so the NH₂ protection was not undertaken. In addition, the formation of the ketal would increase the selectivity for the subsequent 5'-O esterification reaction and the formation and removal

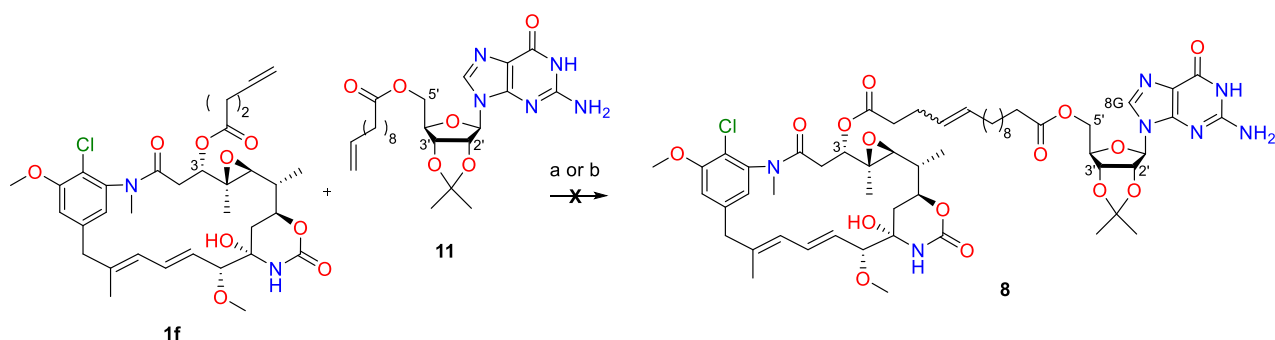
occur easily under acidic conditions. Therefore, guanosine was treated with perchloric acid in acetone providing **10** quantitatively. The literature reports wide reaction conditions useful to perform acylation at 5' position of 2',3'-isopropylidene guanosine, by acyl halides, anhydrides, and acids under coupling conditions.^[31,33,38] The chosen approach was the coupling with the carboxylic acids, therefore compound **10** was esterified with undecylenic acid in the presence of EDC as a coupling reagent, providing **11** in 86% yield (Scheme 2-4).

Having **1f** and **11** in hands, the trials to perform the cross metathesis reaction using the



Scheme 2-4. Reaction conditions: a) HClO_4 60%, acetone, 18h, quant.; b) undecylenic acid 1.5 eq, EDC-HCl 1.8 eq, TEA 2.2 eq, DMAP 0.5 eq, DCM, 18h, **11** 86%

Grubbs 2nd gen. or Hoveyda-Grubbs 2nd gen. (10 or 20 mol%) were performed. However, the



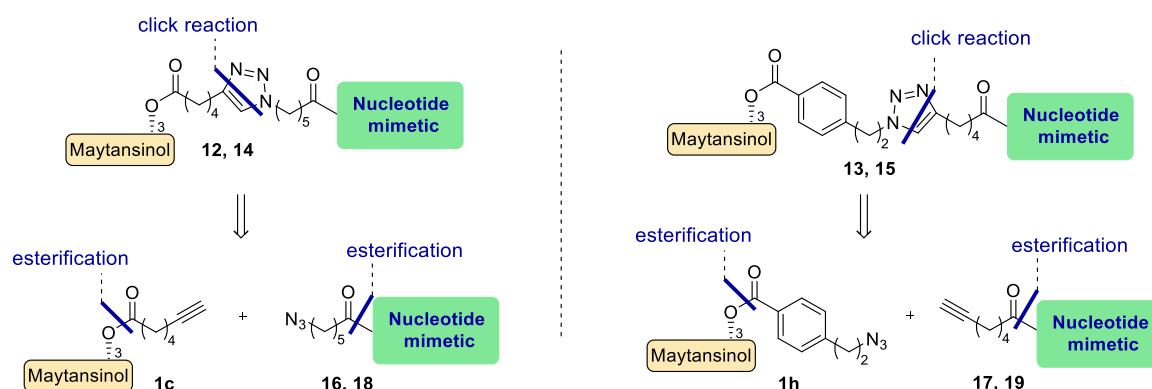
Scheme 2-5. Reaction conditions: a) Grubbs 2nd gen 10 mol%, DCM, 40 °C to r.t., 12h b) Hoveyda-Grubbs 2nd gen 20 mol%, DCM, r.t., 12h

reaction led to the complex mixture of products, impossible to purify.

Possibly, the purine ring of the guanosine could interfere with this reaction, as compounds containing N-heteroaromatics are known to be poor partners in cross-metathesis reactions, supposedly due to catalyst deactivation.^[39]

Considering the high cost and low availability of maytansinol, we have decided not to proceed with any additional trials for this approach. Instead, we focused in more detail on the linkers which could allow the conjugation of the compounds of interest by means of CuAAC click reaction. It is known for its high efficiency and regioselectivity, and wide

applicability in the conjugation of various types of molecules, including complex natural products.

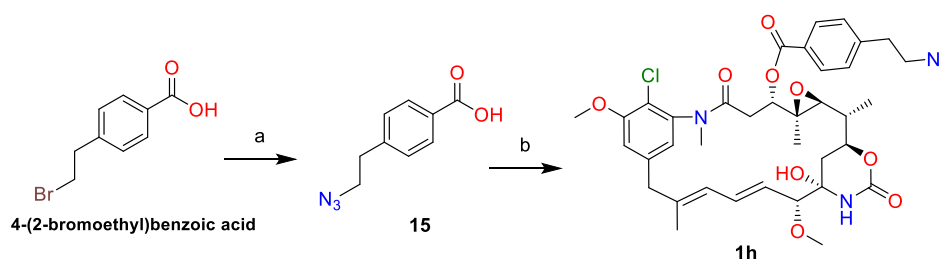


Scheme 2-6. Retrosynthetic pathway for the synthesis of maytansinoid conjugates **8-11**

Based on computational studies, 54 possible linkers were considered in which the position of the triazole group and the length of the carbon tails attached to it varied. The interactions established by the nucleotide and its mimetics with β -tubulin were analyzed as well (discussed in more detail in the *Computational studies* Section).

Conjugate compounds **12-15** can be obtained by a CuAAC reaction between the fragment of an alkyne (**1c**, **17**, **19**) and an azide (**1h**, **16**, **18**) providing the corresponding triazole derivatives (Scheme 2-6). Both fragments can be prepared as esters starting from maytansinoid and guanosine, or acyclovir, by condensation with carboxylic acids. The alkyne maytansinoid **1c** was already prepared previously, during the maytansinoid optimization studies, using the Steglich esterification with 6-heptynoic acid, as described above (Table 2-1).

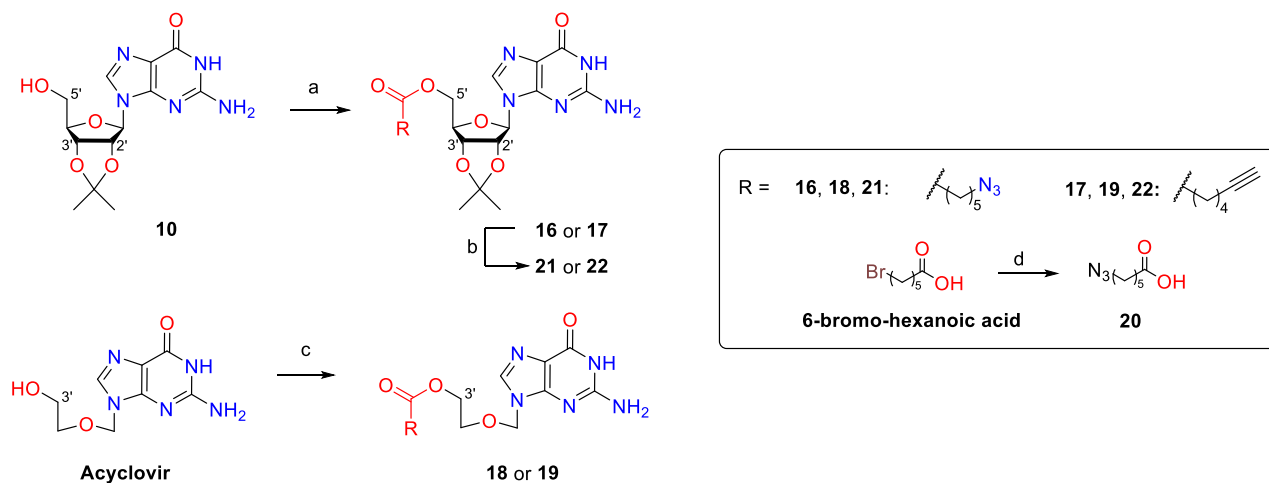
Similarly, compound **1h** was synthesized using the ZnCl_2 catalyzed Steglich esterification with 4-(2-azidoethyl)benzoic acid (**15**), which was prepared by treating the corresponding 4-(2-bromoethyl)benzoic acid with NaN_3 (Scheme 2-7).



Scheme 2-7. Synthesis of maytansinoid **1h**. *Reaction conditions:* a) NaN_3 1.1 eq, DMSO, rt, 20 h, **15** 86% ; b) **15** 3 eq, maytansinoid 1 eq, DMAP 3 eq, DCC 3.3 eq in DCM, ZnCl_2 3 eq, DCM (+10% DMF), 24h, **1h** 68%.

To obtain the nucleotide mimetic fragments **16-19**, 5'-O- and 3'-O-esterification was performed on 2',3'-isopropylidene-guanosine **10** and acyclovir, respectively (Scheme 2-8).

Compound **10** and acyclovir were similarly esterified with 6-azidohexanoic acid (**20**) or 6-heptynoic acid in the presence of EDC-HCl as a coupling reagent. **20** was obtained by treating the corresponding 6-bromohexanoic acid with NaN_3 . The reactions on 2',3-O-isopropylidene-guanosine were performed in DCM as solvent giving 71% and 78% of **16** and **17**, respectively. In the case of acyclovir, a mixture of DCM/DMF was used to overcome the solubility issues, obtaining **18** and **19** with a yield of 65% and 43%, respectively.



Scheme 2-8. Reaction conditions: a) 6-azidohexanoic acid (or 6-heptynoic acid) 1.5 eq, EDC-HCl 1.8 eq, TEA 2.2 eq, DMAP 0.6 eq, DCM, 18h, **13** 71% (or **15** 78%); b) TFA 80% aq, 30 min, **18** 81% (or **19** 98%); c) 6-azidohexanoic acid (or 6-heptynoic acid) 1.5 eq, EDC-HCl 2.1 eq, TEA 2.1 eq, DMAP 0.5 eq, DCM/DMF 1:1.5, 18h, **14** 64% (or **16** 43%). d) NaN_3 1.1 eq, DMSO, rt, 18 h, 91%.

Considering that deprotection of guanosine in acidic condition could affect the maytansinol part in the final step of conjugation, the cleavage of isopropylidene was carried out before the click reaction. Therefore, compound **16** and **17** were treated with TFA 80% aq^[34,35,38] giving the desired products **21** and **22** with 81% and 98% of yield, respectively. The alkyne- and azide- building blocks were joined by performing the CuAAC. The reactions carried out on the pairs of maytansinoid/guanosine **1c/21** and **1h/22** with catalytic quantities of CuSO_4 in the presence of Na-ascorbate as reducing agent in $\text{H}_2\text{O}/t\text{-BuOH}$ 1:4 did not lead to any product. The triazole ring was not obtained neither performing the reaction in $\text{H}_2\text{O}/\text{DMSO}$ 1:2 as solvent nor by increasing the quantities of the reagents.

In order to better support the solubility of guanosine and the reaction, a new route to carry out the CuAAC was considered. The strategy involved performing the click using the isopropylidene-protected guanosine intermediates **16** and **17** and then cleaving the ketal in the final adduct. For this purpose, the experimental conditions to remove protecting group without altering the sensitive structure of maytansinol required a careful condition screening (Table 2-3).

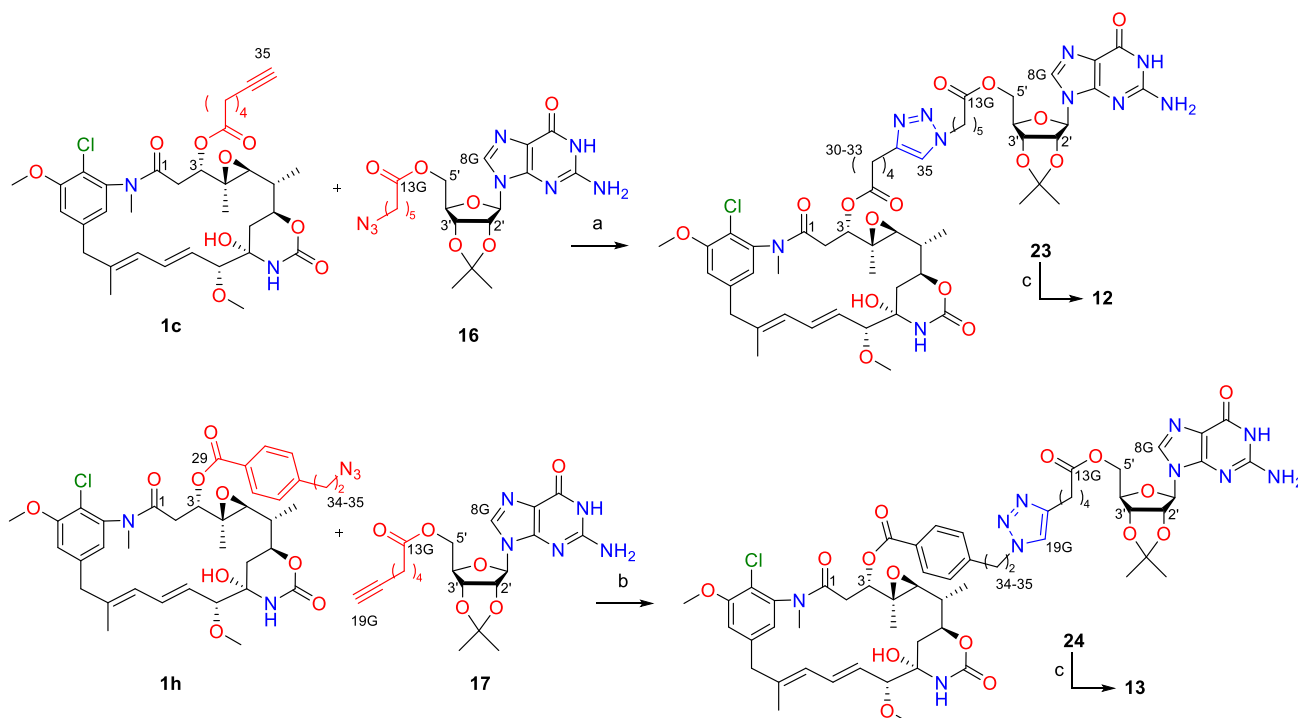
All conditions except the use of PdCl_2 did not affect maytansinol, but at the same time failed to cleave the ketal. Although the use of formic acid with the conditions reported in the literature for the specific removal of acetonide from guanosine produced no results,

increasing the acid concentration and heating slightly to 40°C achieved the goal. By ¹H-NMR analysis the integrity of maytansinol and deprotection of guanosine was confirmed.

Table 2-3. Cleavage conditions of isopropylidene on guanosine in the presence of maytansinol.

Cleavage Condition	T [°C]	Time [h]	Result
AcOH 80% aq	25	48	n.r.
AcOH 80% aq	65	18	n.r.
PdCl ₂ (CH ₃ CN) ₂	60	24	degradation
CAN	25	48	n.r.
PPTS	25	48	n.r.
CuCl ₂ ·2H ₂ O	0 to 25	48	n.r.
HCOOH 50% aq ^[35]	25	48	n.r.
HCOOH 70% aq	25	48	n.r.
HCOOH 70% aq	40	2	ketal cleavage

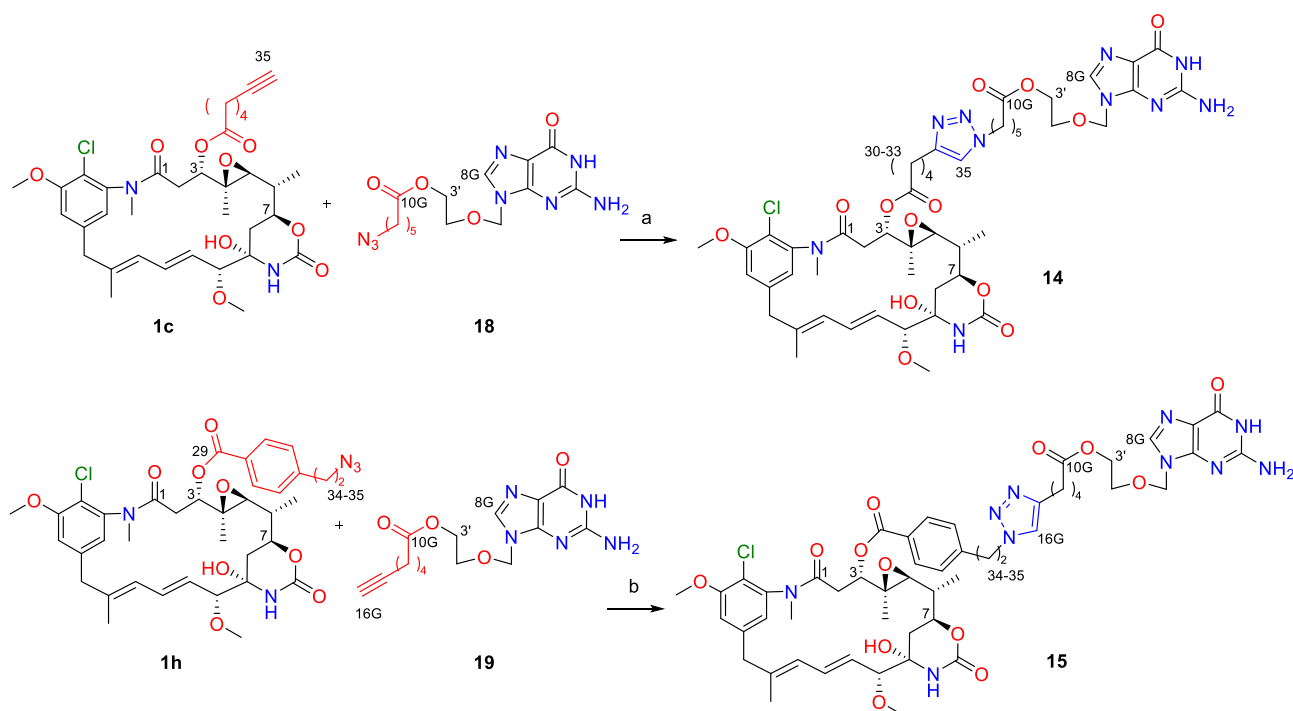
The CuAAC reaction was repeated by treating maytansinoid **1c** and protected 5'-O-acylguanosine **16** with an excess of CuSO₄ and Na-ascorbate in H₂O/DMSO 1:2. As expected, the protecting group improved the solubility of guanosine obtaining a positive result. The



Scheme 2-9A. Reaction conditions: a) **1c** 1 eq, **16** 1.5 eq, CuSO₄·5H₂O 1.6 eq, Na-ascorbate 6.4 eq, H₂O/DMSO 1:2, 3h, **23** 89%; b) **1h** 1 eq, **17** 1.5 eq, CuSO₄·5H₂O 1.6 eq, Na-ascorbate 6.4 eq, H₂O/DMSO 1:2, 3h, **24** 85%; c) HCOOH 70% aq, 40°C, 4h, **12** 62% (or **13** 77%);

triazole ring was formed in few hours with a yield of 89% in the isolation of compound **23**. The same approach was used on **1h/17** fragment pair to get compound **24** with 85% of yield (Scheme 2-9A). Then, both products were treated with formic acid 70% aq at 40°C providing the final conjugate compounds **12** and **13** after 4 hours with yields of 62% and 77%, respectively.

In case of maytansinoid-acyclovir conjugates, similar conditions were applied. However, in these reactions catalytic quantities of CuSO₄ and Na-ascorbate were sufficient for the reactions to proceed, a mixture of H₂O/DMF 1:2 was used as solvent. The desired final products **14** and **15** were obtained in 55% and 35%, respectively (Scheme 2-9B).



Scheme 2-9B. Reaction conditions: a) **1c** 1 eq, **18** 1.2 eq, CuSO₄·5H₂O 0.4 eq, Na-ascorbate 4 eq, H₂O/DMF 1:2, 5h, **14** 55%; b) **1h** 1 eq, **19** 1.2 eq, CuSO₄·5H₂O 0.4 eq, Na-ascorbate 4 eq, H₂O/DMF 1:2, 6h, **15** 35%.

The NMR elucidations were completed to confirm the structures, and the shifting of the diagnostic signals demonstrated the formation of triazole on maytansinol-guanosine conjugates **23** and **24** and maytansinol-acyclovir conjugates **14** and **15** (Table 2-4). The four conjugates were submitted for biological evaluation and the X-ray crystallography structure determination.

Table 2-4. Diagnostic ¹H NMR spectroscopic data of triazole formation DMSO-d₆.

Atom	¹ H-NMR ^{a,b}		¹³ C-NMR ^{a,c}		
	from	to	from	to	
23	33	2.28 ^e	2.65	18.04 ^e	28.82
	34	-	-	84.20 ^e	146.89
	35	1.95 ^e	7.85	69.0 ^e	122.13
	18G	3.29	4.25	51.59	49.38
24	35	3.70 ^d	4.64	52.48 ^d	50.23
	17G	2.14	2.53	18.50	25.07
	18G	-	-	85.28	146.84
	19G	2.74	7.78	72.40	121.96
14	33	2.28 ^e	2.65 ^f	18.04 ^e	28.81 ^f
	34	-	-	84.20 ^e	146.91 ^f
	35	1.95 ^e	7.85 ^f	69.0 ^e	122.33 ^f
	15G	3.32 ^f	4.23 ^f	51.59	49.42 ^f
15	35	3.70 ^d	4.64 ^f	52.48 ^d	49.78 ^f
	14G	2.15 ^f	2.53 ^f	18.50	25.53 ^f
	15G	-	-	85.28	146.58 ^f
	16G	2.74 ^f	7.82 ^f	72.40	121.72 ^f

Computational studies

The design of the synthesized compounds was based on the computational studies, performed by Helena Pérez-Peña from the group of Prof. Stefano Pieraccini, University of Milan.

Docking analysis of short chain-maytansinoids 1-5

Docking was used to predict the spatial coordinates of the binding mode acquired by the synthesized maytansinoids **1-5**, using the docking engine Autodock Vina. In all cases, the orientation of the maytansinol ring remained in the same spatial arrangement, acquiring a similar binding mode to the parent compound, maytansine. The introduction of bulky substituents at position C3 did not alter the predicted three-dimensional (3D) arrangement of the core of the molecule. Thus, it was assumed that binding of maytansinoids to β -tubulin

is very tolerant to modifications of the C3-hydroxyl group and expected that the binding mode of the investigated molecules resembles the one of maytansine.

Modelling of Long-chain Maytansinoids with S4MPLE

The docking tool used to model the long-chain maytansinoids **6** and **7** via molecular growth was the Sampler for Multiple Protein-Ligand Entities (S4MPLE).^[40] The high-resolution crystallographic structure used for the docking studies of the long-chain maytansinoids was obtained from the Protein Data Bank (PDB) entry with ID 4TV8.^[41] The docking studies showed that the designed long-chain maytansinoids could accommodate in the pocket similarly to maytansine and establish the interactions with Mg^{2+} . For the alkene chains, the E/Z isomerism did not seem to influence the outcome since both stereo isomers were able to establish the same interactions with the Mg^{2+} even if the pose of the linkers slightly differed from each other (Figure 2-5).

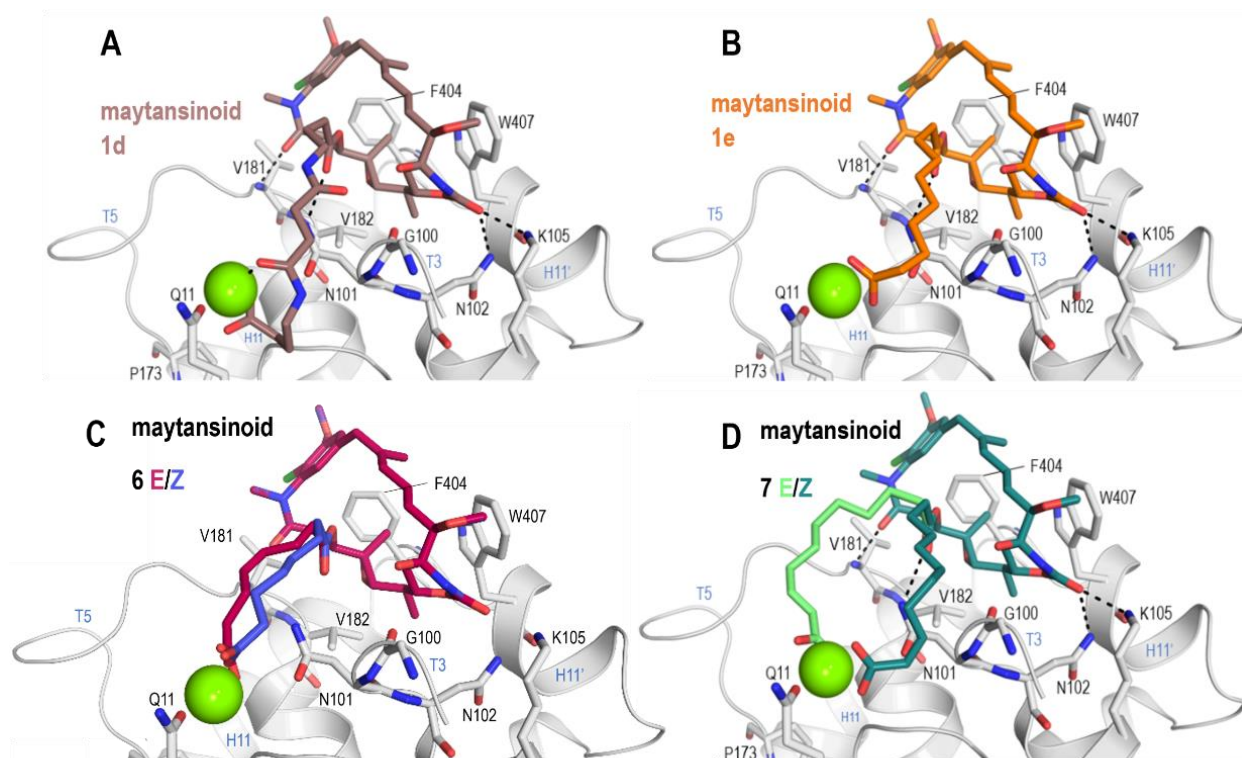


Figure 2-5. Docking results of the compounds (A) **1d**, (B) **1e** (C) **6** and (D) **7**. β -tubulin is depicted in grey, Mg^{2+} is depicted as a green ball. The structural renderings were obtained using PyMol 2.3.4.

Design of maytansinoid conjugates

In the linker-design stage, the main goal was to define a proper length and flexibility to secure the accommodation of maytansinol and nucleotide-like scaffolds in their respective β -tubulin binding sites. For the triazole-containing linkers, a library of 54 possible linkers in which the position of the triazole group and the length of the carbon tails attached to it varied. Since the measured spatial distance between the two functional groups of interest

was of ~ 12 Å, linker lengths ranging from 12-14 atoms were considered. Therefore, the linker size was rationally chosen by determining that the sum of A and B should be always greater or equal to 5 and smaller or equal to 13.

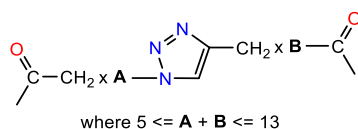


Figure 2-6. Linker design strategy: schematic version of the applied approach followed for the generation of 54 triazole-containing linkers of different lengths.

For the linker screening, the maytansinol and the guanosine molecules were treated as fragments and were fixed in their states seen in the crystal structure 4TV8. Then, the linker screening was carried out using the docking software S4MPLE^[40] to search for the linker that best bridged the gap between the two fragments (maytansinol and guanosine). None of the generated linkers put any strain on the anchor fragments, therefore the linkers were chosen upon synthetic convenience (**12**, **14**). In case of a more rigid linker possessing a phenyl ring in the side chain of maytansinol the degrees of freedom of the linker were reduced, thus better orienting the linker moiety towards the nucleotide pocket (**13**, **15**). The validity of the chosen linkers were analyzed via template docking. The results showed that both of the linkers can flexibly connect both the maytansinol and the guanosine entities in a suitable distance, which allows the two entities to bind tubulin by maintaining a proper geometry. The interactions established by the nucleotide with β -tubulin were analyzed as well. It was observed that the guanine moiety established the main interactions within the site *via* very specific hydrogen bonds and pi-stacking. Therefore, conjugate compounds containing acyclovir were designed (**14**, **15**). Docking studies confirmed that the 5-membered ring of

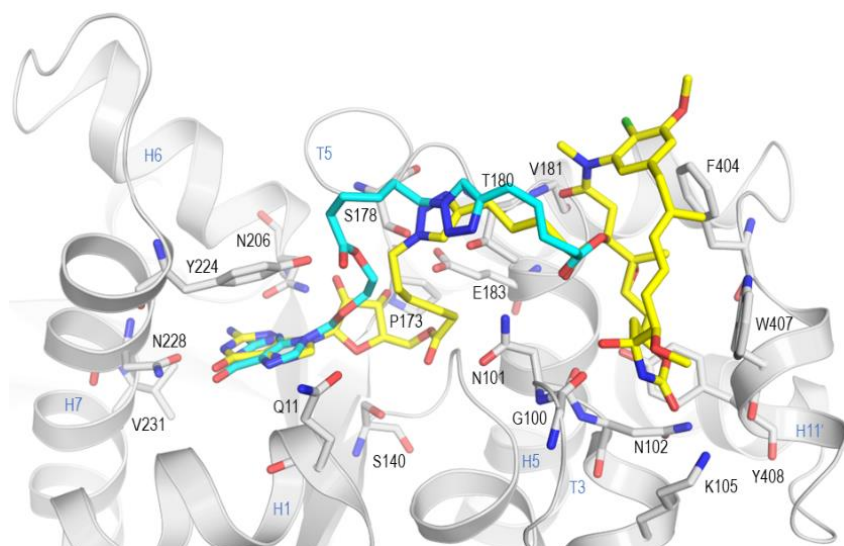


Figure 2-7A. Docking result of the maytansinoid-guanosine conjugate **12** (yellow) superimposed to the docking result of the maytansinoid-acyclovir conjugate **14** (cyan) when bound to tubulin (grey).

the ribose can be substituted without disturbing major interactions of the guanine moiety with β -tubulin. Further, superposition of the docked structure shows that a binding mode resembling the original guanosine one can be adopted (Figure 2-7A,B).

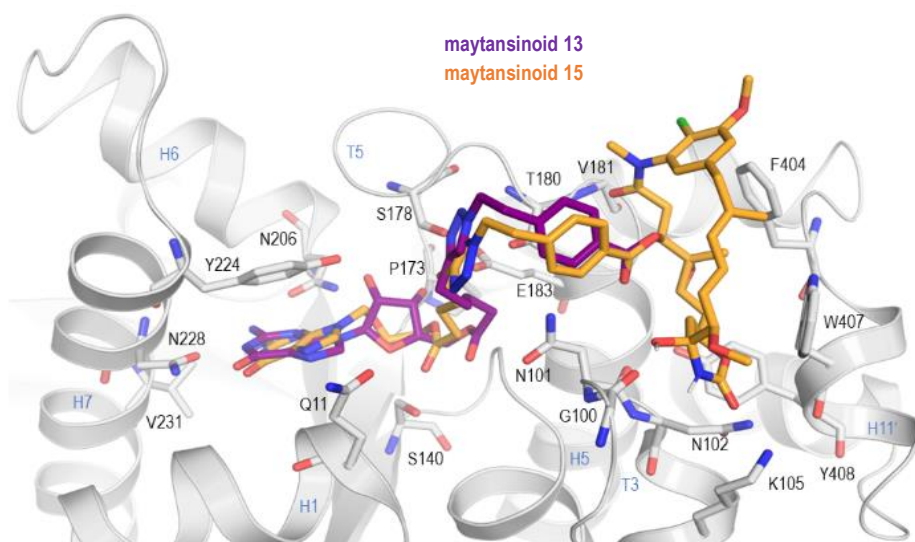


Figure 2-7B. Docking result of the maytansinoid-guanosine conjugate **13** (violet) superimposed to the docking result of the maytansinoid-acyclovir conjugate **15** (orange) when bound to tubulin (grey).

Biological evaluation

To evaluate the activity of the representative compounds **1a-c**, **2**, **3a-c**, **4a**, **5a** (1st series), as well as **1f-g**, **7**, **12-15** (2nd series) on tubulin and microtubules, the compounds were sent to the group of Dr. J.F. Díaz, Centro de Investigaciones Biológicas Margarita Salas, Madrid, Spain. First, their effect on microtubule assembly dynamics was studied, and subsequently their binding affinities to tubulin dimers and their cell toxicity was determined.

Inhibition of tubulin assembly

Maytansine site ligands preclude tubulin assembly by blocking the addition of new tubulin subunits onto the microtubule.^[11] We therefore tested the selected compounds for their ability to inhibit tubulin assembly (Figure 2-8). Maytansine, which completely abolishes tubulin polymerization, and maytansinol, which has a noticeable effect at stoichiometric concentrations, were used as controls.

All the compounds assayed inhibited tubulin assembly into microtubules at stoichiometric ratios with tubulin, however, they showed different potencies. From the first series, compounds **1a**, **1b**, **1c**, **3a**, **3b**, **4a** were strong inhibitors that completely abolished microtubule assembly, compounds **2**, **3c** and **5a** showed only a mild inhibition (Figure 2-8A,B). From the second series, compounds **1f**, **1g**, **7**, **14** and **15** showed the most potent effect. Dose-response polymerization assays were performed for the second series as well,

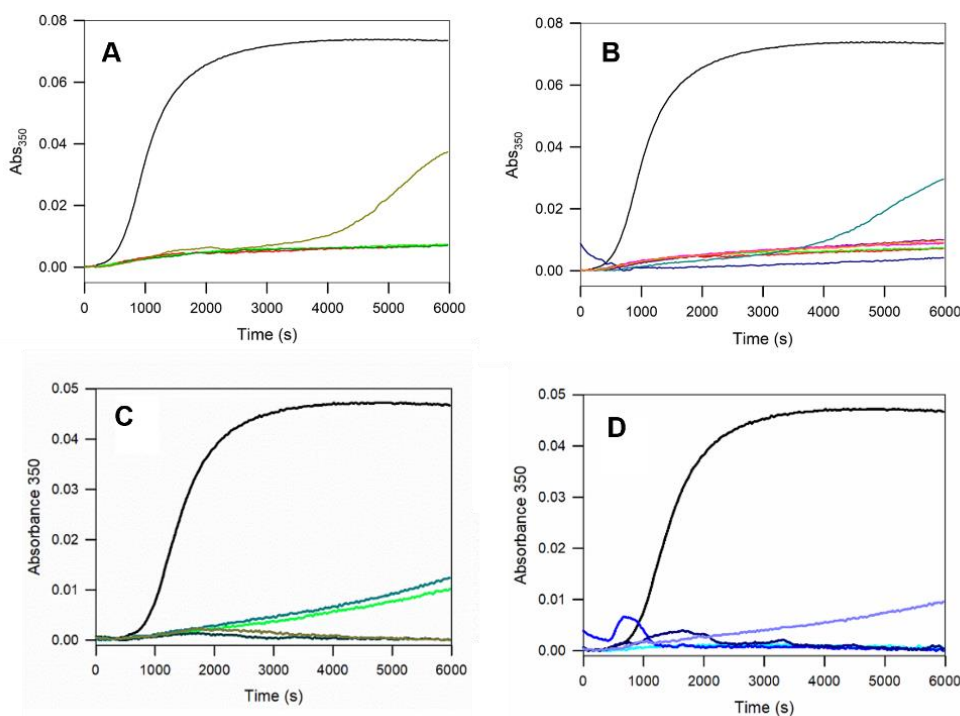


Figure 2-8. Inhibition of tubulin assembly activity by selected compounds. All experiments were performed as duplicates of two independent experiments. The graphs represent time courses of assembly of 25 μM tubulin in GAB buffer in the presence of vehicle (DMSO; black lines) or 27.5 μM of: (A) **maytansine** (red), **maytansinol** (green), **2** (dark yellow), **1a** (dark red); (B) **maytansine** (red), **maytansinol** (green), **1b** (pink), **1c** (orange), **3a** (dark blue), **3b** (dark pink), **3c** (dark cyan). (C) **12** (light green), **13** (teal), **14** (dark green), **15** (dark yellow); or (D) **1f** (cyan), **1g** (blue), **1h** (light purple), **7** (dark blue).

demonstrating a clear difference between between 5 μM (incomplete inhibition) and 10 μM (complete inhibition) concentrations of the compounds and distinguishing compound **1g** as the best in the series. Interestingly, in the polymerization assays maytansinol-acyclovir conjugates demonstrated a higher destabilizing effect compared to maytansinol-guanosine ones.

Binding affinities

In order to correlate the tubulin assembly inhibition with the binding affinities of the compounds for the maytansine site, these were determined by means of competition against Fc maytansine (Table 2-5).^[16] Surprisingly and oppositely to other microtubule-targeting agents, the potency did not correlate well with the determined binding affinities. The reason for this is that all the compounds assayed have at least μM affinity. Tubulin assembly inhibition is dependent on two factors. First, the binding affinity of the compound for the site has to be significant at the concentrations of the inhibition assay. Since the concentrations of both tubulin and drugs employed in the assay were nearly one order of magnitude higher than the weakest dissociation constant measured for **4a** (3 mM), we

expected that all the ligands employed were bound to the protein. Therefore, the binding affinity should not influence the *in vitro* assembly inhibition activity in the way we observed.

According to the mechanism of action proposed by Prota *et al.*,^[11] ligand binding to the maytansine site should have a strong influence on MT-assembly. Maytansine site ligands bind at a shallow pocket at the top of the tubulin β -subunit where the interaction with a longitudinal aligned tubulin-dimer in the protofilament takes place, thereby inhibiting the

Table 2-5. Binding affinities of selected maytansinoids

Compound	Mean Kb (M ⁻¹)	Kd (nM)
maytansine	9±1x10 ⁷	11±1
maytansinol	1.30±0.06 x10 ⁶	780±40
1a	2.0±0.1x10 ⁷	51±3
1b	9±1x10 ⁷	11±1
1c	5.4±0.5x10 ⁷	19±2
1f	9±2x10 ⁶	111±12
1g	6±1x10 ⁶	166±24
1h	1.3±0.3x10 ⁷	77±15
2	1.20±0.03x10 ⁶	830±20
3a	9.2±0.3 x10 ⁵	1090±40
3b	1.17±0.04x10 ⁶	860±30
3c	5.6±0.4x10 ⁵	1800±120
4a	6±2x10 ⁵	3000±100
5a	5.0±0.5x10 ⁵	2000±200
7	5.3±0.7x10 ⁶	188±22
12	1.2±0.2x10 ⁷	83±12
13	1.3±0.1x10 ⁷	83.4±7.8
14	7.3±0.8x10 ⁶	137±14
15	8±1x10 ⁶	125±14

Data are the mean ± SEM values of three independent experiments with duplicates in each one.

addition of tubulin subunits at the plus ends of growing microtubules. From the ligands studied, **1b** (11 nM) and **1c** (19 nM) showed the highest affinities with dissociation constants close to the one of maytansine (11 nM), indicating that aliphatic chains of different nature can easily replace the N-acetyl-N-methyl-L-alanine. Other short- and long-chain maytansinoids **1a**, **1f-h** and **7**, as well as maytansinol conjugates **12-15**, have slightly lower affinities but still much-improved compared to that of unsubstituted maytansinol. However, the series of compounds lacking the hydroxyl at position C9 showed binding affinities in the 1 mM range (**2** 830 nM, **3a** 1090 nM, **3b** 860 nM), thereby suggesting that the C9-hydroxyl may serve as a critical anchoring point to allow establishing the interaction with the site. Finally, the remaining three compounds also lacking the hydroxyl at position C9 with modifications either at the C3, the oxazinanone-nitrogen or both, displayed the lowest affinities in the sub mM range: **3c** (1800 nM), **4a** (3000 nM) and **5a** (2000 nM).

In summary, two modifications resulted in a strong impact on the binding affinity, namely the lack of esterification of the C3-hydroxyl (maytansinol) and the elimination of the C9-hydroxyl. Moreover, changes in the nature of the ester side chain at the C3 position do not interfere with the high affinity of maytansinoids. For most derivatives, binding affinity is well conserved indicating low or neglectable influence of the side chain and maytansinol conjugation on the interaction of the maytansine core with tubulin, but also suggesting little interaction of the nucleotide moiety in case of maytansinoid conjugates.

Cytotoxicity

To correlate the potency of binding with the toxicity, and to investigate the potential of the compounds to overcome membrane pumps mediated multidrug resistance, we determined the cytotoxicity of the compounds both in A549 (ovarian cell carcinoma) and in the isogenic pair A2780/A2780AD (pGp overexpressing) cell lines (Table 2-6). Cytotoxicity requires effective binding of a ligand to tubulin at concentrations, which are about one order of magnitude lower than the dissociation constants of the corresponding ligand.^[42]

The cytotoxicities determined in this study correlated well with the binding affinities: compounds with high affinity **1a-h**, **7**, **14** and **15** show very good activity against the tumoral cells, being some of them even more active than the parental compound maytansine (nano- to sub-nanomolar cytotoxicities), while compounds with submicromolar and micromolar affinities were less cytotoxic. However, our data also highlight that the compounds were better substrates of pGp than maytansine, displaying higher resistance indexes than the

Table 2-6. IC₅₀ of maytansinoid compounds in A549 and A2780/A2780AD cell lines

Compound	A549 IC ₅₀ (nM)	A2780 IC ₅₀ (nM)	A2780AD IC ₅₀ (nM)	R/S
<i>maytansine</i>	0.278±0.04	0.31±0.02	19.5±1.14	29
<i>maytansinol</i>	60±3	23.78±1.65	1459.94±148.27	
1a	0.24±0.03	0.11±0.01	11±1	100
1b	1.2±0.3	0.25±0.01	20±1	80
1c	0.07±0.008	0.033±0.003	4.7±0.6	142
1f	0.26±0.01	0.07±0.02	11±2	157
1g	0.27±0.01	0.37±0.02	33±3	89
1h	1.1±0.2	0.14±0.01	17±3	121
2	28±2	74±4	>19706	
3a	>570	338.40±4.65	2626.48±186.56	
3b	190±40	130±20	>6156	
3c	320±40	225±15	>7956	
4a	>1030	2088.08±99	13477.38±622.59	
5a	47±6	241,27±32.14	3495.97±319.71	
7	4.9±0.3	2.0±0.4	400±70	200
12	11600±700	620±50	21000±1000	34
13	4800±300	160±10	16000±2000	100
14	10.4±0.5	4.4±0.5	900±100	204
15	49±3	35±4	3600±500	103

Data are the mean ± SEM values of three independent experiments with duplicates in each one. In green – compounds with higher cytotoxicity than that of maytansine; in yellow – higher than that of maytansinol

parental compound. On the other hand, the maytansinol-guanosine conjugates underwent a severe loss of activity without losing binding affinity, which suggests that the resulting side chain precludes internalization in the cells. It most likely has something to do with the ribose of the guanosine, as maytansinol-acyclovir conjugates present much higher cytotoxicity.

Effects on tubulin cytoskeleton

In order to finish the characterization of the synthesized maytansinoids, we further investigated the effect of one of the most potent compounds **1a** on cellular microtubules. To do so, fluorescence microscopy using A549 cells was performed. The cells were incubated with increasing concentrations of the ligand for 48 h and compared the effects with those of the reference ligands maytansine, maytansinol and the vehicle (Figure 2-9). In interphase the microtubule network is covering the whole cytoplasm, while in dividing cells during metaphase there are regular bipolar spindles that allow the correct positioning and segregation of chromosomes in the subsequent division steps. Scale bar in all the images: 10 μm . Maytansine (5 nM) effects on interphase (upper panel) and mitotic cells (lower panel). In interphase we can observe a disorganized microtubule network with incipient signs of depolymerization, in an irregular bi-nucleated cell. Moreover, there are multipolar anomalous spindles in mitosis with DNA starting to condense. Maytansinol requires 100 nM

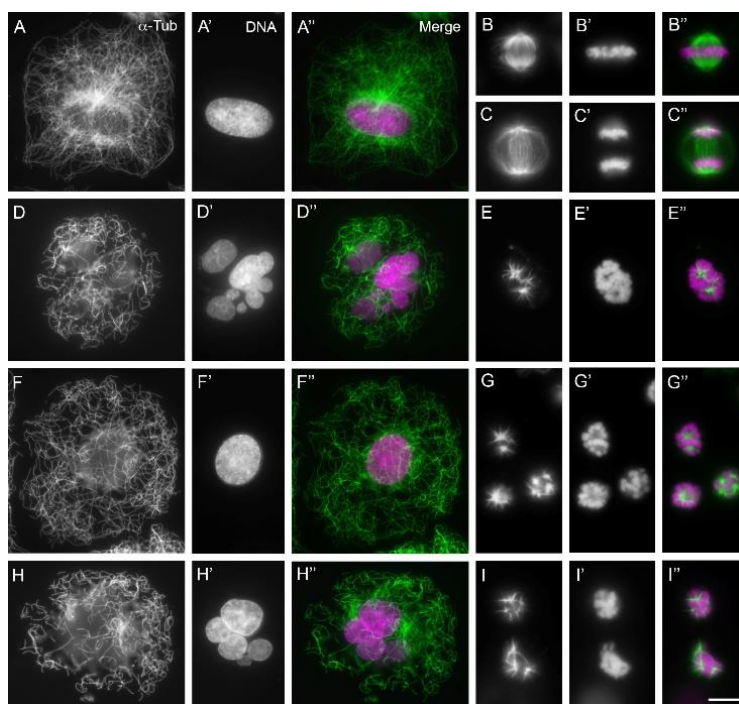


Figure 2-9. Effects of maytansinoids on cells in interphase and mitosis. The effect of these compounds on the microtubule network and mitotic spindle was characterized in A549 tumor cells by fluorescence microscopy. Cells were treated for 24 hours with the different compounds analyzed: control-DMSO 0.5% (A-C'') **maytansine** 5 nM (D-E''), **maytansinol** 100 nM (F-G'') and **1a** 5 nM (H-I''). Cells were immunostained for α -tubulin (A-I), stained for DNA (A'-I') and images obtained were merged (tubulin in green and DNA in magenta) (A''-I''). (A-A'') Interphase cell treated with drug vehicle (DMSO) notice the regular microtubule network evenly distributed in the cytoplasm. (B-B'') Control metaphase cell with a normally distributed

concentrations in interphasic cells and 50 nM in mitotic cells to observe the same destabilizing effect seen with maytansine. With **1a** 10 nM concentrations in interphasic cells and 5nM in mitotic cells are enough to observe similar effects to those noticed with maytansine in interphasic cells.

X-ray crystallography structures determination

In order to validate the computational analysis and to complement the biological assays we sought to determine the crystal structures of the respective tubulin-maytansinoid complexes. Compounds **1a-c**, **2**, **3a-c** (1st series) and **1f-h**, **6**, **7**, **12-15** (2nd series) were sent to Paul Scherrer Institut, Switzerland, where Anne-Catherine Abel and Dr. Andrea Prota evaluated and analyzed their binding to tubulin based on X-ray crystallography experiments.

Crystals of the T₂R-TTL protein complex, containing two α,β -tubulin dimers, the stathmin-protein RB3 and the tubulin tyrosine ligase TTL were grown as described by Prota *et al.*^[43,44] The above listed compounds were either soaked into the crystals at 5 mM final concentration for 6 - 16 h or added to the crystallization mixture. High resolution data (ranging from 1.9 Å to 2.7 Å) was collected and DIMPLE^[45] was used to spot densities of bound ligands. The overall T₂R-TTL-maytansinoid structures superimposed very well with the protein structure obtained in the absence of a ligand (PDB ID 4I55), suggesting that the binding of the maytansinoids has no effect on the overall conformation of tubulin.

The binding pose of all the maytansinoids within the maytansine site closely resembles the one described for the parent compound,^[11] and all the main interactions are conserved. Briefly, all compounds form hydrogen-bonds between the C1-O and the main chain nitrogen atom of Val181 and between the C24-O and the side chains of Lys105 and Asn102. Additionally, compounds possessing the C9-OH group establish a hydrogen bond to the main chain carbonyl group of Gly100. In Figure 2-10 the binding pose of the maytansinoid **1a** is shown and compared to **1b**, as well as the maytansine orientation. In the studied maytansinoids, all the modifications introduced at the C3 position point towards the solvent and do not perturb the close environment of the maytansine site. For the larger C3-substituents, such as the phenyl ring, we observed a slight reorientation of the C3 carbonyl group, which increases the distance to the Asn101 carbonyl group, thereby weakening this interaction. However, our biological assays showed that this minor change in coordination of the ligand does not have an impact on the efficacy and the binding constants. Thus, we can conclude that even attachment of larger groups at this position has no apparent impact on the binding pose, affinity or efficacy.

The structural analysis of the maytansinoids **2**, **3a-c** further reveals that the elimination of the C9-hydroxyl group does not affect the binding mode of the ligands. As shown in Figure 2-10D, the heterocycle is anchored by two hydrogen bonds established between the C24-O and the side-chains of Asn102 and Lys105, which highlights that the interaction is not affected by the introduction of the double bond.

However, the loss of one hydrogen bond between the C9-OH group and the main chain carbonyl of Gly100 cannot fully account for the observed lower affinities and efficacies of these maytansinoids compared to their hydroxylated analogues, suggesting a contribution by other factors such as compound solubility or decreased stability (Figure 2-10B).

For what concerns the 2nd series of compounds containing also longer-chain maytansinoids maytansinoid conjugates, consistently with the biochemical data we observed ligand shaped

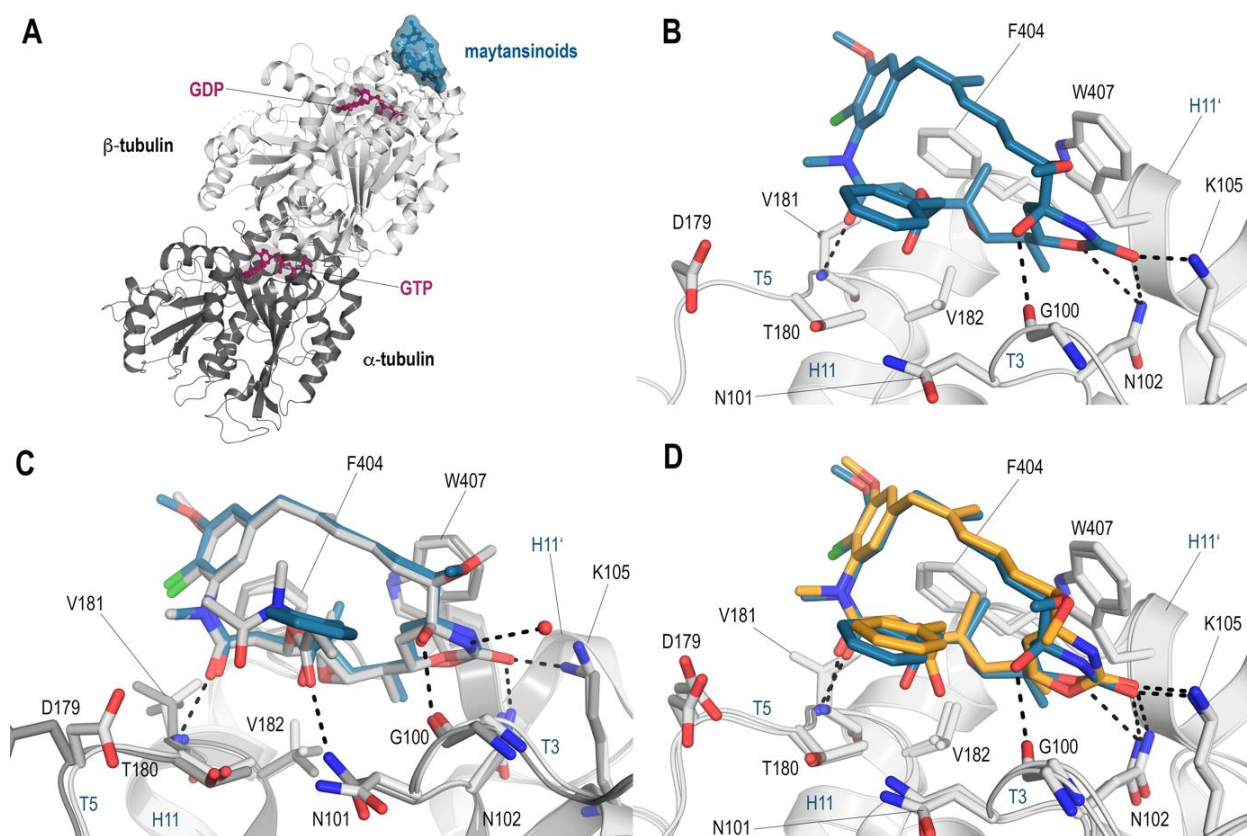


Figure 2-10. X-ray analysis of the T_2R -TTL-maytansinoid complexes of the 1st series. **(A)** Overall view of the interaction between the maytansinoids (blue) and tubulin (grey) in relation to the bound nucleotides (purple). The maytansine binding site is located on the β -tubulin surface in close proximity to the bound GDP molecule. The tubulin molecule is in ribbon representation (grey) and the interacting maytansinoid and nucleotides are in surface and stick representation, respectively. **(B)** Close-up view of the interaction between the maytansinoid **1a** (blue) and tubulin (grey). Interacting residues and ligand are represented as sticks. Oxygen atoms are color coded in red, nitrogens are blue, and the chlorine atom is in bright green. Hydrogen bonds are displayed as black dashed lines. **(C)** Superposition of the T_2R -TTL-maytansine structure (PDB ID 4TV8, maytansine in grey) and the **1a**- T_2R -TTL structure (**1a** in blue). The dashed lines indicate the hydrogen-bond interactions established by the maytansine molecule. **1a** adopts the same binding pose as its parent compound, except for the interaction of the Acyl group with Asn101, which is less pronounced and thus not displayed in the PM71C structure, all interactions are conserved. **(D)** The superposition of the T_2R -TTL-**1a** (**1a** in blue) and the T_2R -TTL-**3a** (**3a** in orange) structures shows that the elimination of the C8-OH group in **3a** has no major effect on the coordination of the ligand. Although the heterocycle moiety is flattened by the double bond in **3a**, the position of the ring is anchored at its position by coordination to Asn102 and Lys105.

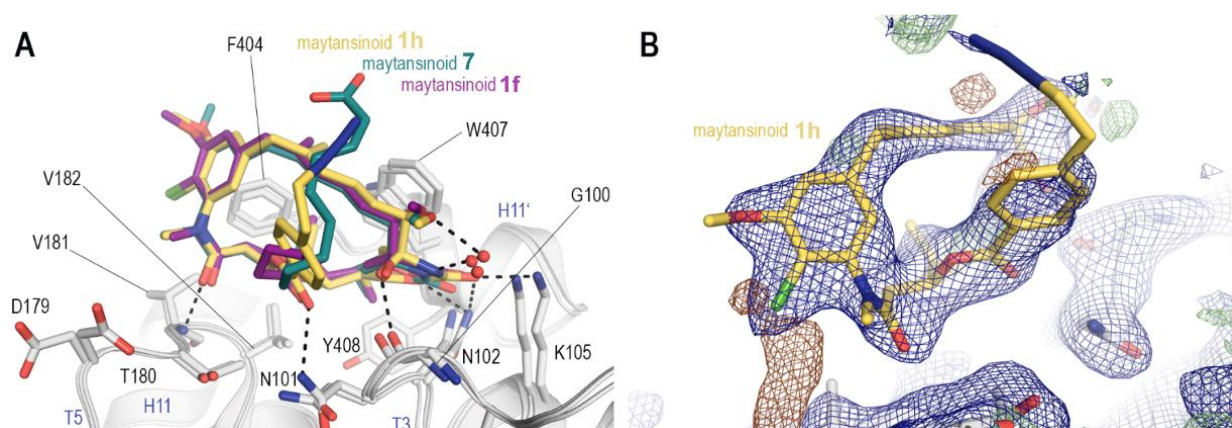


Figure 2-11. Binding poses of maytansinoids **1f**, **7** and **1h** (PDB IDs: 8B7A, 8B7B, 8B7C) and their fit into the electron density. The molecular interactions of the three superimposed structures of maytansinoids **4** (purple), **6** (cyan) and **12** (yellow) in complex with β -tubulin are displayed in A. The protein backbone (grey) is shown in ribbon representation and interacting residues and ligands are shown in sticks. Oxygen, nitrogen and chlorine atoms are colored red, blue and green, respectively, while water molecules are shown as red spheres. All three maytansinoids adopt the same pose as their parent compound maytansine and establish hydrogen bonds to the main chain carbonyl and amide of Gly100 and Val181, respectively, and direct or water-mediated hydrogen bonds to the side chains of Asn101, Asn102 and Lys105 as indicated by the dashed black lines. The long chains attached via esterification of C3-O in **6** and **12** are highly mobile and adopt many different conformations, therefore, there is no defined electron density visible for these long carbon chains, as shown in panel B. The highlighted definition and extension of the electron density to just 2-3 atoms beyond the well-defined C3-ester moiety is representative for all the soaked maytansinoids **4-10** and **12**. The electron density maps $2mF_o-DF_c$ (blue mesh) and mF_o-DF_c (green/red mesh) are contoured at $+1.0 \sigma$ and 3.0σ , respectively.

difference density at the maytansine site for all compounds, highlighting that none of the introduced moieties precluded binding in the crystal system. However, only the central ring of the maytansine scaffold was well resolved, while the introduced linkers were not defined in any structure of the obtained maytansinoid-tubulin complexes. These results are in line with the measured binding constants. The crystal structures of the representative compounds with different side-chain substituents and high cytotoxicity, **1f**, **7**, and **1h**, were further refined to determine their detailed molecular interactions (PDB IDs 8B7A, 8B7B and 8B7C). In general, all three determined structures superposed well with the structure of the parent compound (PDB ID: 4TV8; RMSD of superposition over Ca: 0.380 \AA (1993 atoms), 0.256 \AA (1992 atoms) and 0.330 \AA (1982 atoms) for T2R-TTL **1f**, **7** and **1h** respectively), and there were no major alterations in the binding mode (Figure 2-11). The insertion of long chains via acylation reaction at the C3-O has no impact on the previously described interactions, namely the hydrogen bonds of the C1 carbonyl to the Val181 main chain nitrogen, the C24 carbonyl to the Lys105 and Asn102 sidechain amine groups and C9-OH to the Gly100 main chain carbonyl.

The observed ligand density in these structures extended up to 2-3 carbons beyond the well resolved ester-group linking the chain to the C3 carbon, indicating that the introduced linker-moieties adapt multiple conformations. Accordingly, the carbon chains in all the three

structures were modeled and refined in their most probable conformations. Our data highlight the C3-O position as an excellent point to introduce modifications on the maytansine scaffold, allowing the accommodation of long flexible chains or even bulky moieties.

The lack of defined density and thus a stable conformation of the linker chain showed that compound 6 is not coordinating the Mg²⁺ ion, since the coordination would result in a fixed position of the carbonic acid linker. Presumably, the exposed nature of the binding site and the high flexibility of the long carbon chains precluded the stable coordination of the Mg²⁺ ion. Moreover, we cannot exclude an additional impact on the interaction by the presence of GDP:Mg²⁺ at the E-site in our crystal system.

Further, we could not observe any evidence for the exchange of the GDP by our nucleotide mimetics neither by soaking nor in co-crystallization experiments. Likely, the very high affinity of nucleotides to tubulin prevents the exchange of the previously bound nucleotide.

2.1.4 CONCLUSIONS AND FUTURE DIRECTIONS

In summary, we synthesized a series of maytansinoids containing novel scaffold modifications through the extensive investigation of maytansinol acylation reaction and have established synthetic pathways that allow to place large substituents on a complex natural product, maytansinol. We were able to shift the acylation reaction of maytansinol towards the specific product formation by screening different reaction conditions. We noted that compounds missing the C9-OH group show significantly lower impact on cells and tubulin in all the performed assays, proving that C9-OH and C3 esterification are crucial for full biological activity of maytansinoids. By introducing alkene or alkyne moieties via acylation reaction in position C-3 we opened up the scaffold for the straight-forward attachment of more functional probes. It allows to attach a whole variety of new molecules to the maytansine scaffold by either cross metathesis or click chemistry reactions. Guided by computational studies, we generated a whole set of maytansinoids carrying either long carbon chains, carboxylic acids or nucleotide mimetics. All of the tested compounds showed distinct effects on tubulin assembly *in vitro*. Our compiled data on the inhibition of tubulin assembly and binding affinities, together with the structural information confirms that even these long and heavy groups are tolerated easily. They neither impact the binding mode on tubulin nor dramatically reduce the scaffolds affinity, with even the lowest measured KD within the nM range. Unexpectedly, the cell permeability is likely affected by the introduction of the larger groups, as observed in their lowered cytotoxicity. Therefore, our work lays the foundation to further exploit the C3 position of maytansinoids by introducing functional modifications, such as specific fluorophores or chelators, which could potentially serve as probes to study MT dynamics *in vitro*. Furthermore, these modifications could comprise other types of chemical entities for the development of maytansinol-based

bivalent compounds capable to recruit specific proteins of interest, e.g. proteolysis targeting chimeras (PROTACs).

2.1.5 EXPERIMENTAL PART

Chemistry

General Experimental Procedures

Unless otherwise stated, reagents were purchased from general suppliers (Sigma Aldrich and Fluorochem) and used without further purification. All solvents were of reagent grade or HPLC grade. All reactions were carried out in oven-dried glassware and dry solvents, under nitrogen atmosphere and were monitored by glasses or aluminium TLC on silica gel (Merck precoated 60F254 plates), with detection by UV light (254 nm), or by TLC stains as permanganate, or by HPLC Agilent 1100. Analytical HPLC was performed on Agilent 1100 Series System RP column ZORBAX SB-C8 (3.5 μ m x 4.6 x 150 mm). The pressure was about 85 bar, with a constant flow rate of 1 mL/min. UV spectra were recorded at 254 nm and 210 nm with DAD detection. The mobile phase consisted of a mixture of H₂O/ACN and the gradient was programmed using the following method: isocratic for 1 min at 50% ACN, then gradient for 10 min to 90% ACN.

Products were purified by flash column chromatography, using silica gel Merk 60 (230-400 mesh) as stationary phase or by flash purification using Biotage Isolera™ One System and Biotage® Sfär C18 6 g D Duo 30 μ m as cartridges (BIOTAGE). The products were eluted from the column with a mixture of H₂O/ACN, running with a gradient from 10% ACN to 95% ACN (unless otherwise specified).

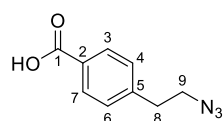
¹H NMR and ¹³C-NMR spectra were recorded on a Bruker Avance Spectrometer 400 MHz using commercially available deuterated solvents (chloroform-d, methanol-d₄, acetone-d₆, DMSO-d₆, dichloromethane-d₂) at room temperature. Chemical shifts (δ) are reported in parts per million (ppm) and are reported relative to TMS, used as an internal standard. Data for ¹H NMR are reported as follows: chemical shift (δ /ppm), multiplicity, coupling constants (Hz). Multiplicities are reported as follows: s = singlet, d = doublet, t = triplet, m = multiplet, br s = broad singlet. Data for ¹³C NMR are reported in terms of chemical shift (δ /ppm).

High resolution mass spectra (HR-MS) were recorded on a Water QToF Premier high resolution UPLC ES MS/MS.

Synthesis of 4-(2-azidoethyl)benzoic acid:

To a solution of 4-(2-bromoethyl)benzoic acid (80 mg, 0.35 mmol) in DMSO (1.4 ml), was added NaN₃ (24.2 mg, 0.38 mmol). The mixture was stirred at room temperature for 20 hours. Then, water (2.8 mL) was added, and the solution was extracted with EtOAc (4 x 6 mL). The organic layer was washed with brine, and the combined organic layers were dried over Na₂SO₄ and concentrated under reduced pressure. The crude product was not purified to provide the product (57.5 mg, 0.30 mmol, 86% yield) as white solid.

Analytical characterization

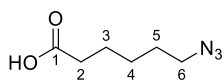


^1H NMR (400 MHz, chloroform-*d*) δ 8.0 (d, $J = 8.2$ Hz, 2H, 3, 7), 7.3 (d, $J = 8.1$ Hz, 2H, 4, 6), 3.5 (t, $J = 7.1$ Hz, 2H, 9), 2.9 (t, $J = 7.1$ Hz, 2H, 8).

^{13}C NMR (101 MHz, chloroform-*d*) δ 170.35 (1), 144.30 (5), 131.00 (3, 7), 130.76 (2), 129.46 (4, 6), 52.63 (9), 36.00 (8).

Synthesis of 6-azidohexanoic acid

To a solution of 6-bromohexanoic acid (195 mg, 1 mmol) in DMSO (4 ml), was added NaN_3 (69 mg, 1.1 mmol). The mixture was stirred at room temperature for 20 hours. Then, water (4 mL) was added, and the solution was extracted with EtOAc (4 \times 8 mL). The organic layer was washed with brine, and the combined organic layers were dried over Na_2SO_4 and concentrated under reduced pressure. The crude product was not purified to provide the product (142 mg, 0.91 mmol, 91% yield) as white solid.



^1H NMR (400 MHz, chloroform-*d*) δ 3.3 (t, $J = 6.9$ Hz, 2H, 6), 2.4 (t, $J = 7.4$ Hz, 2H, 2), 1.7 (m, 4H, 3, 5), 1.5 (m, 2H, 4).

^{13}C NMR (101 MHz, chloroform-*d*) δ 180.19 (1), 51.86 (6), 34.49 (2), 29.20 (5), 26.82 (4), 24.83 (3).

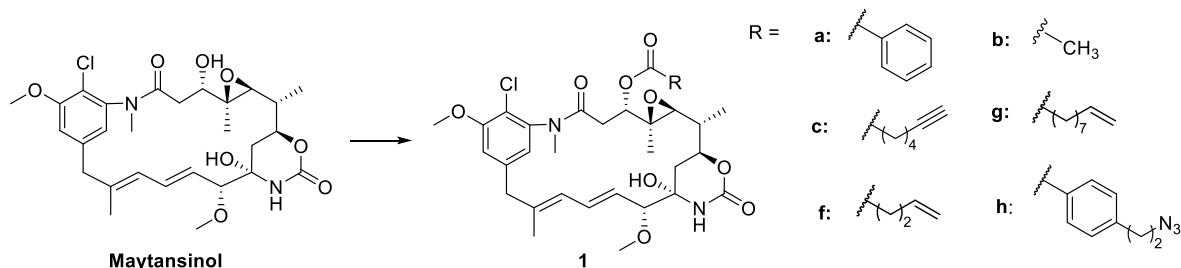
General procedures for the acylation of maytansinol with carboxylic acids:

Procedure 1: To a solution of maytansinol (50 mg, 0.088 mmol) in dry CH_2Cl_2 (440 μL) were added DMAP and the carboxylic acid at room temperature under a nitrogen atmosphere. Then, a solution of 1.3 M of DCC in dry CH_2Cl_2 was slowly added (or were added EDC-HCl followed by dropwise trimethylamine freshly distilled). The mixture was stirred at room temperature for a specific time (more details follow below) before filtering off the DCU using cold CH_2Cl_2 (or quenching with an aqueous saturated solution of NH_4Cl , in the case of EDC). The organic phase was washed with H_2O (4 \times 1 mL), with brine (1 \times 1 mL), then dried over Na_2SO_4 , and concentrated under reduced pressure. Column chromatography of the residue on silica gel (elution: $\text{CH}_2\text{Cl}_2/\text{MeOH}$ 96:4), or purification with Biotage Isolera™ One System, provided the products as white powders.

Procedure 2: To a solution of maytansinol (50 mg, 0.088 mmol, 1 eq) in dry CH_2Cl_2 (440 μL) were added DMF dry (44 μL), DMAP (33 mg, 0.26 mmol), the carboxylic acid (0.26 mmol), and ZnCl_2 (36 mg, 0.26 mmol) at room temperature under a nitrogen atmosphere. Then, a solution of DCC in dry CH_2Cl_2 (60 mg, 0.29 mmol, 1.3 M) was slowly added. The mixture was stirred at room temperature for 48 h before filtering off the DCU using cold CH_2Cl_2 . The organic phase was washed with H_2O (4 \times 1 mL), with brine (1 \times 1 mL), then dried over Na_2SO_4 , and concentrated under reduced pressure. The residue was purified with Biotage Isolera™ One System (gradient program from 10% ACN to 95% ACN in 25 CV) to provide the desired product as a white powder.

*Synthesis and analytical characterization of maytansinoids **2**, **3a-c**, **4a** and **5a** was done as reported by our group.^[17,46]

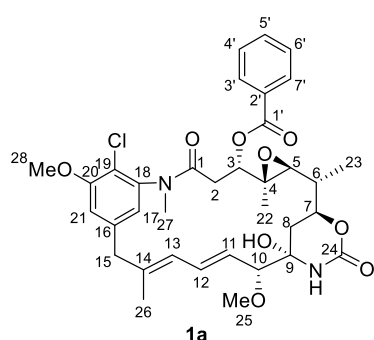
Table 2-7. Synthesis of **1a-c**; **1f-h** via procedures 1 and 2.



Carboxylic acid	Product	Procedure 1: yield %	Procedure 2: yield %
	1a	35	62
	1b	42	64
	1c	37	66
	1f	45	68
	1g	39	57
	1h	41	68

Analytical characterization of maytansinoids **1a-c**; **1f-h**.

Maytansinol 3-benzoate (**1a**)



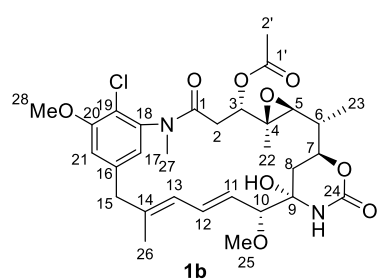
¹H NMR (400 MHz, Acetone-*d*₆) δ 8.21 – 8.08 (m, 2H, 3', 7'), 7.77 – 7.59 (m, 3H, 4', 5', 6'), 7.27 (d, *J* = 1.9 Hz, 1H, 21), 7.19 (d, *J* = 1.8 Hz, 1H, 17), 6.61 (dd, *J* = 15.5, 11.1 Hz, 1H, 12), 6.33 (s, 1H, NH), 6.04 (d, *J* = 11.0 Hz, 1H, 13), 5.04 – 4.85 (m, 2H, 3, 11), 4.47 (s, 1H, OH), 4.31 – 4.14 (m, 1H, 7), 4.04 (s, 3H, 28), 3.59 (d, *J* = 12.6 Hz, 1H, 15a), 3.50 (d, *J* = 9.1 Hz, 1H, 10), 3.36

(d, $J = 12.7$ Hz, 1H, 15b), 3.24 (s, 3H, 25), 3.13 (s, 3H, 27), 3.05 (d, $J = 9.5$ Hz, 1H, 5), 2.88 – 2.79 (m, 1H, 2a), 2.26 (dd, $J = 14.4, 3.1$ Hz, 1H, 2b), 1.77 (s, 3H, 26), 1.59 (dt, $J = 13.6, 1.9$ Hz, 1H, 8b), 1.54 – 1.39 (m, 2H, 6, 8a), 1.24 (d, $J = 6.4$ Hz, 3H, 23), 0.97 (s, 3H, 22).

^{13}C NMR (101 MHz, Acetone- d_6) δ 168.0 (1), 165.9 (1'), 156.2 (20), 151.1 (24), 142.4 (18), 141.3 (16), 139.6 (14), 133.1 (5'), 132.4 (12), 130.5 (2'), 129.9 (3', 7'), 128.6 (11), 128.2 (4', 6'), 124.7 (13), 122.1 (17), 118.7 (19), 113.5 (21), 88.9 (10), 80.5 (9), 77.5 (3), 73.8 (7), 66.4 (5), 60.5 (4), 56.2 (28), 55.8 (25), 46.3 (15), 38.7 (6), 36.2 (8), 34.6 (27), 32.7 (2), 14.9 (26), 14.0 (23), 12.1 (22).

HRMS (ESI) m/z $[\text{M}+\text{Na}]^+$ 691.2396 (calcd for $\text{C}_{35}\text{H}_{41}\text{ClN}_2\text{O}_9\text{Na}$, 691.2398)

Maytansinol 3-acetate (1b)



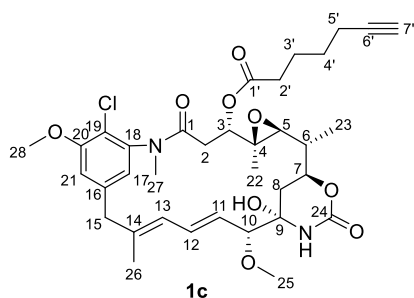
^1H NMR (400 MHz, Acetone- d_6) δ 7.25 (d, $J = 1.9$ Hz, 1H, 21), 6.97 (d, $J = 1.8$ Hz, 1H, 17), 6.75 (dd, $J = 15.5, 11.1$ Hz, 1H, 12), 6.42 (s, 1H, NH), 6.38 (d, $J = 11.1$ Hz, 1H, 13), 5.65 (dd, $J = 15.4, 9.0$ Hz, 1H, 11), 4.99 (s, 1H, OH), 4.83 (dd, $J = 11.9, 2.7$ Hz, 1H, 3), 4.20 (ddd, $J = 12.5, 10.5, 2.3$ Hz, 1H, 7), 4.02 (s, 3H, 28), 3.72 – 3.60 (m, 2H, 10, 15a), 3.37 (d, $J = 2.3$ Hz, 4H, 15b, 25), 3.12 (s, 3H, 27), 2.75 (d, $J = 9.8$ Hz, 1H, 5), 2.60 (dd, $J = 13.8, 11.9$

Hz, 1H, 2a), 2.22 (s, 3H, 2'), 2.07 – 1.98 (m, 1H, 2b), 1.77 (s, 3H, 26), 1.72 – 1.62 (m, 1H, 8a), 1.62 – 1.43 (m, 2H, 6, 8b), 1.21 (d, $J = 6.3$ Hz, 3H, 23), 0.95 (s, 3H, 22).

^{13}C NMR (101 MHz, Acetone- d_6) δ 169.7 (1'), 168.8 (1), 156.6 (20), 151.7 (24), 143.0 (18), 141.8 (16), 140.2 (14), 133.0 (12), 129.5 (11), 125.6 (13), 123.1 (17), 119.2 (19), 114.3 (21), 89.1 (10), 81.5 (9), 77.4 (3), 74.5 (7), 66.8 (5), 61.2 (4), 56.7 (28), 56.5 (25), 46.9 (15), 38.7 (6), 36.7 (8), 35.3 (27), 33.2 (2), 20.9 (2'), 15.5 (26), 14.5, 12.1 (22).

HRMS (ESI) m/z $[\text{M}+\text{Na}]^+$ 629.2244 (calcd for $\text{C}_{30}\text{H}_{39}\text{ClN}_2\text{O}_9\text{Na}$, 629.2242)

Maytansinol 3-hept-6-ynoate (1c)



^1H NMR (400 MHz, chloroform- d) δ 6.83 (d, $J = 2.0$ Hz, 1H, 21), 6.79 (d, $J = 1.8$ Hz, 1H, 17), 6.44 (dd, $J = 15.5, 11.0$ Hz, 1H, 12), 6.31 (s, 1H, NH), 6.16 (d, $J = 10.9$ Hz, 1H, 13), 5.49 (dd, $J = 15.5, 8.9$ Hz, 1H, 11), 4.89 (dd, $J = 11.9, 3.0$ Hz, 1H, 3), 4.25 (ddd, $J = 12.4, 10.6, 2.0$ Hz, 1H, 7), 3.99 (s, 3H, 28), 3.56 – 3.46 (m, 2H, 10, 15a), 3.36 (s, 3H, 25), 3.21 (d, $J = 13.0$ Hz, 1H, 15b), 3.17 (s, 3H, 27), 2.89 (d, $J = 9.7$ Hz, 1H, 5), 2.57 – 2.44 (m, 2H, 2'a, 2b), 2.44 – 2.31 (m, 1H, 2'b),

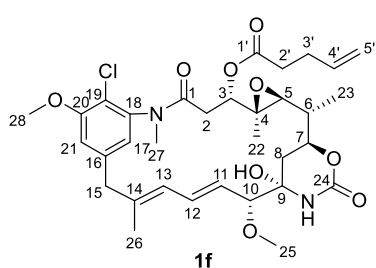
2.26 (td, $J = 6.9, 2.7$ Hz, 2H, 5'), 2.23 – 2.15 (m, 1H, 2a), 1.95 (t, $J = 2.6$ Hz, 1H, 7'), 1.81 (p, J

= 7.6 Hz, 2H, 3'), 1.68 (s, 3H, 26), 1.66 – 1.54 (m, 3H, 4', 8b), 1.54 – 1.42 (m, 1H, 6), 1.28 (d, J = 6.4 Hz, 3H, 23), 1.26 – 1.18 (m, 1H, 8a), 0.83 (s, 3H, 22).

^{13}C NMR (101 MHz, chloroform- d) δ 171.9 (1), 168.8 (1'), 156.2 (20), 152.4 (24), 142.7 (18), 140.2 (16), 140.1 (14), 132.5 (12), 128.2 (11), 124.6 (13), 122.3 (17), 119.6 (19), 113.1 (21), 88.3 (10), 84.2 (6'), 81.1 (9), 77.0 (3), 74.4 (7), 69.0 (7'), 66.5 (5), 60.4 (4), 56.9 (25), 56.7 (28), 47.3 (15), 38.6 (6), 35.9 (8), 35.7 (27), 33.7 (2'), 32.9 (2), 27.9 (4'), 23.9 (3'), 18.4 (5'), 15.9 (26), 14.6 (23), 12.2 (22).

HRMS (ESI) m/z $[\text{M}+\text{Na}]^+$ 695.2710 (calcd for $\text{C}_{35}\text{H}_{45}\text{ClN}_2\text{O}_9\text{Na}$, 695.2711)

Maytansinol 3-pent-4-enoate (1f)



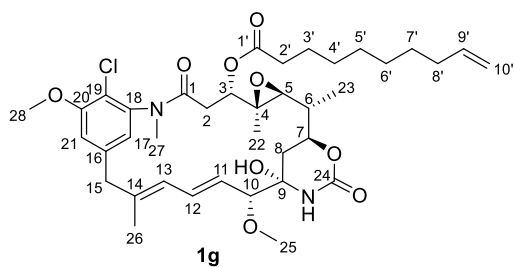
^1H NMR (400 MHz, Acetone- d_6) δ 7.23 (d, J = 1.9 Hz, 1H, 21), 6.96 (d, J = 1.9 Hz, 1H, 17), 6.73 (dd, J = 15.5, 11.1 Hz, 1H, 12), 6.62 (d, J = 5.7 Hz, 1H, OH), 6.40 (s, 1H, NH), 6.32 (d, J = 11.1 Hz, 1H, 13), 5.91 (ddt, J = 16.9, 10.3, 6.5 Hz, 1H, 4'), 5.62 (dd, J = 15.5, 8.9 Hz, 1H, 11), 5.19 – 5.07 (m, 1H, 5'a), 5.02 (d, J = 11.1 Hz, 1H, 5'b), 4.83 (dd, J = 12.0, 2.7 Hz, 1H, 3), 4.25 – 4.09 (m, 1H, 7), 4.00 (s, 3H, 28), 3.62 (m, 2H, 10, 15a), 3.39 – 3.28

(m, 4H, 15b, 25), 3.11 (s, 3H, 25), 2.76 (d, J = 9.9 Hz, 1H, 5), 2.74 – 2.54 (m, 4H, 2, 2'), 2.48 – 2.31 (m, 2H, 3'), 1.75 (s, 3H, 26), 1.70-1.58 (m, 2H, 8), 1.58 – 1.45 (m, 1H, 6), 1.20 (d, J = 6.3 Hz, 3H, 23), 0.93 (s, 3H, 22).

^{13}C NMR (101 MHz, CD_2Cl_2) δ 171.6 (1), 168.6 (1'), 156.2 (20), 151.8 (24), 142.6 (18), 140.4 (16), 140.4 (14), 137.0 (4'), 132.6 (12), 128.0 (11), 124.4 (13), 122.3 (17), 115.5 (19), 115.1 (5'), 113.3 (21), 88.2 (10), 81.2 (9), 76.9 (3), 74.3 (7), 66.3 (5), 60.6 (4), 56.7 (25), 56.6 (28), 47.1 (15), 38.5 (6), 35.8 (8), 35.4 (27), 33.4 (2'), 32.9 (2), 28.7 (3'), 15.6 (26), 14.3 (23), 12.1 (22).

HRMS (ESI) m/z $[\text{M}+\text{Na}]^+$ 669.2553 (calcd for $\text{C}_{33}\text{H}_{43}\text{ClN}_2\text{O}_9\text{Na}$, 669.2555)

Maytansinol 3-dec-9-enoate (1g)



^1H NMR (400 MHz, Acetone- d_6) δ 7.23 (d, J = 1.9 Hz, 1H, 21), 6.96 (d, J = 1.9 Hz, 1H, 17), 6.73 (dd, J = 15.5, 11.0 Hz, 1H, 12), 6.40 (s, 1H, NH), 6.33 (d, J = 11.1 Hz, 1H, 13), 5.80 (ddt, J = 17.0, 10.3, 6.7 Hz, 1H, 9'), 5.62 (dd, J = 15.5, 8.9 Hz, 1H, 11), 5.08 – 4.74 (m, 3H, 10', 3), 4.22 – 4.12 (m, 1H, 7), 4.01

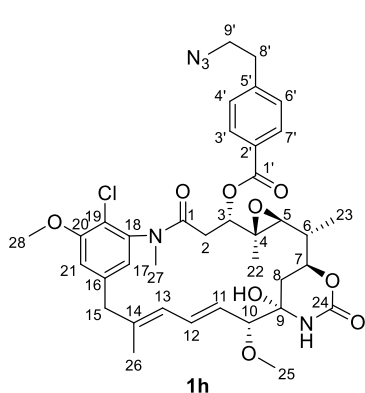
(s, 3H, 28), 3.70 – 3.54 (m, 2H, 10, 15a), 3.40 – 3.31 (m, 4H, 25, 15b), 3.11 (s, 3H, 27), 2.76 (d, J = 9.7 Hz, 1H, 5), 2.65 – 2.45 (m, 3H, 2b, 2'), 2.09 – 1.99 (m, 2H, 8', overlap with

(CD₃)₂CO)), 1.70 – 1.59 (m, 3H, 3', 8a), 1.55 – 1.25 (m, 10H, 8b, 6, 4', 5', 6', 7'), 1.19 (d, J = 6.4 Hz, 3H, 23), 0.93 (s, 3H, 22).

¹³C NMR (101 MHz, Acetone) δ 172.8 (1), 169.0 (1'), 156.9 (20), 152.0 (24), 143.3 (18), 142.0 (16), 140.5 (14), 139.8 (9'), 133.3 (12), 129.7 (11), 125.8 (13), 123.3 (17), 119.5 (19), 114.7 (10'), 114.5 (21), 89.4 (10), 81.7 (9), 77.5 (3), 74.8 (7), 67.1 (5), 61.5 (4), 57.0 (25), 56.8 (28), 47.2 (15), 39.1 (6), 36.9 (8), 35.6 (27), 34.7 (2'), 34.5 (8'), 33.5 (2), 30.2 (6'), 29.8 (7'), 29.7 (5'), 29.7 (4'), 25.7 (3'), 15.8 (26), 14.8 (23), 12.5 (22).

HRMS (ESI) *m/z* [M+Na]⁺ 739.3320 (calcd for C₃₈H₅₃ClN₂O₉Na, 739.3337)

Maytansinol 3-(2-azidoethyl)benzoate (1h)



¹H NMR (400 MHz, acetone-*d*₆) δ 8.1 (d, J = 8.2 Hz, 2H, 3', 7'), 7.6 (d, J = 8.0 Hz, 2H, 4', 6'), 7.3 (d, J = 1.9 Hz, 1H, 21), 7.2 (d, J = 1.8 Hz, 1H, 17), 6.6 (dd, J = 15.4, 11.0 Hz, 1H, 12), 6.3 (s, 1H, NH), 6.1 (d, J = 11.0 Hz, 1H, 13), 5.1 – 4.9 (m, 2H, 3, 11), 4.4 (d, J = 2.1 Hz, 1H, OH), 4.2 (ddd, J = 12.5, 10.5, 2.3 Hz, 1H, 7), 4.0 (s, 3H, 28), 3.7 (td, J = 7.0, 2.1 Hz, 2H, 9'), 3.6 (d, J = 12.6 Hz, 1H, 15a), 3.5 (d, J = 9.1 Hz, 1H, 10), 3.4 (d, J = 12.6 Hz, 1H, 15b), 3.2 (s, 3H, 25), 3.1 (s, 3H, 27), 3.1 – 3.0 (m, 3H, 5, 8'), 2.8 (d, J = 14.4 Hz, 1H, 2a), 2.3 (dd, J = 14.4, 3.2 Hz, 1H, 2b), 1.8 (s, 3H, 26), 1.6

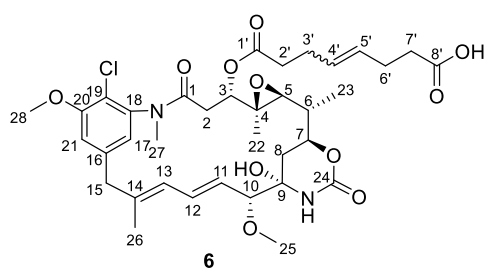
(dt, J = 13.5, 2.0 Hz, 1H, 8a), 1.5 – 1.4 (m, 2H, 6, 8b), 1.2 (d, J = 6.4 Hz, 3H, 23), 1.0 (s, 3H, 22).

¹³C NMR (101 MHz, acetone-*d*₆) δ 168.7 (1), 166.4 (1'), 156.9 (20), 151.7 (24), 145.0 (5'), 143.1 (18), 142.0 (16), 140.1 (14), 133.0 (12), 130.8 (3', 7'), 129.6 (2'), 129.5 (4', 6'), 129.3 (11), 125.5 (13), 122.8 (17), 119.3 (19), 114.2 (21), 89.5 (10), 81.2 (9), 78.0 (3), 74.4 (7), 67.0 (5), 61.2 (4), 56.8 (28), 56.4 (25), 52.5 (9'), 46.9 (15), 39.4 (6), 36.8 (8), 35.6 (8'), 35.2 (27), 33.4 (2), 15.5 (26), 14.7 (23), 12.8 (22).

HRMS (ESI) *m/z* [M+Na]⁺ 760.2732 (calcd for C₃₇H₄₄ClN₅O₉Na, 760.2725).

Synthesis of maytansinol-3-oxooct-4-enoic acid (6)

To a solution of **1f** (27 mg, 0.042 mmol, 1 eq) in dry CH₂Cl₂ (1.4 ml) were added 4-pentenoic acid (9.6 ul, 0.095 mmol) and Hoveyda-Grubbs 2nd gen. catalyst (3.94 mg, 15 mol%), predissolved in CH₂Cl₂ (0.2 ml). The reaction was stirred at reflux (40 °C) for 6h, after which additional catalyst was added (1.31 mg, 5 mol%) and the reaction was continued to stir overnight at r.t. The solvent was evaporated under reduced pressure. The crude was purified with Biotage Isolera™ One System (gradient H₂O/ACN) providing the product (13,2 mg, 44%) as a white powder.



^1H NMR (400 MHz, Acetone- d_6) δ 7.23 (d, J = 1.8 Hz, 1H, 21), 6.97 (d, J = 1.8 Hz, 1H, 17), 6.69 (dd, J = 15.4, 11.1 Hz, 1H, 12), 6.49 (s, 1H, NH), 6.33 (d, J = 11.1 Hz, 1H, 13), 5.70 – 5.55 (m, 3H, 4', 5', 11), 4.83 (dd, J = 11.9, 2.7 Hz, 1H, 3), 4.2 (ddd, J = 12.5, 10.5, 2.3 Hz, 1H, 7), 4.00 (s, 3H, 28), 3.67 – 3.56 (m, 2H, 10, 15a), 3.35 (s, 3H, 25), 3.31 (m, 1H, 15b), 3.12 (s, 3H, 27), 2.79 – 2.51 (m, 5H, 5, 3', 6'), 2.44 – 2.16 (m, 4H, 2', 7'), 1.88-1.78 (m, 2H, 2), 1.74 (s, 3H, 26), 1.71 – 1.23 (m, 3H, 6, 8), 1.20 (d, J = 6.4 Hz, 3H, 23), 0.93 (s, 3H, 22).

^{13}C NMR (101 MHz, Acetone) δ 172.3 (1), 169.1 (1'), 158.3 (20), 152.1 (24), 143.2 (18), 142.1 (16), 140.3 (14), 133.2 (12), 131.2 (5', 4'), 130.0 (11), 125.8 (13), 123.4 (17), 123.0 (19), 114.6 (21), 89.6 (10), 81.6 (9), 77.6 (3), 74.5 (7), 67.0 (5), 59.4 (4), 57.0 (28), 56.9 (25), 47.2 (15), 39.1 (6), 36.9 (8), 35.7 (27), 34.6 (2'), 34.5 (7'), 33.5 (2), 28.3 (3'), 26.5 (6'), 15.8 (26), 14.8 (23), 12.4 (22).

HRMS (ESI) m/z $[\text{M}+\text{Na}]^+$ 741.2766 (calcd for $\text{C}_{36}\text{H}_{47}\text{ClN}_2\text{O}_{11}\text{Na}$, 741.2768).

Synthesis of (E)-maytansinol-3-oxoundec-9'-enoic acid (7)

To a solution of **1g** (20 mg, 0.0279 mmol) in dry CH_2Cl_2 (1.2 ml) were added acrylic acid (5.0 mg, 0.070 mmol) and Hoveyda-Grubbs 2nd gen. catalyst (2.63 mg, 15 mol%), predissolved in CH_2Cl_2 (0.2 ml). The reaction was stirred at reflux (40 °C) for 6h, after which additional catalyst was added (0.88 mg, 5 mol%) and reaction was continued to stir overnight. The solvent was evaporated under reduced pressure. The crude was purified with Biotage Isolera™ One System (gradient $\text{H}_2\text{O}/\text{ACN}$) providing the product (9.7 mg, 46%) as a white powder.

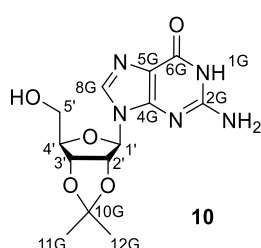
^1H NMR (400 MHz, Acetone- d_6) δ 7.23 (d, J = 1.8 Hz, 1H, 21), 6.96 (d, J = 1.8 Hz, 1H, 17), 6.95 – 6.84 (m, 1H, 9'), 6.73 (dd, J = 15.4, 11.1 Hz, 1H, 12), 6.43 (bs, 1H, NH), 6.33 (d, J = 11.1 Hz, 1H, 13), 5.82 (d, J = 15.6 Hz, 1H, 10'), 5.62 (dd, J = 15.4, 8.9 Hz, 1H, 11), 4.83 (dd, J = 11.9, 2.7 Hz, 1H, 3), 4.18 (ddd, J = 12.5, 10.4, 2.2 Hz, 1H, 7), 4.01 (s, 3H, 28), 3.68 – 3.55 (m, 2H, 10, 15a), 3.39 – 3.25 (m, 4H, 25, 15b), 3.11 (s, 3H, 27), 2.76 (d, J = 9.7 Hz, 1H, 5), 2.67 – 2.40 (m, 4H, 2, 2'), 2.27 – 2.18 (m, 2H, 8'), 2.05 – 2.02 (m, 2H, 8), 1.75 (s, 3H, 26), 1.71 – 1.60 (m, 2H, 3'), 1.52 – 1.46 (m, 3H, 7', 6), 1.45 – 1.35 (m, 6H, 4', 5', 6'), 1.20 (d, J = 6.4 Hz, 3H, 23), 0.93 (s, 3H, 22).

^{13}C NMR (101 MHz, Acetone) δ 172.8 (1), 169.1 (1'), 167.7 (11'), 156.9 (20), 152.1 (24), 149.8 (9'), 143.3 (18), 142.0 (16), 140.5 (14), 133.3 (12), 129.7 (11), 125.8 (13), 123.3 (17), 122.6 (10'), 119.5 (19), 114.5 (21), 89.5 (10), 81.7 (9), 77.5 (3), 74.8 (7), 67.1 (5), 61.5 (4), 57.0 (28),

56.8 (25), 47.2 (15), 39.1 (6), 36.9 (8), 35.6 (27), 34.7 (2'), 33.5 (6'), 32.6 (2), 28.9 (5'), 26.5 (7'), 25.8 (4'), 25.7 (3'), 15.8 (26), 14.8 (23), 12.5 (22).

HRMS (ESI) m/z $[M+Na]^+$ 783.3235 (calcd for $C_{39}H_{53}ClN_2O_{11}Na$, 783.3236).

Synthesis of 2-amino-9-((3aR,4R,6R,6aR)-6-(hydroxymethyl)-2,2-dimethyltetrahydrofuro[3,4-d][1,3]dioxol-4-yl)-1,9-dihydro-6H-purin-6-one; 2',3'-O-Isopropylidene-guanosine (10)



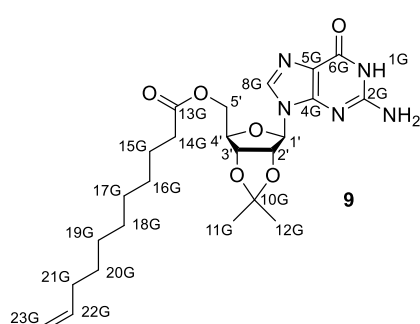
To a suspension of guanosine (200 mg, 0.706 mmol) in dry acetone (11.8 ml) was added an aqueous solution of 60% $HClO_4$ 60% (95 μ L, 0.946 mmol) and the clear reaction obtained was stirred for 2 h at room temperature. The reaction was quenched by dropping an aqueous solution of 30% NH_4OH at $0^\circ C$. The precipitate was recovered by filtration on Buchner washing with cold Et_2O . The solid was dried in *vacuum* to provide 229 mg (>98%) of product as white solid.

1H NMR (400 MHz, $DMSO-d_6$) δ 7.9 (s, 1H, 8G), 6.4 (s, 2H, NH_2), 5.9 (d, $J = 2.8$ Hz, 1H, 1'), 5.2 (dd, $J = 6.4, 2.8$ Hz, 1H, 2'), 5.0 (dd, $J = 6.4, 2.5$ Hz, 1H, 3'), 4.1 (dt, $J = 4.7, 2.5$ Hz, 1H, 4'), 3.6 (t, $J = 4.7$ Hz, 2H, 5'), 2.1 (s, 1H, OH), 1.5 (s, 3H, 11G), 1.3 (s, 3H, 12G).

^{13}C NMR (101 MHz, $DMSO$) δ 157.18 (6G), 154.17 (2G), 151.22 (4G), 136.30 (8G), 117.36 (5G), 113.56 (10G), 89.07 (1'), 87.14 (4'), 84.11 (2'), 81.71 (3'), 62.15 (5'), 27.55 (11G), 25.76 (12G).

Synthesis of ((3aR,4R,6R,6aR)-6-(2-amino-6-oxo-1,6-dihydro-9H-purin-9-yl)-2,2-dimethyltetrahydrofuro[3,4-d][1,3]dioxol-4-yl)methyl undec-10-enoate (9)

To a solution of **10** (100 mg, 0.309 mmol) in dry CH_2Cl_2 (2.5 mL) were added undecylenic acid (93.75 μ L, 0.464 mmol), DMAP (18.9 mg, 0.155 mmol), EDC-HCl (106 mg, 0.557 mmol), and triethylamine dry (95 μ L, 0.680 mmol) at room temperature under a nitrogen atmosphere. The reaction was stirred for 18 h before to add H_2O (1×2 mL). The organic layer was dried over Na_2SO_4 , and concentrated under reduced pressure. Purification with Biotage Isolera™ One System (gradient H_2O/ACN) provided the product (130 mg, 86%) as a white powder.

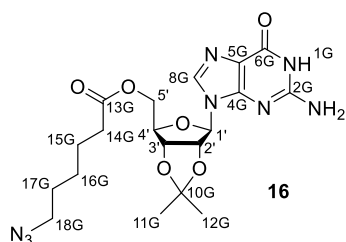


1H NMR (400 MHz, $DMSO-d_6$) δ 10.71 (s, 1H, NH), 7.85 (s, 1H, 8G), 6.56 (s, 2H, NH_2), 6.01 (d, $J = 2.5$ Hz, 1H, 1'), 5.78 (m, 1H, 22G), 5.25 (dt, $J = 5.6, 2.7$ Hz, 1H, 2'), 5.12 (dd, $J = 6.4, 3.2$ Hz, 1H, 3'), 5.03 – 4.89 (m, 2H, 23G), 4.28 – 4.20 (m, 2H, 4', 5'a), 4.12 (dd, $J = 11.3, 8.0$, 1H, 5'b), 2.33 – 2.13 (m, 2H, 14G), 1.99 (t, $J = 7.1$ Hz, 2H, 21G), 1.51 (d, $J = 3.0$ Hz, 3H, 11G), 1.49-1.41 (m, 3H, 15G), 1.37-1.29 (m, 5H, 12G, 20G), 1.27-1.20 (m, 8H, 18G, 17G, 16G, 15G).

^{13}C NMR (101 MHz, DMSO) δ 172.71 (13G), 156.71 (6G), 153.69 (4G), 150.51 (2G), 138.85 (22G), 136.12 (8G), 116.95 (5G), 114.66 (10G), 113.30 (23G), 88.31 (1'), 84.21 (4'), 83.69 (2'), 81.08 (3'), 63.93 (5'), 33.72 (14G), 33.21 (21G), 28.70 (18G), 28.64 (16G), 28.47 (19G), 28.38 (20G), 28.26 (17G), 27.02 (11G), 25.32 (12G), 24.33 (15G).

HRMS (ESI) m/z $[\text{M}+\text{Na}]^+$ 512.2485 (calcd for $\text{C}_{14}\text{H}_{20}\text{N}_8\text{O}_4\text{Na}$ 512.2487)

Synthesis of ((3aR,4R,6R,6aR)-6-(2-amino-6-oxo-1,6-dihydro-9H-purin-9-yl)-2,2-dimethyltetrahydrofuro[3,4-d][1,3]dioxol-4-yl)methyl 6-azidohexanoate (16)



To a solution of **10** (100 mg, 0.309 mmol) in dry CH_2Cl_2 (2.5 mL) were added 6-azidohexanoic acid (72 mg, 0.464 mmol), DMAP (22 mg, 0.185 mmol), EDC-HCl (106 mg, 0.557 mmol), and triethylamine dry (95 μL , 0.680 mmol) at room temperature under a nitrogen atmosphere. The reaction was stirred for 18 h before to add H_2O (1×2 mL). The organic layer was dried over Na_2SO_4 , and concentrated under reduced pressure. Purification

with Biotage Isolera™ One System (gradient from 5% to 40% ACN in 22 CV) provided the product (101 mg, 71%) as a white powder.

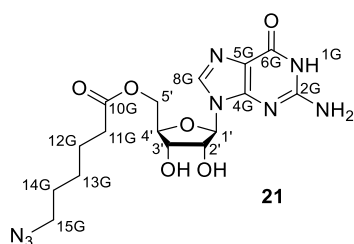
^1H NMR (400 MHz, $\text{DMSO}-d_6$) δ 10.7 (s, 1H, NH), 7.9 (s, 1H, 8G), 6.6 (s, 2H, NH_2), 6.2 – 5.9 (m, 1H, 1'), 5.5 – 5.2 (m, 1H, 2'), 5.1 (dd, $J = 5.9, 3.4$ Hz, 1H, 3'), 4.2 (dd, $J = 8.0, 4.0$ Hz, 2H, 4', 5'a), 4.1 (dd, $J = 12.6, 8.0$ Hz, 1H, 5'b), 3.3 (t, $J = 6.9$ Hz, 2H, 18G), 2.3 (dt, $J = 7.0, 3.4$ Hz, 2H, 14G), 1.6 – 1.4 (m, 7H, 11G, 15G, 17G), 1.3 (s, 5H, 12G, 16G).

^{13}C NMR (101 MHz, $\text{DMSO}-d_6$) δ 173.65 (13G), 157.81 (6G), 154.78 (4G), 151.61 (2G), 137.25, 118.07 (5G), 114.40 (10G), 89.44 (1'), 85.32 (4'), 84.77 (2'), 82.19 (3'), 65.05 (5'), 51.58 (18G), 34.18 (14G), 29.01 (17G), 28.12 (11G), 26.66 (15G), 26.43 (12G), 24.96 (16G).

HRMS (ESI) m/z $[\text{M}+\text{Na}]^+$ 485.1881 (calcd for $\text{C}_{19}\text{H}_{26}\text{N}_8\text{O}_6\text{Na}$, 485.1873)

Synthesis of ((2R,3S,4R,5R)-5-(2-amino-6-oxo-1,6-dihydro-9H-purin-9-yl)-3,4-dihydroxytetrahydrofuran-2-yl)methyl 6-azidohexanoate (21)

To a solution of **16** (49 mg, 0.11 mmol) was added aqueous TFA 80% (1.52 mL). The mixture was stirred at room temperature for 30 min. Then, the solvent was removed in *vacuum*, a solution of EtOH +1% Et_3N (2.5 mL) were added and the solvent was evaporated to remove the TFA salt form. Purification of the crude with Biotage Isolera™ One System (gradient from 5% to 40% ACN in 22 CV) provided the product (46 mg, >98%) as a white powder.



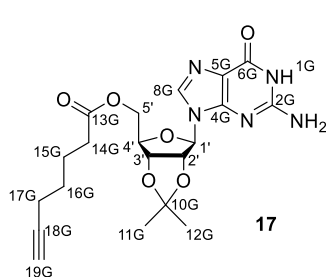
^1H NMR (400 MHz, $\text{DMSO}-d_6$) δ 10.8 (s, 1H, 1G), 7.9 (s, 1H), 6.6 (s, 2H, NH_2), 5.7 (d, $J = 5.1$ Hz, 1H, 1'), 4.4 (t, $J = 5.2$ Hz, 1H), 4.3 (dd, $J = 12.0, 3.7$ Hz, 1H, 5'a), 4.2 (dt, $J = 9.8, 5.3$ Hz, 2H, 3', 5'b), 4.0 (q, $J = 4.8$ Hz, 1H), 3.3 (d, $J = 7.2$ Hz, 2H, 15G), 2.3 (t, $J = 7.4$ Hz, 2H, 11G), 1.5 (h, $J = 6.8$ Hz, 4H, 12G, 14G), 1.3 (p, $J = 4.8, 4.2$ Hz, 2H, 13G).

^{13}C NMR (101 MHz, $\text{DMSO-}d_6$) δ 173.78 (10G), 157.82 (6G), 154.94 (2G), 152.42 (4G), 136.50 (8G), 117.82 (5G), 87.83 (1'), 82.46 (4'), 74.20 (2'), 71.41 (3'), 64.95 (5'), 51.60 (15G), 34.30 (11G), 29.03 (14G), 26.69 (13G), 25.03 (12G).

HRMS (ESI) m/z $[\text{M}+\text{Na}]^+$ 445.1569 (calcd for $\text{C}_{16}\text{H}_{22}\text{N}_8\text{O}_6\text{Na}$, 445.1560)

Synthesis of ((3aR,4R,6R,6aR)-6-(2-amino-6-oxo-1,6-dihydro-9H-purin-9-yl)-2,2-dimethyltetrahydrofuro[3,4-d][1,3]dioxol-4-yl)methyl hept-6-ynoate (17)

To a solution of **10** (150 mg, 0.464 mmol) in dry CH_2Cl_2 (3.8 mL) were added 6-heptynoic acid (88 μL , 0.696 mmol), DMAP (34 mg, 0.278 mmol), EDC-HCl (160 mg, 0.835 mmol), and triethylamine dry (142 μL , 1.021 mmol) at room temperature under a nitrogen atmosphere. The reaction was stirred for 18 h before to add H_2O (1 \times 3 mL). The organic layer was dried over Na_2SO_4 , and concentrated under reduced pressure. Purification with Biotage Isolera™ One System (gradient from 5% to 40% ACN in 22 CV) provided the product (156 mg, 78%) as a white powder.



^1H NMR (400 MHz, $\text{DMSO-}d_6$) δ 10.7 (s, 1H, 1G), 7.9 (s, 1H, 8G), 6.5 (s, 2H, NH_2), 6.0 (d, $J = 2.0$ Hz, 1H, 1'), 5.3 (dd, $J = 6.3, 2.0$ Hz, 1H, 2'), 5.1 (dd, $J = 6.3, 3.5$ Hz, 1H, 3'), 4.3 (dt, $J = 6.1, 4.3$ Hz, 2H, 4', 5'a), 4.1 (dd, $J = 12.8, 7.9$ Hz, 1H, 5'b), 2.7 (t, $J = 2.6$ Hz, 1H, 19G), 2.3 (td, $J = 7.4, 3.2$ Hz, 2H, 14G), 2.1 (dq, $J = 7.0, 3.1$ Hz, 2H, 17G), 1.6 – 1.5 (m, 2H, 15G), 1.5 (s, 3H, 11G), 1.4 (p, $J = 7.2$ Hz, 2H, 16G), 1.3 (s, 3H, 12G).

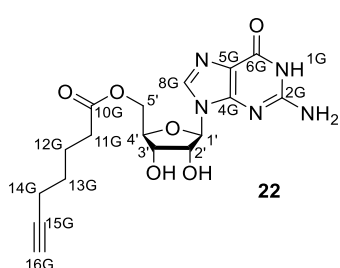
^{13}C NMR (101 MHz, $\text{DMSO-}d_6$) δ 173.61 (13G), 157.81 (6G), 154.80 (2G), 151.63 (4G), 137.26 (8G), 118.09 (5G), 114.44 (10G), 89.43 (1'), 85.31 (18G), 85.28 (4'), 84.76 (2'), 82.21 (3'), 72.40 (19G), 65.08 (5'), 33.78 (14G), 28.36 (16G), 28.13 (11G), 26.44 (12G), 24.59 (15G), 18.50 (17G).

HRMS (ESI) m/z $[\text{M}+\text{Na}]^+$ 454.1710 (calcd for $\text{C}_{20}\text{H}_{25}\text{N}_5\text{O}_6\text{Na}$, 454.1703)

Synthesis of ((2R,3S,4R,5R)-5-(2-amino-6-oxo-1,6-dihydro-9H-purin-9-yl)-3,4-dihydroxytetrahydrofuran-2-yl)methyl hept-6-ynoate (22)

To a solution of **17** (52 mg, 0.12 mmol) was added aqueous TFA 80% (1.71 mL). The mixture was stirred at room temperature for 30 min. Then, the solvent was removed in *vacuum*, a solution of EtOH +1% Et_3N (2.5 mL) were added and the solvent was evaporated to remove the TFA salt form. Purification of the crude with Biotage Isolera™ One System (gradient from 5% to 40% ACN in 22 CV) provided the product (46 mg, >98%) as a white powder.

^1H NMR (400 MHz, $\text{DMSO-}d_6$) δ 10.7 (s, 1H, 1G), 7.9 (s, 1H, 8G), 6.5 (s, 2H, NH_2), 5.8 – 5.7 (m, 1H, 1'), 5.5 (d, $J = 5.4$ Hz, 1H, 2'OH), 5.3 (d, $J = 4.8$ Hz, 1H, 3'OH), 4.4 (d, $J = 5.0$ Hz, 1H, 2'), 4.3 (dd, $J = 11.9, 3.5$ Hz, 1H, 5'a), 4.2 – 4.1 (m, 2H, 3', 5'b), 4.0 (q, $J = 5.9, 4.5$ Hz, 1H, 4'), 2.7 (d, $J = 2.4$ Hz, 1H, 16G), 2.3 (t, $J = 7.2$ Hz, 2H, 11G), 2.2 (td, $J = 6.9, 2.4$ Hz, 2H, 14G), 1.6 (q, $J = 7.4$ Hz, 2H, 12G), 1.5 (q, $J = 7.2$ Hz, 2H, 13G).

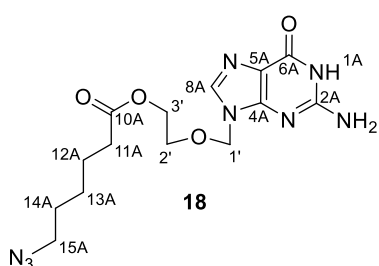


^{13}C NMR (101 MHz, $\text{DMSO-}d_6$) δ 173.73 (10G), 157.85 (6G), 154.83 (2G), 152.44 (4G), 136.56 (8G), 117.84 (5G), 87.79 (1'), 85.31 (15G), 82.48 (4'), 74.15 (2'), 72.42 (16G), 71.41 (3'), 65.00 (5'), 33.87 (11G), 28.36 (13G), 24.65 (12G), 18.50 (14G).

HRMS (ESI) m/z $[\text{M}+\text{Na}]^+$ 414.1396 (calcd for $\text{C}_{17}\text{H}_{21}\text{N}_5\text{O}_6\text{Na}$, 414.1390)

Synthesis of 2-((2-amino-6-oxo-1,6-dihydro-9H-purin-9-yl)methoxy)ethyl 6-azidohexanoate (18)

To a solution of acyclovir (150 mg, 0.666 mmol) in dry CH_2Cl_2 (1.0 mL) and dry DMF (1.5 mL) were added 6-azidohexanoic acid (158 mg, 1.006 mmol), DMAP (41 mg, 0.336 mmol), EDC-HCl (269 mg, 1.405 mmol), and triethylamine dry (196 μL , 1.405 mmol) at room temperature under a nitrogen atmosphere. The reaction was stirred overnight. Then, the solvent was removed under reduced pressure. The crude was purified with Biotage Isolera™ One System, providing the product (154,8 mg, 64%) as a white powder.



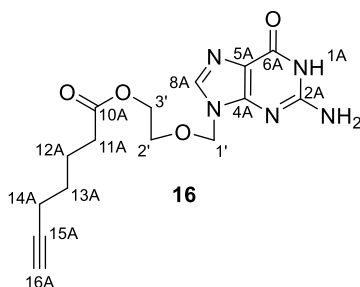
^1H NMR (400 MHz, $\text{DMSO-}d_6$) δ 10.63 (s, 1H, NH), 7.81 (s, 1H, 8A), 6.51 (s, 2H, NH_2), 5.35 (s, 2H, 1'), 4.09 (t, $J = 4.5$ Hz 1H, 3'), 3.66 (t, 1H, $J = 4.5$ Hz, 2'), 3.31 (t, $J = 6.8$ Hz, 2H, 15A), 2.24 (t, $J = 7.4$ Hz, 2H, 11A), 1.57 – 1.43 (m, 4H, 12A, 14A), 1.35 – 1.23 (m, 2H, 13A).

^{13}C NMR (101 MHz, DMSO) δ 172.72 (10A), 156.89 (6A), 153.97 (2A), 151.48 (4A), 116.51 (5A), 71.84 (1'), 66.58 (2'), 62.63 (3'), 50.52 (15A), 33.17 (11A), 27.92 (14A), 25.59 (13A), 23.90 (12A).

HRMS (ESI) m/z $[\text{M}+\text{Na}]^+$ 387.1522 (calcd for $\text{C}_{14}\text{H}_{20}\text{N}_8\text{O}_4\text{Na}$ 387.1505)

Synthesis of 2-((2-amino-6-oxo-1,6-dihydro-9H-purin-9-yl)methoxy)ethyl hept-6-ynoate (19)

To a solution of acyclovir (150 mg, 0.666 mmol) in dry CH_2Cl_2 (1.25 mL) and dry DMF (1.25 mL) were added 6-heptynoic acid (135 mg, 1.07 mmol), DMAP (41mg, 0.336 mmol), EDC-HCl (269 mg, 1.405 mmol), and triethylamine dry (196 μL , 1.405 mmol) at room temperature under a nitrogen atmosphere. The reaction was stirred overnight. The crude was purified with Biotage Isolera™ One System, providing the product (95,5 mg, 43%) as a white powder.

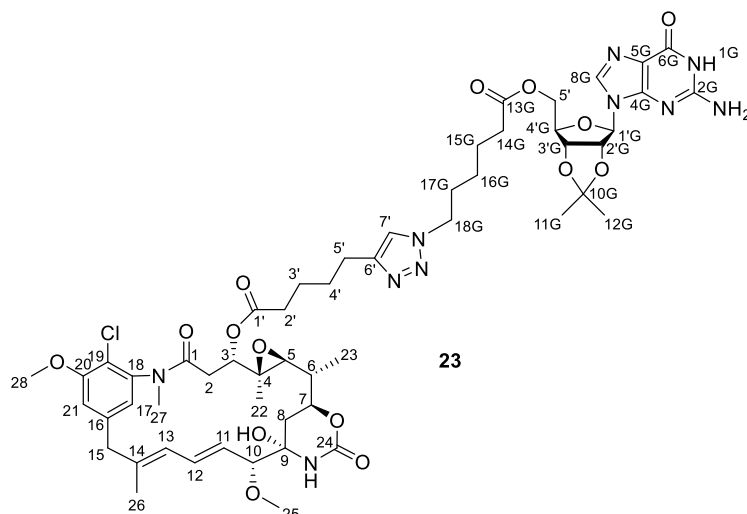


^1H NMR (400 MHz, $\text{DMSO-}d_6$) δ 7.81 (s, 1H, 8A), 6.49 (s, 2H, NH_2), 5.35 (s, 2H, 1'), 4.12 – 4.06 (t, $J = 4.9$ Hz, 2H, 3'), 3.70 – 3.63 (t, $J = 4.9$ Hz 2H, 2'), 2.74 (t, $J = 2.7$ Hz, 1H, 16A), 2.25 (t, $J = 7.4$ Hz, 2H, 11A), 2.15 (td, $J = 7.0, 2.7$ Hz, 2H, 14A), 1.62 – 1.50 (m, 2H, 12A), 1.42 (p, $J = 7.0$ Hz, 2H, 13A).

^{13}C NMR (101 MHz, DMSO- d_6) δ 172.64 (10A), 156.77 (6A), 153.90 (2A), 151.42 (4A), 137.67 (8A), 116.49 (5A), 84.21 (15A), 71.81 (1'), 71.32 (16A), 66.54 (2'), 62.62 (3'), 32.75 (11A), 27.22 (13A), 23.51 (12A), 17.36 (14A).

HRMS (ESI) m/z $[\text{M}+\text{Na}]^+$ 356.1330 (calcd for $\text{C}_{15}\text{H}_{19}\text{N}_5\text{O}_4\text{Na}$ 356.1335)

Synthesis of maytansinoid-guanosine conjugate (**23**)



To a solution of **1c** (21 mg, 0.031 mmol) and **16** (21 mg, 0.047 mmol) in DMSO (690 μL) were added water (225 μL), $\text{CuSO}_4 \cdot 5\text{H}_2\text{O}$ (15 mg, 0.050 mmol), then a solution of Na-ascorbate (39 mg, 0.19 mmol) in H_2O (115 μL) was added dropwise. The mixture was stirred at room temperature for 2 h. Then, water was added (1.4 mL) and the aqueous layer was extracted in DCM. The organic layer was washed with H_2O and brine, dried over Na_2SO_4 and concentrated in *vacuum*. Purification of the crude with Biotage Isolera™ One System (gradient from 5% to 60% ACN in 22 CV) provided the product (31 mg, 89%) as a white powder.

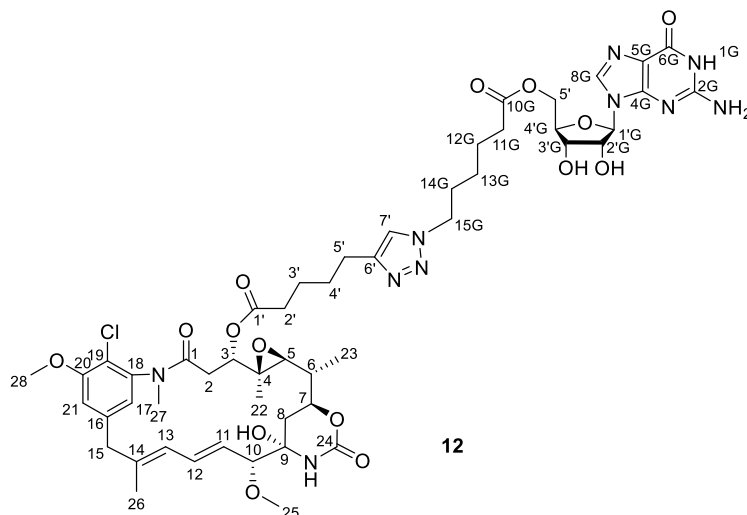
^1H (600 MHz, DMSO- d_6) δ 7.9 (s, 1H, 7'), 7.8 (d, $J = 2.0$ Hz, 1H, 8G), 7.2 (d, $J = 1.8$ Hz, 1H, 21), 7.0 (s, 2H, NH_2), 6.9 (s, 1H, NH), 6.8 (d, $J = 1.8$ Hz, 1H, 17), 6.6 (dd, $J = 15.4, 11.1$ Hz, 1H, 12), 6.2 (d, $J = 11.1$ Hz, 1H, 13), 6.0 (d, $J = 2.0$ Hz, 1H, 1'G), 5.4 (dd, $J = 15.4, 8.9$ Hz, 1H, 11), 5.3 (dd, $J = 6.3, 2.1$ Hz, 1H, 2'G), 5.1 (dd, $J = 6.3, 3.4$ Hz, 1H, 3'G), 4.6 (dd, $J = 11.9, 2.7$ Hz, 1H, 3), 4.3 – 4.2 (m, 4H, 4'G, 5'Ga, 18G), 4.2 – 4.0 (m, 2H, 5'Gb, 7), 3.9 (s, 3H, 28), 3.6 – 3.5 (m, 2H, 10, 15a), 3.3 (s, 1H, 15b), 3.2 (s, 3H, 25), 2.9 (s, 3H, 27), 2.7 (dt, $J = 13.6, 7.4$ Hz, 2H, 5'), 2.6 (d, $J = 9.8$ Hz, 1H, 5), 2.5 – 2.4 (m, 3H, 2', 2a), 2.3 (td, $J = 7.6, 4.9$ Hz, 2H, 14G), 2.0 (dd, $J = 13.5, 2.3$ Hz, 1H, 2b), 1.7 (dt, $J = 13.3, 6.8$ Hz, 4H, 3', 17G), 1.7 – 1.6 (m, 5H, 4', 26), 1.5 (s, 3H, 11G), 1.5 – 1.4 (m, 4H, 6, 8a, 15G), 1.4 – 1.3 (m, 1H, 8b), 1.3 (s, 3H, 12G), 1.2 – 1.1 (m, 2H, 16G), 1.1 (d, $J = 6.4$ Hz, 3H, 23), 0.8 (s, 3H, 22).

^{13}C NMR (151 MHz, DMSO- d_6) δ 172.98 (13G), 172.25 (1'), 168.51 (1), 155.70 (20), 154.88 (6G), 151.77 (24), 151.74 (2G), 151.05 (4G), 146.89 (6'), 141.89 (18), 141.45 (16), 139.51 (14), 136.31 (8G), 132.34 (12), 129.15 (11), 125.00 (13), 122.32 (17), 122.13 (7'), 117.90 (19),

117.37 (5G), 114.38 (21), 113.74 (10G), 88.77 (1'G), 88.54 (10), 84.64 (4'G), 84.10 (2'G), 81.57 (3'G), 80.65 (9), 76.52 (3), 73.85 (7), 66.21 (5), 64.39 (5'G), 61.06 (4), 57.03 (28), 56.65 (25), 49.39 (18G), 46.09 (15), 37.81 (6), 36.54 (8), 35.46 (27), 33.49 (2'), 33.46 (2), 32.74 (14G), 30.23 (4'), 29.88 (17G), 28.84 (5'), 28.77 (11G), 28.66 (12G), 25.37 (3'), 24.56 (15G), 15.72 (26), 14.84 (23), 11.84 (22).

HRMS (ESI) m/z $[M+Na]^+$ 1157.4691 (calcd for $C_{54}H_{71}ClN_{10}O_{15}Na$ 1157.4687);

Synthesis of maytansinoid-guanosine conjugate (**12**)



To compound **23** (18.3 mg, 0.016 mmol) was added aq. 70% HCOOH (650 μ L) and the reaction was stirred for 4 hours at 40°C. Then, the solvent was removed under reduced pressure and the acid was co-evaporated by adding and evaporating three times MeOH. Purification of the crude with Biotage Isolera™ One System (gradient from 5% to 60% ACN in 22 CV) provided the product (11 mg, 62%) as a white powder.

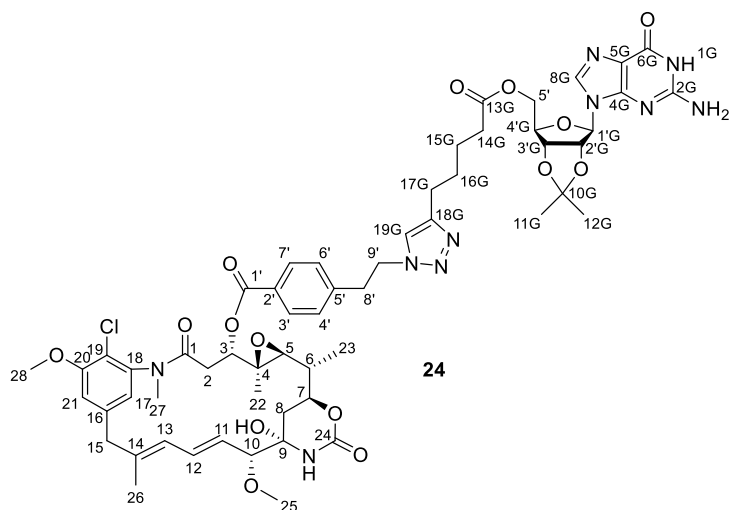
1H (600 MHz, DMSO- d_6) δ 7.9 (s, 2H, 7', 8G), 7.3 – 7.2 (m, 1H, 21), 6.9 (s, 1H, NH), 6.8 – 6.7 (m, 1H, 17), 6.6 (s, 2H, NH₂), 6.6 (dd, J = 15.3, 11.2 Hz, 1H, 12), 6.2 (d, J = 11.1 Hz, 1H, 13), 5.7 (d, J = 5.1 Hz, 1H, 1'G), 5.4 (dd, J = 15.3, 8.9 Hz, 1H, 11), 4.6 (dd, J = 11.9, 2.3 Hz, 1H, 3), 4.4 (t, J = 5.1 Hz, 1H, 2'G), 4.3 (dd, J = 11.9, 3.7 Hz, 1H, 5'Ga), 4.2 (t, J = 7.1 Hz, 2H, 15G), 4.2 (dt, J = 12.8, 5.5 Hz, 2H, 3'G, 5'Gb), 4.1 (t, J = 11.9 Hz, 1H, 7), 4.0 (q, J = 4.8 Hz, 1H, 4'G), 3.9 (s, 3H, 28), 3.5 (d, J = 12.6 Hz, 1H, 15a), 3.5 (d, J = 8.8 Hz, 1H, 10), 3.3 (d, J = 12.7 Hz, 1H, 15b), 3.2 (s, 3H, 25), 2.9 (s, 3H, 27), 2.6 (q, J = 6.8 Hz, 2H, 5'), 2.6 (d, J = 9.7 Hz, 1H, 5), 2.5 – 2.4 (m, 3H, 2', 2b), 2.3 (dt, J = 7.8, 3.8 Hz, 2H, 11G), 2.0 (d, J = 11.9 Hz, 1H, 2a), 1.8 – 1.7 (m, 4H, 3', 14G), 1.6 (s, 5H, 4', 26), 1.6 – 1.4 (m, 4H, 6, 8b, 12G), 1.3 (d, J = 12.5 Hz, 1H, 8a), 1.2 (p, J = 7.6 Hz, 2H, 13G), 1.1 (d, J = 6.3 Hz, 3H, 23), 0.8 (s, 3H, 22).

^{13}C NMR (151 MHz, DMSO- d_6) δ 173.12 (10G), 172.25 (1'), 168.51 (1), 157.39 (6G), 155.70 (20), 154.41 (2G), 151.80 (4G), 151.73 (24), 146.90 (6'), 141.89 (18), 141.45 (16), 139.51 (14), 135.39 (8G), 132.34 (12), 129.14 (11), 125.19 (13), 122.32 (17), 122.14 (7'), 117.89 (19), 117.17 (5G), 114.37 (21), 88.53 (10), 87.14 (1'G), 81.77 (4'G), 80.63 (9), 76.52 (3), 73.85 (7), 73.55 (2'G), 70.74 (3'G), 66.21 (5), 64.29 (5'G), 61.06 (4), 57.03 (28), 56.65 (25), 49.39 (15G),

46.08 (15), 37.81 (6), 36.71 (8), 35.47 (27), 33.56 (2'), 33.49 (11G), 32.73 (2), 29.89 (14G), 28.81 (4'), 25.77 (5'), 25.36 (13G), 24.56 (12G), 24.20 (3'), 15.72 (26), 14.84 (23), 11.87 (22).

HRMS (ESI) m/z $[M+Na]^+$ 1117.4380 (calcd for $C_{51}H_{67}ClN_{10}O_{15}Na$ 1117.4374);

Synthesis of maytansinoid-guanosine conjugate (**24**)



To a solution of **1h** (16 mg, 0.022 mmol) and **17** (14 mg, 0.032 mmol) in DMSO (482 μ L) were added water (159 μ L), $CuSO_4 \cdot 5H_2O$ (10 mg, 0.035 mmol), then a solution of Na-ascorbate (28 mg, 0.139 mmol) in H_2O (82 μ L) was added dropwise. The mixture was stirred at room temperature for 2 h. Then, water was added (1.4 mL) and the aqueous layer was extracted in DCM. The organic layer was washed with H_2O and brine, dried over Na_2SO_4 and concentrated in *vacuum*. Purification of the crude with Biotage Isolera™ One System (gradient from 5% to 60% ACN in 22 CV) provided the product (22 mg, 85%) as a white powder.

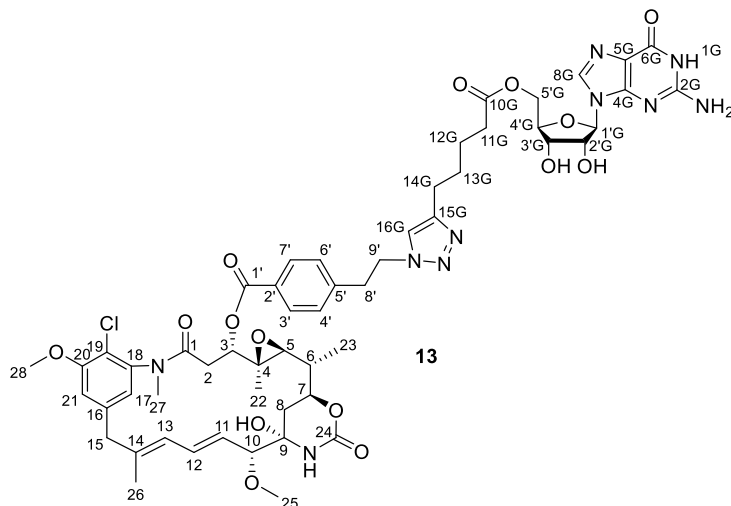
1H (600 MHz, $DMSO-d_6$) δ 7.9 – 7.8 (m, 3H, 3', 7', 8G), 7.8 (s, 1H, 19G), 7.5 (d, $J = 8.1$ Hz, 2H, 4', 6'), 7.2 (s, 1H, 21), 6.9 (s, 1H, 17), 6.8 (s, 1H, NH), 6.7 (s, 2H, NH_2), 6.5 (dd, $J = 15.4, 11.1$ Hz, 1H, 12), 6.0 – 6.0 (m, 1H, 1'G), 5.9 (d, $J = 11.1$ Hz, 1H, 13), 5.3 (dd, $J = 6.2, 1.6$ Hz, 1H, 2'G), 5.1 (dd, $J = 6.0, 3.4$ Hz, 1H, 3'G), 4.9 (dd, $J = 15.4, 9.2$ Hz, 1H, 11), 4.7 (dd, $J = 12.0, 2.6$ Hz, 1H, 3), 4.6 (t, $J = 7.2$ Hz, 2H, 9'), 4.3 – 4.2 (m, 2H, 4'G, 5'Gb), 4.2 – 4.1 (m, 2H, 5'Ga, 7), 4.0 (s, 3H, 28), 3.4 (d, $J = 12.6$ Hz, 1H, 15a), 3.4 (d, $J = 9.2$ Hz, 1H, 10), 3.3 (d, $J = 7.7$ Hz, 3H, 8', 15b), 3.2 (s, 3H, 25), 3.0 (s, 3H, 27), 2.8 (d, $J = 9.7$ Hz, 1H, 5), 2.6 – 2.6 (m, 1H, 2a), 2.5 (d, $J = 6.7$ Hz, 2H, 17G), 2.3 – 2.2 (m, 3H, 2b, 14G), 1.6 (s, 3H, 26), 1.5 (s, 3H, 12G), 1.5 – 1.4 (m, 6H, 6, 8b, 15G, 16G), 1.3 (s, 4H, 8a, 11G), 1.1 (d, $J = 6.3$ Hz, 3H, 23), 0.8 (s, 3H, 22).

^{13}C NMR (151 MHz, $DMSO-d_6$) δ 173.00 (13G), 168.45 (1), 165.68 (1'), 157.38 (6G), 155.90 (20), 154.38 (2G), 151.67 (24), 150.99 (4G), 146.84 (18G), 144.00 (5'), 141.94 (18), 141.63 (16), 139.47 (14), 136.09 (8G), 132.25 (12), 129.91 (3', 7'), 129.20 (4', 6'), 129.04 (11), 128.44 (2'), 124.97 (13), 122.20 (17), 121.96 (19G), 117.98 (19), 117.39 (5G), 114.24 (21), 113.76 (10G), 88.91 (10), 88.76 (1'G), 84.62 (4'G), 84.10 (2'G), 81.51 (3'G), 80.43 (9), 76.85 (3), 73.73 (7), 65.84 (5), 64.40 (5'G), 61.10 (4), 57.09 (28), 56.54 (25), 50.23 (9'), 46.13 (15), 38.42 (6),

36.72 (8), 36.09 (8'), 35.54 (27), 33.35 (2, 14G), 28.67 (15G), 27.46 (11G, 12G), 25.06 (17G), 24.28 (16G), 15.78 (26), 15.03 (23), 12.53 (22).

HRMS (ESI) m/z $[M+Na]^+$ 1191.4546 (calcd for $C_{57}H_{69}ClN_{10}O_{15}Na$ 1191.4530).

Synthesis of maytansinoid-guanosine conjugate (13)



To compound **24** (11 mg, 0.009 mmol) was added aq. 70% HCOOH (235 μ L) and the reaction was stirred for 4 hours at 40°C. Then, the solvent was removed under reduced pressure and the acid was co-evaporated by adding and evaporating three times MeOH. Purification of the crude with Biotage Isolera™ One System (gradient from 5% to 60% ACN in 22 CV) provided the product (8 mg, 77%) as a white powder.

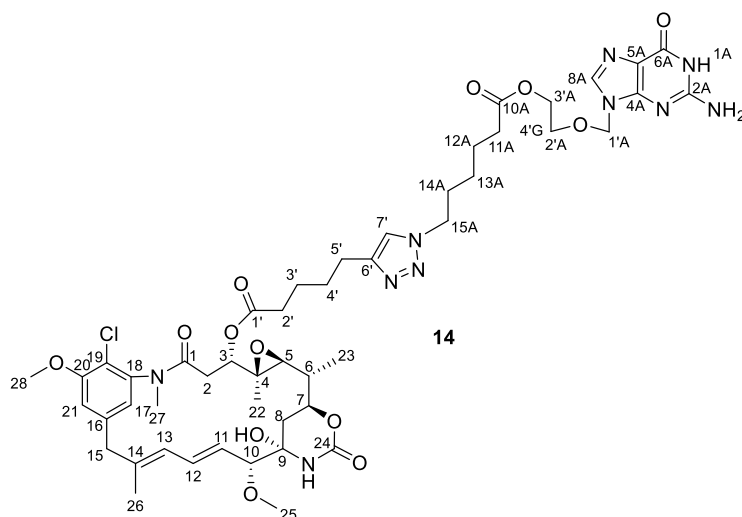
1H (600 MHz, DMSO- d_6) δ 7.8 (d, J = 7.1 Hz, 3H, 3', 7', 8G), 7.8 (s, 1H, 16G), 7.5 (d, J = 8.1 Hz, 2H, 4', 6'), 7.2 (s, 1H, 21), 6.9 (s, 1H, 17), 6.8 (s, 1H, 1G), 6.7 (s, 2H, NH₂), 6.5 (dd, J = 15.3, 11.3 Hz, 1H, 12), 5.9 (d, J = 11.3 Hz, 1H, 13), 5.7 (d, J = 5.1 Hz, 1H, 1'G), 4.9 (dd, J = 15.3, 9.1 Hz, 1H, 11), 4.7 (dd, J = 12.0, 2.7 Hz, 1H, 3), 4.6 (t, J = 7.1 Hz, 2H, 9'), 4.4 (t, J = 5.0 Hz, 1H, 2'G), 4.3 (dd, J = 11.8, 3.3 Hz, 1H, 5'Ga), 4.2 – 4.1 (m, 3H, 3'G, 5'Gb, 7), 4.0 (q, J = 4.5 Hz, 1H, 4'G), 4.0 (s, 3H, 28), 3.4 (d, J = 12.5 Hz, 1H, 15b), 3.4 (d, J = 9.1 Hz, 1H, 10), 3.3 – 3.2 (m, 3H, 8', 15a), 3.2 (s, 3H, 25), 3.0 (s, 3H, 27), 2.8 (d, J = 9.7 Hz, 1H, 5), 2.6 (t, J = 13.9 Hz, 1H, 2a), 2.6 – 2.5 (m, 2H, 14G), 2.3 (q, J = 7.4 Hz, 2H, 11G), 2.2 (d, J = 12.1 Hz, 1H, 2b), 1.6 (s, 3H, 26), 1.6 – 1.5 (m, 4H, 12G, 13G), 1.5 – 1.4 (m, 2H, 6, 8a), 1.3 (d, J = 12.6 Hz, 1H, 8b), 1.1 (d, J = 6.3 Hz, 3H, 23), 0.8 (s, 3H, 22).

^{13}C NMR (151 MHz, DMSO- d_6) δ 173.13 (10G), 168.47 (1), 165.71 (1'), 157.35 (6G), 155.91 (20), 154.40 (2G), 151.80 (4G), 151.70 (24), 146.87 (15G), 144.02 (5'), 141.94 (18), 141.65 (16), 139.48 (14), 136.22 (8G), 132.27 (12), 129.92 (3', 7'), 129.23 (4', 6'), 129.07 (11), 128.45 (2'), 124.98 (13), 122.21 (17), 121.97 (16G), 117.97 (19), 117.16 (5G), 114.26 (21), 88.91 (10), 87.13 (1'G), 81.81 (4'G), 80.43 (9), 76.86 (3), 73.73 (2'G), 73.59 (7), 70.76 (3'G), 65.86 (5), 64.33 (5'G), 61.10 (4), 57.10 (28), 56.56 (25), 50.23 (9'), 46.12 (15), 39.57, 38.42 (6), 37.78 (8), 36.08 (8'), 35.55 (27), 33.49 (2), 33.46 (11G), 28.70 (12G), 25.09 (14G), 24.37 (13G), 15.78 (26), 15.04 (23), 12.52 (22).

HRMS (ESI) m/z $[M+Na]^+$ 1151.4226 (calcd for $C_{54}H_{65}ClN_{10}O_{15}Na$ 1151.4217);

Synthesis of maytansinoid-acyclovir conjugate (**14**)

To a solution of **1c** (14 mg, 0.02 mmol) and **18** (9.1 mg, 0.025 mmol) in H_2O/DMF as solvents (1:2, 400 μL) were added a solution of $CuSO_4 \cdot 5H_2O$ (11.2 μL of 0.75 M solution, 0.084 mmol), and a solution of Na-ascorbate (83.9 μL of 1M solution, 0.0084 mmol). The mixture



was stirred at room temperature for 6h. Crude was purified with Biotage Isolera™ One System (gradient H_2O/ACN), providing the product (7 mg, 35%) as a white powder.

1H NMR (400 MHz, $DMSO-d_6$) δ 7.87 (d, $J = 4.9$ Hz, 1H, 7), 7.80 (s, 1H, 8A), 7.23 (d, $J = 1.7$ Hz, 1H, 21), 6.94 – 6.87 (bs, 1H, NH), 6.77 (d, $J = 1.7$ Hz, 1H, 17), 6.65 (s, 2H, NH_2), 6.58 (dd, $J = 15.4, 11.1$ Hz, 1H, 12), 6.22 (d, $J = 11.1$ Hz, 1H, 13), 5.98 (s, 1H, 1A, NH), 5.45 (dd, $J = 15.4, 8.9$ Hz, 1H, 11), 5.35 (s, 2H, 1'A), 4.64 (dd, $J = 11.9, 2.6$ Hz, 1H, 3), 4.25 (t, $J = 7.1$ Hz, 2H, 3'A), 4.13 – 4.02 (m, 4H, 2'A, 15A'), 3.95 (s, 3H, 28), 3.70 – 3.64 (m, 2H, 7, 10), 3.51 (d, $J = 9.3$ Hz, 1H, 15a), 3.31-3.23 (m, 4H, 15b, 25), 2.95 (s, 3H, 27), 2.67 – 2.64 (m, 2H, 5'), 2.61 (d, $J = 9.7$ Hz, 1H, 5), 2.44 – 2.38 (m, 1H, 2b), 2.22 (t, $J = 7.2$ Hz, 2H, 11A'), 2.15 – 2.10 (m, 2H, 2'), 2.01 (d, $J = 12.9$ Hz, 1H, 2a), 1.79 – 1.69 (m, 4H, 3', 14A'), 1.65-1.60 (m, 5H, 26, 4'), 1.56 – 1.43 (m, 4H, 6, 12A', 8b), 1.39 – 1.33 (m, 1H, 8a), 1.22-1.18 (m, 2H, 13A'), 1.12 (d, $J = 6.3$ Hz, 3H, 23), 0.82 (s, 3H, 22).

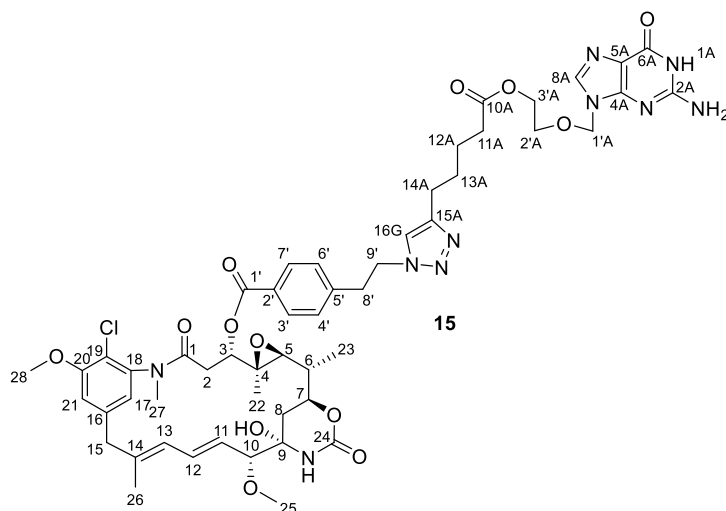
^{13}C NMR (101 MHz, $DMSO-d_6$) δ 172.63 (10A), 171.42 (1'), 168.03 (1), 156.65 (6A), 155.21 (20), 154.03 (2A), 151.45 (4A), 151.24 (24), 146.42 (6'), 141.41 (18), 140.97 (16), 139.02 (14), 131.87 (12), 128.67 (11), 124.72 (13), 121.84 (17), 121.66 (7'), 117.42 (19), 116.49 (5A), 113.89 (21), 88.06 (10), 80.17 (9), 76.05 (3), 73.37 (7), 71.77 (1A'), 66.52 (2'A), 65.74 (5), 62.59 (3'A), 60.58 (4), 56.55 (28), 56.17 (25), 50.54 (15A), 48.93 (15), 35.77 (6), 34.98 (27), 33.34 (8), 33.06 (2'), 29.36 (11A), 28.32 (2), 25.31 (14A), 25.26 (4'), 24.89 (5'), 24.45 (13A), 24.07 (12A), 23.71 (3'), 15.28 (26), 14.40 (23), 11.37 (22).

HRMS (ESI) m/z $[M+Na]^+$ 1059.4302 (calcd for $C_{49}H_{65}ClN_{10}O_{13}Na$ 1059.4319)

Synthesis of maytansinoid-acyclovir conjugate (**15**)

To a solution of **1h** (11 mg, 0.015 mmol) and **19** (6 mg, 0.018 mmol) in H₂O/DMF as solvents (1:2, 300 μ L) were added a solution of CuSO₄*5H₂O (8 μ L of 0.75 M solution, 0.06 mmol), and a solution of Na-ascorbate (60 μ L of 1M solution, 0.006 mmol). The mixture was stirred at room temperature for 5h. Crude was purified with Biotage Isolera™ One System (gradient H₂O/ACN), providing the product (8.8 mg, 55%) as a white powder.

¹H NMR (400 MHz, DMSO-*d*₆) δ 7.83 (m, 4H, 8A, 3', 7', 16A), 7.46 (d, *J* = 8.1 Hz, 2H, 4', 6'),



7.26 (d, *J* = 1.8 Hz, 1H, 21), 6.93 (d, *J* = 1.8 Hz, 1H, 17), 6.80 (s, 1H, NH), 6.55 (s, 2H, NH₂), 6.48 (dd, *J* = 15.3, 11.0 Hz, 1H, 12), 5.93 (d, *J* = 11.0 Hz, 1H, 13), 5.53 (s, 1H, 1A), 5.35 (s, 2H, 1'A), 4.94 (dd, *J* = 15.3, 9.0 Hz, 1H, 11), 4.75 (dd, *J* = 12.0, 3.0 Hz, 1H, 3), 4.64 (t, *J* = 7.2 Hz, 2H, 9'), 4.17 – 4.06 (m, 3H, 3'A, 7), 3.96 (s, 3H, 28), 3.70 – 3.63 (m, 2H, 2'A), 3.45 (d, *J* = 12.5 Hz, 1H, 15a), 3.41 – 3.22 (m, 4H, 10, 8', 15b), 3.17 (s, 3H, 25), 2.99 (s, 3H, 27), 2.83 (d, *J* = 9.6 Hz, 1H, 5), 2.67 – 2.52 (m, 3H, 2a, 14A), 2.31 – 2.2 (m, 3H, 2b, 11A), 1.64 (s, 3H, 26), 1.56 – 1.41 (m, 5H, 8b, 13A, 12A), 1.38 – 1.18 (m, 2H, 8a, 6), 1.13 (d, *J* = 6.4 Hz, 3H, 23), 0.83 (s, 3H, 22).

¹³C NMR (101 MHz, DMSO-*d*₆) δ 172.92 (10A), 168.21 (1), 165.42 (1'), 157.02 (6A), 155.66 (20), 154.15 (2A), 151.64 (4A), 151.44 (24), 147.01 (15A), 143.77 (5'), 141.69 (18), 141.40 (16), 139.25 (14), 135.01 (8A), 132.02 (12), 129.68 (3',7'), 128.98 (4',6'), 128.82 (11), 128.19 (2'), 124.73 (13), 121.98 (17), 121.72 (16A), 117.72 (19), 116.70 (5A), 113.99 (21), 88.66 (10), 80.18 (9), 76.54 (3), 73.46 (7), 72.01 (1'A), 66.74 (2'A), 65.53 (5), 62.81 (3'A), 60.86 (4), 56.85 (28), 56.31 (25), 49.99 (9'), 45.87 (15), 38.17 (6), 36.46 (8), 35.85 (8'), 35.29 (27), 33.56 (2), 33.18 (11A), 28.44 (12A), 24.81 (14A), 24.09 (13A), 15.55 (26), 14.79 (23), 12.29 (22).

HRMS (ESI) *m/z* [M+Na]⁺ 1093.4210 (calcd for C₅₂H₆₃ClN₁₀O₁₃Na 1093.4162)

2.1.6 REFERENCES

- [1] S. M. Kupchan, Y. Komoda, W. A. Court, G. J. Thomas, R. M. Smith, A. Karim, C. J. Gilmore, R. C. Haitiwanger, R. F. Bryan, *J. Am. Chem. Soc.* **1972**, *94*, 1354–1356.
- [2] S. Remillard, L. I. Rebhun, G. A. Howie, S. M. Kupchan, *Science (80-.)*. **1975**, *189*, 1002–1005.
- [3] M. Lopus, E. Oroudjev, L. Wilson, S. Wilhelm, W. Widdison, R. Chari, M. A. Jordan, *Mol. Cancer Ther.* **2010**, *9*, 2689–2699.
- [4] B. F. Issell, S. T. Crooke, *Cancer Treat. Rev.* **1978**, *5*, 199–207.
- [5] J. M. Cassady, K. K. Chan, H. G. Floss, E. Leistner, *Chem. Pharm. Bull.* **2004**, *52*, 1–26.
- [6] L. Amiri-Kordestani, G. M. Blumenthal, Q. C. Xu, L. Zhang, S. W. Tang, L. Ha, W. C. Weinberg, B. Chi, R. Candau-Chacon, P. Hughes, A. M. Russell, S. P. Miksinski, X. H. Chen, W. D. McGuinn, T. Palmby, S. J. Schrieber, Q. Liu, J. Wang, P. Song, N. Mehrotra, L. Skarupa, K. Clouse, A. Al-Hakim, R. Sridhara, A. Ibrahim, R. Justice, R. Pazdur, P. Cortazar, *Clin. Cancer Res.* **2014**, *20*, 4436–4441.
- [7] S. Wedam, L. Fashoyin-Aje, X. Gao, E. Bloomquist, S. Tang, R. Sridhara, K. B. Goldberg, B. L. King-Kallimanis, M. R. Theoret, A. Ibrahim, L. Amiri-Kordestani, R. Pazdur, J. A. Beaver, *Clin. Cancer Res.* **2020**, *26*, 4180–4185.
- [8] S. García-Alonso, A. Ocaña, A. Pandiella, *Trends in Cancer* **2020**, *6*, 130–146.
- [9] J. I. Geller, J. G. Pressey, M. A. Smith, R. A. Kudgus, M. Cajaiba, J. M. Reid, D. Hall, D. A. Barkauskas, S. D. Voss, S. Y. Cho, S. L. Berg, J. S. Dome, E. Fox, B. J. Weigel, *Cancer* **2020**, 5303–5310.
- [10] P. Zhao, Y. Zhang, W. Li, C. Jeanty, G. Xiang, Y. Dong, *Acta Pharm. Sin. B* **2020**, *10*, 1589–1600.
- [11] A. E. Prota, K. Bargsten, J. F. Diaz, M. Marsh, C. Cuevas, M. Liniger, C. Neuhaus, J. M. Andreu, K. H. Altmann, M. O. Steinmetz, *Proc. Natl. Acad. Sci. U. S. A.* **2014**, *111*, 13817–21.
- [12] S. M. Kupchan, Y. Komoda, A. R. Branfman, A. T. Sneden, W. A. Court, G. J. Thomas, H. P. J. Hintz, R. M. Smith, A. Karim, G. A. Howie, A. K. Verma, Y. Nagao, R. G. Dailey, V. A. Zimmerly, W. C. Sumner, *J. Org. Chem.* **1977**, *42*, 2349–2357.
- [13] S. J. M. Hale, R. D. Perrins, C. E. García, A. Pace, U. Peral, K. R. Patel, A. Robinson, P. Williams, Y. Ding, G. Saito, M. Á. Rodríguez, I. Perera, A. Barrientos, K. Conlon, S. Damment, J. Porter, T. Coulter, *Bioconjug. Chem.* **2019**, *30*, 703–713.
- [14] J. Porter, Y. Ding, S. J. M. Hale, R. D. Perrins, A. Robinson, M. P. Mazanetz, Y. Wu, Y. Ma, K. Conlon, T. Coulter, *Bioorganic Med. Chem. Lett.* **2020**, *30*, 127634.
- [15] C.-F. Lo, T.-Y. Chiu, Y.-T. Liu, P.-Y. Pan, K.-L. Liu, C.-Y. Hsu, M.-Y. Fang, Y.-C. Huang, T.-K. Yeh, T.-A. Hsu, C.-T. Chen, L.-R. Huang, L. K. Tsou, *J. Med. Chem.* **2022**, *65*, 12802–12824.
- [16] G. Menchon, A. E. Prota, D. Lucena-Agell, P. Bucher, R. Jansen, H. Irschik, R. Müller, I. Paterson, J. F. Díaz, K. H. Altmann, M. O. Steinmetz, *Nat. Commun.* **2018**, *9*, 2106.
- [17] P. Marzullo, Z. Boiarska, H. Pérez-Peña, A. C. Abel, B. Álvarez-Bernad, D. Lucena-Agell, F. Vasile, M. Sironi, K. H. Altmann, A. E. Prota, J. F. Díaz, S. Pieraccini, D. Passarella, *Chem. - A Eur. J.* **2022**, *28*, e202103520.
- [18] S. Ikeyama, M. Takeuchi, *Biochem. Pharmacol.* **1981**, *30*, 2421–2425.
- [19] T. W. Yu, H. G. Floss, in *Anticancer Agents from Nat. Prod.*, **2005**.
- [20] W. Li, M. Huang, Y. Li, A. Xia, L. Tan, Z. Zhang, Y. Wang, J. Yang, *Biochem. Biophys. Res. Commun.* **2021**, *566*, 197–203.
- [21] A. Kawai, H. Akimoto, Y. Kozai, K. Ootsu, S. Tanida, N. Hashimoto, H. Nomura, *Chem. Pharm. Bull.* **1984**, *32*, 3341–3351.
- [22] W. C. Widdison, S. D. Wilhelm, E. E. Cavanagh, K. R. Whiteman, B. A. Leece, Y. Kovtun, V. S. Goldmacher, H. Xie, R. M. Steeves, R. J. Lutz, R. Zhao, L. Wang, W. A. Blättler, R. V. J. Chari, *J. Med. Chem.* **2006**, *49*, 4392–4408.
- [23] T. Nittoli, M. P. Kelly, F. Delfino, J. Rudge, A. Kunz, T. Markotan, J. Spink, Z. Chen, J. Shan, E. Navarro, M. Tait, K. Provoncha, J. Giurleo, F. Zhao, X. Jiang, D. Hylton, S. Makonnen, C. Hickey, J. R. Kirshner, G. Thurston, N. Papadopoulos, *Bioorganic Med. Chem.* **2018**, *26*, 2271–2279.

- [24] W. C. Widdison, J. F. Ponte, J. A. Coccia, L. Lanieri, Y. Setiady, L. Dong, A. Skaletskaya, E. E. Hong, R. Wu, Q. Qiu, R. Singh, P. Salomon, N. Fishkin, L. Harris, E. K. Maloney, Y. Kovtun, K. Veale, S. D. Wilhelm, C. A. Audette, J. A. Costoplus, R. V. J. Chari, *Bioconjug. Chem.* **2015**, *26*, 2261–2278.
- [25] J. A. Costoplus, K. H. Veale, Q. Qiu, J. F. Ponte, L. Lanieri, Y. Setiady, L. Dong, A. Skaletskaya, L. M. Bartle, P. Salomon, R. Wu, E. K. Maloney, Y. V. Kovtun, O. Ab, K. Lai, R. V. J. Chari, W. C. Widdison, *ACS Med. Chem. Lett.* **2019**, *10*, 1393–1399.
- [26] Y. Liang, S. Li, X. Wang, B. He, B. He, W. Dai, H. Zhang, X. Wang, Y. Wang, D. Zhou, Q. Zhang, *Theranostics* **2017**, *7*, 3306–3318.
- [27] B. H. White, K. Whalen, K. Kriksciukaite, R. Alargova, T. Au Yeung, P. Bazinet, A. Brockman, M. Dupont, H. Oller, C. A. Lemelin, P. Lim Soo, B. Moreau, S. Perino, J. M. Quinn, G. Sharma, R. Shinde, B. Sweryda-Krawiec, R. Wooster, M. T. Bilodeau, *J. Med. Chem.* **2019**, *62*, 2708–2719.
- [28] T. W. Traut, *Mol. Cell. Biochem.* **1994**, *140*, 1–22.
- [29] H. J. Schaeffer, *Am. J. Med.* **1982**, *73*, DOI 10.1016/0002-9343(82)90054-7.
- [30] E. De Clercq, *J. Clin. Virol.* **2004**, *30*, DOI 10.1016/j.jcv.2004.02.009.
- [31] S. Vertuani, A. Baldisserotto, K. Varani, P. A. Borea, B. De Marcos Maria Cruz, L. Ferraro, S. Manfredini, A. Dalpiaz, *Eur. J. Med. Chem.* **2012**, *54*, 202–209.
- [32] Y. Pavan Kumar, P. Saha, D. Saha, I. Bessi, H. Schwalbe, S. Chowdhury, J. Dash, *ChemBioChem* **2016**, *17*, 388–393.
- [33] J. Camacho-García, C. Montoro-García, A. M. López-Pérez, N. Bilbao, S. Romero-Pérez, D. González-Rodríguez, *Org. Biomol. Chem.* **2015**, *13*, 4506–4513.
- [34] Y. Xu, H. Jin, Z. Yang, L. Zhang, L. Zhang, *Tetrahedron* **2009**, *65*, 5228–5239.
- [35] B. Zhang, Z. Cui, L. Sun, *Org. Lett.* **2001**, *3*, 275–278.
- [36] R. Shah, A. Strom, A. Zhou, K. M. Maize, B. C. Finzel, C. R. Wagner, *ACS Med. Chem. Lett.* **2016**, *7*, 780–784.
- [37] S. Vincent, S. Grenier, A. Valleix, C. Salesse, L. Lebeau, C. Mioskowski, *J. Org. Chem.* **1998**, *63*, 7244–7257.
- [38] Y. Xiong, J. Lu, J. Hunter, L. Li, D. Scott, H. G. Choi, S. M. Lim, A. Manandhar, S. Gondi, T. Sim, K. D. Westover, N. S. Gray, *ACS Med. Chem. Lett.* **2017**, *8*, 61–66.
- [39] K. Lafaye, C. Bosset, L. Nicolas, A. Guérinot, J. Cossy, *Beilstein J. Org. Chem.* **2015**, *11*, DOI 10.3762/bjoc.11.241.
- [40] L. Hoffer, C. Chira, G. Marcou, A. Varnek, D. Horvath, *Molecules* **2015**, *20*, 8997–9028.
- [41] A. E. Prota, K. Bargsten, J. F. Díaz, M. Marsh, C. Cuevas, M. Liniger, C. Neuhaus, J. M. Andreu, K. H. Altmann, M. O. Steinmetz, *Proc. Natl. Acad. Sci. U. S. A.* **2014**, *111*, 13817–13821.
- [42] R. Matesanz, I. Barasoain, C. G. Yang, L. Wang, X. Li, C. de Inés, C. Coderch, F. Gago, J. J. Barbero, J. M. Andreu, W. S. Fang, J. F. Díaz, *Chem. Biol.* **2008**, *15*, 573–585.
- [43] A. E. Prota, K. Bargsten, D. Zurwerra, J. J. Field, J. F. Díaz, K. H. Altmann, M. O. Steinmetz, *Science (80-.)*. **2013**, *339*, 587–590.
- [44] A. E. Prota, M. M. Magiera, M. Kuijpers, K. Bargsten, D. Frey, M. Wieser, R. Jaussi, C. C. Hoogenraad, R. A. Kammerer, C. Janke, M. O. Steinmetz, *J. Cell Biol.* **2013**, *200*, 259–270.
- [45] M. Wojdyr, R. Keegan, G. Winter, A. Ashton, *Acta Crystallogr. Sect. A Found. Crystallogr.* **2013**, *69*, 299.
- [46] P. Marzullo, *ORGANIC SYNTHESIS AND MODIFICATION OF NATURE-INSPIRED PRODUCTS*, **2022**.

2.2 SYNTHETIC EFFORTS TOWARDS THE TOTAL SYNTHESIS OF A NATURAL PRODUCT GLYCYBRIDIN B

Abstract: Currently, most known tubulin binders are natural products of great chemical complexity, difficult to modify or to functionalize. Searching for new potential tubulin binders, we have identified a promising natural product, glycybridin B. Based on computational studies, this molecule has been predicted to bind to maytansine site of tubulin. Here, we report the synthetic efforts focused on its total synthesis.

Declaration of contribution: This is a multidisciplinary project performed within TubInTrain network. The computational studies, which allowed to identify the glycybridin B as a potential tubulin binder, were performed by Maxim Shevelev, University of Strasbourg, France. As a result, we have decided to undertake the total synthesis of glycybridin B and I planned the synthetic pathway and performed the synthetic work in the first part of the project. In parallel, I screened the intermediates derived from this synthesis using X-ray crystallography experiments. After the completion of the secondment, I have been once more involved in the synthetic part of this project.

2.2.1 INTRODUCTION

The amount of known maytansine site ligands is quite limited, and most of the current representatives are characterized by their structural complexity, including the above described maytansinoids, or plocabulin, disorazole Z or spongistatin-1 (discussed in 1.3.3). To identify new maytansine site ligands, computational studies were performed by Maxim Shevelev, Laboratory of Chemoinformatics, University of Strasbourg. Using the LigandScout^[1] software and the crystal structure of the tubulin-disorazole Z protein-ligand complex (PDB ID: 6FJM), a pharmacophore model for maytansine site was derived. This model was then used to screen ChEMBL database, and allowed to identify 1035 virtual hits, which have been further examined by means of protein-ligand docking. The latter has established 104 molecules that were calculated to have a docking score better than that calculated for the active molecule used to derive the pharmacophore model itself (disorazole Z). Further filtering of the hits was applied based on the cytotoxicity assays reported in the ChEMBL database for the found virtual hits. Eventually, 6 compounds reported exerting cytotoxic activity of unidentified mechanism were considered (Figure 2-11).

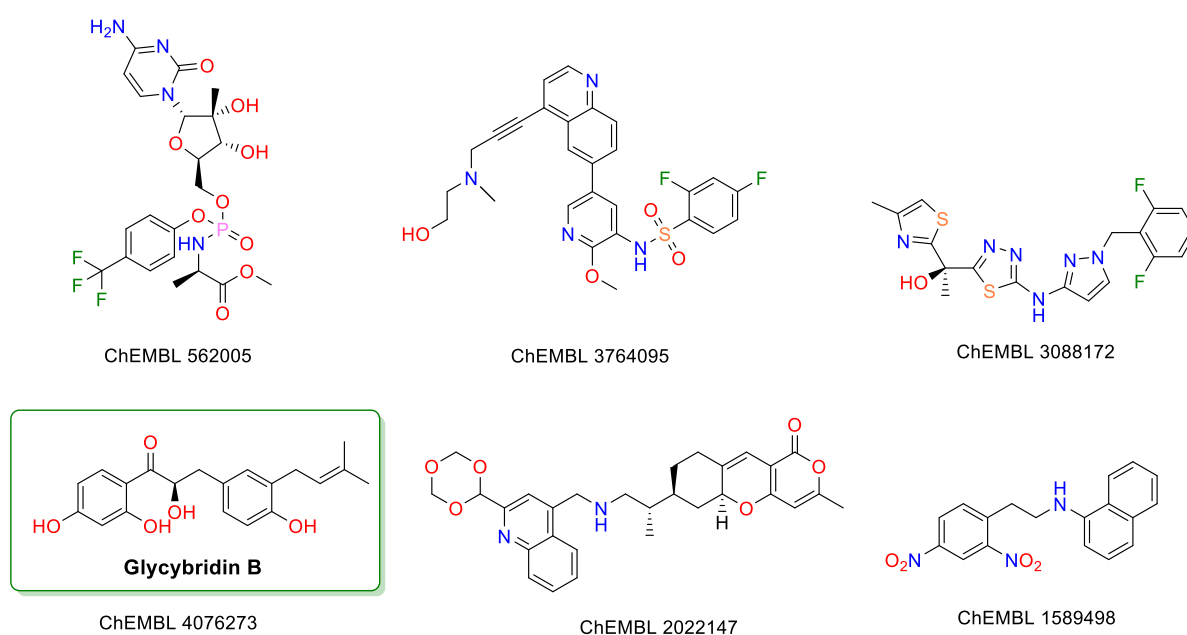


Figure 2-11. Chemical structures of promising maytansine site binders based on computational screening.

Out of the identified hits, compound ChEMBL 4076273, is a natural product, glycybridin B. Glycybridin B is a natural product isolated for the first time in 2017, from the herbal medicine *Glycyrrhiza glabra*, widely known as licorice, by Kai Li and co-workers.^[2] A range of different studies attribute to it a variety of biological activities, including moderate cytotoxicity in MCF7 human breast cancer cell line and hepatoprotective activity against CCl₄ and acetaminophen-induced liver injury in HepG2 cells.^[2,3] Furthermore, remarkable biological activities were shown by a glycybridin B chalcone precursor, licoagrochalcone A, which

showed noticeable tyrosinase inhibitory activities and inhibited PTP1B with the IC_{50} of 0.97 μM .^[4]

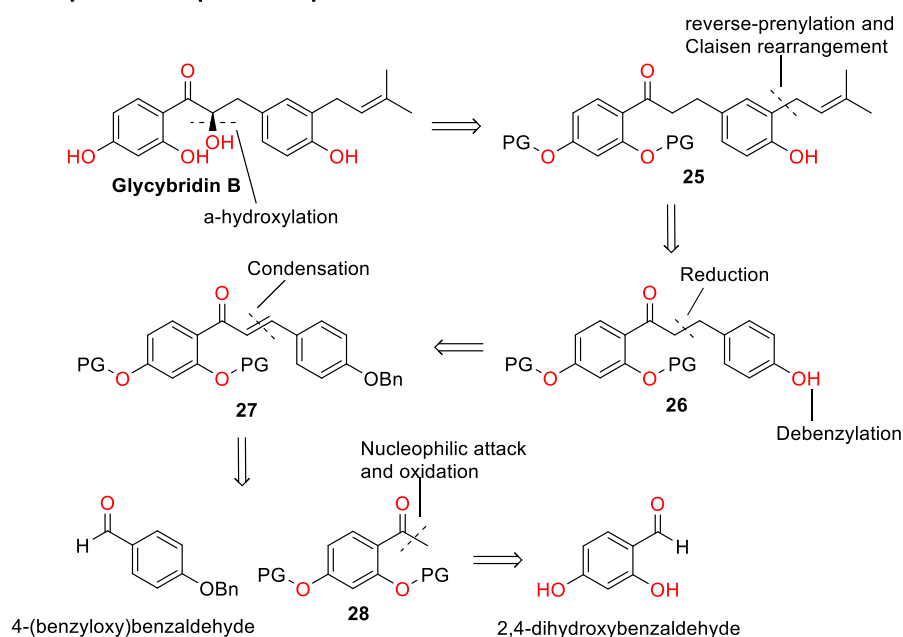
2.2.2 AIM OF THE PROJECT

Considering a variety of potential biological activities of glycybridin B and its analogues as well as the fact that its total synthesis has not yet been reported in literature, we aimed to undertake a total synthesis of this compound. We considered a retrosynthetic pathway that would include the chalcone precursor, as chalcones are known to bind to the colchicine site of tubulin.^[5] In this way, it would be possible not only to obtain a potential maytansine site ligand, but also investigate the specificity between the ligand binding to maytansine and colchicine sites. Furthermore, we have planned to evaluate the activity of the compounds and its precursors based on its effect on tubulin assembly and X-ray crystallography experiments.

2.2.3 RESULTS AND DISCUSSION

Chemistry

2.2.3.1 Retrosynthetic pathway



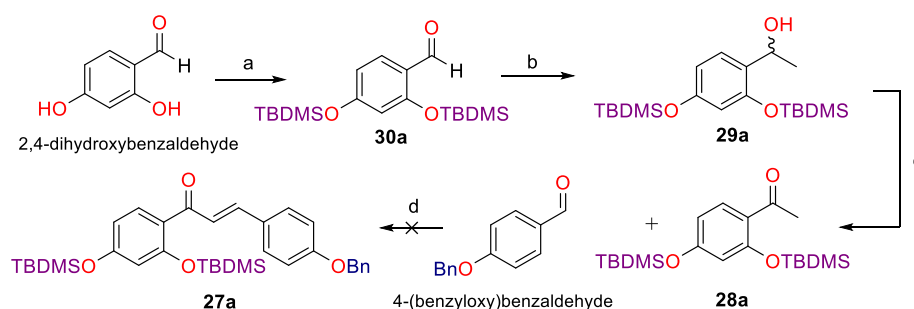
Scheme 2-10. Retrosynthetic approach toward glycybridin B

The synthesis of glycybridin B was planned according to the retrosynthetic approach depicted in Scheme 2-10. Namely, glycybridin B could be obtained through an α -hydroxylation reaction of compound **25**, which derives from the reverse-prenylation and subsequent Claisen rearrangement of compound **26**. The latter can be obtained

through the double bond reduction and debenzoylation of chalcone **27**, which in turn can be obtained from a Claisen-Schmidt condensation reaction between ketone **28** and 4-(benzyloxy)benzaldehyde. Finally, compound **28** could be obtained via a nucleophilic attack with methylmagnesium bromide on the protected 2,4-dihydroxybenzaldehyde, followed by oxidation of the resulting alcohol.

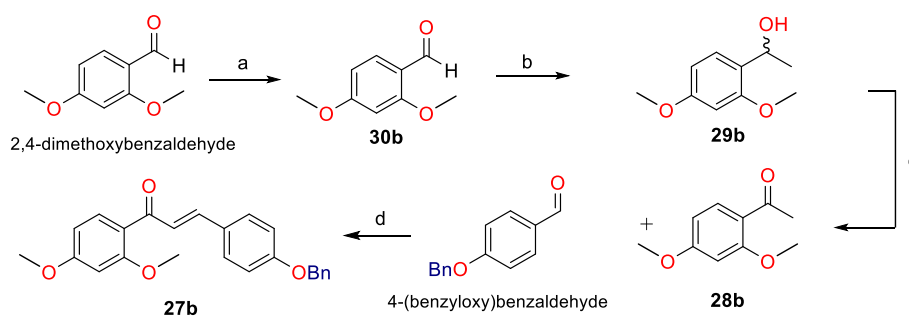
2.2.3.2 Synthesis of chalcone **27**

Initially, the tert-butyldimethylsilyl (TBDMS) group was selected to protect the phenolic functions of the aldehyde, due to its wide application in organic synthesis and its theoretical stability in the conditions of planned synthesis. The respective synthetic pathway is reported in Scheme 2-11. The synthesis of chalcone **27a** was not successful due to the unexpected instability issues of the TBDMS group in basic aqueous conditions. To verify that the cleavage of protecting groups is indeed interfering with the reaction, the starting ketone **28a** was subjected to the reaction conditions without the addition of the second reactant, and the TBDMS removal was confirmed by NMR spectroscopy.



Scheme 2-11. Reaction conditions: a) TBDMSCl, DIPEA, CH₂Cl₂, 0°C to rt, 2h, **30a** 72%; b) CH₃MgBr, THF, -70°C, 1,5h, **29a** 85%; c) DMP, CH₂Cl₂, rt, 1.5h, **28a** 75%; d) NaOH, EtOH, H₂O, 40°C, 2h.

As a result, we decided to change the protecting group of the phenolic functions. Methoxy protecting groups, characterized by a higher stability under a wide range of reaction conditions, were chosen. The synthesis of compound **27b** was completed in three steps. The first step involved the protection of the phenolic functions of 2,4-dihydroxybenzaldehyde.



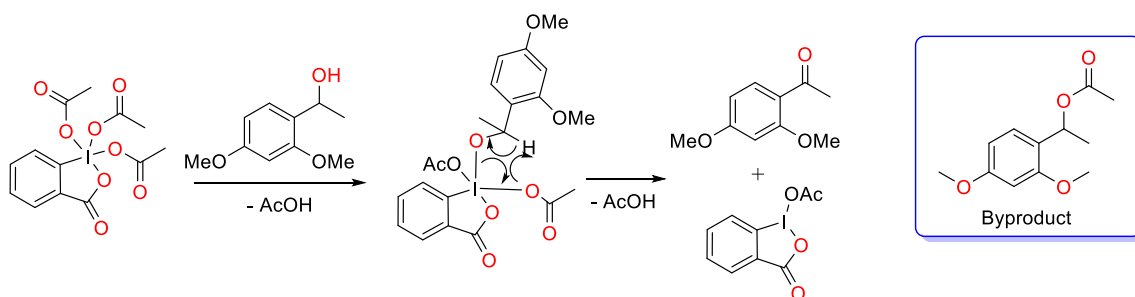
Scheme 2-12. Reaction conditions: a) MeI, K₂CO₃, acetone, reflux, 5h, **30b** 93% ; b) CH₃MgBr, THF, -70°C to rt, 3h, **29b** 88%; c) DMP, CH₂Cl₂, rt, 2h, **28b** 61%; d) NaOH, EtOH H₂O, THF, 40°C, 28h, **27b** 88%;

Such methoxy-protected phenol **30b** was subjected to a nucleophilic attack with methylmagnesium bromide, and the resulted alcohol **29b** was oxidized to the desired ketone **28b** with Dess-Martin periodinane, DMP (Scheme 2-12). As demonstrated in Table 2-7, the step of oxidation highly depended on the scale of the reaction, eq. of DMP used and the reaction time. Entry provided the desired product in 61 % yield, while increasing the scale of the reaction or the equivalents of DMP led to lower yields.

Table 2-7. Oxidation reaction of alcohol **29b**

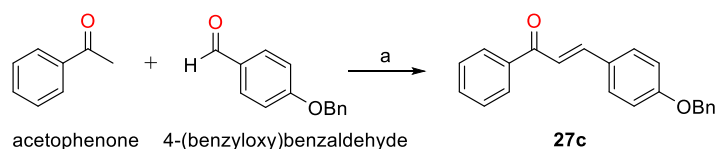
Entry	Scale (mg)	DMP eq.	Reaction time (h)	Yield
1	850	1	2.5	14%
2	420	1	3	10%
3	130	3	28	10%
4	130	2	2	61%
5	300	1.3	1.5	38%
6	300	2	1	18%

This may be explained by the mechanism of the DMP oxidation (Scheme 2-13). First, the



Scheme 2-13. Mechanism of DMP oxidation and the possible by-product formed

alcohol moiety is complexed with the iodine function, providing a diacetoxyalkoxyperiodinane intermediate, and releasing one equivalent of acetic acid. Then, the alcohol gets deprotonated by another acetic acid function present, providing the oxidized product. Acetic acid is indeed produced during the reaction, and it could attack the

Scheme 2-14. Reaction conditions: a) NaOH, EtOH, H₂O, THF, 40°C, 28h, **27c** 80%;

unreacted alcohol, forming the reported ester as a possible by-product and lowering the overall yield of the reaction.

Additionally, a chalcone analogue **27c** without any substituents on the phenyl ring, was synthesized in one step, through a Claisen-Schmidt reaction between acetophenone and 4-(benzyloxy) benzaldehyde (Scheme 2-14). The latter serves as a model chalcone for the challenging steps of the synthesis e.g. α -hydroxylation and could allow to better understand the biological function of these two hydroxyl groups.

2.2.3.3 Chalcone hydrogenation and debenzoylation

The hydrogenation and debenzoylation of the chalcone to obtain compound **26** can be performed either in one or two steps.

Initially, a one-step catalytic hydrogenation was planned to reduce the double bond and remove the benzyl group. Using a mixture of methanol/DCM as solvents, only completely reduced compound was obtained (Table 2-7). The disappearance of the carbonyl function was confirmed by NMR spectroscopy and a qualitative test based on Brady's reagents, which is a red to orange solid of 2,4-dinitrophenylhydrazine (DNPH), methanol, and sulfuric acid that reacts with carbonyl compounds such as aldehydes and ketones. The presence of carbonyl function is signalled by a yellow precipitate, for aliphatic carbonyls, or red to orange precipitate, for aromatic carbonyls, but in our case the solution remained clear.

Table 2-7. Initial trials of the hydrogenation reaction

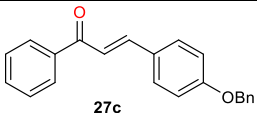
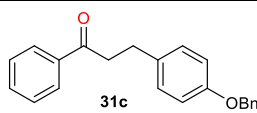
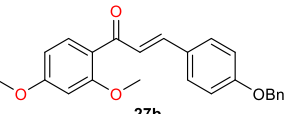
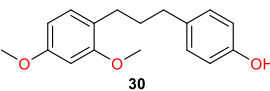
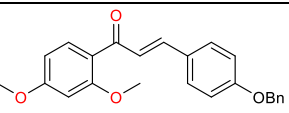
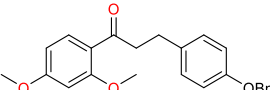
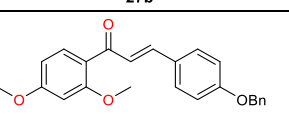
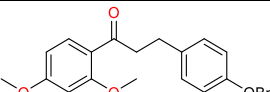
Entry	Substrate	Reagents	Reaction conditions	Time	Outcome
1		H ₂ , Pd/C 10% (0.25eq)	rt, MeOH/CH ₂ Cl ₂ (1:1)	o/n	
2		H ₂ , Pd/C 10% (0.5 eq)	rt, MeOH/CH ₂ Cl ₂ (1:1)	3h	

In parallel, we decided to probe the strategy consisting of two separate hydrogenation and debenzoylation steps.

First, we focused our attention on the chalcone's double bond reduction. As reported in the Table 2-9, the use of Et₃SiH and TFA in room temperature gave a completely product without the carbonyl function, confirming the extreme sensibility of the **27b** against the reduction reactions. For comparison, the same conditions were applied to chalcone **27c**. Interestingly, in that case the desired product was obtained in 54%. Therefore, the methoxy groups of

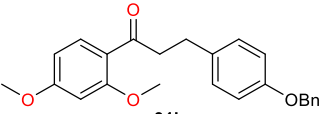
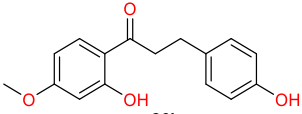
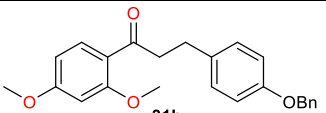
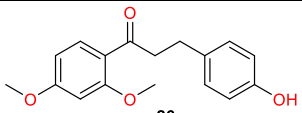
chalcone **27b** could interfere with the reaction. An attempt to lower the reaction temperature and time led to the isolation of the desired product **31b** in only 20 % yield. Furthermore, the monitoring of the reaction showed the formation of the completely reduced product. Considering these results, we have decided to try out milder reductive conditions based on chalcone *in situ* hydrogenation.^[6] Thus, hydrogenation with Et₃SiH and 0.5 equivalents of Pd/C 10 % in EtOAc/MeOH resulted in the formation of the desired product in 77% yield (Table 2-8).

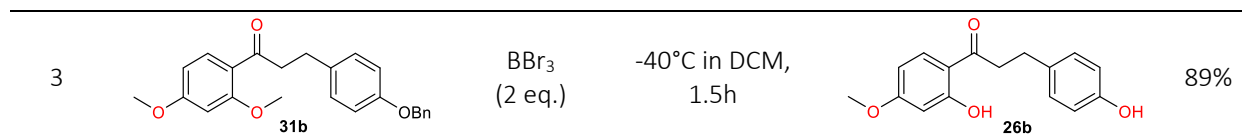
Table 2-8. Reduction of the double bond of chalcone **27b** and **27c**.

Entry	Substrate	Reagents	Reaction conditions	Time	Outcome	Yield
1		Et ₃ SiH, TFA	rt in CH ₂ Cl ₂	45h		54%
2		Et ₃ SiH, TFA	rt in CH ₂ Cl ₂	o/n		40%
3		Et ₃ SiH, TFA	0°C in CH ₂ Cl ₂	2h		20%
4		Et ₃ SiH, Pd/C 10% (0.5 eq)	r.t in EtOAc, MeOH	30 min		77%

Having successfully obtained **31b**, we focused our attention on the debenzylation reaction. At first, we selected to use BBr₃ as a deprotecting agent, aware of the possibility that also the methoxy groups could be removed. The first attempt to remove the benzyl group with BBr₃ at -10°C for 15 minutes resulted in the formation of product **26b**, lacking one of the methoxy groups in ortho position, in 64% yield. Reducing the number of equivalents of BBr₃ and the temperature led to the formation of initially desired product **26**, however only in 23% yield.

Table 2-9. Debenzylation reaction of compound **31**.

Entry	Substrate	Reagents	Reaction conditions	Outcome	Yield
1		BBr ₃ (10 eq.)	-10°C in DCM, 15 min		64%
2		BBr ₃ (0.3 eq)	-78°C in DCM, 40 min		23%



Eventually, we have decided to proceed the synthesis with the compound **26b**, as lower reactivity of the sterically hindered demethylated hydroxyl group could be expected. By carefully adjusting the reaction conditions, **26b** could be obtained in 89% yield (Table 2-9).

Though compound **26b** was chosen to continue with the synthesis, further literature search prompted us to perform additional trials of hydrogenation reaction, in order to optimize the synthetic pathway. Thus, a hydrogenation reaction in DCM as a solvent allowed to obtain both compounds **26** and **31b**. Furthermore, the ratios of the isolated products depended on the reaction time (Table 2-10). Therefore, this approach could be a useful alternative either for one-step or two step pathways to obtain the debenzylated dihydrochalcone.

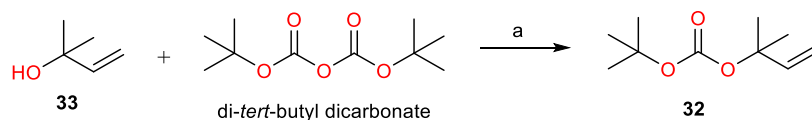
Table 2-10. Optimized hydrogenation conditions of **27b**.

Entry	Substrate	Reagents	Reaction conditions	Time	Outcome
1		H ₂ , Pd/C 10% (0.5 eq)	rt, CH ₂ Cl ₂	24h	 26, 42% 31b, 32%
2		H ₂ , Pd/C 10% (0.5 eq)	rt, CH ₂ Cl ₂	36h	 26, 55% 31b, 17%

2.2.3.4 Synthesis of prenylated intermediate 25

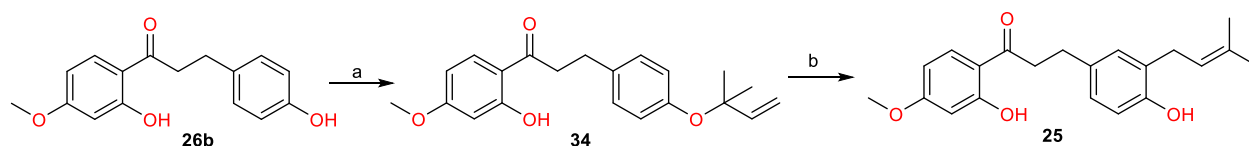
The synthesis of compound **25** involves a nucleophilic attack of the reverse-prenylation to the hydroxylic function via a Tsuji-Trost-type etherification, followed by a Claisen rearrangement.

The reverse-prenylation agent **32** was synthesized through the reaction between dimethyl vinyl carbinol **33** and di-tert-butyl dicarbonate in THF, giving the desired product in 55% yield (Scheme 2-15).



Scheme 2-15. Reaction conditions: a) n-BuLi, THF, -40°C to 0°C, 3,5 h, 55%.

The isolated **32** was then used in a Tsuji-Trost-type etherification of **26b** in the presence of



Scheme 2-16. Reaction conditions: a) **32**, Pd[P(Ph)₃]₄, THF, 0°C to rt, 72h, **34** 67%; b) N,N-diethylaniline, microwave, 250°C, 1h, **25** 10%.

catalytic amount of Pd[P(Ph)₃]₄, furnishing the aryl reverse-prenyl ether **34** in 67% yield. The latter was then subjected to the Claisen rearrangement to obtain **25** (Scheme 2-16).

Table 2-11. Trials of the reverse-prenylation reaction.

Entry	32 equiv.	Reaction time	Yield
1	1.5	4.5 h	-
2	2	40 h	12%
3	2	48 h	15%
4	2	72 h	67%

It is worth noting that product **34** was prone to degradation during the purification step via silica-gel chromatography and the first attempts to obtain the product resulted in low yields (Table 2-11). This problem could be solved by increasing

the reaction time and lowering the amount of silica used for the purification step.

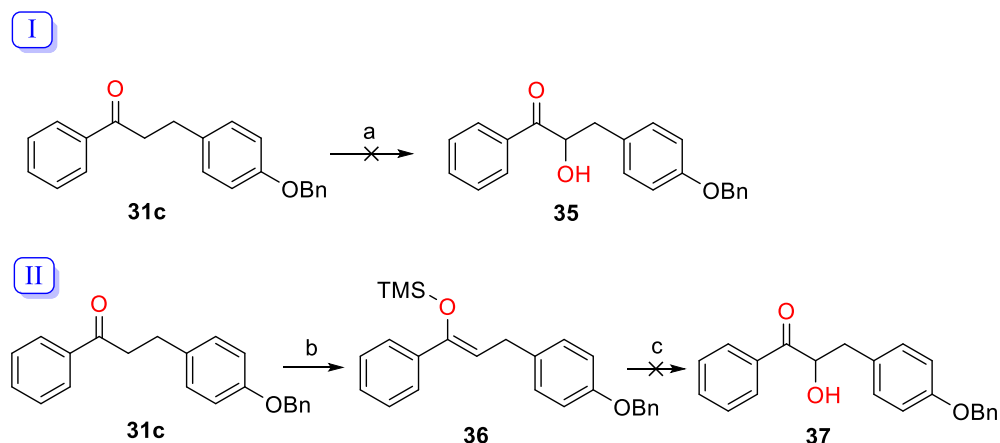
In its turn, the step of Claisen rearrangement was initially attempted by simply heating compound **34** in toluene at reflux. However, the reaction didn't occur and only starting material was recovered. The use of Eu(Fod)₃ as a catalyst resulted in the formation of **27b**. Finally, conducting the reaction in the microwave at 250°C gave the desired product, which was isolated in 10% yield.

Table 2-12. Trials of the Claisen rearrangement reaction done.

Entry	Reaction conditions	Reaction time	Catalyst	Yield	Comments
1	Toluene, reflux	13 h	-	-	Starting material recovered
2	Toluene, reflux	4 h	Eu(Fod) ₃	-	Obtained product 27b
3	N,N-diethylaniline, microwave, 250°C	1 h	-	10%	

2.2.3.5 Trials of alfa-hydroxylation reaction

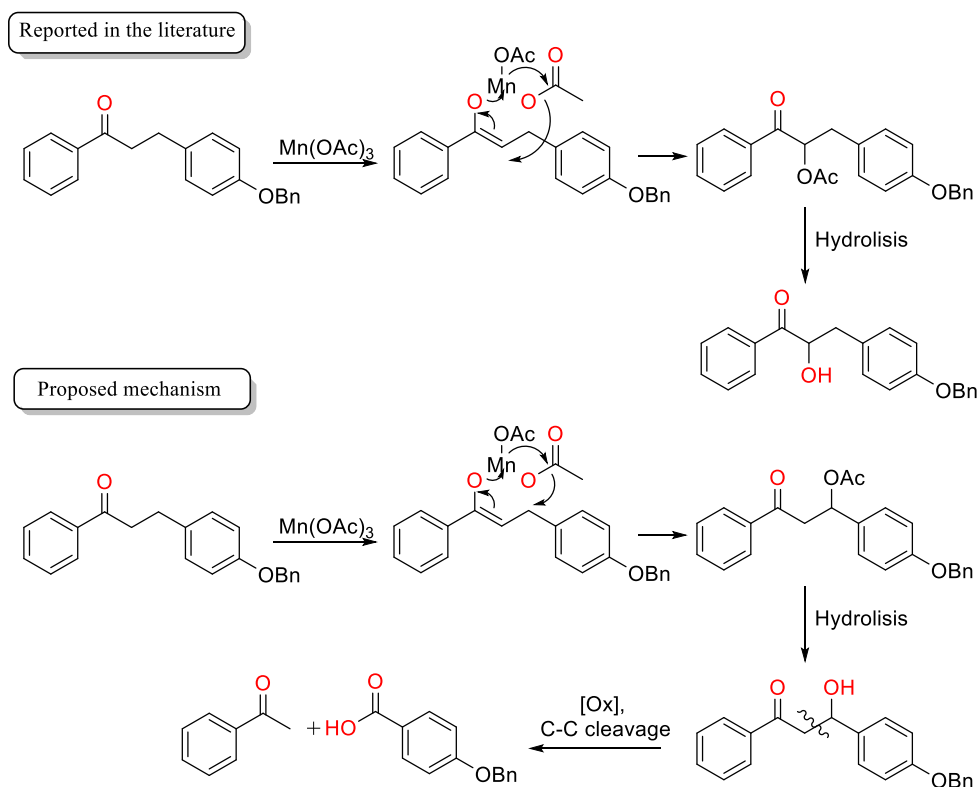
The α -hydroxylation reaction is the crucial step of the total synthesis towards glycybridin B.



Scheme 2-17. Reaction conditions: a) $\text{Mn}(\text{OAc})_3$, chloroacetic acid, toluene, reflux, 64h, b) LiHDMS , TMSCl , THF, 0°C to rt, 3,5h; c) $m\text{-CPBA}$, NaHCO_3 , CH_2Cl_2 , 0°C to rt, 6h.

First, the reaction was carried out using an analogue substrate **31c**, to investigate the feasibility of the reaction.

In the first attempt with $\text{Mn}(\text{OAc})_3$ and chloroacetic acid, only a degraded molecule which structure is reported in Figure 2-12, as confirmed by mass analysis. To explain the formation



Scheme 2-18. Mechanism of α -hydroxylation reaction reported in the literature and proposed.

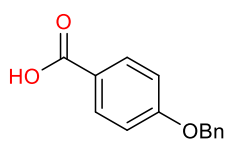


Figure 2-12. The structure of the degraded product of **31c**.

of this degraded product, we analysed the mechanism of the reaction reported in literature.^[7] At this stage we proposed a new mechanism considering the product obtained from the reaction (Scheme 2-18). We suppose that after the formation of the Mn complex with the carbonyl group, the acetate group is transferred to the β position, which is much more prone to oxidation. After that the acetate get hydrolysed, and further oxidation, followed by C-C cleavage, leads to the formation of the degraded product.

In the second attempt, we have decided to try out the Rubottom oxidation reaction (Scheme 2-17II). This reaction passes through the formation of the silyl-enol ether **36**, then without any purifications, which then gets epoxidized with meta-chloroperoxybenzoic acid (m-CPBA), and the resulted epoxide would rearrange to the α -hydroxy ketone **37**. In this case we could only obtain the starting material as outcome of the reaction, probably because of the instability of the silyl-enol ether. Further attempts to perform the alfa-hydroxylation reaction are ongoing in our research group.

Evaluation of the key intermediates

The intermediate compounds **25**, **26b**, **27b** and **34** were submitted for X-ray crystallography evaluation at Paul Scherrer Institut, Switzerland and biochemical evaluation at CSIC, Spain. Although binding in the maytansine site was not detected for any of the compounds, compound **25** showed a slight destabilizing effect on tubulin (Figure 2-13).

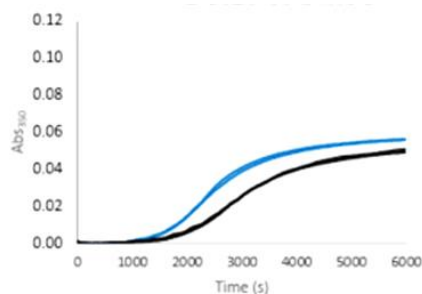


Figure 2-13. Inhibition of tubulin assembly by compound **25**. All experiments were performed as duplicates of two independent experiments. The curve of the control of DMSO is shown in blue, the curve of the compound is shown in black.

2.2.4 EXPERIMENTAL PART

Chemistry

General Experimental Procedures

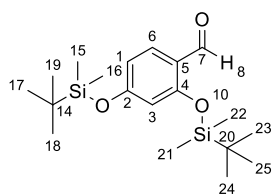
Unless otherwise stated, reagents were purchased from general suppliers (Sigma Aldrich and Fluorochem) and used without further purification. All solvents were of reagent grade or HPLC grade. All reactions were carried out in oven-dried glassware and dry solvents, under nitrogen atmosphere and were monitored by glasses or aluminium TLC on silica gel (Merck precoated 60F254 plates), with detection by UV light (254 nm), or by TLC stains as permanganate or p-anisaldehyde stain.

Purification of intermediates and final products was mostly carried out by flash chromatography using as stationary phase high purity grade silicagel (Merck Grade, pore size 60 Å, 230-400 mesh particle size, Sigma Aldrich). Alternatively, purification was performed by a Biotage® system in normal phase using Biotage® Sfär Silica D cartridges (10/25 g).

¹H NMR and ¹³C-NMR spectra were recorded on a Bruker Avance Spectrometer 400 MHz using commercially available deuterated solvents (chloroform-d, methanol-d₄) at room temperature. Chemical shifts (δ) are reported in parts per million (ppm) and are reported relative to TMS, used as an internal standard. Data for ¹H NMR are reported as follows: chemical shift (δ/ppm), multiplicity, coupling constants (Hz). Multiplicities are reported as follows: s = singlet, d = doublet, t = triplet, m = multiplet, br s = broad singlet. Data for ¹³C NMR are reported in terms of chemical shift (δ/ppm).

Synthesis of 2,4-bis((tert-butyl dimethylsilyl)oxy)benzaldehyde, 30a:

To a stirred solution of 2,4-dihydroxybenzaldehyde (1g, 7.2 mmol, 1 eq.) in anhydrous CH₂Cl₂ (20 mL), DIPEA (1.52g, 15 mmol, 2.4 eq.) was added at rt. The reaction mixture was left stirring for 10 minutes at rt, then TBDMSCl (2.26g, 15 mmol, 2.4 eq.) was added at 0°C. After the complete dissolution of the reagent, the ice bath was removed, and the reaction mixture was stirred for 2 hours. Then the reaction mixture was extracted with 40 mL of water for two times, and with 40 mL of a NaHCO₃ saturated solution. The collected organic phase was dried over Na₂SO₄, filtered and the solvent was removed under rotary evaporation. The crude product was purified by flash chromatography on silica gel (Hexane:EtOAc 93:7) obtaining 1.91g (5.18 mmol) of compound **8a**, with an overall yield of 72%.

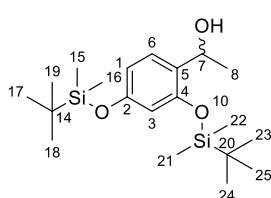


¹H NMR (400 MHz, chloroform-*d*) δ 10.33 (s, 1H, **H8**), 7.75 (d, 1H, **H6**), 6.55 (dd, 1H, **H1**), 6.33 (d, 1H, **H3**), 1.05 (s, 9H, **H23-H24-H25**), 1.03 (s, 9H, **H17-H18-H19**), 0.31 (s, 6H, **H21-H22**), 0.27 (s, 6H, **H15-H16**).

^{13}C NMR (101 MHz, chloroform-*d*) δ 188.83, 162.66, 160.71, 129.99, 122.00, 114.43, 111.10, 25.77, 25.67, 18.46, 18.38, 4.19

Synthesis of 1-(2,4-bis((tert-butyldimethylsilyl)oxy)phenyl)ethan-1-ol, 29a:

TBDMS protected aldehyde **30a** (1g, 2.7 mmol, 1 eq.) was dissolved in dry THF (13 mL), under nitrogen atmosphere. Methylmagnesium bromide (3M solution in Et₂O, 5.4 mmol, 1.8 mL, 2 eq.) was added dropwise to the reaction mixture at -78°C. After 15 minutes, the reaction mixture was warmed to room temperature and left stirring for 1 hour and 30 minutes, upon completion of the reaction monitored by TLC. The reaction was quenched with a sat. aq. of NH₄Cl (15 mL). THF was removed under rotary evaporation, and the resulted aqueous phase was extracted two times with CH₂Cl₂ (20 mL). The combined organic phases were dried over Na₂SO₄, filtered and the solvent removed under rotary evaporation. The product **29a** was obtained without any purifications in 85% yield.

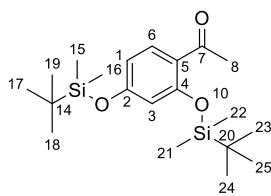


^1H NMR (400 MHz, chloroform-*d*) δ 7.23 (d, 1H, **H6**), 6.48 (dd, 1H, **H1**), 6.34 (d, 1H, **H3**), 5.12 (q, 1H, **H7**), 1.48 (d, 3H, **H8**), 1.04 (s, 9H, **H23-H24-H25**), 1.00 (s, 9H, **H17-H18-H19**), 0.31 (s, 6H, **H21-H22**), 0.22 (s, 6H, **H15-H16**).

^{13}C NMR (101 MHz, chloroform-*d*) δ 188.83, 162.66, 160.71, 129.99, 122.00, 114.43, 111.10, 25.77, 25.67, 18.46, 18.38, 4.19

Synthesis of 1-(2,4-bis((tert-butyldimethylsilyl)oxy)phenyl)ethan-1-one, 28a:

TBDMS protected alcohol **29a** (415mg, 1.08 mmol, 1 eq.) was dissolved in dry CH₂Cl₂ (5mL) at room temperature under vigorous stirring. After 10 minutes Dess-Martin periodinane was added, observing the formation of a milky solution. After 1 hour and 30 minutes the reaction mixture was diluted with 5 mL of CH₂Cl₂ and washed with a sat. aq. solution of Na₂S₂O₃ (12 mL), and then with a sat. aq. solution of NaHCO₃ (12 mL). The extract was dried over Na₂SO₄, filtered and the solvent removed under rotary evaporation. The crude product was purified by flash chromatography on silica gel (Hexane:EtOAc 90:10) obtaining 304 mg (0.8 mmol) of compound **5a**, with an overall yield of 75%.



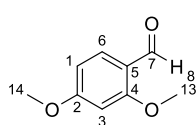
^1H NMR (400 MHz, chloroform-*d*) δ 7.65 (d, 1H, **H6**), 6.50 (dd, 1H, **H1**), 6.35 (d, 1H, **H3**), 2.60 (s, 3H, **H8**), 1.03 (s, 9H, **H23-H24-H25**), 1.01 (s, 9H, **H17-H18-H19**), 0.32 (s, 6H, **H21-H22**), 0.25 (s, 6H, **H15-H16**).

^{13}C NMR (101 MHz, chloroform-*d*) δ 198.78, 160.06, 156.81, 132.57, 124.45, 113.57, 111.92, 31.30, 27.37, 25.75, 18.54, -3.85, -4.69.

Synthesis of 2,4-dimethoxybenzaldehyde, 30b:

2,4-Dihydroxybenzaldehyde (2g, 14.5 mmol, 1 eq.) was dissolved in dry acetone (72.5 mL) and then methyl iodide (4.6g, 32.5 mmol, 2 mL, 2.25 eq.) and K₂CO₃ (6g, 43.4 mmol, 3 eq.)

were added. The temperature was brought to 60°C (acetone reflux). After 5 hours EtOAc was added to the reaction mixture, and then it was washed with sat. aq. solution of Na₂S₂O₃, H₂O and brine. The organic phase was dried over Na₂SO₄, filtered, and the solvent removed under rotary evaporation. The crude product was purified by recrystallization in EtOH, obtaining 2.24g (13.5 mmol) of pure compound **30b** in 93% yield.

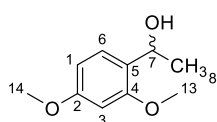


¹H NMR (400 MHz, chloroform-*d*) δ 10.24 (s, 1H, **H8**), 7.75 (d, 1H, **H6**), 6.49 (dd, 1H, **H1**), 6.40 (d, 1H, **H3**), 3.85 (s, 3H, **H13**), 3.83 (s, 3H, **H14**).

¹³C NMR (101 MHz, chloroform-*d*) δ 188.19, 166.19, 163.60, 130.53, 118.92, 105.85, 97.80, 55.58, 55.55.

Synthesis of 1-(2,4-dimethoxyphenyl)ethan-1-ol, **29b**:

Aldehyde **30b** (2g, 12 mmol, 1 eq.) was dissolved in dry THF (26 mL). Methylmagnesium bromide (3M solution in THF, 8 mL, 24 mmol, 2 eq.) was carefully added dropwise at -70°C to the reaction mixture. After 10 minutes the bath was removed, and the reaction mixture was left stirring at room temperature for 3 h. The reaction was quenched with a sat. aq. solution of NH₄Cl, then the THF was evaporated under reduced pressure. 10 mL of brine were added, and the resulted aqueous phase was extracted with CH₂Cl₂ (2 times 20mL). The collected organic phases were dried over Na₂SO₄, filtered, and concentrated under rotary evaporation. The crude product was purified by flash chromatography on silica gel (Hexane:EtOAc 80:20) obtaining 1.93 g (10.6 mmol) of compound **29b**, with an overall yield of 88%.

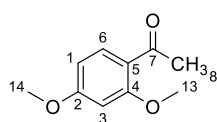


¹H NMR (400 MHz, chloroform-*d*) δ 7.28 (d, 1H, **H6**), 6.52 (dd, 1H, **H1**), 6.50 (d, 1H, **H3**), 5.07 (t, 1H, **H7**), 3.87 (s, 3H, **H13**), 3.84 (s, 3H, **H14**), 1.52 (d, 3H, **H8**).

¹³C NMR (101 MHz, chloroform-*d*) δ 159.7, 157.9, 127.2, 126.7, 104.2, 99.4, 68.83, 55.3, 55.2, 22.9

Synthesis of 1-(2,4-dimethoxyphenyl)ethan-1-ol, **29b**:

Alcohol **29b** (130 mg, 0.71 mmol, 1 eq.) was dissolved in dry CH₂Cl₂ (3 mL) at room temperature. Then, Dess-Martin periodinane (605 mg, 1.43 mmol, 2 eq.) was added under stirring using a drying tube. The reaction mixture was left reacting under vigorous stirring for 2 hours. After that the reaction mixture was diluted with CH₂Cl₂ (3 mL) and washed with a sat. aq. solution of Na₂S₂O₃, and then with a sat. aq. solution of NaHCO₃. The organic extract was dried over Na₂SO₄, filtered, and concentrated under rotary evaporation. The crude product was purified by flash chromatography on silica gel (Hexane:EtOAc 90:10) obtaining 78 mg (0.43 mmol) of compound **28b**, with an overall yield of 61%.

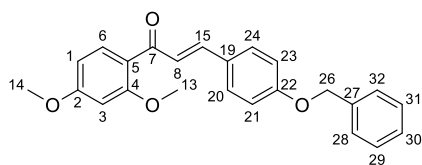


$^1\text{H-NMR}$ (400 MHz, chloroform-*d*) δ $^1\text{H-NMR}$ (400 MHz, CDCl_3): δ 7.85 (d, 1H, **H6**), 6.54 (dd, 1H, **H1**), 6.48 (d, 1H, **H3**), 3.91 (s, 3H, **H13**), 3.87 (s, 3H, **H14**), 2.59 (s, 3H, **H8**).

$^{13}\text{C-NMR}$ (101 MHz, chloroform-*d*) δ 197.77, 164.55, 161.11, 132.68, 121.22, 105.08, 98.33, 55.52, 55.45, 31.83

Synthesis of (2E)-3-(4-(benzyloxy)phenyl)-1-(2,4-dimethoxyphenyl)prop-2-en-1-one, **27b**:

A solution of 4-benzyloxybenzaldehyde (3.5 g, 16.7 mmol, 1 eq.) and ketone **28b** (3 g, 16.7 mmol, 1 eq.) in EtOH and THF (respectively 42.6 mL and 35 mL) was added dropwise to a solution of NaOH (6.12 g, 153 mmol, 13.8 eq.) in EtOH and H_2O (respectively 23.8 mL and 14.5 mL). The reaction was left reacting under stirring at 40°C for 28 hours. The reaction mixture was cooled down to room temperature, and then ice was added observing the precipitation of a yellow solid. The solid product was filtered with Buckner, and 5.4 g of the pure product **27b** were isolated, with an overall yield of 64%.



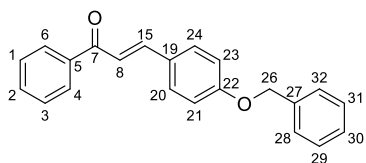
$^1\text{H-NMR}$ (400 MHz, chloroform-*d*) δ 7.74 (d, 1H, **H6**), 7.67 (d, 1H, **H15**), 7.62 (d, 2H, **H20-H24**), 7.48 (d, 1H, **H8**), 7.45 (m, 2H, **H28-H32**), 7.42 (t, 2H, **H29-H31**), 7.39 (t, 1H, **H30**), 7.05 (m, 2H, **H21-H23**), 6.61 (dd, 1H, **H1**), 6.57 (d, 1H, **H3**),

5.15 (s, 2H, **H26**), 3.94 (s, 3H, **H13**), 3.91 (s, 3H, **H14**).

$^{13}\text{C-NMR}$ (400 MHz, chloroform-*d*) δ 190.65, 164.76, 161.10, 161.01, 142.03, 137.42, 133.15, 130.71, 130.60, 129.26, 128.78, 128.25, 125.95, 124.32, 122.51, 115.89, 115.79, 105.98, 99.13, 70.69, 56.43, 56.20

Synthesis of (2E)-3-(4-(benzyloxy)phenyl)-1-phenylprop-2-en-1-one, chalcone **27c**:

A solution of 4-Benzyloxybenzaldehyde (441 mg, 2.08 mmol, 1 eq.) and acetophenone (250 mg, 2.08 mmol, 1 eq.) in EtOH (4 mL) and THF (2,5 mL) was added dropwise to a solution of NaOH (383 mg, 9.57 mmol, 4.6 eq.) in H_2O (4 mL) and EtOH (2 mL). The reaction mixture was left stirring at 40°C for 2 hours. The reaction mixture was acidified with a sat. aq. solution of NH_4Cl , and a bright yellow solid was precipitated. The solid was filtered and washed with cold water, and in the end dried under vacuum. The crude solid obtained was purified by flash chromatography on silica gel (Hexane:EtOAc 90:10) obtaining 523 mg (1.66 mmol) of chalcone **27c**, with an overall yield of 80%.

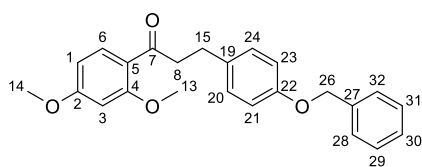


$^1\text{H-NMR}$ (400 MHz, chloroform-*d*) δ 8.05 (m, 2H, **H4-H6**), 7.82 (d, 1H, **H15**), 7.64 (d, 2H, **H20-H24**), 7.53 (d, 1H, **H2**), 7.50 (d, 1H, **H8**), 7.43 (m, 2H, **H1-H3**), 7.41 (d, 2H, **H28-H32**), 7.39 (m, 1H, **H30**), 7.37 (d, 2H, **H29-H31**), 7.05 (d, 2H, **H21-H23**), 5.15 (s, 2H, **H26**).

$^{13}\text{C-NMR}$ is in accordance with the literature.

Synthesis of 3-(4-(benzyloxy)phenyl)-1-(2,4-dimethoxyphenyl)propan-1-one, 31b:

To a solution of chalcone **27b** (1.31 g, 3.51 mmol, 1 eq.) in dry EtOAc and MeOH (respectively 25 mL and 12.5 mL) was added Pd/C (80 mg, 10%). Et₃SiH (2.04 g, 17.5 mmol, 2.81 mL, 5 eq.) was slowly added to the reaction mixture, and after complete addition, the reaction was kept at room temperature for 1h (it was observed the formation of H₂ bubbles and the disappearance of the light-yellow colour). Then the catalyst was filtered over celite, and the solvents were removed at reduced pressure. The crude mixture obtained was purified by flash chromatography on silica gel (Hexane:EtOAc 85:15) obtaining 1.02 g (2.7 mmol) of ketone **31b**, with an overall yield of 77%.

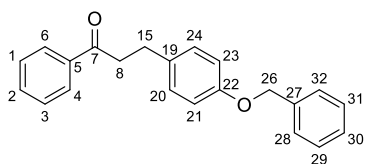


¹H-NMR (400 MHz, chloroform-*d*): δ 7.85 (d, 1H, **H6**), 7.45 (m, 2H, **H28-H32**), 7.39 (m, 2H, **H29-H31**), 7.33 (m, 1H, **H30**), 7.18 (d, 2H, **H20-H24**), 6.93 (d, 2H, **H21-H23**), 6.54 (dd, 1H, **H1**), 6.48 (d, 1H, **H3**), 5.07 (s, 2H, **H26**), 3.89 (s, 3H, **H13**), 3.88 (s, 3H, **H14**), 3.26 (t, 2H, **H8**), 2.98 (t, 2H, **H15**).

¹³C-NMR (400 MHz, chloroform-*d*) δ 200.23, 165.04, 161.43, 157.73, 137.94, 135.05, 133.44, 130.07, 129.17, 128.55, 128.09, 121.81, 115.45, 105.73, 99.03, 70.74, 56.18, 56.13, 46.23, 30.48.

Synthesis of 3-(4-(benzyloxy)phenyl)-1-phenylpropan-1-one, 31c:

To a solution of chalcone **27c** (150 mg, 0.477 mmol, 1 eq.) in dry CH₂Cl₂ (3.2 mL) was added trifluoroacetic acid (354 mg, 3.1 mmol, 0.24 mL, 6.5 eq.) and Et₃SiH (56 mg, 0.477 mmol, 0.08 mL, 1 eq.). The reaction mixture was left stirring at room temperature overnight. After 24 h it was added 4.3 eq. of trifluoroacetic acid and 2 eq. of Et₃SiH. After 30 h another 4.3 eq. of trifluoroacetic acid and 2 eq. of Et₃SiH were added. Trifluoroacetic acid was removed at reduced pressure, and then the reaction mixture was washed with 8 mL of water. The aqueous phase was further extracted with CH₂Cl₂ (2X 10 mL). The collected organic phases were dried over Na₂SO₄, filtered and the solvent removed under rotary evaporation. The crude mixture obtained was purified by flash chromatography on silica gel (Hexane:EtOAc 90:10) obtaining 81 mg (0.25 mmol) of ketone **31c** in 54% yield.

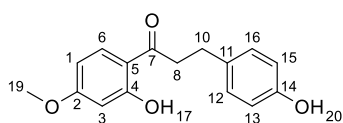


¹H-NMR (400 MHz, chloroform-*d*) δ 7.99 (m, 2H, **H4-H6**), 7.59 (t, 1H, **H2**), 7.50 (d, 2H, **H1-H3**), 7.45 (m, 2H, **H28-H32**), 7.41 (m, 2H, **H29-H31**), 7.35 (t, 1H, **H30**), 7.20 (d, 2H, **H20-H24**), 6.95 (d, 2H, **H21-H23**), 5.08 (s, 2H, **H26**), 3.31 (t, 2H, **H8**), 3.05 (t, 2H, **H15**).

¹³C NMR is in accordance with the literature.

Synthesis of 1-(2-hydroxy-4-methoxyphenyl)-3-(4-hydroxyphenyl)propan-1-one, 26b:

A solution of ketone **31b** (770 mg, 2.04 mmol, 1 eq.) in dry CH₂Cl₂ (30 mL) was treated at -40°C with BBr₃ (1 M in CH₂Cl₂, 4.08 ml, 4.08 mmol, 2 eq.). The reaction mixture was stirred at -40°C for 1 h and 30 min. The reaction was quenched with water and the two phases were separated. Then the aqueous phase was further extracted with Et₂O for 3 times. The collected organic phases were dried over Na₂SO₄, filtered and the solvent was removed under rotary evaporation. The crude mixture was purified by a flash purification on Biotage (Direct Phase, Sfar Silica D (80 g) cartridge, Hexane/EtOAc 97:3 to 75:25), obtaining 494 mg of ketone **26b** in 89% yield.

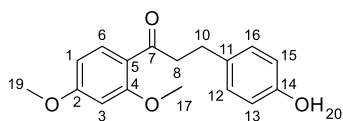


¹H-NMR (400 MHz, chloroform-*d*) δ 12.85 (s, 1H, **H17**), 7.66 (d, 1H, **H6**), 7.14 (d, 2H, **H12-H16**), 6.80 (d, 2H, **H13.H15**), 6.45 (d, 1H, **H3**), 6.43 (m, 1H, **H1**), 5.11 (s, 1H, **H20**), 3.87 (s, 3H, **H19**), 3.23 (t, 2H, **H8**), 3.01 (t, 2H, **H10**).

¹³C-NMR (400 MHz, chloroform-*d*) δ 203.99, 166.05, 165.34, 154.12, 132.84, 131.60, 129.51, 115.46, 113.44, 107.80, 100.99, 55.62, 40.00, 29.62.

Synthesis of 1-(2,4-dimethoxyphenyl)-3-(4-hydroxyphenyl)propan-1-one, 26 and 3-(4-(benzyloxy)phenyl)-1-(2,4-dimethoxyphenyl)propan-1-one, 31b, via hydrogenation reaction:

To a deoxygenated solution of the chalcone **27b** (150 mg, 0.4 mmol) in DCM (20 mL) 10% was added Pd/C (0.5 eq.) The reaction flask was thrice evacuated and flushed with hydrogen gas and the resulting mixture was stirred at room temperature under hydrogen atmosphere. After 24 h, the mixture was filtered through a Celite® pad and the solvent was removed under reduced pressure. The reaction mixture was purified on Biotage (Direct Phase, Sfar Silica D (12 g) cartridge, Hexane/EtOAc gradient), obtaining **26b** in 42% yield and mg of **31b** in 32% yield.



¹H-NMR (400 MHz, chloroform-*d*) δ 7.80 (d, *J* = 8.7 Hz, **H6**), 7.14 (d, 2H, **H12-H16**), 6.79 (d, 2H, **H13.H15**), 6.53 (dd, *J* = 8.7, 2.3 Hz, 5H), 6.45 (d, *J* = 2.3 Hz, 1H, **H1**), 5.1 (bs, 1H, **H20**), 3.86 (d, *J* = 5.7 Hz, 6H, **H17,H19**), 3.23 (t, 2H, **H8**), 2.93 (t, 2H, **H10**).

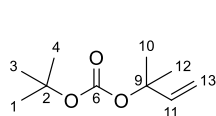
¹³C-NMR (400 MHz, chloroform-*d*) δ 199.55, 164.09, 160.92, 153.87, 134.22, 132.93, 129.69, 115.34, 105.28, 98.53, 55.68, 55.62, 45.70, 29.93.

The ¹H-NMR and ¹³C-NMR of **31b** are as described above.

Synthesis of tert-butyl (2-methylbut-3-en-2-yl) carbonate, 32:

To a solution of *n*-Buthyl lithium (1.6M, 11.6 mmol, 7.5 mL, 1 eq.) in hexane was added dropwise a solution of 2-Methyl-3-buten-2-ol (1 g, 11.6 mmol, 1.21 mL, 1 eq.) in dry THF (23 mL) at -40°C. The resulted mixture was stirred for 20 minutes, then a solution of Boc₂O (2M, 11.6 mmol, 5.8 mL, 1 eq.) in THF was added to the reaction mixture. The reaction was

warmed at 0°C and left reacting for 3 hours and 30 minutes. Then the reaction was quenched with a sat. aq. solution of NaHCO₃ and it was extracted with Et₂O. The collected organic layer was washed with H₂O and brine, and it was dried over Na₂SO₄. The solvent was removed under rotary evaporation. The crude mixture obtained was purified by flash chromatography on silica gel (Hexane:EtOAc 95:5) obtaining 1.178 g (6.38 mmol) of carbonate **32** in 55% yield.

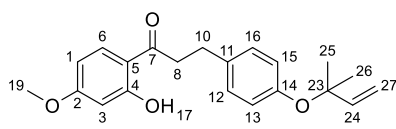


¹H-NMR (400 MHz, chloroform-*d*) δ 6.13 (dd, 1H, **H11**), 5.18 (m, 2H, **H13**), 1.56 (s, 6H, **H10-H12**), 1.49 (s, 9H, **H1-H3-H4**).

¹³C NMR is in accordance with the literature*

Synthesis of 1-(2-hydroxy-4-methoxyphenyl)-3-(4-((2-methylbut-3-en-2-yl)oxy)phenyl)propan-1-one, **34**:

To a solution of Pd[P(Ph)₃]₄ (84 mg, 0.073 mmol, 0.2 eq.) in dry THF (0.9 mL) was added ketone **26b** (100 mg, 0.367 mmol, 1 eq.) and carbonate **32** (137 mg, 0.734 mmol, 2 eq.) dropwise at 0°C. The reaction was warmed at room temperature and stirred for 72h. Then the solvent was removed under rotary evaporation without the heating bath. The crude mixture obtained was purified by flash chromatography on silica gel (Hexane:EtOAc 85:15), using only half of the amount of silica respect to standard purifications, obtaining 83.6 mg (0.24 mmol) of reverse-prenylated ketone **34** in 67% yield.



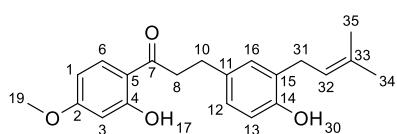
¹H-NMR (400 MHz, chloroform-*d*) δ 12.85 (s, 1H, **H17**), 7.64 (d, 1H, **H6**), 7.10 (d, 2H, **H12-H16**), 6.93 (d, 2H, **H13-H15**), 6.43 (d, 1H, **H3**), 6.41 (d, 1H, **H1**), 6.15 (dd, 1H, **H24**), 5.16 (m, 2H, **H27**), 3.84 (s, 3H, **H19**), 3.21 (t, 2H, **H8**), 3.00 (t, 2H, **H10**), 1.45 (s, 6H, **H25-H26**).

¹³C-NMR (400 MHz, chloroform-*d*) δ 204.45, 166.65, 166.06, 154.96, 145.07, 135.24, 132.20, 129.29, 122.65, 114.07, 113.70, 108.29, 101.59, 80.05, 56.18, 40.49, 30.30, 27.56.

Synthesis of 3-(4-hydroxy-3-(3-methylbut-2-en-1-yl)phenyl)-1-(2-hydroxy-4-methoxyphenyl)propan-1-one, **25**:

A solution of isoprenylated ketone **34** (136 mg, 0.4 mmol, 1 eq.) in *N,N*-diethyl aniline (4 mL) was heated at 250°C in the microwave for 1 hour. After cooling, the reaction mixture was diluted with EtOAc and washed with 1M HCl to remove aniline. The organic layer was dried over Na₂SO₄, filtered, and the solvent was removed under rotary evaporation. The crude mixture was purified by a flash purification on Biotage

(Direct Phase, Sfar Silica D (10 g) cartridge, Hexane/EtOAc 97:3 to 70:30), obtaining 13 mg (0.04 mmol) of prenylated ketone **25** in 10% yield.



$^1\text{H-NMR}$ (400 MHz, chloroform-*d*) δ 12.87 (s, 1H, **H17**), 7.66 (d, 1H, **H6**), 7.02 (d, 1H, **H1**), 7.00 (d, 1H, **H3**), 6.77 (d, 1H, **H13**), 6.45 (d, 1H, **H16**), 6.43 (d, 1H, **H12**), 5.33 (t, 1H, **H32**), 5.12 (s, 1H, **H30**), 3.36 (s, 3H, **H19**), 3.22 (t, 2H, **H8**), 2.99 (t, 2H, **H10**), 1.80 (s, 6H, **H34-H35**).

$^{13}\text{C-NMR}$ (400 MHz, chloroform-*d*) δ 204.52, 166.66, 166.07, 153.40, 135.39, 133.63, 132.18, 130.59, 127.87, 127.60, 122.41, 116.47, 114.18, 108.29, 101.62, 56.21, 40.74, 30.49, 30.35, 26.44, 18.54.

2.2.5 REFERENCES

- [1] G. Wolber, T. Langer, *J. Chem. Inf. Model.* **2005**, *45*, DOI 10.1021/ci049885e.
- [2] K. Li, S. Ji, W. Song, Y. Kuang, Y. Lin, S. Tang, Z. Cui, X. Qiao, S. Yu, M. Ye, *J. Nat. Prod.* **2017**, *80*, DOI 10.1021/acs.jnatprod.6b00783.
- [3] Y. Kuang, Y. Lin, K. Li, W. Song, S. Ji, X. Qiao, Q. Zhang, M. Ye, *Phytomedicine* **2017**, *34*, DOI 10.1016/j.phymed.2017.08.005.
- [4] Y. Lin, Y. Kuang, K. Li, S. Wang, W. Song, X. Qiao, G. Sabir, M. Ye, *Bioorganic Med. Chem.* **2017**, *25*, DOI 10.1016/j.bmc.2017.05.009.
- [5] W. Liu, M. He, Y. Li, Z. Peng, G. Wang, *J. Enzyme Inhib. Med. Chem.* **2022**, *37*, DOI 10.1080/14756366.2021.1976772.
- [6] A. R. Jesus, A. P. Marques, A. P. Rauter, in *Pure Appl. Chem.*, **2016**.
- [7] A. S. Demir, N. Camkerten, Z. Gercek, N. Duygu, O. Reis, E. Arıkan, *Tetrahedron* **1999**, *55*, DOI 10.1016/S0040-4020(99)00036-8.

2.3 SYNTHESIS OF SIMPLIFIED BIOTINYLATED PIRONETIN ANALOGUES

Abstract: Covalent probes are characterized by prolonged duration of action, improved potency, and exquisite selectivity. Moreover, they could be used e.g., to immobilize the protein of interest, tubulin. With this aim, we have considered possible pironetin, a natural product that covalently binds α -tubulin, and the possibility of its biotinylation to use then biotin capturing on streptavidin for protein immobilization. Taking into consideration the low availability and time-consuming synthesis of natural pironetin, we have envisioned and performed the synthesis of the simplified biotinylated pironetin analogues.

Declaration of contribution: My work comprised the design of the synthesized compounds in collaboration with the computational team represented by Helena Perez-Pena, the planning of the synthetic pathway and the performance of the synthetic work described. The X-ray crystallography experiments were performed by Anne-Catherine Abel.

2.3.1 INTRODUCTION

In the last decades, the rational design of covalent drugs has become increasingly popular. Many covalent drugs with a wide range of targets are used in clinics, including an anti-inflammatory aspirin, the proton pump inhibitor omeprazole or a tyrosine kinase inhibitor ibrutinib. As covalent drugs form strong and long-lasting bonds with their targets and remain bound to their targets for an extended period resulting, they are usual characterized by increased potency, target engagement and selectivity.^[1,2] At the same time, lack of reversibility could result in higher toxicity. While high cytotoxicity of covalent ligands sometimes precludes their application as drugs, they have found a great application as chemical probes. For instance, covalent ligands could be used to immobilize the protein of interest. An immobilized protein is a valuable tool in many assays for studying protein-protein and protein-ligand interactions, as its use allows for selective capture and detection of interacting molecules and provides a more detailed understanding of protein function and interactions. For instance, it can be used surface plasmon resonance (SPR) or grating-coupled interferometry screening, as well as the fabrication of functional protein microarrays, biosensors, or continuous flow reactor systems.^[3]

As described in Section 1.3.3, pironetin is the only ligand able to covalently target α -tubulin through the reaction of Michael addition between pironetin α,β -unsaturated δ -lactone and α Cys316. Over the years, many pironetin analogues have been synthesized. A series of simplified pironetin analogues was synthesized by Marco et al. in 2011 and 2013 (Figure 2-14A), however they were found less cytotoxic than pironetin itself by three orders of magnitude.^[4,5]

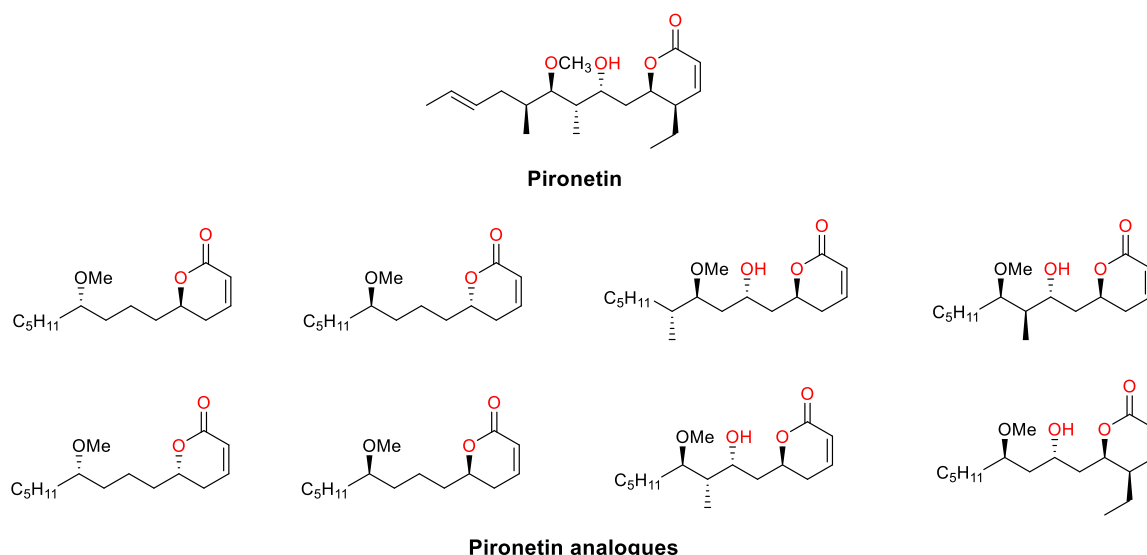


Figure 2-14A. Chemical structure of pironetin and examples of pironetin analogues previously synthesized.

Moreover, our research group synthesized a series of pironetin-dumetorine hybrids (Figure 2-14B), which have shown slight to moderate impact on microtubule formation.^[6]

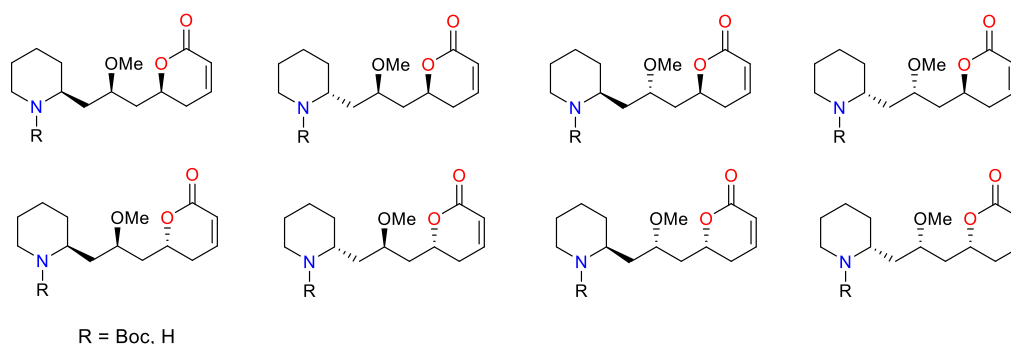


Figure 2-14B. Examples of pironetin-dumetorine hybrids previously synthesized in our group.

2.3.2 AIM OF THE PROJECT

Considering the application of covalent binders for protein immobilization and continuing the interest of our research group in pironetin, we have considered the potential of pironetin for tubulin immobilization. The unique location of the pironetin binding site at the bottom of the α/β -heterodimer could allow the biotinylation of the compound and use of biotin/streptavidin interaction to attach the tubulin the sensor chip surface (Figure 2-15). The biotinylation has been inspired by the previous experiments using biotinylated pironetin probes, which has shown that such modified pironetin is able to bind to tubulin.^[7]

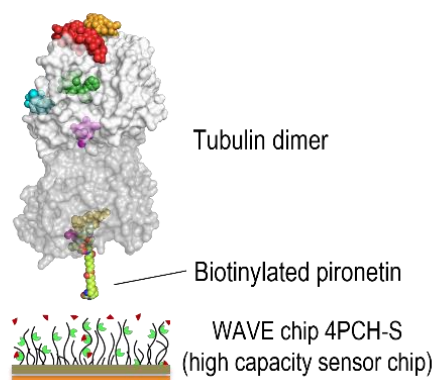


Figure 2-15. Schematic application of biotinylated pironetin for immobilization of tubulin on the streptavidin chip.

Up to date, a few total syntheses of pironetin have been proposed^[8–10], however the difficulties in forming the six centers stereoselectively have been underlined in all synthetic approaches described. For instance, Crimmins et al. proposed the enantioselective total synthesis of pironetin in 11 steps, with all the stereocenters formed by using Evan's chemistry and an overall yield of 12.5%.^[10]

Therefore, to facilitate the synthesis, in collaboration with computational team of Prof. Pieraccini, we have envisioned the synthesis of simplified pironetin analogues with only two stereogenic centers at C5 and C7. We have planned to maintain the same absolute conformation of the C5 as that of pironetin and synthesize two diastereomers, **38a** and **38b**, as the effect of the configuration at C7 position is not known. The simplified analogues would then be biotinylated to obtain **39a** and **39b**, which structure can be divided into three parts:

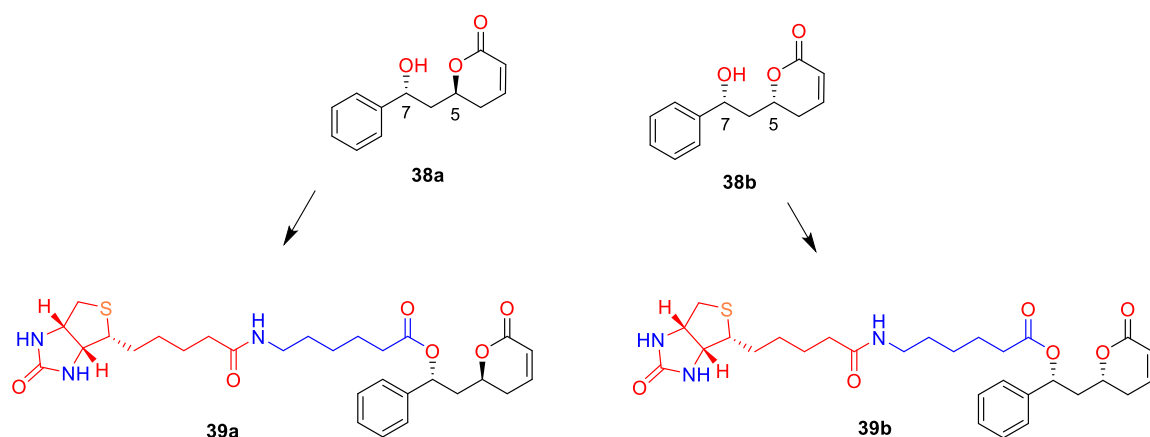


Figure 2-16. Chemical structures of the planned simplified pironetin analogues and their biotinylated derivatives.

the pironetin-like moiety, bearing the lactone moiety and an alkyl chain (in black); a C6 linker derived from ϵ -aminocaproic acid (in blue) and a biotin moiety (in red) (Figure 2-16).

The group of Prof. Pieraccini performed the non-covalent docking of the designed pironetin derivatives with Audock Vina^[11] using the crystal structure of pironetin-tubulin solved by Prota et al. (PDB ID: 5LA6).^[12] The results of the *in silico* investigation indicated that the optimal binding modes of the various pironetin derivatives depended on the positioning the lactone ring in a manner similar to the parent compound pironetin and suggested that these molecules could have the potential to covalently interact with α Cys316, similar to the way pironetin does.

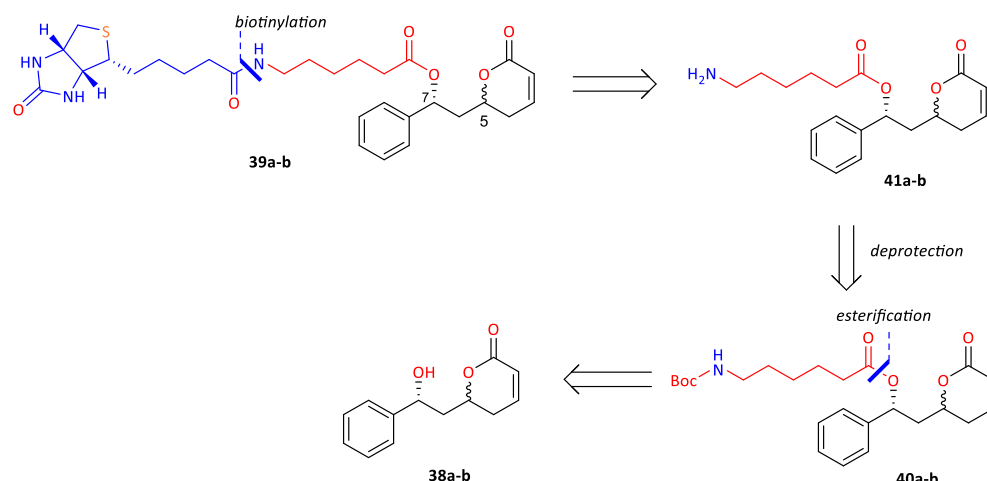
2.3.3 RESULTS AND DISCUSSION

Chemistry

2.3.3.1 Retrosynthetic pathway

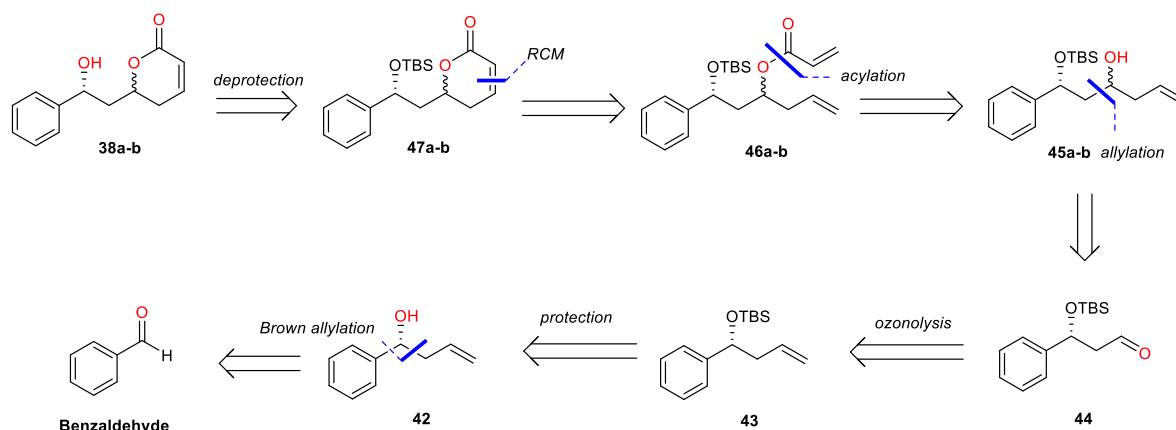
The final biotinylated derivatives **39a-b** can be synthesized from compounds **38a-b**, through the esterification with the appropriate linker and subsequent biotinylation, according to the retrosynthetic approach represented on Scheme 2-19.

Compounds **38a-b** can be synthesized via seven synthetic steps starting from benzaldehyde (Scheme 2-20). The lactone moiety of **38a-b** can be obtained through a ring closing metathesis reaction, RCM, from **46a-b**, followed by a deprotection of **47a-b**. Compound **46a-b** derives from the acylation of **45a-b**. The latter can be obtained either as a mixture of diastereoisomers by performing a symmetric allylation on aldehyde **44** or as a specific



Scheme 2-19. Retrosynthetic approach towards the synthesis of biotinylated derivatives **39a-b**.

diastereomer by stereoselective Brown allylation reaction. In its turn, the aldehyde **44** can be obtained in a result of ozonolysis reaction of **43**, which results from a tert-butyldimethylsilyl, TBDMS, protection of alcohol **42**. Finally, alcohol **42** derives from an asymmetric Brown allylation on commercially available benzaldehyde.

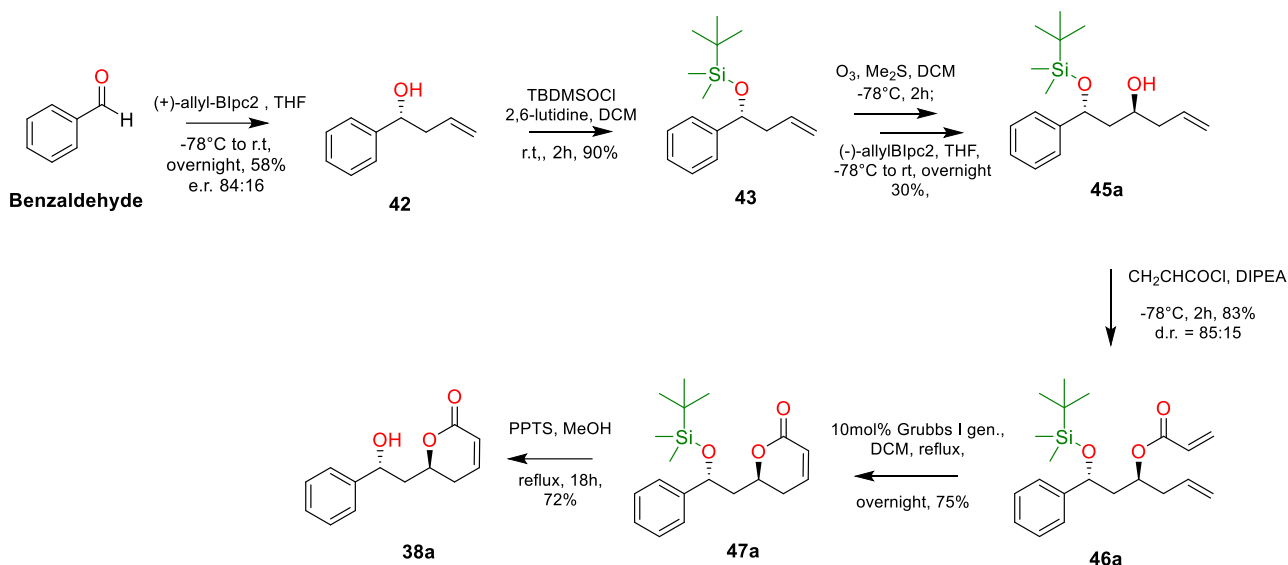


Scheme 2-20. Retrosynthetic approach towards the synthesis of simplified pironetin analogues **38a-b**.

2.3.3.2 Synthesis of simplified pironetin analogues **38a-b**

Initially, the synthesis of compound **38a** was performed in a fully stereoselective fashion, by applying the asymmetric Brown allylation reaction to furnish both stereogenic centers at C5 and C7 (Figure 2-21). This reaction has been chosen as it is a well-known efficient tool for the synthesis of chiral homoallylic alcohols and has been applied to synthesize valuable intermediates and versatile building blocks in the synthesis of complex natural products.^[13] Moreover, it has been previously applied in our group.^[6,14] Therefore, a first asymmetric Brown allylation was applied to benzaldehyde, to obtain homoallylic alcohol **42** in 58% yield. The desired absolute (R)-configuration resulted from the use of the (+)-

allyldiisopinocampheylborane, (+)-(Ipc)₂B-allyl as a chiral agent, which was formed *in situ* from chlorodiisopinocampheylborane, (+)-DIP-chloride and allylMgBr. In this reaction, boron, acting as a Lewis acid, coordinates the oxygen of the carbonyl by proceeding through



Scheme 2-21. Synthesis of **38a** in a stereoselective fashion.

a closed and rigid six-membered chair-like transition state (Zimmerman-Traxler like, Figure 2-17). Due to the rigid six-membered transition state observed with boron, steric interactions between the axial Ipc ligands and the allyl group are minimized, giving high-stereoselective outcomes. Therefore, the stereoselectivity of the reaction depends on the chiral ligand used. After the reaction was complete, an alkaline oxidative work-up was done to obtain the desired alcohol.

To establish the enantiomeric excess of **42**, an HPLC analysis was performed. A racemic mixture of the corresponding allylic alcohol was prepared. After performing the direct analysis by using a chiral stationary phase OD, the elution time of the enantioenriched sample **42** was compared with the two retaining peaks belonging respectively to (R) and (S)-allylic alcohols in the racemic mixture. Thus, an enantiomeric ratio of 84:16 was determined and an enantiomeric excess of 68% was calculated.

The homoallylic alcohol **42** was then protected with TBDMS group to give **43** in 90% yield, using the TBDMS triflate and 2,6-lutidine as a base. Alternatively, a protection using the TBDMS chloride and 1H-imidazole was tried out, but a protected product was isolated in much lower yield of 47 %.

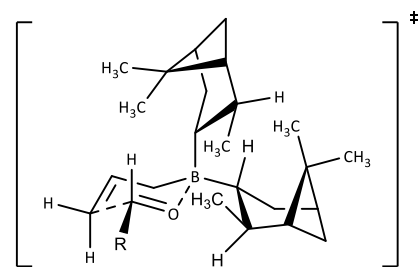
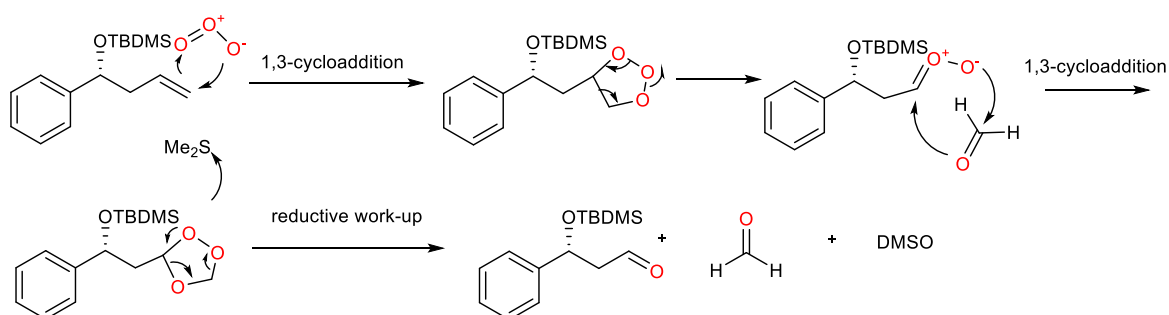


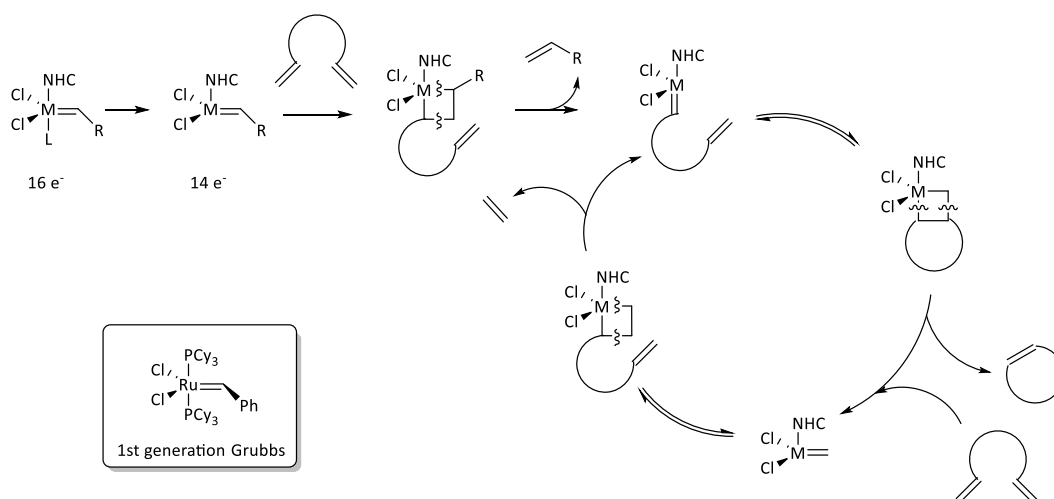
Figure 2-17. Ipc₂B-(Z)-allyl transition state.

In the next step an oxidative cleavage of **43** double bond, followed by a reductive work up, led to the formation of aldehyde **44** (via mechanism represented on Scheme 2-22). However, due to the extreme instability of the obtained product the compound could not be purified. The formation of the desired aldehyde was observed using $^1\text{H-NMR}$ (appearance of a signal at 8.85 ppm), and **44** was directly used as a crude in the next Brown allylation



Scheme 2-22. Mechanism of ozonolysis of compound **43**.

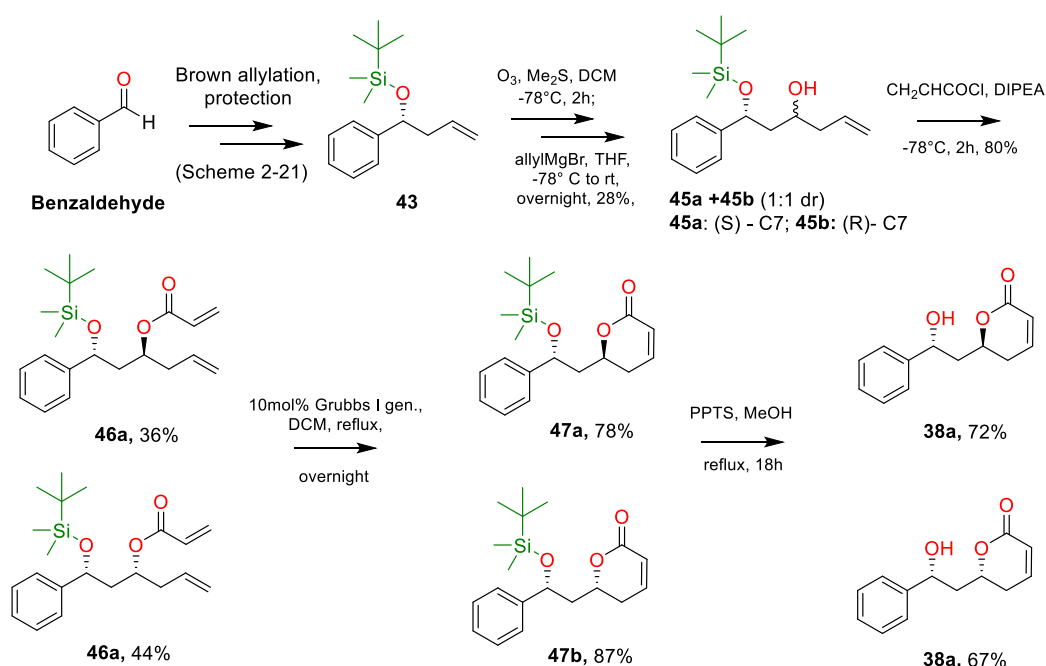
reaction. To obtain **45a**, (-)-(Ipc)₂B-allyl was used, formed *in situ* by (-)-DIP-chloride and allylMgBr. **45a** was obtained in a modest yield of 30% over the two steps of ozonolysis and allylation, and subjected to acylation with acryloyl chloride and DIPEA, giving **46a** in 83% yield. The $^1\text{H-NMR}$ spectra of **46a** allowed to assess the diastereomeric ratio of the compound, determined at 85:15. Then, an RCM reaction (RCM catalytic cycle is shown in Scheme 2-23) using 10% of Grubbs first-generation catalyst allowed to obtain **47a** in 75 % yield.



Scheme 2-23. General catalytic mechanism of RCM reaction.

Finally, compound **47a** was deprotected to obtain **38a**, using pyridinium *p*-toluenesulfonate (PPTS). It is worth noting that standard deprotection conditions of silyl ethers using e.g. tetra-*n*-butylammonium fluoride, TBAF, cannot be applied due to the instability of a lactone ring.^[15]

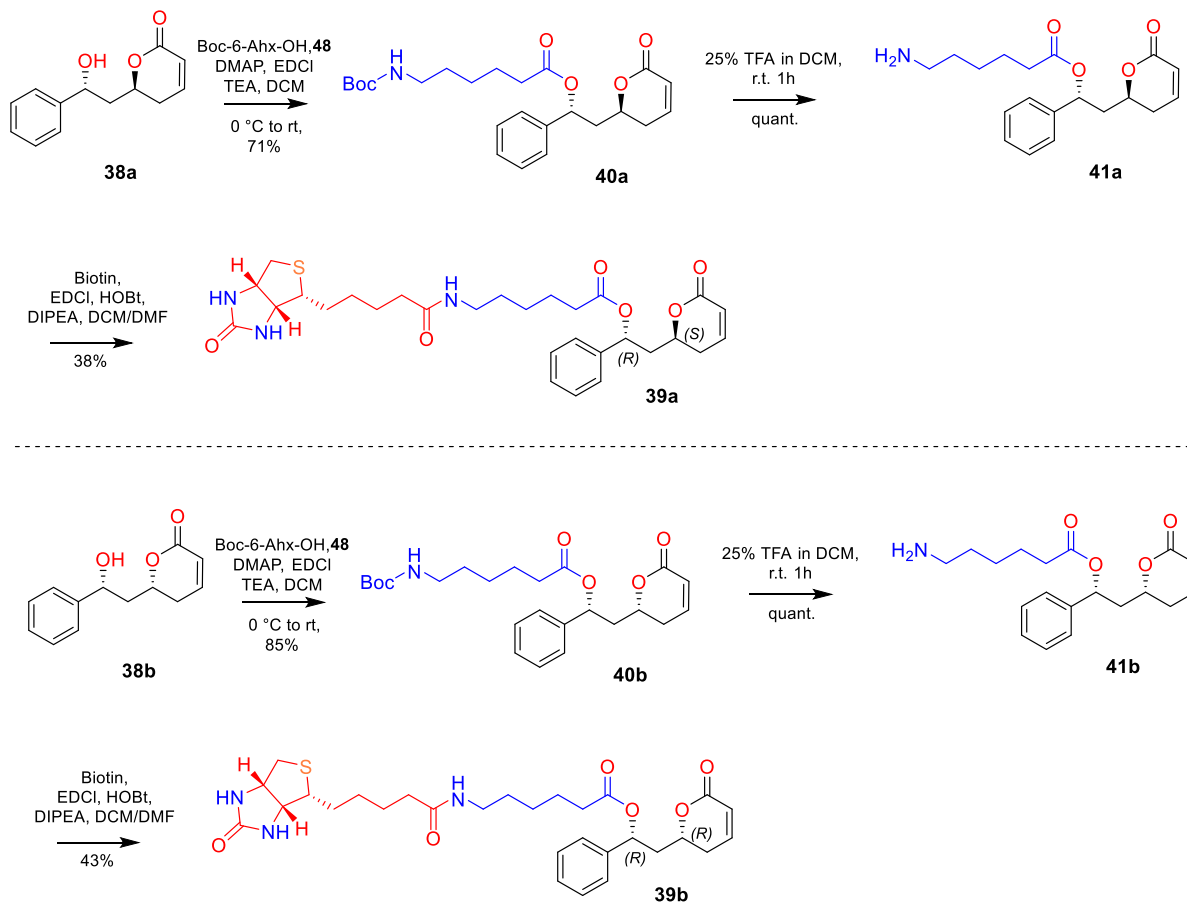
To obtain both diastereomers **38a** and **38b** in one synthetic pathway, the second Brown allylation was substituted with a non-stereoselective allylation. Therefore **44**, without purification, was directly reacted with allylMgBr at -78°C to obtain a mixture of diastereomers, **45**, in 28% yield. Only a small part of each diastereomer **45a** and **45b** could be separated by a flash chromatography, therefore an acylation reaction was performed on a diastereomeric mixture. Fortunately, the two diastereomers **46** and **46b** could be successfully separated at this point. It was possible to distinguish between (R,R) and (R,S)-diastereomers by confronting the $^1\text{H-NMR}$ signals to previously obtained allylic (R,S)-**46a** obtained using a stereoselective Brown allylation. Using the same conditions as described above, subsequent RCM and deprotection reactions allowed to obtain **38a** and **38b** (Scheme 2-24).



Scheme 2-24. Synthesis of diastereomers **38a** and **38b**.

2.3.3.3 Synthesis of biotinylated derivatives **39a-b**

To obtain the biotinylated derivatives **39a-b**, such obtained **38a-b** were subjected to an amide coupling reaction with the Boc-protected ϵ -aminocaproic acid **48**, to obtain respectively **40a** and **40b**. The deprotection with TFA provided **41a-b** in quantitative yields, which were biotinylated in the last step using commercially available D-biotin and applying the EDCl/HOBt/DIPEA amide coupling. The **39a** and **39b** were obtained in 38 and 43 % yields, respectively (Scheme 2-25).



Scheme 2-25. Synthesis of biotinylated simplified pironetin analogues **39a** and **39b**.

Crystallographic and computational evaluation

The four compounds **38a-b** and **39a-b** were submitted for X-ray crystallography experiments in the Paul Scherrer Institut, Switzerland. To our surprise, the compounds were not bound in the pironetin site, but binding of compound **38a** was detected in the newly discovered

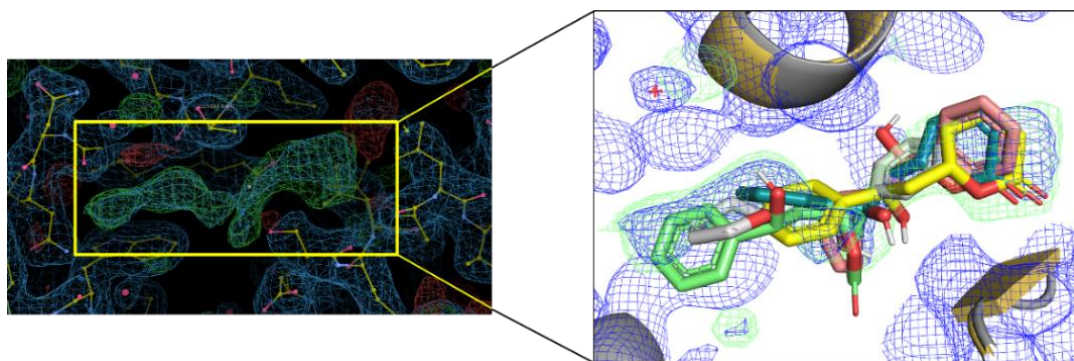


Figure 2-18. The density detected for the compound **38a** in the Todalam site and the possible orientations of the ligand in the site as predicted by computational studies.

Todalam site. However, the density indicated that compound can adapt in the pocket at least in two different configuration, making it difficult to model it in the crystal structure. Molecular docking was then performed to predict possible orientations adapted by the ligand **38a** (Figure 2-18).

2.3.4 EXPERIMENTAL PART

Chemistry

General Experimental Procedures

Unless otherwise stated, reagents were purchased from general suppliers (Sigma Aldrich and Fluorochem) and used without further purification. All solvents were of reagent grade or HPLC grade. All reactions were carried out in oven-dried glassware and dry solvents, under nitrogen atmosphere and were monitored by glasses or aluminium TLC on silica gel (Merck precoated 60F254 plates), with detection by UV light (254 nm), or or using TLC stains as Cerium Ammonium Molybdate stain (Hanessian's stain).

Purification of intermediates and final products was mostly carried out by flash chromatography using as stationary phase high purity grade silicagel (Merck Grade, pore size 60 Å, 230-400 mesh particle size, Sigma Aldrich). Alternatively, purification was performed by a Biotage® system in normal phase using Biotage® Sfär Silica D cartridges (6/10/25 g).

¹H NMR and ¹³C-NMR spectra were recorded on a Bruker Avance Spectrometer 400 MHz using commercially available deuterated solvents (chloroform-d, methanol-d₄) at room temperature. Chemical shifts (δ) are reported in parts per million (ppm) and are reported relative to TMS, used as an internal standard. Data for ¹H NMR are reported as follows: chemical shift (δ/ppm), multiplicity, coupling constants (Hz). Multiplicities are reported as follows: s = singlet, d = doublet, t = triplet, m = multiplet, br s = broad singlet. Data for ¹³C NMR are reported in terms of chemical shift (δ/ppm).

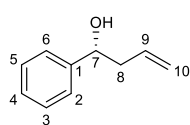
HPLC analysis were recorded on a 1220 Infinity II LC Agilent chromatograph, using HPLC grade solvents commercially available.

Synthesis of (R)-1-phenylbut-3-en-1-ol, 42:

(+)-DIP-Cl (3.18 g, 9.9 mmol) was dissolved in anhydrous THF (40.5 mL) and cooled at -78°C. Allylmagnesium bromide (1.0 M solution, 8.58 mL, 8.58 mmol) was added dropwise. The reaction mixture was stirred for 1 h at 0°C and then the white solid precipitated. The benzaldehyde (6.6 ml, 6.4 mmol) was dissolved in anhydrous THF (19.5 mL) and added to the supernatant solution of the previous mixture, cooled at -78°C. After 1 h, the reaction was warmed to r.t. and stirred overnight. The mixture was concentrated and a saturated solution of NaH₂PO₄ / KH₂PO₄ (30mL) was added, followed by MeOH (30 mL) and H₂O₂ 30% (14mL). The mixture was stirred for 30 min; a saturated solution of NaHCO₃ was added.

The layers were separated and the aqueous one was extracted with EtOAc. The combined organic layers were washed with brine, dried over Na₂SO₄, filtered and concentrated under

vacuum. The crude product was purified by column chromatography on silica gel (hexane: EtOAc = 7.5:2.5, second column DCM), to give **42** (564.2 mg, 58%) as a light-yellow oil.



$^1\text{H-NMR}$ (400 MHz, CDCl_3): δ 7.42–7.36 (m, 4H, **2-3H**, **5-6H**), 7.34 – 7.27 (m, 1H, **H4**), 5.84 (m, 1H, **H9**), 5.18 (m, 2H, **H10**), 4.75 (m, 1H, **H7**), 2.53 (m, 2H, **H8**).

Analytical data about ^{13}C NMR is in accordance with the literature.^[16]

Rf: 0.35 (Hexane:EtOAc 8:2, ceric ammonium molybdate);

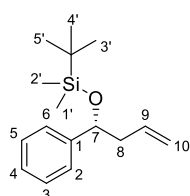
Chiral HPLC: The mixture has an ee of 68%. It was determined by chiral HPLC analysis using a Chiralcel® OD column, Hexane/IPA 97:3, room temperature, flow= 1.0 mL/min, λ = 254 nm. It has been established that the (S)-enantiomer elutes second. t_R = 10.75 min.

$[\alpha]_{\text{D}20}$: +46.7 (c = 1, CHCl_3).

Synthesis of (R)-tert-butyl dimethyl((1-phenylbut-3-en-1-yl)oxy)silane, **43**:

Procedure 1: TBDMSOTf (1.63 ml, 7.11 mmol) was added to a solution of **42** (841 mg, 5.6 mmol) and 2,6-lutidine (1 ml, 8.53 mmol) in anhydrous DCM (22 mL), previously cooled at 0 °C. After 2 hours, the reaction mixture was washed with HCl (1M) and NaHCO_3 . The aqueous layer was extracted with DCM and the collected organic phases were dried over Na_2SO_4 , filtered and concentrated under vacuum. The crude product was purified by column chromatography on silica gel (hexane: EtOAc = 6:4), to give **2** (869.2 mg, 90%) as a yellow oil.

Procedure 2: 1H-imidazole (1.09 g, 15.8 mmol, 2.0 eq.) was added to a solution of **42** (1.17 g, 7.89 mmol, 1.0 eq.) in anhydrous DCM (25 mL) at room temperature. Then, TBDMSCl (2.29 g, 15.8 mmol, 1.5 eq.) was added to the cooled mixture at 0°C. Afterwards, the mixture was warmed at room temperature and left stirring overnight. Upon completion, the reaction mixture was diluted with DCM (10 mL), washed with a 5% aq. sol. of citric acid (40 mL), an aq. sat. NaHCO_3 (35 mL) and brine (35 mL). The organic layer was dried over Na_2SO_4 , filtered and evaporated under vacuum. The crude was purified by flash chromatography on silica gel (Hexane:EtOAc 93:7) to give silyl ether **42** (918 mg, 47%) as a yellow oil.



$^1\text{H NMR}$ (400 MHz, CDCl_3): δ 7.41 – 7.36 (m, 4H, **2-3H**, **5-6H**), 7.34 – 7.27 (m, 1H, **H4**), 5.97 – 5.79 (m, 1H, **H9**), 5.15 – 5.04 (m, 2H, **H10**), 4.78 (dd, J = 7.2, 5.2 Hz, 1H, **H7**), 2.66 – 2.40 (m, 2H, **H8**), 0.99 (s, 9H, **H3'**, **4'**, **5'**), 0.13 (d, J = 1.6 Hz, 6H, **H1'**, **2'**).

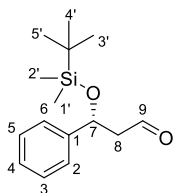
^{13}C NMR (400 MHz, CDCl_3) δ 145.1, 135.3, 128.0, 126.9, 125.9, 116.8, 75.0, 45.5, 25.8, 25.7, -4.7.

Rf: 0.67 (Hexane:EtOAc 8:2, acidic ceric ammonium molybdate).

$[\alpha]_{\text{D}20}$: 6,44 ($c = 0.56$, CHCl_3).

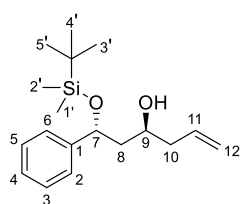
Synthesis of (1R,3S)-1-((tert-butyldimethylsilyl)oxy)-1-phenylhex-5-en-3-ol, 45a:

Step I - ozonolysis: Ozone was fluxed through a solution of **43** (826 mg, 3.08 mmol) in DCM (10 mL), cooled at -78°C . The reaction mixture slowly turned a pale blue color. After 2 h, the residual ozone was removed from the solution fluxing nitrogen for 10 min. Me_2S (0.45 mL, 6.16 mmol) was added at 0°C , then the reaction mixture was stirred for 2 h at r.t. The solvent was removed under vacuum, and the product **44** was used without purification in the next step.



Rf: 0.75 (Hexane:EtOAc 97:3, acidic ceric ammonium molybdate).

Step II – Brown allylation: (-)-DIP-Cl (1.5 g, 4.68 mmol) was dissolved in anhydrous THF (20 mL) and cooled at -78°C . Allylmagnesium bromide (1.0 M solution, 4.05 mL, 4.05 mmol) was added dropwise. The reaction mixture was stirred for 1 h at 0°C and then the white solid precipitated. Product **44** (824 mg, 3.12 mmol) was dissolved in anhydrous THF (10 mL) and added to the supernatant solution of the previous mixture, cooled at -78°C . After 1 h, the reaction was warmed to r.t. and stirred overnight. The mixture was concentrated and a saturated solution of $\text{NaH}_2\text{PO}_4 / \text{KH}_2\text{PO}_4$ (15 mL) was added, followed by MeOH (15 mL) and H_2O_2 30% (8 mL). The mixture was stirred for 30 min; a saturated solution of NaHCO_3 was added. The layers were separated and the aqueous one was extracted with EtOAc. The combined organic layers were washed with brine, dried over Na_2SO_4 , filtered and concentrated under vacuum. The crude product was purified by column chromatography on silica gel (hexane: EtOAc = 7:3) to give **45a** (276.6 mg, 30%) as light-yellow oil.



$^1\text{H-NMR}$ (400 MHz, CDCl_3): 7.34 – 7.27 (m, 4H, **2-3H**, **5-6H**), 7.23 – 7.17 (m, 1H, **H4**), 5.81 – 5.66 (m, 1H, **H11**), 5.09 – 4.98 (m, 3H, **H7**, **H12**), 3.88 – 3.75 (m, 1H, **H9**), 2.19 – 2.12 (m, 1H, **H10**), 1.83 – 1.73 (m, **H8**), 0.88 (s, 9H, **H3',4',5'**), 0.08 (s, 6H, **H1',2'**).

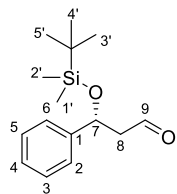
$^{13}\text{C NMR}$ (400 MHz, CDCl_3) δ 144.32, 134.88, 134.72, 128.33, 128.20, 127.51, 127.08, 126.02, 125.70, 117.55, 117.43, 77.36, 77.04, 76.73, 76.42, 73.43, 70.57, 67.39, 46.56, 45.73, 42.15, 42.02, 25.85, 25.82, 18.16, -4.74, -5.22.

$[\alpha]_{\text{D}20}$: +42.9 ($c = 1$, CHCl_3).

Synthesis of a diastereomeric mixture of (1R,3S)-1-((tert-butyldimethylsilyl)oxy)-1-phenylhex-5-en-3-ol, 45a and (1R,3R)-1-((tert-butyldimethylsilyl)oxy)-1-phenylhex-5-en-3-ol, 45b:

Step I - ozonolysis: Ozone was fluxed through a solution of compound **43** (890 mg, 3.39 mmol, 1.0 eq.) in DCM (15 mL) cooled at -78°C . The reaction mixture slowly assumed a pale blue color.

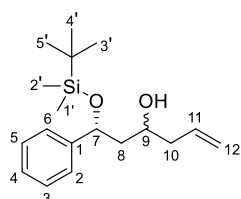
Upon completion, the mixture is left stirring under nitrogen atmosphere for 10 minutes to eliminate the excess of ozone. At 0°C, Me₂S (0.50 mL, 6.78 mmol, 2.0 eq.) was added to the reaction mixture and it was left stirring for two hours. Then, the reaction mixture was concentrated in *vacuo*. The reaction mixture was extracted with water (2x) and DCM (4x).



Organic layers were dried over Na₂SO₄, filtered and solvent was evaporated under rotary evaporation to obtain a yellow oil that was used without further purification in the next step.

R_f: 0.75 (Hexane:EtOAc 97:3, acidic ceric ammonium molybdate).

Step II – non-stereoselective allylation: AllylMgBr (1.0 M in Et₂O, 6.20 mmol, 6.20 mL, 1.5 eq.) was added dropwise to a solution of aldehyde **3** (820 mg, 3.10 mmol, 1.0 eq.) in anhydrous THF (10 mL) and cooled down to –78°C using a dry ice bath. Slowly, the temperature was warmed to 0°C and then to rt. The reaction mixture was left stirring upon completion of the reaction monitored by TLC. The reaction was quenched with sat. aq. of NH₄Cl at 0°C and the combined aqueous phases were extracted with diethyl ether (4x). The combined organic layers were dried over Na₂SO₄, filtered and concentrated in *vacuo*. The crude was purified by flash column chromatography on silica gel (Hexane:EtOAc 9:1) to give allylic alcohol **45a-b** as a mixture of diastereomers (253 mg, 28% o2s, d.r. 1:1).



¹H-NMR (400 MHz, CDCl₃): δ = 7.35–7.28 (m, 10H, **2-6H**), 5.89 – 5.70 (m, 2H, **H11**), 5.16 – 5.09 (m, 4H, **12H**), 4.48 – 4.34 (m, 2H, **H7**), , 3.91 – 3.73 (m, 2H, **H9**), 2.30 – 2.15 (m, 4H, **H10**), 1.90 – 1.67 (m, 4H, **H8**), 0.95 (s, 9H, **H3',4',5'**), 0.88 (s, 9H, **H3',4',5'**), 0.07 (s, 6H, **H1', H2'**), 0.05 (s, 6H, **H1', H2'**).

R_f **45a (1R,3S)** : 0.25 (Hexane:EtOAc 9:1, acidic ceric ammonium molybdate).

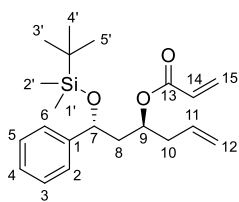
R_f **45b (1R,3R)**: 0.23 (Hexane:EtOAc 9:1, acidic ceric ammonium molybdate).

¹³C NMR in accordance with the reported above for **45a**.

Synthesis of (1R,3S)-1-((tert-butyldimethylsilyloxy)-1-phenylhex-5-en-3-yl acrylate, **46a**:

(*R,S*)-alcohol **45a** (21.7 mg, 0.07 mmol, 1.0 eq.) was dissolved in anhydrous DCM (3.5 mL) under nitrogen atmosphere at –78° C. DIPEA (80 μL, 0.46 mmol, 6.5 eq.) and 2-propenoylchloride (41.6 μL, 0.46 mmol, 6.5 eq.) were added and the mixture was left to stirring for 2 hours at the same temperature. Afterwards, the reaction mixture was warmed to rt and a sat. aq. NaHCO₃ was added and the biphasic mixture was stirred for 15 min. The phases were separated, the organic layer washed with sat. aq. NaHCO₃ (2x) and brine (2x). The aqueous layers were extracted with DCM (2x). The combined organic phases were dried over Na₂SO₄, filtered and concentrated under vacuum. The crude was purified by flash

column chromatography on silica gel (Hexane:EtOAc 95:5) to give **46a** (21.2 mg, 83%) as a transparent oil.



$^1\text{H-NMR}$ (400 MHz, CDCl_3): δ 7.42 – 7.17 (m, 5H, **H2-6**), 6.43 (dd, $J = 17.3, 1.4$ Hz, 1H, **H15a**), 6.23 – 6.02 (m, 1H, **H14**), 5.86 – 5.70 (m, 2H, **H15b, H11**), 5.26 – 5.16 (m, 1H, **H12a**), 5.11 – 5.03 (m, 2H, **H12b, H9**), 4.75-4.69 (m, 1H, **H7**), 2.42 (d, $J = 6.8$ Hz, 2H, **H10**), 2.02 – 1.82 (m, 2H, **H8**), 0.89 (s, 9H, **H3', 4', 5'**), -0.01 (s, 3H, **H1'**), -0.27 (s, 3H, **H2'**).

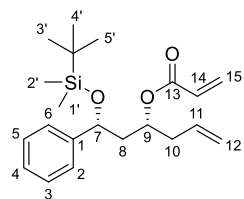
$^{13}\text{C NMR}$ (400 MHz, CDCl_3): δ 145.3, 134.0, 131.0, 129.4, 128.9, 127.9, 126.7, 118.6, 72.8, 71.6, 45.0, 39., 26.5, 26.3, 15.0 ppm;

R_f : 0.49 (Hexane/EtOAc 95:5, acidic ceric ammonium molybdate).

Synthesis of (1R,3S)-1-((tert-butyldimethylsilyl)oxy)-1-phenylhex-5-en-3-yl acrylate, **45a**, and (1R,3R)-1-((tert-butyldimethylsilyl)oxy)-1-phenylhex-5-en-3-yl acrylate, **46b**:

46a-b (126.4 mg, 0.41 mmol, 1.0 eq.) was dissolved in anhydrous DCM (3.5 mL) under nitrogen atmosphere at -78°C . DIPEA (0.47 ml, 2.68 mmol, 6.5eq.) and 2-propenoylchloride (0.22 ml, 2.68 mmol, 6.5 eq.) were added and the mixture was left to stirring for 2 hours at the same temperature. Afterwards, the reaction mixture was warmed to rt and a sat. aq. NaHCO_3 was added and the biphasic mixture was stirred for 15 min. The phases were separated, the organic layer washed with sat. aq. NaHCO_3 (2x) and brine (2x). The aqueous layers were extracted with DCM (2x). The combined organic phases were dried over Na_2SO_4 , filtered and concentrated under vacuum. The crude was purified by flash column chromatography on silica gel (Hexane:EtOAc 95:5) to give **47a** (53.5 mg, 36%) and **47b** (65.4 mg, 44%) as a colorless oils.

Analytical characterization for **46a** described above.



$^1\text{H-NMR}$ (400 MHz, CDCl_3): $\delta = 7.50 - 7.09$ (m, 5H, **H2-6**), 6.32 (dd, $J=17.3, 1.3$, 1H, **H15a**), 6.02 (dd, $J=17.3, 10.4$, 1H, **H14**), 5.88 – 5.70 (m, 1H, **H15b**), 5.76 – 5.60 (m, 1H, **H11**), 5.09 – 4.98 (m, 1H, **H12a**), 4.99 – 4.86 (m, 1H, **H12b**), 4.70 (t, $J=6.4$, 1H, **H9**), 2.48 – 2.22 (m, 2H, **H10**), 2.13-1.90 (m, 1H, **H8**), 0.92 – 0.79 (m, 9H, **H3', 4', 5'**), 0.01 (s, 3H, **H1'**), -0.27 (s, 3H,

H2') ppm;

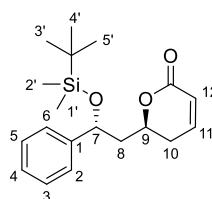
$^{13}\text{C-NMR}$ (101 MHz, CDCl_3) $\delta = 133.98, 131.01, 129.40, 128.83, 127.88, 126.66, 118.57, 72.77, 71.33, 54.12, 44.95, 39.22, 26.46$ ppm;

R_f : 0.35 (Hexane/EtOAc 9.5:0.5, ceric ammonium molybdate).

Synthesis of (S)-6-((R)-2-((tert-butyldimethylsilyl)oxy)-2-phenylethyl)-5,6-dihydro-2H-pyran-2-one, 47a

Product **46a** (50 mg, 0.13 mmol) was dissolved in anhydrous DCM (13 ml) under N₂. Grubbs I generation catalyst (10 mg, 0.013 mmol) was then added. The reaction was stirred at reflux overnight.

The crude product was purified by column chromatography on silica gel (hexane: EtOAc = 7:3) to give **47a** (35.3 mg, 78%) as a yellow oil.



¹H NMR (400 MHz, CDCl₃) δ 7.41 – 7.20 (m, 5H, **H2-6**), 6.97 – 6.87 (m, 1H, **H11**), 6.10 – 6.03 (m, 1H, **H12**), 5.11 – 5.00 (m, 1H, **H7**), 4.82 – 4.65 (m, 1H, **H9**), 2.36 – 2.29 (m, 2H, **H10**), 1.97 – 1.82 (m, 2H, **H8**), 0.88 (s, 9H, **H4', 5', 6'**), 0.05 (s, 3H, **H1'**), -0.16 (s, 3H, **H2'**).

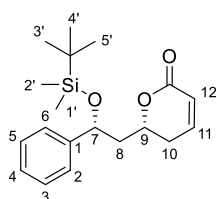
¹³C NMR (400 MHz, CDCl₃): δ 145.33, 134.00, 131.01, 129.41, 128.85, 127.91, 126.68, 118.58, 72.78, 71.59, 44.95, 39.22, 26.47, 26.28, 14.98 ppm;

R_f 0.3 (Hexane/EtOAc 8:2, ceric ammonium molybdate).

[α]_{D20}: -9.94 (c= 1.0, CHCl₃).

Synthesis of (R)-6-((R)-2-((tert-butyldimethylsilyl)oxy)-2-phenylethyl)-5,6-dihydro-2H-pyran-2-one, 47b:

(R,R)-silyl ether **46b** (40 mg, 0.10 mmol, 1.0 eq.) was dissolved in anhydrous DCM (13 mL) under nitrogen atmosphere. Afterwards, Grubbs first generation catalyst (8.70 mg, 0.01 mmol, 0.1 eq.) was added. Then, the reaction mixture was stirred at reflux overnight. Upon completion, the solvent was removed in vacuum. The crude was purified by flash column chromatography (Hexane:EtOAc 8:2) to yield **47b** (29.8 mg, 87%).



¹H-NMR (400 MHz, CDCl₃): δ = 7.50 – 7.09 (m, 5H, **H2-6**), 6.77 – 6.69 (m, 1H, **H11**), 5.94 – 5.86 (m, 1H, **H12**), 4.93 – 4.85 (m, 1H, **H7**), 4.16 – 4.00 (m, 1H, **H9**), 2.38 – 2.16 (m, 2H, **H10**), 1.99 – 1.75 (m, 2H, **H8**), 0.79 (s, 9H, **H4', 5', 6'**), -0.04 (s, 3H, **H1'**), -0.24 (s, 3H, **H2'**).

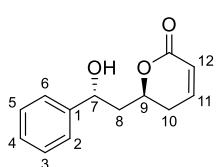
¹³C-NMR (101 MHz, CDCl₃) δ = 133.98, 131.01, 129.40, 128.83, 127.88, 126.66, 118.57, 72.77, 71.33, 54.12, 44.95, 39.22, 26.46 ppm;

[α]_{D20}: 11.52 (c= 1.0, CHCl₃).

R_f: 0.35 (Hexane/EtOAc 8:2, ceric ammonium molybdate).

Synthesis of (S)-6-((R)-2-hydroxy-2-phenylethyl)-5,6-dihydro-2H-pyran-2-one, 38a

Product **47a** (43 mg, 0.13 mmol) was dissolved MeOH (7.5 ml) and H₂O (0.75 ml) and PPTS (6.5 mg, 0.03 mmol) was added. The mixture was left stirring at reflux overnight. The mixture was then neutralized with NaHCO₃ solid, filtered, and evaporated. The crude product was purified by column chromatography on silica gel (DCM: MeOH= 9:1) to obtain product **38a** as a light-yellow oil (20.3 mg, 72%).



¹H NMR (400 MHz, CDCl₃) δ 7.44 – 7.26(m, 5H, **H2-H6**), 6.96 – 6.82 (m, 1H, **H11**), 6.09 – 5.97 (m, 1H, **H12**), 5.17– 5.09 (m, 1H, **H9**), 4.91 – 4.79 (m, 1H, **H7**), 2.50 – 2.28 (m, 2H, **H10**), 2.17 – 2.06 (m, 1H, **H8a**), 2.02 – 1.91 (m, 1H, **H8b**).

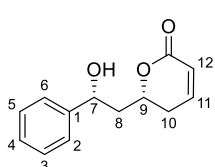
¹³C NMR (400 MHz, CDCl₃) 164.6, 145.5, 144.5, 128.8, 128.1, 127.8, 126.1, 125.7, 121.5, 75.0, 69.6, 44.5, 29.9.

[α]_D20: -42.21 (c= 0.4, CHCl₃).

MS (ESI) m/z [M + Na]⁺ calcd. for C₁₃H₁₄O₃Na: 241.0841, found: 241.0818

Synthesis of (S)-6-((R)-2-hydroxy-2-phenylethyl)-5,6-dihydro-2H-pyran-2-one, **38b**:

(R,R)-silyl ether **47b** (29.8 mg, 0.09 mmol, 1.0 eq.) was dissolved in MeOH (4.5 mL) and water (0.05 mL). PPTS (14.3 mg, 0.05 mmol, 1.0 eq.) was added. The reaction mixture was left refluxing for 22 hours. The dark brown mixture was neutralized by solid NaHCO₃, filtered and evaporated in vacuum. The crude was purified by flash chromatography on silica gel (Hexane:EtOAc 4:6) to give (R,R)-secondary alcohol **38b** (13.1 mg, 67%) as a light-yellow oil.



¹H-NMR (400 MHz, CDCl₃): δ 7.45 – 7.29 (m, 5H, **H2-H6**), 6.97 – 6.83 (m, 1H, **H11**), 6.09 – 5.99 (m, 1H, **H12**), 5.08 – 5.00 (m, 1H, **H9**), 4.49 – 4.37 (m, 1H, **H7**), 2.54 – 2.31 (m, 3H, **H10, H8a**), 2.15 – 1.97 (m, 1H, **H8b**).

¹³C-NMR (400 MHz, CDCl₃) δ = 164.5, 145.6, 143.8, 129.3, 129.1, 128.6, 128.4, 126.6, 121.9, 76.6, 72.1, 44.0, 30.5 ppm;

Rf: 0.35 (Hexane:EtOAc 4:6, ceric ammonium molybdate).

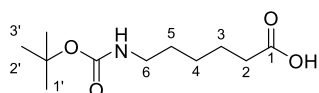
[α]_D20: 40.30 (c= 0.4, CHCl₃).

MS (ESI) m/z [M + Na]⁺ calcd. for C₁₃H₁₄O₃Na: 241.0841, found: 241.0832

Synthesis of 6-[N-(tert-Butoxycarbonyl)amino]caproic acid, **48**:

ε-Aminocaproic acid (300 mg, 2.3 mmol) was dissolved in dioxane (3.45 ml) and NaOH (2.3 ml, 1M) at 0°C. Boc anhydride (649 mg, 2.9 mmol) was added and the reaction was stirred at 0°C for 1h. After checking the pH (≈9-10), the reaction was heated at r.t. and left stirring overnight.

Solvents were evaporated under vacuum to give product **48** (493 mg, 93%) as a white solid.

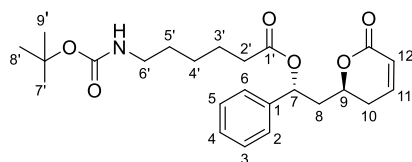


^1H NMR (400 MHz, CDCl_3) δ 3.13 (s, 2H, **H6**), 2.37 (t, $J = 7.4$ Hz, 2H, **H2**), 1.77 – 1.58 (m, 2H, **H3**), 1.57 – 1.43 (m, 11H, **H1'–3'**, **H5**), 1.44 – 1.30 (m, 2H, **H4**).

Analytical data about ^{13}C NMR is in accordance with the literature.^[17]

Synthesis of (R)-2-((S)-6-oxo-3,6-dihydro-2H-pyran-2-yl)-1-phenylethyl 6-((tert-butoxycarbonyl)amino)hexanoate, **40a**:

To a solution of **38a** (10 mg, 0.05 mmol) in dry DCM (0.35 mL) were added 48 (16 mg, 0.069 mmol), DMAP (2.8 mg, 0.02 mmol), EDC-HCl (13mg, 0.07 mmol), and triethylamine dry (9.6 μL , 0.07 mmol) at room temperature under a nitrogen atmosphere. The reaction was stirred for 3 h before to add H_2O (1 \times 2 mL). The organic layer was dried over Na_2SO_4 , and concentrated under reduced pressure. The crude was purified by flash chromatography on silica gel (DCM:MeOH 98:2) to give **40a** as a transparent oil in 71% yield.



^1H NMR (400 MHz, CDCl_3) δ 7.41 – 7.30 (m, 5H, **H2–H6**), 6.95 – 6.81 (m, 1H, **H11**), 6.10 – 5.97 (m, 2H, **H12**, **H9**), 4.62 – 4.50 (m, 1H, **H7**), 3.11 – 3.06 (m, 2H, **H6'**), 2.42 – 2.32 (m, 4H, **H10**, **H2'**), 2.28 – 2.23 (m, 2H, **H8**), 1.68 – 1.58 (m, 2H, **H3'**), 1.52 – 1.41 (m, 11H, **H7'–9'**, **H5'**), 1.37 – 1.24 (m, 2H, **H4**).

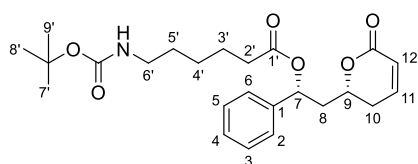
^{13}C NMR (101 MHz, CDCl_3) δ 172.7, 163.1, 156.5, 144.8, 139.6, 128.9, 128.5, 128.4, 126.8, 126.3, 121.6, 79.3, 74.9, 72.3, 41.5, 40.6, 34.4, 29.8, 29.5, 28.5, 26.4, 24.6.

MS (ESI) m/z [$M + \text{Na}$] $^+$ calcd. for $\text{C}_{23}\text{H}_{30}\text{NO}_6\text{Na}$: 439.1971, found: 439.1966

$[\alpha]_{\text{D}20}$: -14.6 ($c = 1$, CHCl_3).

Synthesis of (R)-2-((R)-6-oxo-3,6-dihydro-2H-pyran-2-yl)-1-phenylethyl 6-((tert-butoxycarbonyl)amino)hexanoate, **40b**:

To a solution of **38b** (10 mg, 0.05 mmol) in dry DCM (0.35 mL) were added 48 (16 mg, 0.069 mmol), DMAP (2.8 mg, 0.02 mmol), EDC-HCl (13mg, 0.07 mmol), and triethylamine dry (9.6 μL , 0.07 mmol) at room temperature under a nitrogen atmosphere. The reaction was stirred for 3 h before to add H_2O (1 \times 2 mL). The organic layer was dried over Na_2SO_4 , and concentrated under reduced pressure. The crude was purified by flash chromatography on silica gel (DCM:MeOH 98:2) to give **40b** as a transparent oil in 85% yield.



^1H NMR (400 MHz, CDCl_3) δ 7.43 – 7.29 (m, 5H, **H2–H6**), 6.91 – 6.81 (m, 1H, **H11**), 6.10 – 5.97 (m, 2H, **H12**, **H9**), 4.52 (bs, 1H, NH), 4.36 – 4.24 (m, 1H, **H7**), 3.12 – 3.05 (m, 2H, **H6'**), 2.60 – 2.49 (m, 1H, **H10a**), 2.44 – 2.27 (m, 4H, **H10b**, **H2'**, **H8a**), 2.14 – 2.03 (m, 1H, **H8b**), 1.70 – 1.57 (m, 2H, **H3'**), 1.53 – 1.41 (m, 11H, **H7'–9'**, **H5'**), 1.37 – 1.25 (m, 2H, **H4**).

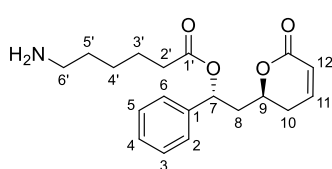
^{13}C NMR (101 MHz, CDCl_3) δ 172.2, 163.4, 156.1, 144.7, 139.6, 128.9, 128.5, 126.8, 126.3, 121.6, 79.3, 75.3, 72.3, 41.5, 40.6, 34.4, 29.8, 29.5, 28.5, 26.4, 24.6.

$[\alpha]_{\text{D}20}$: 20.27 ($c=1$, CHCl_3).

MS (ESI) m/z $[\text{M} + \text{Na}]^+$ calcd. for $\text{C}_{23}\text{H}_{30}\text{NO}_6\text{Na}$: 439.1971, found: 439.1967

Synthesis of (R)-2-((S)-6-oxo-3,6-dihydro-2H-pyran-2-yl)-1-phenylethyl 6-aminohexanoate, **41a**:

Compound **40a** (14 mg, 0.034 mmol) was dissolved in 25% TFA in DCM (0.7 ml) and left stirring for one hour. The deprotected derivative **41a** was isolated in quantitative yield (11 mg) and used in the next step without further purification.

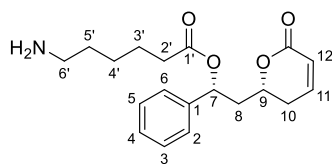


^1H NMR (400 MHz, CDCl_3) δ 7.88 (s, 2H, NH_2), 7.40 – 7.21 (m, 5H, **H2-H6**), 6.94 – 6.79 (m, 1H, **H11**), 6.04 – 5.94 (m, 2H, **H12, H7**), 4.62 – 4.50 (m, 1H, **H10**), 2.91–2.84 (m, 2H, **H6'**), 2.38–2.27 (m, 4H, **H10, H2'**), 2.23–2.18 (m, 2H, **H8**), 1.72–1.53 (m, 4H, **H3', 5'**), 1.38 – 1.30 (m, 2H, **H4'**).

$[\alpha]_{\text{D}20}$: -22.12 ($c=0.53$, CHCl_3).

Synthesis of (R)-2-((R)-6-oxo-3,6-dihydro-2H-pyran-2-yl)-1-phenylethyl 6-aminohexanoate, **41b**:

Compound **40b** (14 mg, 0.034 mmol) was dissolved in 25% TFA in DCM (0.7 ml) and left stirring for one hour. The deprotected derivative **41b** was isolated in quantitative yield (11 mg) and used in the next step without further purification.

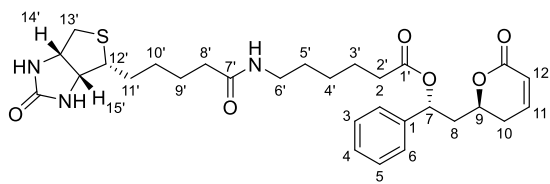


^1H NMR (400 MHz, CDCl_3) δ 7.51 – 7.46 (bs, 2H, NH_2), 7.44 – 7.25 (m, 5H, **H2-H6**), 6.95 – 6.87 (m, 1H, **H11**), 6.06 – 5.97 (m, 2H, **H12, H7**), 4.44 – 4.32 (m, 1H, **H10**), 3.09 – 3.03 (m, 2H, **H6'**), 2.58 – 2.40 (m, 4H, **H10, H2'**), 2.13 – 2.03 (m, 2H, **H8**), 1.77 – 1.58 (m, 4H, **H3', 5'**), 1.47 – 1.38 (m, 2H, **H4'**).

$[\alpha]_{\text{D}20}$: 24.12 ($c=0.55$, CHCl_3).

Synthesis of (R)-2-((S)-6-oxo-3,6-dihydro-2H-pyran-2-yl)-1-phenylethyl 6-(5-((3aR,4R,6aS)-2-oxohexahydro-1H-thieno[3,4-d]imidazol-4-yl)pentanamido)hexanoate, **39a**:

Compound **47a** (14,5 mg, 0.043 mmol) was dissolved in DCM/DMF (1:1). Then, biotin (14 mg, 0.057 mmol), EDCl (25 mg, 0,129 mmol), HOBT (17 mg, 0, 129 mmol) and DIPEA (37 μl) were added. The reaction was left stirring overnight at r.t. The solvent was evaporated under reduced pressure. The crude was purified with a flash column chromatography (eluent: DCM/MeoH 8.8/1.2) to give 9.3 mg of **39a** (38 % yield) as a white solid.



^1H NMR (400 MHz, Acetone- d_6) δ 7.52 – 7.27 (m, 5H, **H2-6**), 7.10 – 6.97 (m, 1H, **H11**), 6.08 – 5.85 (m, 2H, **H12, NH**), 5.66 (bs, 1H, **NH**), 4.55 – 4.47 (m, 1H, **H14'**), 4.39 – 4.30 (m, 1H, **H15'**), 3.38 – 3.11 (m, 3H, **H6', H12'**), 3.04 – 2.91 (m,

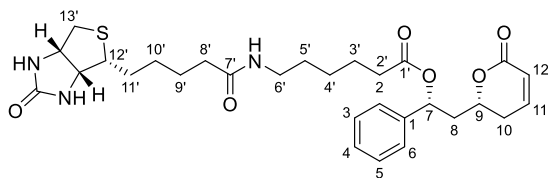
1H, **H13'**), 2.76 – 2.68 (m, 1H, **H13'b**), 2.61 – 2.26 (m, 4H, **H10, H2'**), 2.17 (t, $J = 7.3$ Hz, 2H, **H8'**), 1.86 – 1.74 (m, 2H, **H9'**), 1.73 – 1.55 (m, 4H, **H3', H11'**), 1.55 – 1.35 (m, 2H, **H5'**), 1.38 – 1.27 (m, 2H, **H10'**), 1.24 – 1.04 (m, 2H, **H4'**).

$[\alpha]_{\text{D}20}$: -28.3 ($c = 0.4$, Acetone).

MS (ESI) m/z $[M + \text{Na}]^+$ calcd. for $\text{C}_{29}\text{H}_{39}\text{N}_3\text{O}_6\text{SNa}$: 580.2458, found: 580.2463

Synthesis of (R)-2-((R)-6-oxo-3,6-dihydro-2H-pyran-2-yl)-1-phenylethyl 6-(5-((3aR,4R,6aS)-2-oxohexahydro-1H-thieno[3,4-d]imidazol-4-yl)pentanamido)hexanoate, **39b**:

Compound **47a** (14,5 mg, 0.043 mmol) was dissolved in DCM/DMF (1:1). Then, biotin (14 mg, 0.057 mmol), EDCl (25 mg, 0,129 mmol), HOBT (17 mg, 0, 129 mmol) and DIPEA (37 μl) were added. The reaction was left stirring overnight at r.t. The solvent was evaporated under reduced pressure. The crude was purified with a flash column chromatography (eluent: DCM/MeoH 8.8/1.2) to give 10.5 mg of **39b** (43% yield) as a white solid.



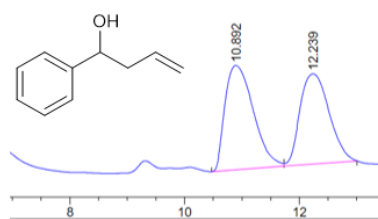
^1H NMR (400 MHz, Acetone- d_6) δ 7.48 – 7.27 (m, 5H, **H2-6**), 7.09 – 6.96 (m, 1H, **H11**), 6.07 – 5.96 (m, 2H, **H12, NH**), 5.96 – 5.88 (m, 1H), 5.77 (bs, 1H, **NH**), 4.55 – 4.46 (m, 1H, **H14'**), 4.40 – 4.28 (m, 1H, **H15'**), 3.30 – 3.03 (m, 3H, **H6', H12'**), 3.00 – 2.90 (m, 1H, **H13'a**), 2.75 – 2.67 (m, 1H, **H13'b**), 2.59 – 2.25 (m, 4H, **H10, H2'**), 2.23 – 2.11 (m, 2H, **H8'**), 1.85 – 1.72 (m, 2H, **H9'**), 1.71 – 1.55 (m, 4H, **H3', H11'**), 1.55 – 1.43 (m, 2H, **H5'**), 1.39 – 1.25 (m, 3H, **H10'**), 1.23 – 1.16 (m, 2H, **H4'**).

^{13}C NMR (101 MHz Acetone- d_6), δ 172.90, 163.69, 147.04, 141.15, 129.43, 128.95, 127.97, 126.99, 121.44, 75.80, 73.47, 62.33, 60.80, 56.49, 41.97, 41.04, 39.47, 36.34, 34.77, 30.41, 29.26, 29.13, 29.07, 27.08, 26.46, 25.31.

$[\alpha]_{\text{D}20}$: 33.27 ($c = 0.34$, Acetone).

$[\alpha]_{\text{D}20}$: 33.27 ($c = 0.34$, Acetone).

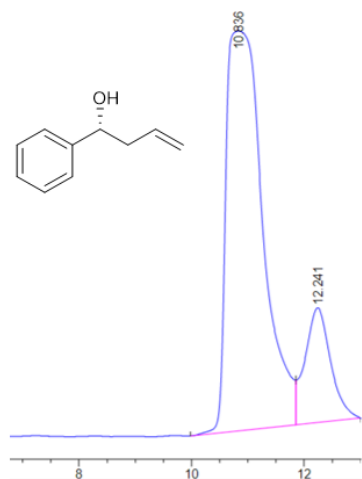
MS (ESI) m/z $[M + \text{Na}]^+$ calcd. for $\text{C}_{29}\text{H}_{39}\text{N}_3\text{O}_6\text{SNa}$: 580.2458, found: 580.2461

HPLC analysis – e.r. determination for compound 42

The ee was determined by chiral HPLC analysis using a chiralcel OD column. It has been established that the (R) enantiomer elutes first.

HPLC Conditions:

Chiralcel OD, Hex:i-PrOH 98:2, 1 mL/min



tR (min)	%
10.836	83.7
12.241	16.3

2.3.5 REFERENCES

- [1] L. Boike, N. J. Henning, D. K. Nomura, *Nat. Rev. Drug Discov.* **2022**, *21*, 881–898.
- [2] J. Singh, R. C. Petter, T. A. Baillie, A. Whitty, *Nat. Rev. Drug Discov.* **2011**, *10*, DOI 10.1038/nrd3410.
- [3] L. S. Wong, F. Khan, J. Micklefield, *Chem. Rev.* **2009**, *109*, DOI 10.1021/cr8004668.
- [4] J. A. Marco, J. García-Pla, M. Carda, J. Murga, E. Falomir, C. Trigili, S. Notararigo, J. F. Díaz, I. Barasoain, *Eur. J. Med. Chem.* **2011**, *46*, DOI 10.1016/j.ejmech.2011.02.011.
- [5] J. Paños, S. Díaz-Oltra, M. Sánchez-Peris, J. García-Pla, J. Murga, E. Falomir, M. Carda, M. Redondo-Horcajo, J. F. Díaz, I. Barasoain, J. A. Marco, *Org. Biomol. Chem.* **2013**, *11*, DOI 10.1039/c3ob40854j.
- [6] D. P. C. Marucci, M. Christodoulou, S. Pieraccini, M. Sironi, F. Dapiaggi, D. Cartelli, A. Calogero, G. Cappelletti, C. Vilanova, Silvia Gazzola, G. Broggin, *European J. Org. Chem.* **2016**, *2016*, 2029–2036.
- [7] T. Usui, H. Watanabe, H. Nakayama, Y. Tada, N. Kanoh, M. Kondoh, T. Asao, K. Takio, H. Watanabe, K. Nishikawa, T. Kitahara, H. Osada, *Chem. Biol.* **2004**, *11*, DOI 10.1016/j.chembiol.2004.03.028.
- [8] G. E. Keck, C. E. Knutson, S. A. Wiles, *Org. Lett.* **2001**, *3*, DOI 10.1021/ol015531m.
- [9] C. Bressy, J. P. Vors, S. Hillebrand, S. Arseniyadis, J. Cossy, *Angew. Chemie - Int. Ed.* **2008**, *47*, DOI 10.1002/anie.200802423.
- [10] M. T. Crimmins, A. M. R. Dechert, *Org. Lett.* **2009**, *11*, DOI 10.1021/ol9003228.
- [11] O. Trott, A. J. Olson, *J. Comput. Chem.* **2009**, *31*, 455–461.
- [12] A. E. Prota, J. Setter, A. B. Waight, K. Bargsten, J. Murga, J. F. Diaz, M. O. Steinmetz, *J. Mol. Biol.* **2016**, *428*, DOI 10.1016/j.jmb.2016.06.023.
- [13] Z. Boiarska, T. Braga, A. Silvani, D. Passarella, *European J. Org. Chem.* **2021**, *2021*, 3214–3222.
- [14] E. Bonandi, G. Tedesco, D. Perdicchia, D. Passarella, *Molecules* **2020**, *25*, DOI 10.3390/molecules25051057.
- [15] Q. Gu, L. Kong, L. Yang, L. Zhu, R. Hong, *Tetrahedron* **2020**, *76*, DOI 10.1016/j.tet.2020.131660.
- [16] R. Mirabdolbaghi, T. Dudding, *Org. Lett.* **2012**, *14*, DOI 10.1021/ol301566f.
- [17] A. C. Biraboneye, S. Madonna, Y. Laras, S. Krantic, P. Maher, J. L. Kraus, *J. Med. Chem.* **2009**, *52*, DOI 10.1021/jm900227u.

2.4 RATIONALLY DESIGNED NOVEL TODALAM ANALOGUES: TOWARDS SITE_SPECIFIC CYSTEINE TARGETING (synthetic part)

Abstract: The seven known tubulin binding sites on tubulin were recently complemented by six novel sites, which emerged out of a combined computational and crystallographic fragment screening.^[1] Further, a fully rationally designed small molecule tubulin inhibitor was described, termed Todalam, which targets one of these novel sites and displays a unique molecular mechanism of action. As of today, the only molecules known to target this site are the small fragments and the compounds possessing the Todalam aminothiazole scaffold.^[2] Having noticed the close proximity of the molecules bound at the Todalam site to α Cys4 and α Cys200, we aimed to rationally develop novel small molecules which differ from the Todalam scaffolds and then, based on the structural data, functionalize the selected molecules with the idea of site-specific covalent targeting. The X-ray crystallography experiments, which allowed to identify the initial hits, and their structural characterization are described in Section 3.3.3. Here, the synthesis of the covalent warhead-bearing ligands is addressed, and the relevant biochemical and X-ray crystallography characterization is presented. Subsequently, the obtained compounds could serve as molecular probes to further investigate MT dynamics in neurons.

Declaration of contribution: This is a multidisciplinary project performed within TubInTrain network, which was born at the Paul Scherrer Institut, Switzerland. The compounds which emerged from the project could be divided into the 1st series (scaffold development) and the 2nd series (warhead-bearing compound for covalent targeting). My work included the X-ray crystallography experiments of the 1st series of Todalam site binders and the synthesis of the 2nd series of compounds. For the design of the warhead-bearing molecules chosen for the synthesis, I strongly collaborated with the computational chemists, in particular Helena Pérez Peña and Maxim Shevelev, who performed the docking experiments. The molecular dynamics simulations and the X-ray crystallography experiments of the 2nd series of compounds were done by Anne-Catherine Abel. The biochemical evaluation was done by Ahmed Soliman and Francesca Bonato, at the Centro de Investigaciones Biológicas Margarita Salas, Spain.

2.4.1 INTRODUCTION

The discovery of novel fragment binding sites on tubulin in a result of crystallographic screening has opened up the possibility to rapidly generate synthetic lead-like tubulin binders.^[1] The first example of such a rationally designed small molecule is Totodam^[2], which binds at the novel site in the interdimer interface, disrupts microtubule dynamics by a unique mechanism of action, arrests cells in G2/M, and induces cell death (discussed in 1.3.1 and 1.3.3).

It is worth noting that currently there is a gap in the development of structurally simpler tubulin ligands, which would benefit from less complex synthetic pathways and would facilitate chemical modifications aimed at their optimization. Totodam was developed based on the small fragments targeting the site with only two rounds of straightforward one-step chemical synthesis, demonstrating for the first time the applicability of time-efficient synthetic approaches in the field of tubulin binders.

Based on the structural data, the Totodam structure can be subdivided into three moieties:

- The anchor point, represented by the acetanilide group.
- The central core, consisting of the aminothiazole.
- The flexible part, in close proximity to Cys4 or Cys200 of α -tubulin.

The acetanilide has been termed an “anchoring group”, as it represented a common binding motif of some fragments bound in the site, as well as Totodam family ligands. The core part is crucial for establishing the hydrogen bonds and the interactions in the site. Various modifications can be introduced in the flexible moiety, termed accordingly. The close proximity of the latter to Cys4 and Cys200 implies the possibility of potential covalent targeting of these residues (Figure 2-19). Considering that the natural product pironetin remains the only covalent α -tubulin binder, targeting those residues could become an alternative strategy to develop selective α -tubulin covalent probes. It could also be particularly relevant considering the scaffold novelty. As mentioned in Section 2.3, covalent ligands can display higher potency, affinity, and duration of action, as opposed to non-covalent derivatives. Furthermore, they could be useful for many applications such as e.g.

tubulin immobilization, tracking of covalently labelled tubulin in cells and *in vivo* or simply development of drug-like molecules.

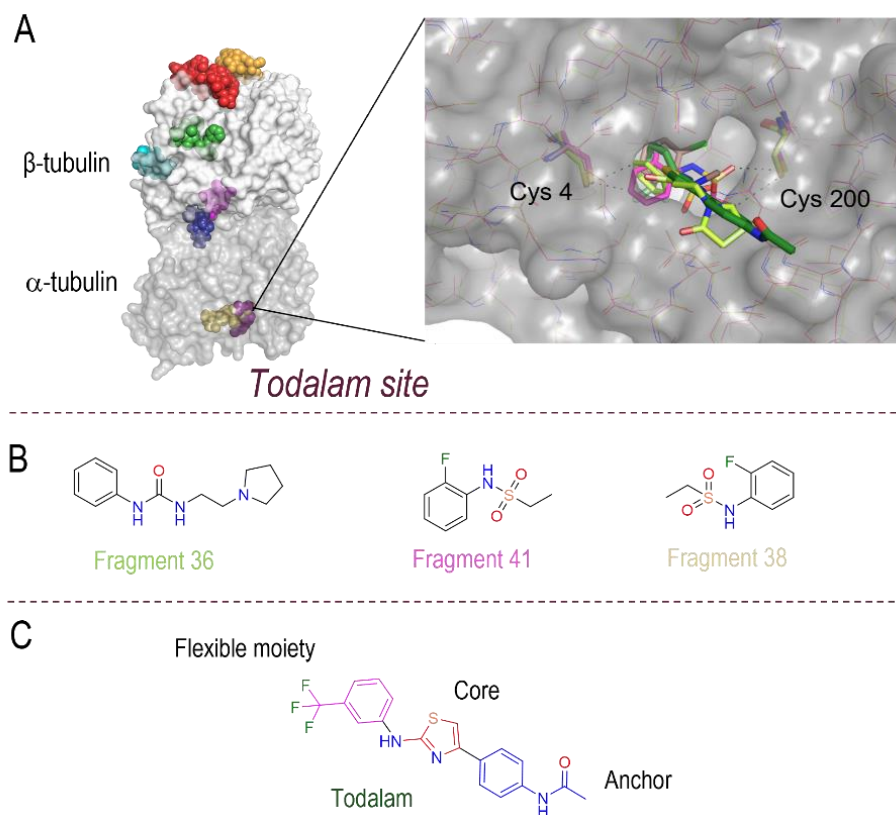


Figure 2-19. (A) Localization of the Todalam site on tubulin and close-up view of the Todalam site with Todalam molecule and fragments bound at the site. Left: The tubulin binding sites are depicted in sphere representation, α - and β -tubulin in grey and white ribbon representation, respectively. Right: The superposition of the fragments 36 (light green), 38 (beige), 41 (pink) and Todalam (dark green) at the binding site, with the ligands shown in sticks. The cysteine residues are labelled and are shown in sticks; (B) Chemical structure of fragments 36, 38 and 41; (C) Chemical structure of Todalam and schematic division of its structure into the three moieties: an anchor point, a central core and a flexible part. Note: the fragment numbering is according to the original numbering stated in ^[2].

2.4.2 AIM OF THE PROJECT

Up to date, the only ligands known to bind to the Todalam site are those belonging to the Todalam family and the small inactive or poorly active fragments that allowed their development.^[2] Considering the data presented above, there is significant potential for further exploration and discovery of Todalam site ligands. Initially, we have aimed to exploit the structural data in order to generate new scaffolds, which are different from Todalam, to target this site. We have considered the substitution of the aminothiazole Todalam core with that of amide, triazole, and urea moieties, as well as the variations in the flexible moieties (Figure 2-20I). Based on the computational studies and the synthetic convenience, we have envisioned the virtual screening and synthetic campaigns to generate a library of compounds. A workflow has been established, according to which the top-scoring molecules

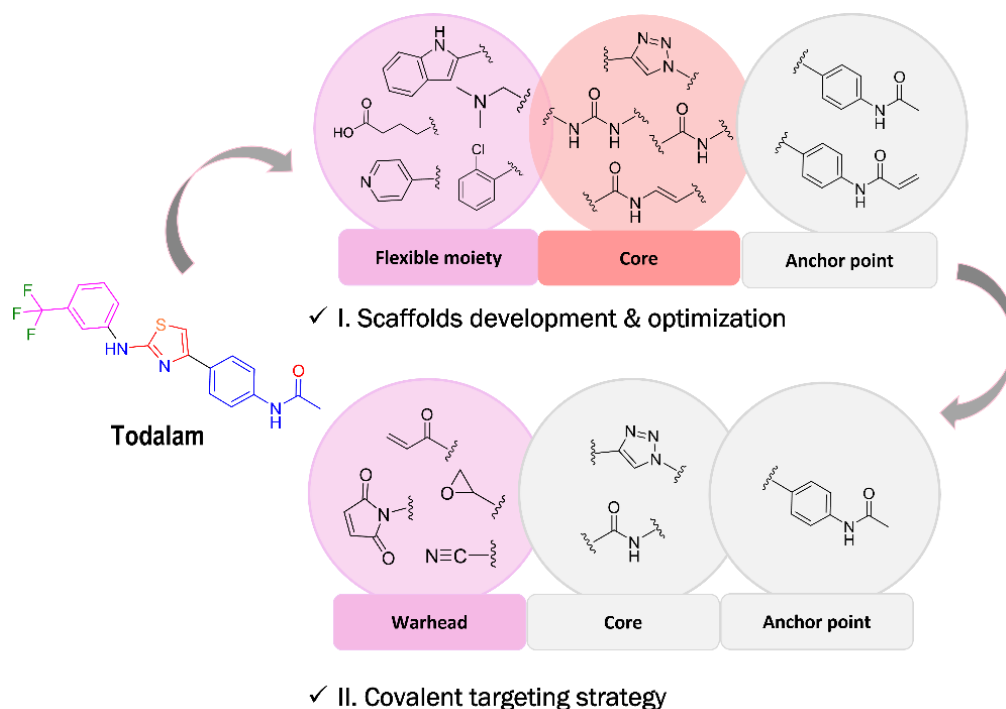


Figure 2-20. Chemical structure of Todalam and a schematic structure of the planned compounds to develop new scaffolds (I) and apply a covalent targeting strategy (II). To develop the scaffolds, focus was put on establishing the new core moieties and evaluating the effects of different modifications in the flexible moieties. Based on the results obtained from the scaffold development and using such developed core moieties, further modifications in the flexible part were envisioned to introduce a warhead.

were filtered by a strict selection process, heavily based on the binding pose, and their stability within the binding pocket as assessed by molecular dynamics simulations. We then planned to evaluate the generated libraries based on X-ray crystallography and tubulin assembly experiments (Figure 2-21).

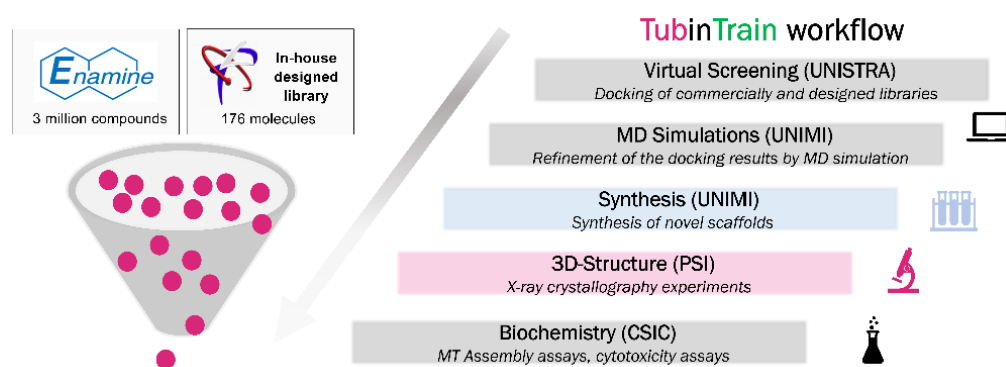


Figure 2-21. The established workflow to develop and characterize the new Todalam site binders. The synthetic and structural work, described in this thesis, are coloured in blue and pink, respectively.

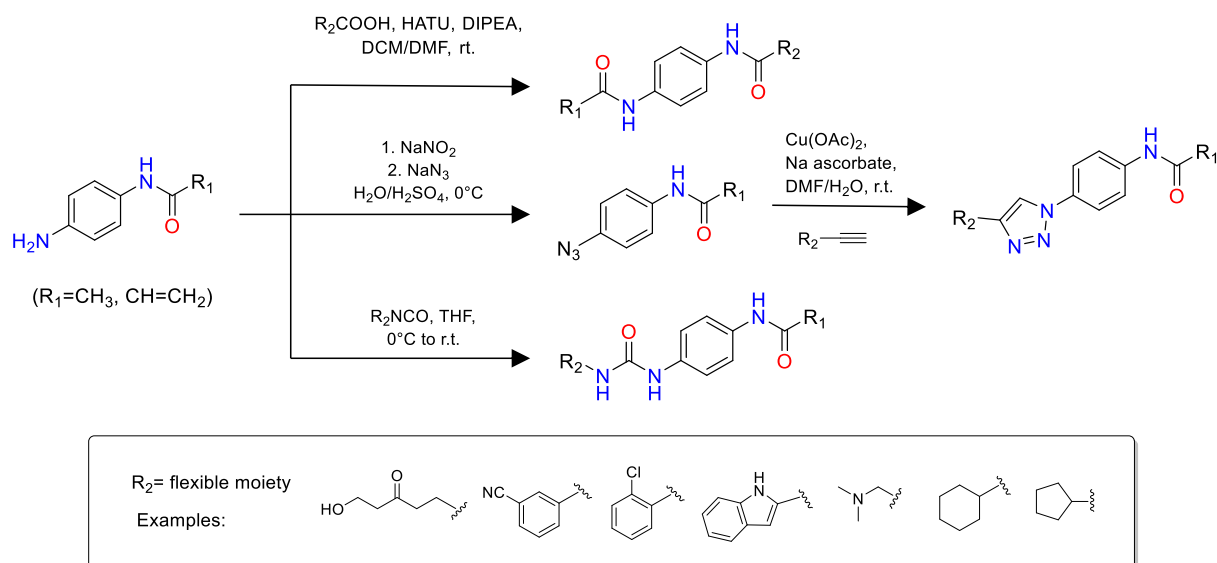
The hits identified from this 1st series of compounds allowed us to identify new scaffolds and comprehensively analyse the possible structural modifications, setting out the next objective of the project, focused on the covalent targeting of the cysteines present in the site. Specifically, we aimed to further optimize the chosen scaffolds by producing a 2nd series of compounds, decorated with the reactive warheads (Figure 2-20II) and to evaluate their ability to covalently interact with tubulin. The most promising hits would be further submitted for the experiments on neuronal cells, to evaluate their potential application as chemical tools to investigate MT dynamics and MT breakdown associated to neurodegeneration.

2.4.3 RESULTS AND DISCUSSION

2.4.3.1 Scaffold development

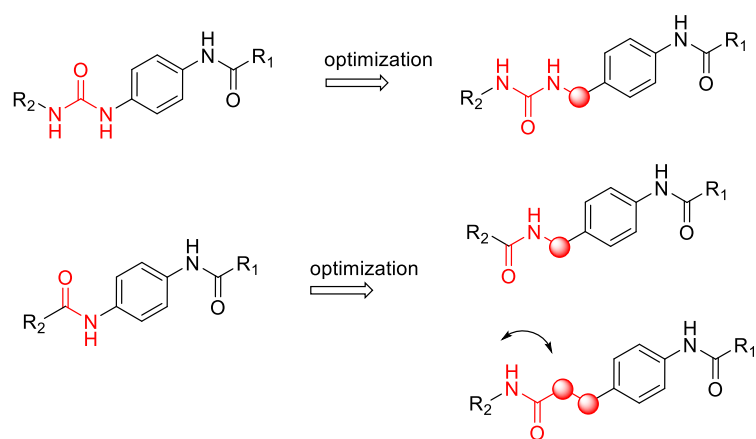
Design and synthesis

In collaboration with the Helena Pérez Peña and Maxim Shevelev, Varnek group at the University of Strasbourg, a library of over 150 in-house designed molecules, represented by the three scaffolds possessing an amide, urea or triazole moiety in place of the Todalam aminothiazole core, were submitted for docking studies. The time-efficient and cost-effective strategies have been chosen, based on click chemistry, amide coupling or urea formation reactions (Scheme 2-26). The acetanilide anchoring moiety has been maintained for most derivatives. The only planned modification in the anchoring part was the introduction of the acrylamide instead of the acetanilide moiety for a small set of derivatives, to investigate the potential influence on the activity and binding. Those were then followed



Scheme 2-26. The synthetic approaches used to synthesize the library of amide, triazole and urea derivatives.

by molecular dynamics simulations, performed by Anne-Catherine Abel, group of Prof. Pieraccini at the University of Milan, allowing to identify the best possible hits that were then chosen for synthesis. Based on the computational and structural data, we have decided to perform additional modifications in the initially designed scaffolds, to optimize the interactions with the protein. The modifications included varying the length of the spacer between the anchoring moiety and the core or inverting the amide moiety (Scheme 2-27).



Scheme 2-27. Further optimization of the amide and urea scaffolds.

In total, over forty different derivatives have been synthesized as a result of a first scaffold development campaign. Additionally, the computational groups have performed a virtual screening of commercially available libraries, providing additional thirty compounds. Both synthesized and purchased derivatives were submitted for crystallographic and biochemical evaluation.

Evaluation of the developed compounds

The X-ray crystallography experiments performed in Paul Scherrer Institute allowed to identify promising hits among the synthesized ligands and analyse their interactions with tubulin, providing foundation for the rational, structure-based development of warhead-bearing molecules. In total, eighteen crystal structures were determined. Amide, triazole and urea derivatives were able to bind to tubulin, showing that all three developed scaffolds can be further used. In case of the amide scaffold, positive results were obtained with the optimized scaffolds represented in Figure 2-26. Furthermore, we have shown that both aromatic and aliphatic substituents in the flexible moiety can be well-tolerated. The structural data is described in detail in Section 3.3.3.

Additionally, the compounds were submitted for *in vitro* biochemical testing to determine their effect on tubulin polymerization dynamics, at the Centro de Investigaciones Biológicas Margarita Salas (CIB-CSIC) in Madrid, Spain. Most of the bound compounds were found inactive in this assay, a feature that could be favourable for the development of the chemical probes.

2.4.3.2 Covalent targeting strategy – 2nd series of Totalam site ligandsDesign and synthesis

Having comprehensively evaluated the 1st series of the developed Totalam analogues, we have envisioned to apply the covalent targeting strategy.

For this purpose, we have designed a library of compounds characterized by three components:

- An acetanilide moiety as an anchoring point:
- A triazole or amide core moiety:
- A warhead, i.e. a moiety with the potential to establish a covalent bond with a cysteine residue.

Based on the results obtained with the 1st series of compounds, we have decided to synthesize a library of covalent ligands possessing a triazole or an amide as a core fragment.

For the triazole derivatives, in particular we have based the design of the covalent library on the data obtained with the compounds **49** and **50** of the 1st series. The fact that compounds **49** and **50** possessed an aliphatic chain reaching out to the α Cys4, stabilized by an additional carbonyl present on the chain, could be exploited to place an aliphatic warhead maintaining a carbonyl moiety (Figure 2-22). Furthermore, the lack of differences in the behaviour of these molecules independently of the variability in the anchoring moiety proved that it was sufficient to plan the warhead-bearing ligands possessing only an acetanilide moiety. Accordingly, no further modifications in the anchoring part were considered.

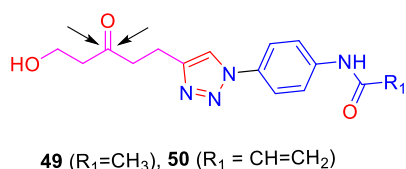


Figure 2-22. Chemical structure of compounds **49** and **50**.

For the amide derivatives, we have based the design of the covalent library on compound **51** of the first series. Having evaluated various amide derivatives, we have noted that maintaining one carbon atom between the anchoring part and the core moiety ensures compound binding, at the same time leaving sufficient space for the introduction of either

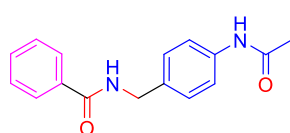
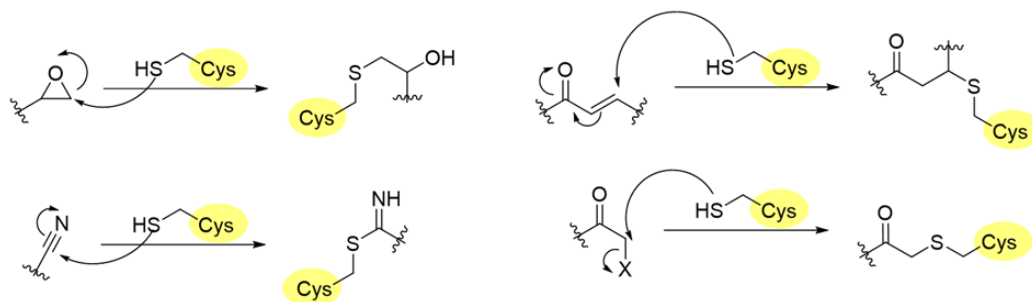


Figure 2-23. Chemical structure of compound **51**.

aliphatic or aromatic warhead. It is worth noting that the amide derivatives with an amide moiety directly attached to the phenyl of the anchor were not bound in the structures, while the choice of the warheads which may be introduced in case of the longer derivatives (e.g. with two carbons between the core and the anchor) was constrained due to the distance between the core and the α Cys4.

Based on the literature and synthetic feasibility, we have considered a different range of warheads which are known to react with cysteines. Due to the large atomic radius of sulfur and the low dissociation energy of the S-H bond, the thiol group of the cysteine has a strong nucleophilic character, and therefore is able to react with electrophilic groups, such as Michael's acceptors or epoxides.^[3]



Scheme 2-28. Examples of nucleophilic groups capable of covalently interacting with a cysteine: epoxide, nitrile, α/β -unsaturated carbonyl and α -halogen carbonyl.

Therefore, a series of compounds decorated with cysteine-targeting warheads, including acrylamide, alkyl halide, nitrile, epoxide, pentafluorophenyl and maleimide, has been designed. The designed compounds have been validated by covalent docking and molecular dynamics simulations, and the most promising triazole and amide derivatives were then synthesized.

2.4.3.2.1 Synthesis of warhead-bearing triazole derivatives

First, we focused on the synthesis of a set of warhead-bearing triazole derivatives to target α Cys4. Seven derivatives, which can be synthesized in one to three synthetic steps, were selected for synthesis (Figure 2-24). The CuAAC click reaction was used to synthesize the 1,2,3-triazole of all derivatives, while the additional steps included amide coupling, esterification or maleimide preparation, depending on the nature of the warhead.

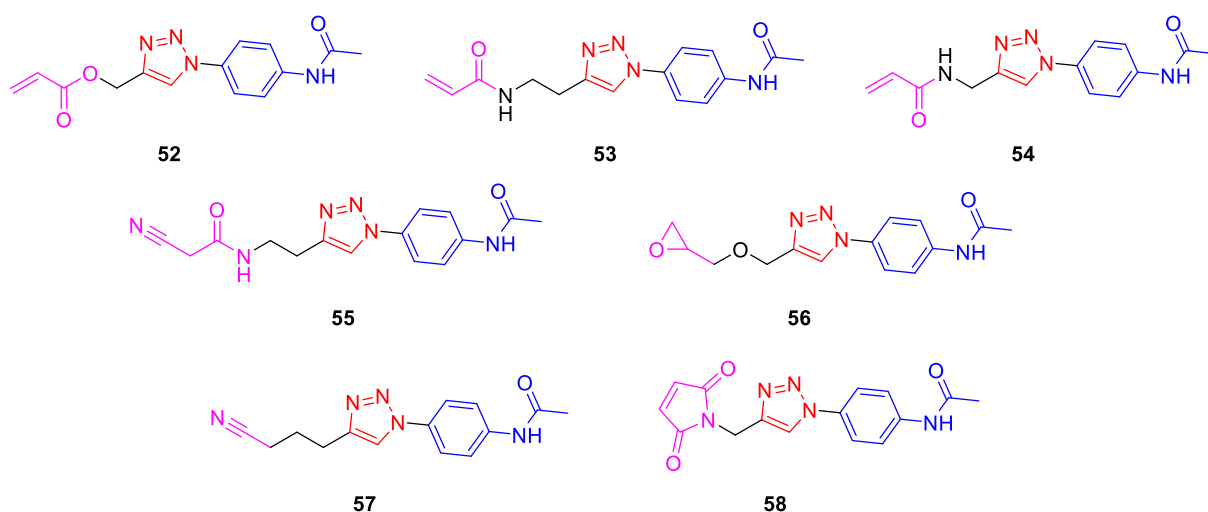
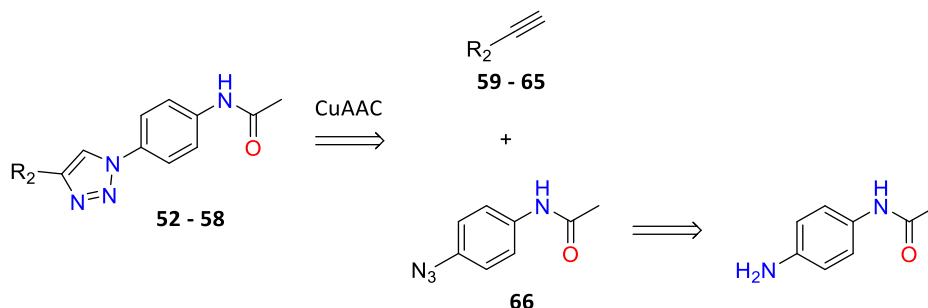


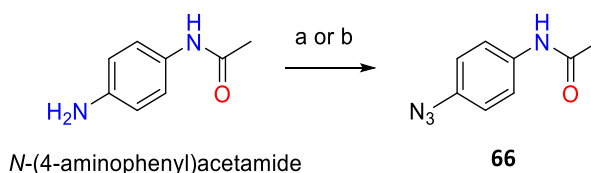
Figure 2-24. Chemical structures of warhead-bearing triazole derivatives selected for synthesis.

A general retrosynthetic pathway for all triazole derivatives is represented in Scheme 2-29. The compounds **52-58** were obtained through a CuAAC reaction between the respective alkynes **59-65** and 4'-azidoacetanilide **66**.



Scheme 2-29A. General retrosynthetic pathway for the synthesis of triazole derivatives.

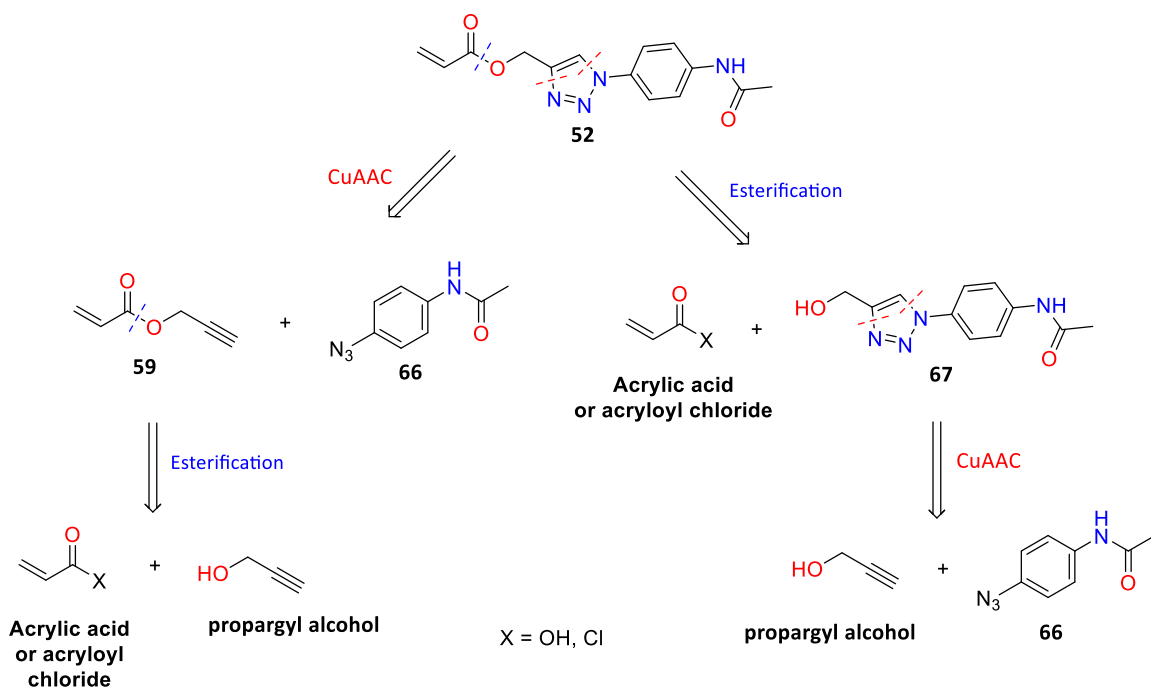
Two different strategies were used to synthesize a 4'-azidoacetanilide **66**, starting from the N-(4-aminophenyl)acetamide. The first strategy involved the use of tert-butyl nitrite (t-BuONO), followed by the addition of trimethylsilyl azide (TMS-N₃). In a first attempt, the reaction was conducted for 25h, with a yield of 55%. A time prolongation to three days allowed to increase the yield up to 95%. The synthetic strategy was changed, first generating the diazonium salt in situ by addition of NaNO₂ to an acidic aqueous solution of N-(4-aminophenyl)acetamide, followed by the addition of NaN₃. This allowed to obtain **66** in 88% yield in much faster time, after only 2h of the reaction (Scheme 2-29B).



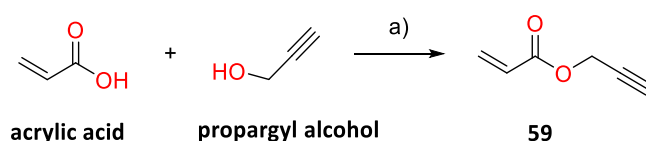
Scheme 2-29B. Reaction conditions: **a)** t-BuONO, TMS-N₃, anhydrous CH₃CN, N₂ atm, 0°C to rt, **66** 55% or three days, **66** 95% ; **b)** NaNO₂, NaN₃, H₂O, H₂SO₄, 0°C, 2h, **66** 88%.

Synthesis of (1-(4-acetamidophenyl)-1H-1,2,3-triazol-4-yl)methyl acrylate (**52**)

Compound **52** can be synthesized through the CuAAC reaction between **66** and alkyne **59**, obtained from the esterification between propargyl alcohol and acryloyl chloride or acrylic acid. Alternatively, it can be obtained from esterification between triazole **67** (the product of the click reaction between propargyl alcohol and 4'-azidoacetanilide **66**) and acryloyl chloride or acrylic acid (Scheme 2-30). Initially, the first approach was tried, however given the low yield of the obtained alkyne **59** (Scheme 2-31), it was decided to try the second approach.

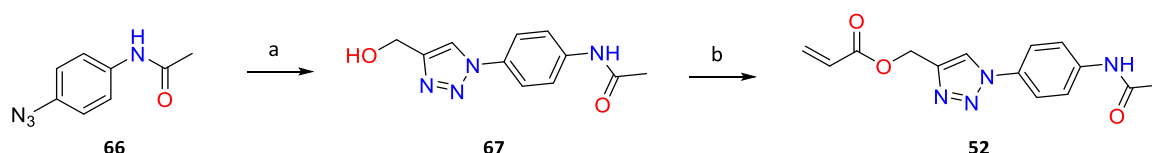


Scheme 2-30. Two possible retrosynthetic pathways of compound **52**.



Scheme 2-31. Reaction conditions: **a)** EDC·HCl, DMAP, TEA, dry CH₂Cl₂, N₂ atm, rt, 6.5h, **59** 13%.

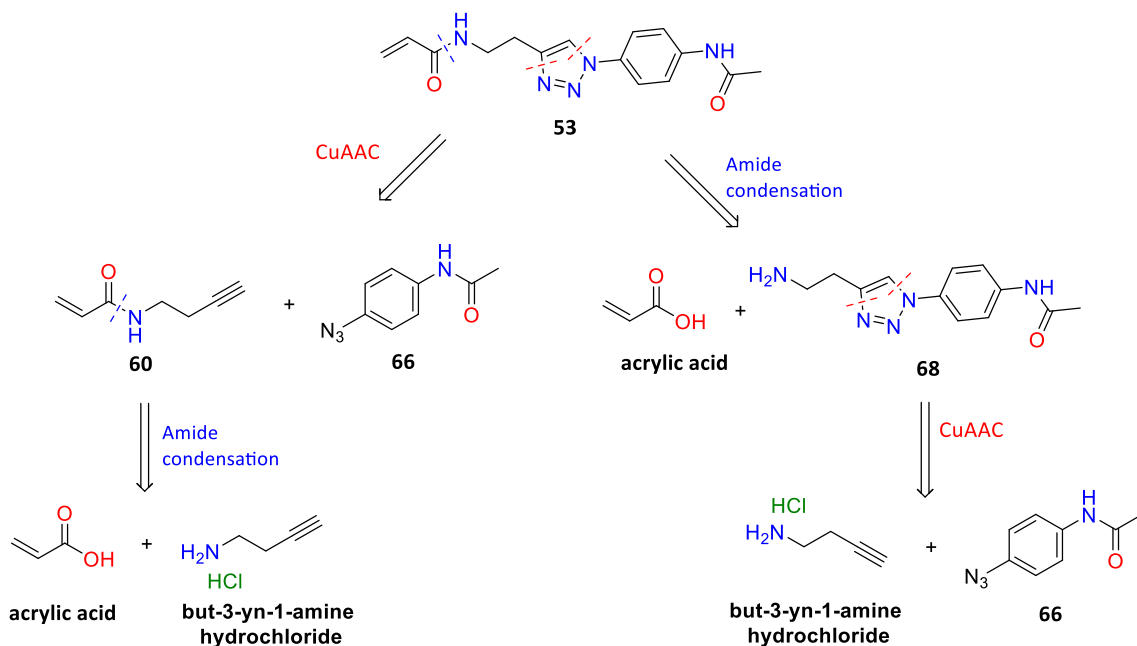
The CuAAC reaction between **66** and propargyl alcohol using the copper II acetate and sodium ascorbate for Cu(I) generation *in situ*, in a 4:1 mixture of DMF: H₂O gave the triazole **67** with an excellent yield of 99%. Then, the Steglich esterification using EDC·HCl, TEA, DMAP in anhydrous DMF gave **52** with a yield of 18%. Despite the low yield of the esterification step, the overall yield of the second strategy was 18% over two steps, making it more convenient than the first approach.



Scheme 3-32. Reaction conditions: **a)** propargyl chloride, Cu(OAc)₂·H₂O, Na-ascorbate, DMF/H₂O 4:1, rt, 6h, **67** 99%; **b)** acrylic acid, EDC·HCl, DMAP, TEA, dry DMF, N₂ atm, 0°C to rt, 23h, **52** 18%.

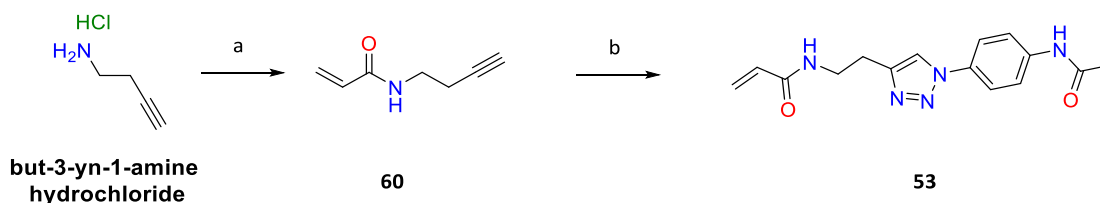
Synthesis of N-(2-(1-(4-acetamidophenyl)-1H-1,2,3-triazol-4-yl)ethyl)acrylamide (**53**)

Similarly to **52**, two retrosynthetic approaches are possible for the synthesis of triazole derivative **53**. In the first approach, **53** is obtained by the click reaction between amide **60** and **66**. In turn **60** derives from the condensation between acrylic acid and but-3-yn-1-amine hydrochloride. In the second approach, **53** results from the amide condensation between the triazole **68** and acrylic acid. In turn, **68** is the product of click chemistry between the but-3-yn-1-amine hydrochloride and **66**.



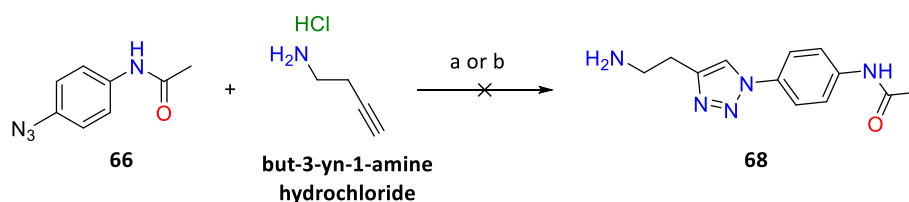
Scheme 2-33. Two possible retrosynthetic pathways of compound **52**.

Amide **60** was successfully synthesized from acrylic acid and but-3-yn-1-amine hydrochloride through condensation with HATU and DIPEA, in 48% yield. Then, a click reaction between **60** and **66** was carried out in DMF/H₂O 4:1 with Cu(OAc)₂·H₂O and Na-ascorbate, and **53** was obtained in 82% yield. The overall yield over the two steps was 39%.



Scheme 3-34. a) HATU, DIPEA, dry DMF, N₂ atm, rt, 5h, **53** 48%; b) **66**, Cu(OAc)₂·H₂O, Na-ascorbate, DMF/H₂O 4:1, rt, 19h, **53** 82%.

It is worth noting that the second approach was also tried out, but the click reaction between but-3-yn-1-chloride and **66** was unsuccessful due to a range of factors, including the high polarity of the product, its' poor solubility in organic solvents and the presence of but-3-yn-1-amine in a salt form, which complicated the handling and purification of the product. A second click reaction was attempted by adding DIPEA into the reaction mixture with the aim of desalting and improving the solubility of the amine and the potentially formed product, however the reaction failed.

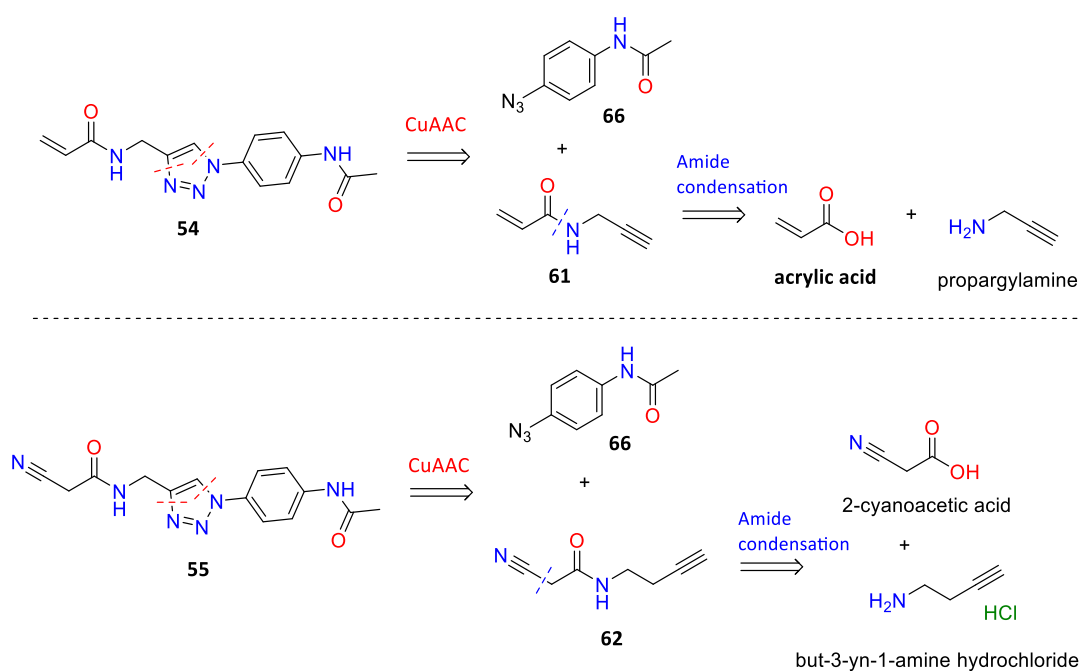


Scheme 3-35. **a)** $\text{Cu}(\text{OAc})_2 \cdot \text{H}_2\text{O}$, Na-ascorbate, DMF/ H_2O 4:1, rt, 20h; **b)** $\text{Cu}(\text{OAc})_2 \cdot \text{H}_2\text{O}$, Na-ascorbate, DIPEA, DMF/ H_2O 4:1, rt, 24h.

It was therefore concluded that it is best to avoid the synthesis of triazole derivatives with free primary amine groups, preferring in such cases the retrosynthetic route in which amide condensation precedes the click reaction.

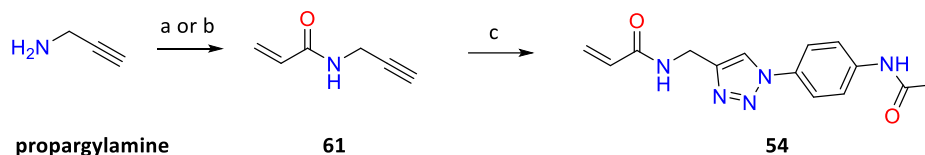
Synthesis of N-((1-(4-acetamidophenyl)-1H-1,2,3-triazol-4-yl)methyl)acrylamide (**54**) and N-((1-(4-acetamidophenyl)-1H-1,2,3-triazol-4-yl)methyl)-2-cyanoacetamide (**55**)

Following the successful strategy used for the synthesis of **53**, the retrosynthetic pathway of compounds **54** and **55** are shown in the Scheme 2-36.



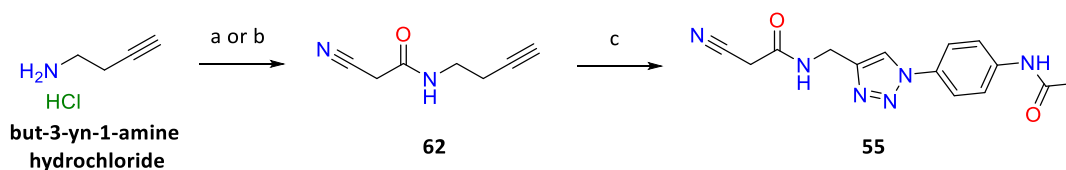
Scheme 2-36. Retrosynthetic pathways for the synthesis of compounds **54** and **55**.

An initial attempt to synthesize **62** from acrylic acid and propargylamine using HATU and DIPEA in dry CH_2Cl_2 failed. The change of reaction conditions employing a Steglich-type amide condensation with EDC·HCl, DMAP and TEA resulted in the formation of **61** in 26% yield. The following CuAAC reaction with **66** allowed to obtain the desired **54** in 33% yield. The overall yield over the two steps was 9% (Scheme 3-37).



Scheme 2-37. a) HATU, DIPEA, dry CH_2Cl_2 , N_2 atm, rt, 6h n.r.; b) EDC·HCl, DMAP, TEA, dry CH_2Cl_2 , N_2 atm, 0°C to rt, 23h, **61** 26%; c) **66**, $\text{Cu}(\text{OAc})_2\cdot\text{H}_2\text{O}$, Na-ascorbate, DMF/ H_2O 4:1, rt, 3h, **54** 33%.

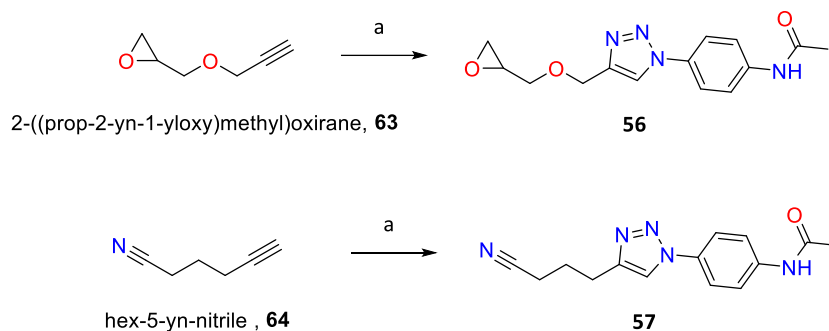
Similarly to compound **61**, the synthesis of **62** was initially attempted by condensing cyanacetic acid and but-3-yn-1-amine hydrochloride using HATU and DIPEA, but without success (Scheme 2-37). Changing the reaction conditions to EDC·HCl, DMAP and TEA allowed to obtain the desired amide **62** in 66% yield. Subsequently, compound **62** underwent the CuAAC reaction with **66**, and the final product **54** was obtained in a 23% yield. The total yield over the two steps was thus 15% (Scheme 2-38).



Scheme 2-38. a) HATU, DIPEA, dry DMF, N_2 atm, rt; n.r. b) EDC·HCl, DMAP, TEA, dry CH_2Cl_2 , N_2 atm, 0°C to rt, 21h, **62** 66%; c) **66**, $\text{Cu}(\text{OAc})_2\cdot\text{H}_2\text{O}$, Na-ascorbate, DMF/ H_2O 4:1, rt, 3h, **55** 23%.

Synthesis of N-(4-(4-((oxiran-2-ylmethoxy)methyl)-1H-1,2,3-triazol-1-yl)phenyl)acetamide (**56**) and N-(4-(4-(3-cyanopropyl)-1H-1,2,3-triazol-1-yl)phenyl)acetamide (**57**)

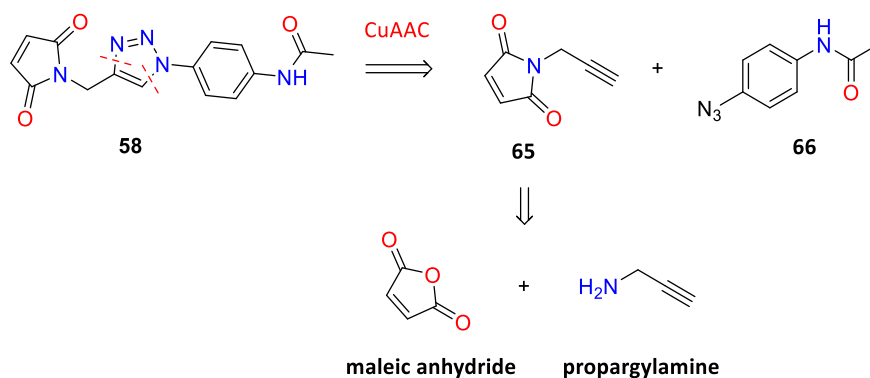
The triazole derivatives **56** and **57** could be obtained in one step, through the click reaction between **66** and commercially available 2-((prop-2-yn-1-yloxy)methyl)oxirane **63** and hex-5-yn-nitrile **64** (Scheme 2-39). Using $\text{Cu}(\text{OAc})_2\cdot\text{H}_2\text{O}$ and Na-ascorbate, in DMF/ H_2O 4:1, the desired products **56** and **57** were obtained in 89 % and 75 % yield, respectively (Scheme 2-39).



Scheme 2-39. a) **66**, Cu(OAc)₂·H₂O, Na-ascorbate, DMF/H₂O 4:1, rt, 5h, **56** 89%; **57** 73%.

Synthesis of N-(4-(4-((2,5-dioxo-2,5-dihydro-1H-pyrrol-1-yl)methyl)-1H-1,2,3-triazol-1-yl)phenyl)acetamide (**58**)

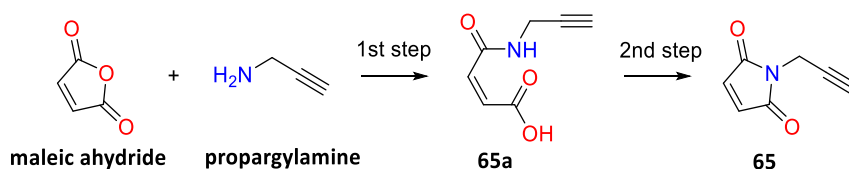
The retrosynthetic route to afford the compound **58** is shown in , according to which the final molecule could be obtained through a click reaction between N-substituted maleimide-bearing alkyne **65** and 4'-azidoacetanilide **66**. In turn, the **65** was synthesized from maleic anhydride and propargylamine.



Scheme 2-40. Retrosynthetic pathways for the synthesis of compound **58**.

The critical step was the synthesis of N-substituted maleimide (Table 2-14).

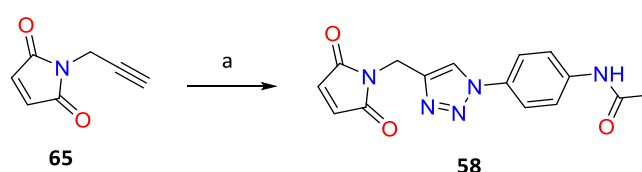
Table 2-14. Synthesis of N-propargylmaleimide **65**.



Entry	1° step, reaction conditions	Intermediate 65a	2° step, reaction conditions	Result
I	Acetone, reflux, 2h	Crude obtained	pTSA, MeOH, reflux, 18h	Failed
II	AcOH, rt, 19h	Crude obtained	Ac ₂ O, AcONa, 65°C, dark, 2h	34% yield
III	One step, pTSA, toluene, 130°C, 3 days			Failed

The conditions of the failed reactions probably induced the polymerization of the final product and/or of the intermediates, as supported by the increase of viscosity of the reaction mixture and by the presence of multiple spots in the TLC. As shown in Table 2-14, the successfully obtained N-propargylmaleimide **65** was synthesized by solubilizing maleic anhydride and propargylamine in AcOH and leaving the mixture at room temperature, in the dark, for 18h. By evaporating the solvent under reduced pressure, the intermediate **65a** was obtained. By subsequent solubilization of the impure crude of **65a** in Ac₂O with AcONa over 2h at 65°C, the cyclic product **65** was obtained in 34% yield over two steps.

Finally, compound **58** was synthesized through a CuAAC reaction with **66**, obtaining the desired product in 22% yield (Scheme 2-41). The overall yield over the three steps was 7%.



Scheme 2-41. a) **66**, Cu(OAc)₂·H₂O, Na-ascorbate, DMF/H₂O 4:1, rt, 4h, **58** 22%.

2.4.3.2.2 Synthesis of warhead-bearing amide derivatives

A set of warhead-bearing amide derivatives to target α Cys4 depicted in the Figure 2-25 was selected for synthesis.

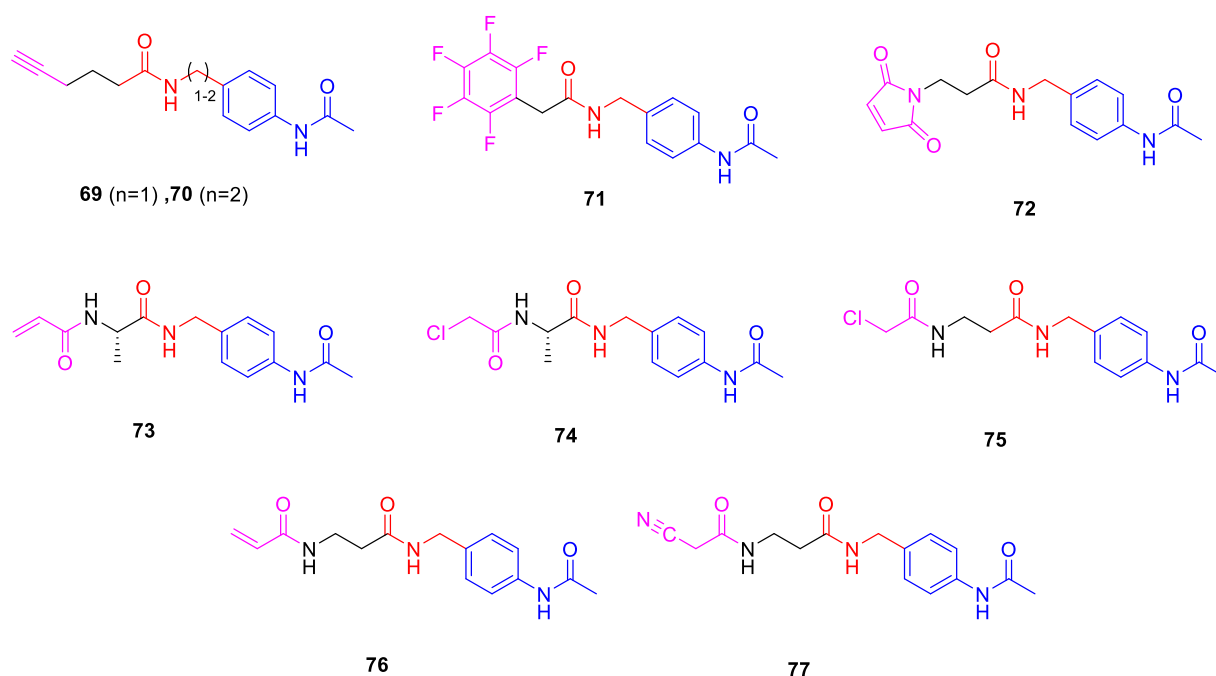
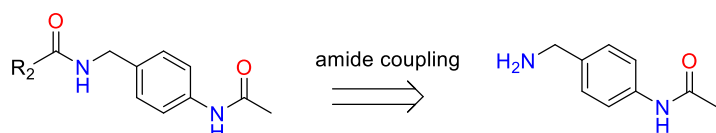


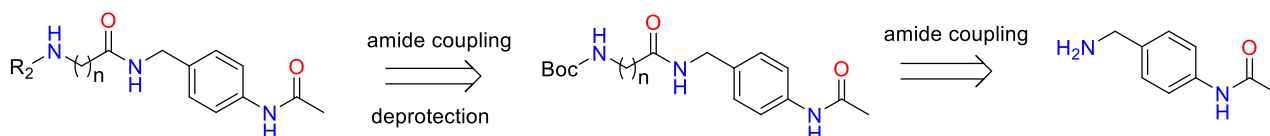
Figure 2-25. Chemical structures of warhead-bearing amide derivatives selected for synthesis.

Compounds **69-72** could be synthesized in one step through an amide coupling reaction (Scheme 2-42A), while compounds **73-77** could be obtained in three steps: amide coupling with a Boc-protected aminoacid, deprotection and the amide coupling with the corresponding warhead moiety (Scheme 2-42B).

A



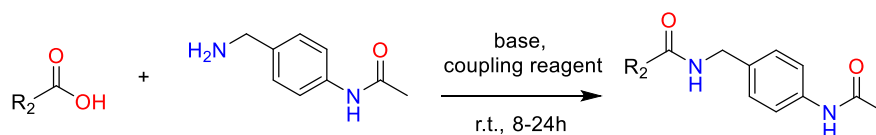
B



Scheme 2-42. General retrosynthetic pathway for the synthesis of amide derivatives.

Synthesis of amide derivatives **69-72**

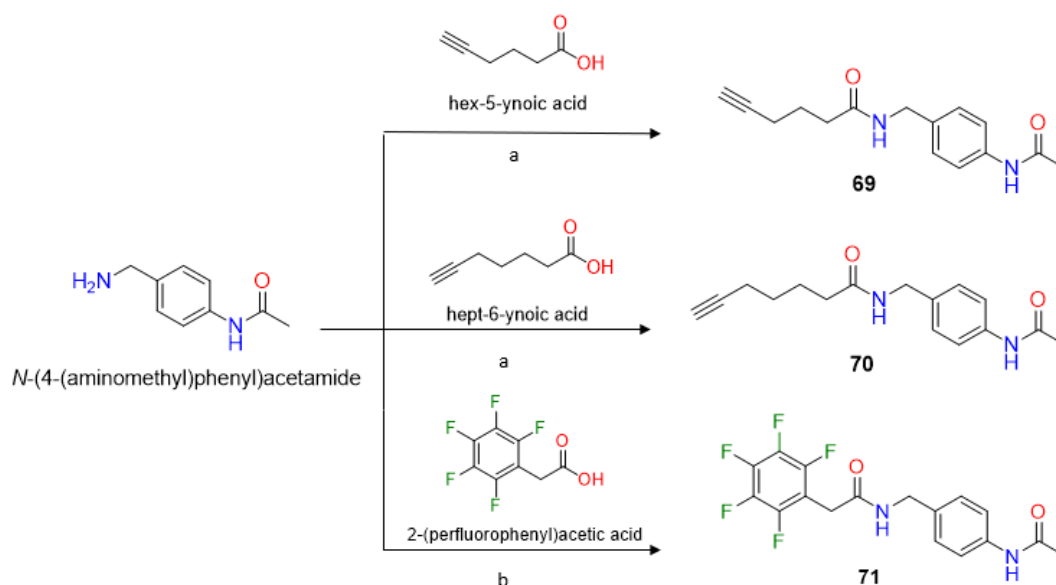
The amide derivatives **69-72** were synthesized directly in one step, starting from the N-(4-(aminomethyl)phenyl)acetamide with the corresponding acid (Scheme 2-43).



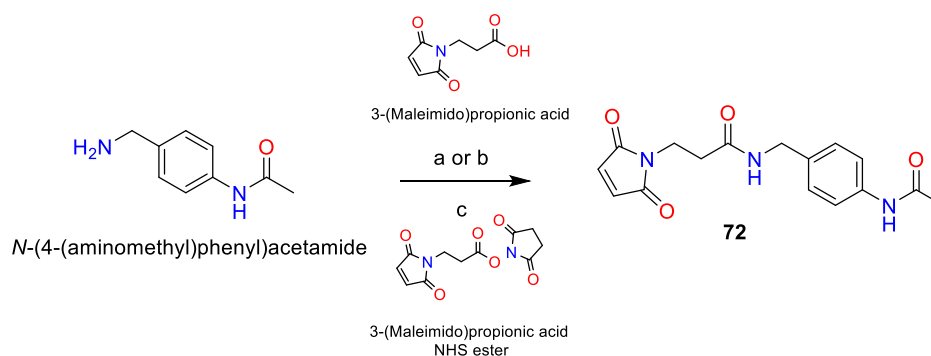
Scheme 2-43. General procedure for amide synthesis.

N-(4-acetamidobenzyl)hex-5-ynamide **69** and N-(4-acetamidobenzyl)hept-6-ynamide **70** were synthesized by coupling of N-(4-(aminomethyl)phenyl)acetamide and hex-5-ynoic and hept-6-ynoic acid, respectively. The reactions were performed using HATU as the condensing agent and DIPEA as the base, in a mixture of anhydrous DCM/DMF as the solvent, giving the desired products in 50% (**69**) and 18% (**70**) yields. In its turn, N-(4-acetamidobenzyl)-2-(perfluorophenyl)acetamide **71** was obtained in 47% yield, by employing EDC·HCl as the condensing agent, in the presence of DMAP and TEA (Scheme 2-44).

However, both synthetic procedures used to obtain **69-70** and **71** failed in the attempt to obtain compound **72** by the reaction of N-(4-(aminomethyl)phenyl)acetamide with 3-(maleimido)propionic acid. Eventually, the synthetic approach was changed and compound **72** was successfully obtained in 37% yield by using the NHS ester of the 3-



Scheme 2-44. Synthesis of **69-71**. **a)** HATU, DIPEA, anhydrous DCM/DMF, N₂ atm rt; 12h, **69** 50%; **70** 18% **b)** EDC-HCl, DMAP, TEA, anhydrous DCM/DMF, N₂ atm, 0°C to rt, 12h, **71** 47%.

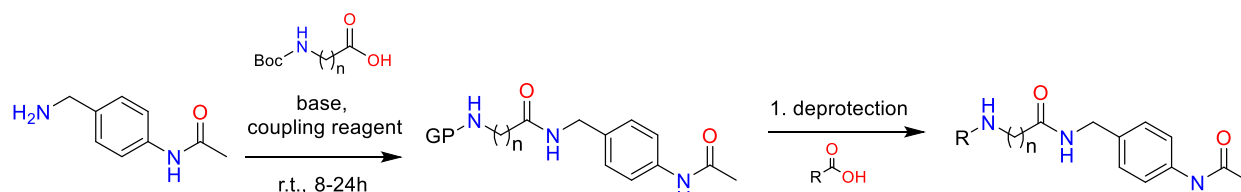


Scheme 2-45. Synthesis of **69-71**. **a)** HATU, DIPEA, anhydrous DCM/DMF, N₂ atm rt; 12h, n.r.; **b)** EDC-HCl, DMAP, TEA, anhydrous DCM/DMF, N₂ atm, 0°C to rt, 12h, n.r.; **c)** DIPEA, anhydrous DCM/DMF, N₂ atm, 0°C to rt, 3h, 37%.

(maleimido)propionic acid in place of the free acid, and in the presence of DIPEA as a base (Scheme 2-45).

Synthesis of amide derivatives **73-77**

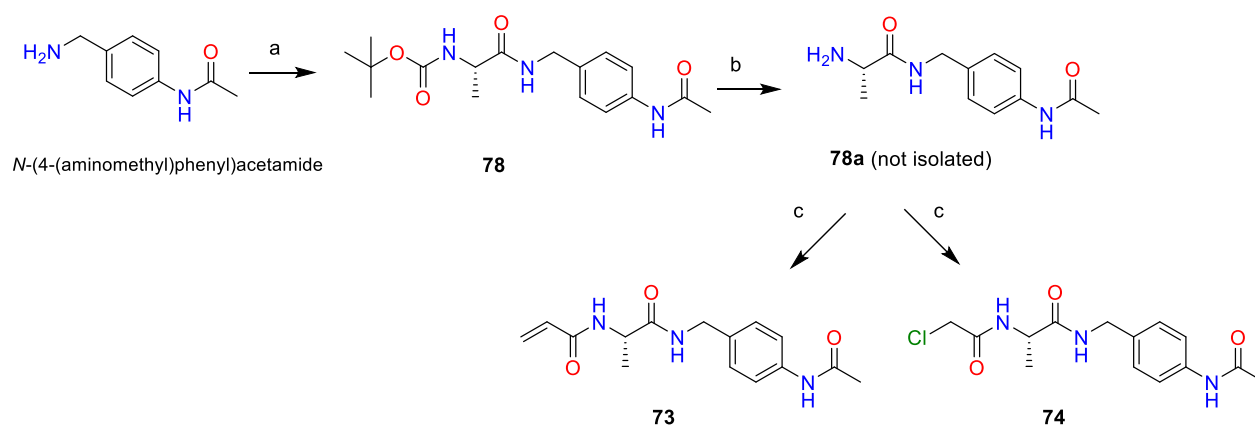
The amide derivatives **73-77** can be synthesized in three steps, starting from the amide coupling of the *N*-(4-(aminomethyl)phenyl)acetamide with Boc-protected alanine or beta-



Scheme 2-46. General procedure for the synthesis of the amide derivatives **73-77**.

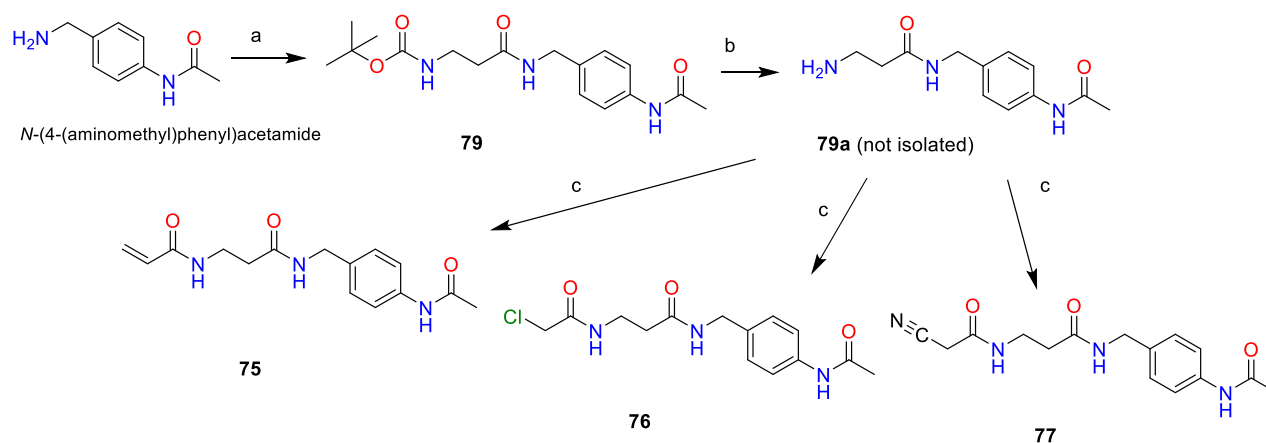
alanine, followed by the deprotection and coupling with the corresponding warhead-bearing acid (Scheme 2-46).

To obtain (S)-N-(1-((4-acetamidobenzyl)amino)-1-oxopropan-2-yl)acrylamide **73** and (S)-N-(4-acetamidobenzyl)-2-(2-chloroacetamido)propenamide **74**, in the first step N-(4-(aminomethyl)phenyl)acetamide was coupled with Boc-protected L-alanine using the above mentioned HATU/DIPEA system, which allowed to obtain the intermediate **78** in 52 % yield. The latter was then deprotected using a 40% solution of TFA in DCM, and directly used in the next coupling with the warhead-bearing acrylic and chloroacetic acids, giving the desired products **73** and **74** in 17% and 24% yield, respectively (Scheme 2-47).



Scheme 2-47. Synthesis of **69-71**. **a)** HATU, DIPEA, anhydrous DCM/DMF, N₂ atm rt; 12h, **78** 52%; **b)** 40% TFA in DCM, o/n, **78a** not isolated; **c)** acrylic acid (**73**) or chloroacetic acid (**74**), EDC·HCl, DMAP, TEA, anhydrous DCM/DMF, N₂ atm, 0°C to rt, 18h, **73** 17%; **74** 24%.

A similar synthetic pathway was used to obtain the compounds **75-77** (Scheme 2-48). *N*-(4-(aminomethyl)phenyl)acetamide was coupled with Boc-protected beta-alanine using EDC·HCl, DMAP and TEA, and the intermediate **79** was obtained in 60% yield. The next steps



Scheme 2-48. Synthesis of **75-77**. **a)** EDC·HCl, DMAP, TEA, anhydrous DCM/DMF, N₂ atm, 0°C to rt, 18h, **79** 60%; **b)** 40% TFA in DCM, o/n, **79a** not isolated; **c)** acrylic acid (**75**) or chloroacetic acid (**76**) or cyanoacetic acid (**77**), EDC·HCl, DMAP, TEA, anhydrous DCM/DMF, N₂ atm, 0°C to rt, 18h, **74** 12%; **76** 26%, **77** 54%.

included its deprotection and amide coupling with the acrylic, chloroacetic and cyanoacetic acids, to obtain **75** (12%), **76** (26%) and **77** (54%).

X-ray crystallography structure determination

The synthesized compounds were submitted for X-ray crystallography experiments at the Paul Scherrer Institute, performed by Anne-Catherine Abel. In a result of soaking experiments, the binding of compounds **69-71** was clearly defined in the pocket. Furthermore, compounds **52**, **69** and **73** were clearly bound in the co-soaking experiments with vinblastine. Currently the work on the crystal structures of the identified hits is ongoing. Additionally, binding was detected for the triazole derivatives **54-56** and amide derivatives **74-76**, however the electron density of those compound was not sufficiently defined to model the correct pose of the compounds in the crystal structures.

Biochemical evaluation

The synthesized compounds were sent to Centro de Investigaciones Biológicas Margarita Salas (CIB-CSIC) in Madrid, Spain, for *in vitro* biochemical testing to determine their effect on tubulin polymerization dynamics. The ligands were tested by incubating them at 37°C with tubulin purified from calf brains and by following the absorption at 350 nm, which

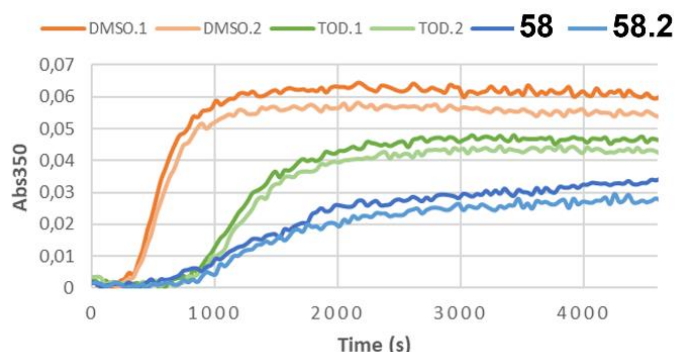


Figure 2-26. Inhibition of tubulin assembly by compound **58**. All experiments were performed as duplicates of two independent experiments.

mirrors the formation of microtubules or other aggregates in solution. Totalam is a weak inhibitor of tubulin assembly, therefore its polymerization curve is characterized by a decrease in the slope and in the plateau of the curve, as well as in a longer lag time which indicates fewer nucleation events occurring in solution. Most of the obtained compounds, including those that which showed clear binding in X-ray crystallographic experiments, showed no effect on tubulin polymerization. Exception constitutes the maleimide-containing triazole derivative **58**, which has showed stronger effect on polymerization than Totalam itself (Figure 2-26). Further experiments with the remaining amide derivatives are ongoing. Moreover, in case of compound **58**, MS analysis experiments will be performed, to confirm the covalent binding of this derivative and its selectivity.

2.4.4 EXPERIMENTAL PART

Chemistry

General Experimental Procedures

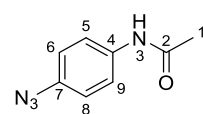
Unless otherwise stated, reagents were purchased from general suppliers (Sigma Aldrich and Fluorochem) and used without further purification. All solvents were of reagent grade or HPLC grade. All reactions were carried out in oven-dried glassware and dry solvents, under nitrogen atmosphere and were monitored by glass or aluminium TLC on silica gel (Merck precoated 60F254 plates), with detection by UV light (254 nm), or by TLC stains, such as potassium permanganate, molybdc reagent, ninhydrin and bromocresol green.

Purification of intermediates and final products was mostly carried out by flash chromatography using as stationary phase high purity grade silicagel (Merck Grade, pore size 60 Å, 230-400 mesh particle size, Sigma Aldrich). Alternatively, purification was performed by a Biotage® system in normal phase using Biotage® Sfar Silica D cartridges (10/25 g).

¹H NMR and ¹³C-NMR spectra were recorded on a Bruker Avance Spectrometer 400 MHz using commercially available deuterated solvents (chloroform-d, methanol-d4) at room temperature. Chemical shifts (δ) are reported in parts per million (ppm) and are reported relative to TMS, used as an internal standard. Data for ¹H NMR are reported as follows: chemical shift (δ/ppm), multiplicity, coupling constants (Hz). Multiplicities are reported as follows: s = singlet, d = doublet, t = triplet, m = multiplet, br s = broad singlet. Data for ¹³C NMR are reported in terms of chemical shift (δ/ppm).

Synthesis of 4'-azidoacetanilide (**66**)

A mixture of H₂SO₄ 96% (665 μL) and H₂O (665 μL) was added to a stirred solution of 4'-aminoacetanilide (**1**) (500 mg, 3.33 mmol, 1 eq.) in H₂O (5 mL) at rt. The reaction mixture was cooled at 0°C, then NaNO₂ 5M (232 mg, 3.36 mmol, 1.01 eq.) in H₂O (672 μL) was added dropwise. After 15 minutes, NaN₃ (268 mg, 4.13 mmol, 1.24 eq.) was added. The reaction mixture was stirred at 0°C for 2 hours, then the mixture was extracted with CH₂Cl₂ (3x20mL). The collected organic phase was washed with H₂O, then dried over Na₂SO₄, filtered and concentrated under reduced pressure. Pure 4'-azidoacetanilide **66** (526.3 mg, 2.92 mmol) was obtained without any further purification, with an overall yield of 88%.

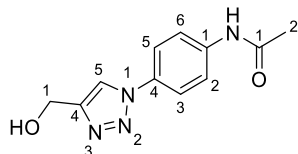


¹H NMR (400 MHz, CDCl₃): δ 7.49 (d, *J* = 8.8 Hz, 2H, **5-H**, **9-H**), 7.29 (s, 1H, **3-NH**), 6.97 (d, *J* = 8.8 Hz, 2H, **6-H**, **8-H**), 2.17 (s, 3H, **1-H**).

¹³C-NMR (101 MHz, CDCl₃): δ 169.20, 136.23, 135.34, 122.00, 119.84, 24.80

Synthesis of *N*-(4-(4-(hydroxymethyl)-1*H*-1,2,3-triazol-1-yl)phenyl)acetamide (**67**)

Cu(OAc)₂ · H₂O (27.9 mg, 0.14 mmol, 0.5 eq.), Na-ascorbate 1M in H₂O (220 μL, 0.22 mmol, 0.8 eq.) and propargyl alcohol (23.5 mg, 0.42 mmol, 1.5 eq.) were added in this order to a stirred solution of 4'-azidoacetanilide **66** (50.0 mg, 0.28 mmol, 1 eq.) in DMF/H₂O 4:1 (5.6 mL + 1.4 mL), at rt. The reaction mixture was stirred for 6 hours. After solvent evaporation under reduced pressure, the crude product was purified by flash chromatography (silicagel, eluent mixture 95:5 CH₂Cl₂/MeOH) providing 65.0 mg (0.28 mmol) of pure *N*-(4-(4-(hydroxymethyl)-1*H*-1,2,3-triazol-1-yl)phenyl)acetamide **67**, with an overall yield of 99%.



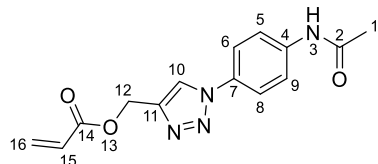
¹H NMR (400 MHz, DMSO-d₆): δ 10.17 (s, 1H, **3-NH**), 8.56 (s, 1H, **10-H**), 7.84 – 7.72 (m, 4H, **5-H, 6-H, 8-H, 9-H**), 5.28 (t, *J* = 5.6 Hz, 1H, **13-OH**), 4.60 (d, *J* = 5.6 Hz, 2H, **12-H**), 2.08 (s, 3H, **1-H**).

¹³C NMR (101 MHz, DMSO-d₆): δ 168.56, 148.94, 139.42, 131.76, 120.74, 120.52, 119.67, 54.96, 24.00.

MS (ESI) *m/z* [M + Na]⁺ calcd. for C₁₁H₁₂N₄O₂Na: 255.09, found: 255.12

Synthesis of (1-(4-acetamidophenyl)-1*H*-1,2,3-triazol-4-yl)methyl acrylate (**52**)

TEA (36.4 mg, 0.36 mmol, 2.1 eq.), EDC·HCl (69.0 mg, 0.36 mmol, 2.1 eq.) and DMAP (11.0 mg, 0.09 mmol, 0.5 eq.) were added in this order to a stirred solution of acrylic acid (14.4 mg, 0.20 mmol, 1.2 eq.) in anhydrous DMF (1.7 mL), at 0°C and under nitrogen atmosphere. After 10 minutes *N*-(4-(4-(hydroxymethyl)-1*H*-1,2,3-triazol-1-yl)phenyl)acetamide **67** (40.0 mg, 0.17 mmol, 1 eq.) was added. The reaction mixture was stirred for 23 hours at rt. After reaction completion and solvent evaporation under reduced pressure, saturated NH₄Cl (10 mL) was added and the aqueous phase was extracted with CH₂Cl₂ (3x20mL). The collected organic phase was washed with saturated NaHCO₃ (10 mL), then dried over Na₂SO₄, filtered, and concentrated under reduced pressure. The crude product was purified by flash chromatography (silicagel, eluent mixture 97:3 CH₂Cl₂/MeOH) providing 8.8 mg (0.03 mmol) of pure (1-(4-acetamidophenyl)-1*H*-1,2,3-triazol-4-yl)methyl acrylate **52**, with an overall yield of 18%.



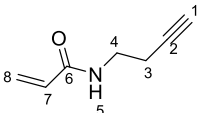
¹H NMR (400 MHz, CDCl₃): δ 8.03 (s, 1H, **10-H**), 7.78 – 7.58 (m, 4H, **5-H, 6-H, 8-H, 9-H**), 6.45 (dd, *J* = 17.3, 1.4 Hz, 1H, **16a-H**), 6.15 (dd, *J* = 17.3, 10.4 Hz, 1H, **15-H**), 5.87 (dd, *J* = 10.5, 1.4 Hz, 1H, **16b-H**), 5.38 (s, 2H, **12-H**), 2.22 (s, 3H, **1-H**).

¹³C NMR (101 MHz, DMSO-d₆): δ 168.62, 165.15, 142.73, 139.71, 132.23, 131.45, 127.92, 122.87, 120.83, 119.65, 57.20, 24.03.

MS (ESI) *m/z* [M + Na]⁺ calcd. for C₁₄H₁₄N₄O₃Na: 309.10, found: 309.14

Synthesis of *N*-(but-3-yn-1-yl)acrylamide (**60**)

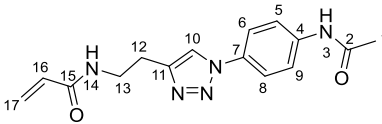
HATU (262 mg, 0.69 mmol, 1 eq.), DIPEA (268 mg, 2.07 mmol, 3 eq.) and but-3-yn-1-amine hydrochloride (110 mg, 1.04 mmol, 1.5 eq.) were added in this order to a stirred solution of acrylic acid (50.0 mg, 0.69 mmol, 1 eq.) in anhydrous DMF (6.9 mL), at rt and under nitrogen atmosphere. The reaction mixture was stirred for 5 hours. After reaction completion and solvent evaporation under reduced pressure, HCl 1M (10 mL) was added and the aqueous phase was extracted with CH₂Cl₂ (3x20mL). The collected organic phase was washed with NaOH 1M (10 mL), then dried over Na₂SO₄, filtered, and concentrated under reduced pressure. The crude product was purified by flash chromatography (silicagel, eluant mixture 99:1 CH₂Cl₂/MeOH) providing 40.5 mg (0.33 mmol) of pure *N*-(but-3-yn-1-yl)acrylamide **60** with an overall yield of 48%.

 ¹H NMR (400 MHz, CDCl₃): δ 6.37 (bs, 1H, **5-NH**), 6.25 (dd, *J* = 17.0, 1.6 Hz, 1H, **8a-H**), 6.12 (dd, *J* = 17.0, 10.1 Hz, 1H, **7**), 5.62 (dd, *J* = 10.1, 1.6 Hz, 1H, **8b-H**), 3.45 (q, *J* = 6.4 Hz, 2H, **4-H**), 2.41 (td, *J* = 6.6, 2.6 Hz, 2H, **3-H**), 1.99 (t, *J* = 2.6 Hz, 1H, **1-H**).

¹³C NMR (101 MHz, CDCl₃): δ 165.72, 130.67, 126.43, 81.35, 69.91, 38.07, 19.22.

Synthesis of *N*-(2-(1-(4-acetamidophenyl)-1*H*-1,2,3-triazol-4-yl)ethyl)acrylamide (**53**)

Cu(OAc)₂ · H₂O (33.9 mg, 0.17 mmol, 0.5 eq.), Na-ascorbate 1M in H₂O (270 μL, 0.27 mmol, 0.8 eq.) and *N*-(but-3-yn-1-yl)acrylamide **60** (41.7 mg, 0.34 mmol, 1 eq.) were added in this order to a stirred solution of 4'-azidoacetanilide **66** (66.7 mg, 0.37 mmol, 1.1 eq.) in DMF/H₂O 4:1 (6.8 mL + 1.7 mL), at rt. The reaction mixture was stirred for 19 hours. After solvent evaporation under reduced pressure, the crude product was purified by flash chromatography (silicagel, eluent mixture 92:8 CH₂Cl₂/MeOH, then 9:1 CH₂Cl₂/MeOH) providing 83.2 mg (0.28 mmol) of pure *N*-(2-(1-(4-acetamidophenyl)-1*H*-1,2,3-triazol-4-yl)ethyl)acrylamide (**50**), with an overall yield of 82%.

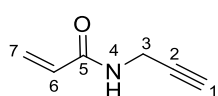
 ¹H NMR (400 MHz, DMSO-d₆): δ 10.18 (s, 1H, **3-NH**), 8.51 (s, 1H, **10-NH**), 8.24 (t, *J* = 5.8 Hz, 1H, **14-NH**), 7.77 (bs, 4H, **5-H**, **6-H**, **8-H**, **9-H**), 6.21 (dd, *J* = 17.1, 10.0 Hz, 1H, **16-H**), 6.08 (dd, *J* = 17.1, 2.3 Hz, 1H, **17a-H**), 5.58 (dd, *J* = 10.0, 2.4 Hz, 1H, **17b-H**), 3.46 (q, *J* = 6.5 Hz, 2H, **13-H**), 2.88 (t, *J* = 7.2 Hz, 2H, **12-H**), 2.08 (s, 3H, **1-H**).

¹³C NMR (101 MHz, DMSO-d₆): δ 168.56, 164.66, 145.38, 139.37, 131.78, 131.76, 125.06, 120.48, 120.42, 119.67, 38.34, 25.50, 24.02.

MS (ESI) *m/z* [M + Na]⁺ calcd. for C₁₅H₁₇N₅O₂Na: 322.13, found: 322.17

Synthesis of *N*-(prop-2-yn-1-yl)acrylamide (**61**)

TEA (140 mg, 1.38 mmol, 2 eq.), EDC·HCl (265 mg, 1.38 mmol, 2 eq.) and DMAP (42.8 mg, 0.35 mmol, 0.5 eq.) were added in this order to a stirred solution of acrylic acid (50.0 mg, 0.69 mmol, 1 eq.) in anhydrous CH₂Cl₂ (6.9 mL), at 0°C and under nitrogen atmosphere. After 10 minutes propargylamine (57.3 mg, 1.04 mmol, 1.5 eq.) was added. The reaction mixture was stirred for 23 hours at rt. Afterwards, the reaction mixture was washed with saturated NH₄Cl (10 mL), then the acid aqueous phase was extracted with CH₂Cl₂ (5x20mL). The collected organic phase was washed with saturated NaHCO₃ (10 mL), then dried over Na₂SO₄, filtered, and concentrated under reduced pressure. The crude product was purified by flash chromatography (silicagel, eluant mixture 95:5 CH₂Cl₂/MeOH) providing 19.3 mg (0.18 mmol) of pure *N*-(prop-2-yn-1-yl)acrylamide **61**, with an overall yield of 26%.

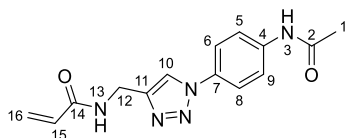


¹H NMR (400 MHz, CDCl₃): δ 6.30 (dd, *J* = 17.0, 1.4 Hz, 1H, **7a-H**), 6.12 (dd, *J* = 17.0, 10.3 Hz, 1H, **6-H**), 5.67 (dd, *J* = 10.3, 1.4 Hz, 1H, **7b-H**), 4.11 (dd, *J* = 5.3, 2.6 Hz, 2H, **3-H**), 2.23 (t, *J* = 2.6 Hz, 1H, **1-H**).

¹³C NMR (101 MHz, DMSO-d₆): δ 164.31, 131.11, 125.86, 80.92, 73.08, 27.87.

Synthesis of *N*-((1-(4-acetamidophenyl)-1*H*-1,2,3-triazol-4-yl)methyl)acrylamide (**54**)

Cu(OAc)₂ · H₂O (18.0 mg, 0.09 mmol, 0.5 eq.), Na-ascorbate 1M in H₂O (140 μL, 0.14 mmol, 0.8 eq.) and *N*-(prop-2-yn-1-yl)acrylamide (**55**) dissolved in a little amount of DMF (19.3 mg, 0.18 mmol, 1 eq.) were added in this order to a stirred solution of 4'-azidoacetanilide (**17**) (36.0 mg, 0.20 mmol, 1.1 eq.) in DMF/H₂O 4:1 (3.6 mL + 0.9 mL), at rt. The reaction mixture was stirred for 3 hours. After solvent evaporation under reduced pressure, the crude product was purified by flash chromatography (silicagel, eluent mixture 93:7 CH₂Cl₂/MeOH) providing 17.9 mg (0.06 mmol) of pure *N*-((1-(4-acetamidophenyl)-1*H*-1,2,3-triazol-4-yl)methyl)acrylamide **54**, with an overall yield of 33%.



¹H NMR (400 MHz, DMSO-d₆): δ 10.17 (s, 1H, **3-NH**), 8.64 (t, *J* = 5.6 Hz, 1H, **13-NH**), 8.56 (s, 1H, **10-H**), 7.83 – 7.73 (m, 4H, **5-H, 6-H, 8-H, 9-H**), 6.27 (dd, *J* = 17.1, 10.1 Hz, 1H, **15-H**), 6.13 (dd, *J* = 17.1, 2.3 Hz, 1H, **16a-H**), 5.62 (dd, *J* = 10.1, 2.3 Hz, 1H, **16b-H**), 4.46 (d, *J* = 5.6 Hz, 2H, **12-H**), 2.08 (s, 3H, **1-H**).

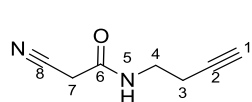
¹³C NMR (101 MHz, DMSO-d₆): δ 168.58, 164.52, 145.49, 139.52, 131.63, 131.49, 125.49, 121.01, 120.58, 119.67, 34.12, 24.03.

MS (ESI) *m/z* [M + Na]⁺ calcd. for C₁₅H₁₅N₅O₂Na: 320.11, found: 320.18

Synthesis of *N*-(but-3-yn-1-yl)-2-cyanoacetamide (**62**)

TEA (209 mg, 2.07 mmol, 3.5 eq.), EDC·HCl (226 mg, 1.18 mmol, 2 eq.) and DMAP (36.7 mg, 0.30 mmol, 0.5 eq.) were added in this order to a stirred solution of cyanoacetic acid (**59**) (50.0 mg, 0.59 mmol, 1 eq.) in anhydrous CH₂Cl₂ (5.9 mL), at 0°C and under nitrogen atmosphere. After 10 minutes but-3-yn-1-amine hydrochloride (94.0 mg, 0.89 mmol, 1.5

eq.) was added. The reaction mixture was stirred for 21 hours at rt. Afterwards, the reaction mixture was washed with saturated NH_4Cl (10 mL), then the acid aqueous phase was extracted with CH_2Cl_2 (10x20mL). The collected organic phase was washed with saturated NaHCO_3 (10 mL), then dried over Na_2SO_4 , filtered, and concentrated under reduced pressure. The crude product was purified by flash chromatography (silicagel, eluant mixture 95:5 $\text{CH}_2\text{Cl}_2/\text{MeOH}$) providing 53.7 mg (0.39 mmol) of pure *N*-(but-3-yn-1-yl)-2-cyanoacetamide **62**, with an overall yield of 66%.



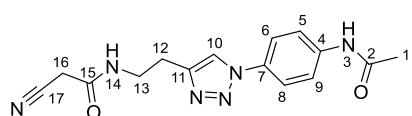
^1H NMR (400 MHz, CDCl_3): δ 6.65 (s, 1H, **5-NH**), 3.45 (q, $J = 6.4$ Hz, 2H, **4-H**), 3.41 (s, 2H, **7-H**), 2.44 (td, $J = 6.5, 2.6$ Hz, 2H, **3-H**), 2.05 (t, $J = 2.6$ Hz, 1H, **1-H**).

^{13}C NMR (101 MHz, CDCl_3): δ 161.79, 114.85, 80.91, 70.58, 38.90, 26.04, 19.12.

$R_f = 0.48$ (95:5 $\text{CH}_2\text{Cl}_2/\text{MeOH}$).

Synthesis of *N*-(2-(1-(4-acetamidophenyl)-1H-1,2,3-triazol-4-yl)ethyl)-2-cyanoacetamide (**55**)

$\text{Cu}(\text{OAc})_2 \cdot \text{H}_2\text{O}$ (39.9 mg, 0.20 mmol, 0.5 eq.), Na-ascorbate 1M in H_2O (310 μL , 0.31 mmol, 0.8 eq.) and *N*-(but-3-yn-1-yl)-2-cyanoacetamide **62** dissolved in a little amount of DMF (53.7 mg, 0.39 mmol, 1 eq.) were added in this order to a stirred solution of 4'-azidoacetanilide **66** (77.5 mg, 0.43 mmol, 1.1 eq.) in DMF/ H_2O 4:1 (7.8 mL + 2.0 mL), at rt. The reaction mixture was stirred for 3 hours. After solvent evaporation under reduced pressure, the crude product was purified by flash chromatography (silicagel, eluent mixture 93:7 $\text{CH}_2\text{Cl}_2/\text{MeOH}$) providing 28.2 mg (0.09 mmol) of pure *N*-(2-(1-(4-acetamidophenyl)-1H-1,2,3-triazol-4-yl)ethyl)-2-cyanoacetamide **55**, with an overall yield of 23%.



^1H NMR (400 MHz, DMSO-d_6): δ 10.18 (s, 1H, **3-NH**), 8.51 (s, 1H, **10-H**), 8.36 (t, $J = 5.6$ Hz, 1H, **14-NH**), 7.77 (bs, 4H, **5-H, 6-H, 8-H, 9-H**), 3.63 (s, 2H, **16-H**), 3.41 (q, $J = 7.1$ Hz, 2H, **13-H**), 2.86 (t, $J = 7.1$ Hz, 2H, **12-H**), 2.08 (s, 3H, **1-H**).

^{13}C NMR (101 MHz, DMSO-d_6): δ 168.61, 162.24, 145.11, 139.41, 131.79, 120.64, 120.47, 119.67, 116.22, 38.80, 25.34, 25.20, 24.04.

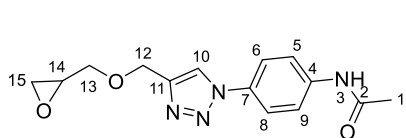
$R_f = 0.17$ (93:7 $\text{CH}_2\text{Cl}_2/\text{MeOH}$).

MS (ESI) m/z [$M + \text{Na}$] $^+$ calcd. for $\text{C}_{15}\text{H}_{16}\text{N}_6\text{O}_2\text{Na}$: 335.12, found: 335.19

Synthesis of *N*-(4-(4-((oxiran-2-ylmethoxy)methyl)-1H-1,2,3-triazol-1-yl)phenyl)acetamide (**56**)

$\text{Cu}(\text{OAc})_2 \cdot \text{H}_2\text{O}$ (27.9 mg, 0.14 mmol, 0.5 eq.), Na-ascorbate 1M in H_2O (220 μL , 0.22 mmol, 0.8 eq.) and 2-((prop-2-yn-1-yloxy)methyl)oxirane **63** (31 μL , 0.28 mmol, 1 eq.) dissolved in

a little amount of DMF were added in this order to a stirred solution of 4'-azidoacetanilide **66** (50 mg, 0.28 mmol, 1.1 eq.) in DMF/H₂O 4:1 (5.6 mL + 1.4 mL), at rt. The reaction mixture was stirred for 5 hours. After solvent evaporation under reduced pressure, the crude was washed with DCM/H₂O. The collected organic phase was dried over anhydrous Na₂SO₄ and concentrated under reduced pressure. The product was purified by flash chromatography (silicagel, eluent mixture 95:5 CH₂Cl₂/MeOH) providing 71.8 mg of pure N-(4-(4-(oxiran-2-ylmethoxy)methyl)-1H-1,2,3-triazol-1-yl)phenyl)acetamide **56** with an overall yield of 89%.



¹H NMR (400 MHz, DMSO-d₆) δ 8.73 (s, 1H, **H10**), 7.80 (m, 4H, **H5-6**, **H8-9**), 4.64 (s, 2H, **H12**), 3.81 (dd, J = 11.5, 2.8 Hz, 1H, **H13a**), 3.36 (dd, J = 11.5, 6.4 Hz, 1H, **H13b**), 3.15 (ddd, J = 6.4, 4.3, 2.5 Hz, 1H, **H14**), 2.74 (t, J = 4.7 Hz, 1H, **H15a**), 2.58 (dd, J = 5.2, 2.7 Hz, 1H, **H15b**), 2.08 (s, 3H, **H1**).

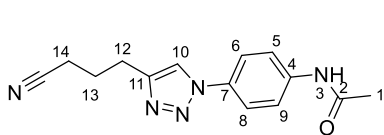
¹³C NMR (101 MHz, DMSO) δ 168.60, 144.72, 139.58, 131.61, 122.06, 120.68, 119.65, 70.80, 63.55, 50.18, 43.46, 24.03.

R_f = 0.42 (95:5 CH₂Cl₂/MeOH).

MS (ESI) m/z [M + Na]⁺ calcd. for C₁₄H₁₆N₄O₃Na: 311.11, found: 311.15

Synthesis of N-(4-(4-(3-cyanopropyl)-1H-1,2,3-triazol-1-yl)phenyl)acetamide (**57**)

Cu(OAc)₂ · H₂O (27.9 mg, 0.14 mmol, 0.5 eq.), Na-ascorbate 1M in H₂O (220 μL, 0.22 mmol, 0.8 eq.) and hex-5-yn-nitrile **64** (31 μL, 0.28 mmol, 1 eq.) dissolved in a little amount of DMF were added in this order to a stirred solution of 4'-azidoacetanilide **66** (50 mg, 0.28 mmol, 1.1 eq.) in DMF/H₂O 4:1 (5.6 mL + 1.4 mL), at rt. The reaction mixture was stirred for 5 hours. After solvent evaporation under reduced pressure, the crude was washed with DCM/H₂O. The collected organic phase was dried over anhydrous Na₂SO₄ and concentrated under reduced pressure. The product was purified by flash chromatography (silicagel, eluent mixture 95:5 CH₂Cl₂/MeOH) providing 71.2 mg of pure N-(4-(4-(3-cyanopropyl)-1H-1,2,3-triazol-1-yl)phenyl)acetamide **57** with an overall yield of 73%.



¹H NMR (400 MHz, DMSO-d₆) δ 10.19 (s, 1H, **NH**), 8.54 (s, 1H, **H10**), 7.80 – 7.75 (m, 4H, **H5-6**, **H8-9**), 2.81 (t, J = 7.6 Hz, 2H, **H14**), 2.60 (t, J = 7.2 Hz, **H12**), 2.08 (s, 3H, **H1**), 2.03 – 1.91 (m, 2H, **H13**).

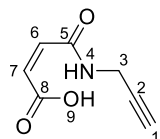
¹³C NMR (101 MHz, DMSO) δ 169.71, 147.42, 140.95, 132.91, 121.60, 121.50, 120.78, 25.72, 25.16, 25.12, 16.94.

R_f = 0.39 (95:5 CH₂Cl₂/MeOH).

MS (ESI) m/z [M + Na]⁺ calcd. for C₁₄H₁₅N₅ONa: 292.12, found: 292.17

Synthesis of (Z)-4-oxo-4-(prop-2-yn-1-ylamino)but-2-enoic acid (**65a**)

A solution of maleic anhydride (500 mg, 5.10 mmol, 1 eq.) and propargylamine (281 mg, 5.10 mmol, 1 eq.) in glacial AcOH (10.2 mL) was stirred for 19 hours at rt in the dark, then the solvent was removed under reduced pressure. 781 mg of crude (Z)-4-oxo-4-(prop-2-yn-1-ylamino)but-2-enoic acid **65a** was obtained and used directly for the next synthetic step.

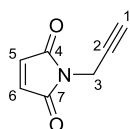


^1H NMR (400 MHz, Acetone- d_6) δ 6.61 (d, J = 12.9 Hz, 1H, **6-H**), 6.32 (d, J = 12.8 Hz, 1H, **7-H**), 4.18 (d, J = 2.6 Hz, 2H, **3-H**), 2.81 (t, J = 2.6 Hz, 1H, **1-H**).

^{13}C -NMR (101 MHz, DMSO- d_6): δ 167.3, 165.8, 132.4, 131.6, 80.5, 74.1, 29.1.

Synthesis of *N*-propargylmaleimide (**65**)

NaOAc (83.7 mg, 1.02 mmol, 0.2 eq.) was added to a stirred suspension of crude (Z)-4-oxo-4-(prop-2-yn-1-ylamino)but-2-enoic acid **65a** (781 mg) in Ac_2O (3.6 mL) at 65°C . The flask was covered with aluminium foil to avoid light exposure. The reaction mixture was stirred for 21 hours at rt in the dark. Afterwards, the reaction mixture was poured into ice water NH_4Cl (10 mL), then the aqueous phase was extracted with Et_2O (4x20mL). The collected organic phase was dried over Na_2SO_4 , filtered, and concentrated under reduced pressure. The crude product was purified by flash chromatography (silicagel, eluant mixture 7:3 n-Hex/EtOAc, then 1:1 n-Hex/EtOAc) providing 231.9 mg (1.72 mmol) of pure *N*-propargylmaleimide (**62**), with an overall yield of 34% starting from maleic anhydride **65**.



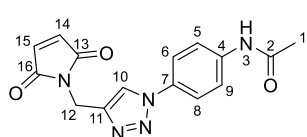
^1H NMR (400 MHz, CDCl_3): δ 6.74 (s, 2H, **6-H**, **7-H**), 4.25 (d, J = 2.5 Hz, 2H, **3-H**), 2.19 (t, J = 2.5 Hz, 1H, **1-H**).

^{13}C -NMR (101 MHz, DMSO- d_6): δ 169.2, 134.4, 76.8, 71.5, 26.6.

R_f = 0.55 (7:3 n-Hex/EtOAc).

Synthesis of *N*-(4-(4-((2,5-dioxo-2,5-dihydro-1H-pyrrol-1-yl)methyl)-1H-1,2,3-triazol-1-yl)phenyl)acetamide (**58**)

$\text{Cu}(\text{OAc})_2 \cdot \text{H}_2\text{O}$ (37.9 mg, 0.19 mmol, 0.5 eq.), Na-ascorbate 1M in H_2O (300 μL , 0.30 mmol, 0.8 eq.) and *N*-propargylmaleimide **65** dissolved in a little amount of DMF (50.0 mg, 0.37 mmol, 1 eq.) were added in this order to a stirred solution of 4'-azidoacetanilide **66** (79.3 mg, 0.44 mmol, 1.2 eq.) in DMF/ H_2O 4:1 (7.4 mL + 1.9 mL), at rt. The reaction mixture was stirred for 4 hours. After solvent evaporation under reduced pressure, the crude product was purified by flash chromatography (silicagel, eluent mixture 95:5 $\text{CH}_2\text{Cl}_2/\text{MeOH}$) providing 25.1 mg (0.08 mmol) of pure *N*-(4-(4-((2,5-dioxo-2,5-dihydro-1H-pyrrol-1-yl)methyl)-1H-1,2,3-triazol-1-yl)phenyl)acetamide **58**, with an overall yield of 22%.



^1H NMR (400 MHz, DMSO- d_6): δ 10.19 (s, 1H, **3-NH**), 8.62 (s, 1H, **10-H**), 7.81 – 7.72 (m, 4H, **5-H**, **6-H**, **8-H**, **9-H**), 7.11 (s, 2H, **14-H**, **15-H**), 4.74 (s, 2H, **12-H**), 2.07 (s, 3H, **1-H**).

^{13}C NMR (101 MHz, DMSO- d_6): δ 170.42, 168.58, 143.43, 139.59, 134.77, 131.49, 121.02, 120.61, 119.62, 32.54, 24.00.

R_f = 0.35 (95:5 $\text{CH}_2\text{Cl}_2/\text{MeOH}$).

MS (ESI) m/z $[\text{M} + \text{Na}]^+$ calcd. for $\text{C}_{15}\text{H}_{13}\text{N}_5\text{O}_3\text{Na}$: 334.09, found: 334.14

General procedure for the synthesis of amide derivatives:

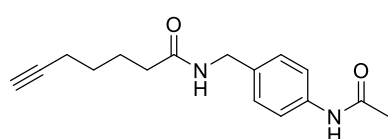
Procedure 1: To a solution of the N-(4-(aminomethyl)phenyl)acetamide (70 mg, 0.349mmol) in dry $\text{CH}_2\text{Cl}_2/\text{DMF}$ (1:1, 1.75 ml) were added HATU (146 mg, 0.384 mmol), the appropriate carboxylic acid (1.5 eq.) and DIPEA (1.047 mmol, 181 μl) at room temperature under a nitrogen atmosphere. The mixture was stirred at room temperature for 12-18h. The organic phase was washed with NH_4Cl , sat. NaHCO_3 , and brine, then dried over Na_2SO_4 , and concentrated under reduced pressure. Column chromatography of the residue on silica gel (elution: $\text{CH}_2\text{Cl}_2/\text{MeOH}$ 9:1 to 9.5:0.5), or purification with Biotage Isolera™ One System.

Procedure 2: To a solution of the N-(4-(aminomethyl)phenyl)acetamide (50 mg, 0.249mmol) in dry $\text{CH}_2\text{Cl}_2/\text{DMF}$ (1:1, 1.25 ml) were added the appropriate carboxylic acid (1.5 eq.), DMAP (15.2 mg, 0.120 mmol), TEA (0.623 mmol, 86.8 μl) and EDCl (119.4 mg, 0.623 mmol) at room temperature under a nitrogen atmosphere. The mixture was stirred at room temperature for 12-18h. The organic phase was washed with NH_4Cl , sat. NaHCO_3 , and brine, then dried over Na_2SO_4 , and concentrated under reduced pressure. Column chromatography of the residue on silica gel (elution: $\text{CH}_2\text{Cl}_2/\text{MeOH}$ 9:1 to 9.5:0.5), or purification with Biotage Isolera™ One System.

Procedure 3: To a solution of the N-(4-(aminomethyl)phenyl)acetamide (70 mg, 0.348 mmol) was added -(maleimido)propionic acid NHS ester (1.25 eq., 116 mg, 0.435 mmol) and DIPEA (2 eq., 0.7 mmol, 125 μl). The reaction was stirred for 3 hours until the completion was observed. Column chromatography of the crude on silica gel with Biotage Isolera™ One System (gradient $\text{CH}_2\text{Cl}_2/\text{MeOH}$) gave the desired product **72** in 37% yield.

N-(4-acetamidobenzyl)hept-6-ynamide (69)

47.5 mg obtained via procedure 1 with 50% yield.



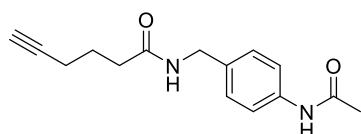
^1H NMR (400 MHz, DMSO) δ 9.90 (s, 1H), 8.26 (s, 1H), 7.50 (s, 2H), 7.15 (s, 2H), 4.19 (s, 2H), 2.75 (s, 1H), 2.15 (s, 4H), 2.02 (s, 3H), 1.60 (s, 2H), 1.43 (s, 2H).

^{13}C NMR (101 MHz, DMSO) δ 172.91, 169.26, 139.11, 135.31, 128.66, 120.04, 85.49, 72.33, 42.73, 35.87, 28.72, 25.59, 25.07, 18.59.

MS (ESI) m/z $[\text{M} + \text{Na}]^+$ calcd. for $\text{C}_{16}\text{H}_{20}\text{N}_2\text{O}_2\text{Na}$: 295.14, found: 295.19

N-(4-acetamidobenzyl)hex-5-ynamide (70)

15.7 mg obtained via procedure 1 with 18% yield.



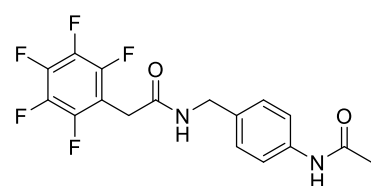
^1H NMR (400 MHz, CDCl_3) δ 7.56 (s, 1H), 7.43 (d, $J = 8.1$ Hz, 2H), 7.19 (d, $J = 8.1$ Hz, 2H), 5.99 (s, 1H), 4.38 (d, $J = 5.7$ Hz, 2H), 2.36 (t, $J = 7.4$ Hz, 2H), 2.26 (td, $J = 6.8, 2.6$ Hz, 2H), 2.16 (s, 3H), 1.96 (t, $J = 2.6$ Hz, 1H), 1.88 (p, $J = 7.1$ Hz, 2H).

^{13}C NMR (101 MHz, CDCl_3) δ 195.84, 163.70, 147.50, 135.60, 128.41, 120.33, 83.72, 69.31, 43.17, 35.04, 24.53, 24.18, 17.87.

MS (ESI) m/z $[\text{M} + \text{Na}]^+$ calcd. for $\text{C}_{15}\text{H}_{18}\text{N}_2\text{O}_2\text{Na}$: 281.13, found: 281.20

N-(4-acetamidobenzyl)-2-(perfluorophenyl)acetamide (71)

43.6 mg obtained via procedure 1 with 18% yield.



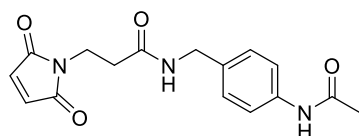
^1H NMR (400 MHz, Methanol- d_4) δ 7.53 (d, $J = 8.3$ Hz, 2H), 7.25 (d, $J = 8.2$ Hz, 2H), 4.37 (s, 2H), 3.75 (s, 2H), 2.13 (s, 3H).

^{13}C NMR (101 MHz, CDCl_3) δ 168.66, 167.16, 139.39, 133.97, 128.11, 119.39, 43.00, 29.26, 24.44 (detectable peaks).

MS (ESI) m/z $[\text{M} + \text{Na}]^+$ calcd. for $\text{C}_{17}\text{H}_{13}\text{F}_5\text{N}_2\text{O}_2\text{Na}$: 395.08, found: 395.33

N-(4-acetamidobenzyl)-3-(2,5-dioxo-2,5-dihydro-1H-pyrrol-1-yl)propanamide (72)

Obtained within procedure 3.



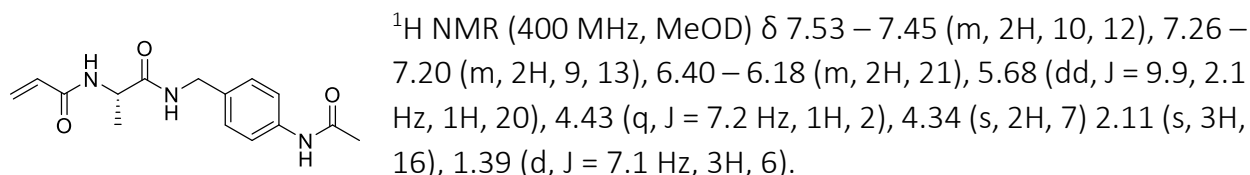
^1H NMR (400 MHz, DMSO- d_6) δ 7.53 – 7.46 (m, 1H), 7.17 – 7.10 (m, 1H), 7.00 (s, 1H), 4.16 (d, $J = 5.8$ Hz, 1H), 3.64 (dd, $J = 7.9, 6.7$ Hz, 1H), 2.41 (dd, $J = 7.9, 6.7$ Hz, 1H), 2.03 (s, 1H).

^{13}C NMR (101 MHz, DMSO) δ 171.21, 169.77, 168.59, 138.51, 135.02, 134.29, 128.09, 119.40, 42.16, 34.55, 34.36, 24.41.

MS (ESI) m/z $[\text{M} + \text{Na}]^+$ calcd. for $\text{C}_{16}\text{H}_{17}\text{N}_3\text{O}_4\text{Na}$: 338.11, found: 338.31

(S)-N-(1-((4-acetamidobenzyl)amino)-1-oxopropan-2-yl)acrylamide (73)

8.8 mg obtained via procedure 2 with 17% yield.

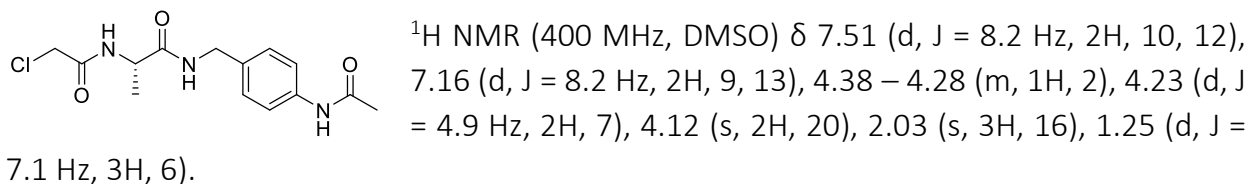


^{13}C NMR (101 MHz, Acetone) δ 174.20, 170.86, 167.07, 138.20, 134.82, 130.98, 128.14, 126.41, 120.46, 49.89, 42.84, 23.01, 17.45.

MS (ESI) m/z $[\text{M} + \text{Na}]^+$ calcd. for $\text{C}_{15}\text{H}_{19}\text{N}_3\text{O}_3\text{Na}$: 312.13, found: 312.17

(S)-N-(4-acetamidobenzyl)-2-(2-chloroacetamido)propenamide (74)

12.7 mg obtained via procedure 2 with 24% yield.

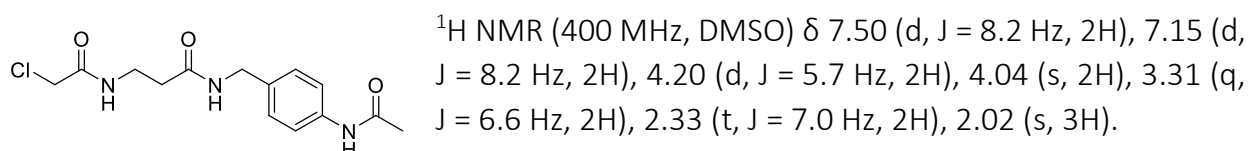


^{13}C NMR (101 MHz, DMSO) δ 172.13, 165.97, 158.46, 138.52, 134.19, 119.37, 49.08, 43.08, 42.07, 24.44, 18.86.

MS (ESI) m/z $[\text{M} + \text{Na}]^+$ calcd. for $\text{C}_{14}\text{H}_{18}\text{ClN}_3\text{O}_3\text{Na}$: 311.10, found: 311.14

N-(4-acetamidobenzyl)-3-(2-chloroacetamido)propenamide (75)

18.1 mg obtained via procedure 1 with 26% yield.



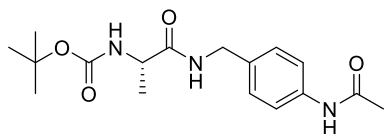
^{13}C NMR (101 MHz, CDCl_3) δ 171.24, 169.26, 166.96, 139.16, 135.03, 128.73, 120.04, 43.71, 42.77, 36.82, 35.95, 25.07.

MS (ESI) m/z $[\text{M} + \text{Na}]^+$ calcd. for $\text{C}_{14}\text{H}_{18}\text{ClN}_3\text{O}_3\text{Na}$: 311.10, found: 311.16

tert-butyl (S)-1-((4-acetamidobenzyl)amino)-1-oxopropan-2-yl carbamate (78)

129.3 mg obtained via procedure 1 with 52% yield.

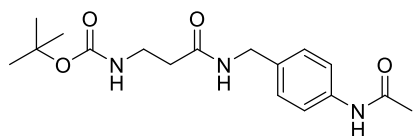
^1H NMR (400 MHz, MeOD) δ 7.51 (d, J = 8.1 Hz, 2H), 7.24 (d, J = 8.1 Hz, 2H), 4.30 (d, J = 15.0 Hz, 2H), 4.11 (q, J = 7.2 Hz, 1H), 2.12 (s, 3H), 1.46 (s, 9H), 1.41 – 1.31 (m, 3H).



^{13}C NMR (101 MHz, MeOD) δ 174.58, 170.18, 156.23, 137.55, 134.19, 119.76, 79.22, 50.51, 42.14, 27.40, 22.56, 17.08.

tert-butyl (3-((4-acetamidobenzyl)amino)-3-oxopropyl)carbamate (79)

162 mg obtained via procedure 2 with 65% yield.



^1H NMR (400 MHz, MeOD) δ 7.53 – 7.45 (m, 2H), 7.24 – 7.17 (m, 2H), 4.30 (s, 2H), 3.30 (dq, J = 10.0, 6.8 Hz, 2H), 2.50 – 2.35 (m, 2H), 2.09 (s, 3H), 1.41 (s, 9H).

^{13}C NMR (101 MHz, MeOD) δ 173.65, 171.54, 158.26, 139.03, 135.58, 128.51, 121.29, 80.11, 43.63, 38.04, 37.19, 28.72, 23.86.

2.4.5 REFERENCES

- [1] T. Mühlethaler, D. Gioia, A. E. Prota, M. E. Sharpe, A. Cavalli, M. O. Steinmetz, *Angew. Chemie - Int. Ed.* **2021**, *60*, 13331–13342.
- [2] T. Mühlethaler, L. Milanos, J. A. Ortega, T. B. Blum, D. Gioia, B. Roy, A. E. Prota, A. Cavalli, M. O. Steinmetz, *Angew. Chemie - Int. Ed.* **2022**, *61*, DOI 10.1002/anie.202204052.
- [3] F. Huang, X. Han, X. Xiao, J. Zhou, *Molecules* **2022**, *27*, DOI 10.3390/molecules27227728.

CHAPTER 3

X-RAY CRYSTALLOGRAPHY STRUCTURE DETERMINATION OF TUBULIN-MTAs COMPLEXES

3.1 DETERMINING PROTEIN-LIGAND INTERACTIONS BY X-RAY CRYSTALLOGRAPHY

3.1.1 General introduction on structural biology

Structural biology is the study of three-dimensional molecular structure and dynamics of biological molecules, which aims to provide a comprehensive understanding of how their structure affects their functions. By incorporating the principles of molecular biology, biochemistry, and biophysics, it gathers a variety of imaging techniques, which allow to investigate molecular basis of life at different levels of organization (Figure 3-1). Most common structural biology techniques include X-ray crystallography, electron cryo-microscopy (cryo-EM), cryo-electron tomography (cryo-ET) and NMR spectroscopy, complemented by small-angle X-ray scattering (SAXS), cross-linking combined with mass spectrometry (XL-MS), Förster resonance energy transfer (FRET) between fluorophores and a range of optical spectroscopies including circular dichroism and fluorescence spectroscopy.^[1] While most of them are primarily adapted for visualization of macromolecules and their complexes, the near-atomic resolution of X-ray crystallography and NMR spectroscopy has also been widely used to elucidate the interactions between proteins and small molecule ligands.^[2,3] Nowadays, some insights into the protein-ligand interactions can also be provided by cryo-EM.^[4] The studied ligands may include pharmaceutical drugs or drug candidates, small fragments or chemical probes, enzyme substrates or and molecules involved in cellular signalling. Structural information of protein-ligand binding can therefore provide insights both into the understanding of biological problems from a mechanistic point of view and contribute to drug discovery process^[5], e.g., by validating a therapeutic approach, confirming the mechanism of action of a hit or identifying additional targets responsible for adverse effects.

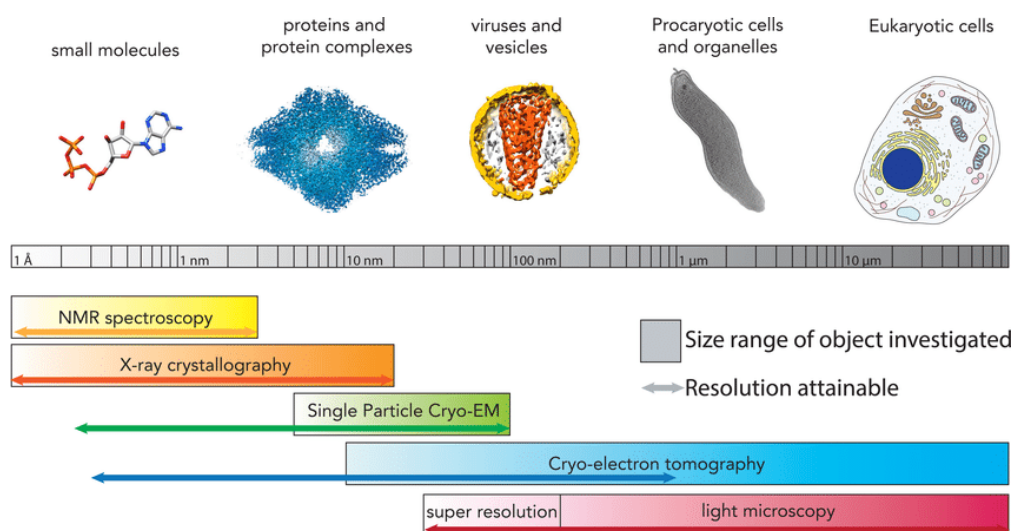


Figure 3-1. An overview of the main structural biology techniques and the biological objects they investigate (adapted from ^[46]).

3.1.2 Foundation of X-ray crystallography

The history of X-ray crystallography goes back to the early 20th century. X-rays as a form of electromagnetic radiation were discovered by a German physicist Wilhelm Conrad Roentgen in 1895.^[6] Due to a higher energy and a shorter wavelength than visible light, they can easily pass through most objects. In 1912, Max von Laue placed a crystal of copper sulphate (CuSO₄) in the path of an X-ray beam and discovered that X-rays could be diffracted by a crystal, producing a characteristic pattern on a photographic plate. Crystals are composed of atoms or molecules arranged in a three-dimensional, repeating pattern. When X-rays reach the crystal, they interact with the electrons inside the crystal. This interaction causes the X-rays to bend, or scatter, in a process known as X-ray diffraction. The scattering of X-rays is visually represented on a diffraction pattern recorded by a detector. The position of each spot in the pattern is determined by the crystal's interplanar distances, orientation, and overall shape, while the intensity of each spot provides information about the relative number of atoms in each type of crystal lattice site. Building on the work of Max von Laue, the Braggs related the angles of diffraction to the distances between the atomic planes in a crystal and described it in the mathematical relationship known as Bragg's law.

Bragg's law states that the angles of diffraction, θ , are given by the equation: $n\lambda = 2d \sin\theta$,

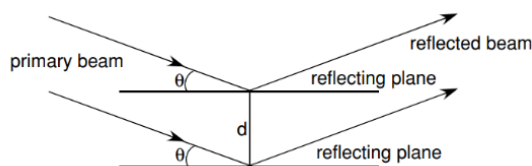


Figure 3-2. Reflection of the primary beam from lattice planes in the crystal according to Bragg's law (adapted from⁸⁾)

where λ is the wavelength of the X-rays, d is the distance between the atomic planes in the crystal, and n is an integer known as the order of the diffraction. It can be used to back-calculate the observed diffraction pattern into the distances between atomic planes of the crystal (Figure 3-

2). The lattice planes of a crystal are defined by the arrangement of atoms within the unit cell, the smallest repeating three-dimensional pattern of atoms or ions in a crystal. Von Laue and the Braggs received Nobel prizes for their pivotal discoveries, which laid the foundation of X-ray crystallography and prompted its rapid development.^[7,8]

In the early 20th century, X-ray crystallography was limited to study the structures of inorganic materials and simple organic molecules. For instance, it was used to elucidate the cubic structure of sodium chloride (NaCl) and the tetrahedral structure of a diamond as well as the crystal structures of hexamethylenetetramine and quartz.^[9] At the time, determination of the exact three-dimensional structure of more complex molecules was impeded due to the inability to obtain the phase information and the electron density map. A key development that allowed for the study of macromolecular structures by X-ray crystallography was the use of Fourier transform, introduced in the late 1940s. The Fourier transform is a mathematical tool that transforms the diffraction data, which consists of the

intensities of X-rays diffracted by the crystal, to the electron density containing information about the phases as well as the amplitudes of the diffracted beams.^[10] The electron density map is then used to build a three-dimensional model of the macromolecule (Figure 3-3).^[11]

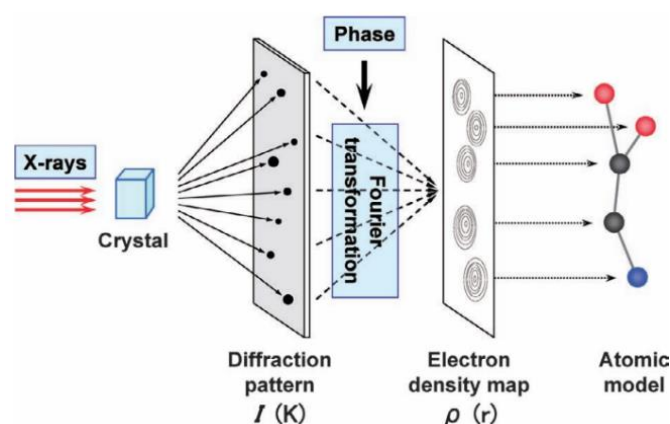


Figure 3-3. Graphical representation of the X-ray diffraction technique. A crystal of the molecule is exposed to a beam of X-rays, and the diffraction pattern produced by the X-rays is recorded. Using the Fourier transformation, the diffraction pattern is used to determine the electron density of the crystal, which in turn can be used to determine the positions of the atoms in the crystal (adapted from ¹¹)

The use of Fourier transform has revolutionized X-ray crystallography as it allowed to obtain the structures of proteins and other macromolecules. Eventually, a double-helix structure of a DNA and crystal structures of myoglobin and lysozyme were obtained, followed by a series of other biologically important macromolecules including the structure of the ribosome and HIV trimer (Figure 3-4).^[9]

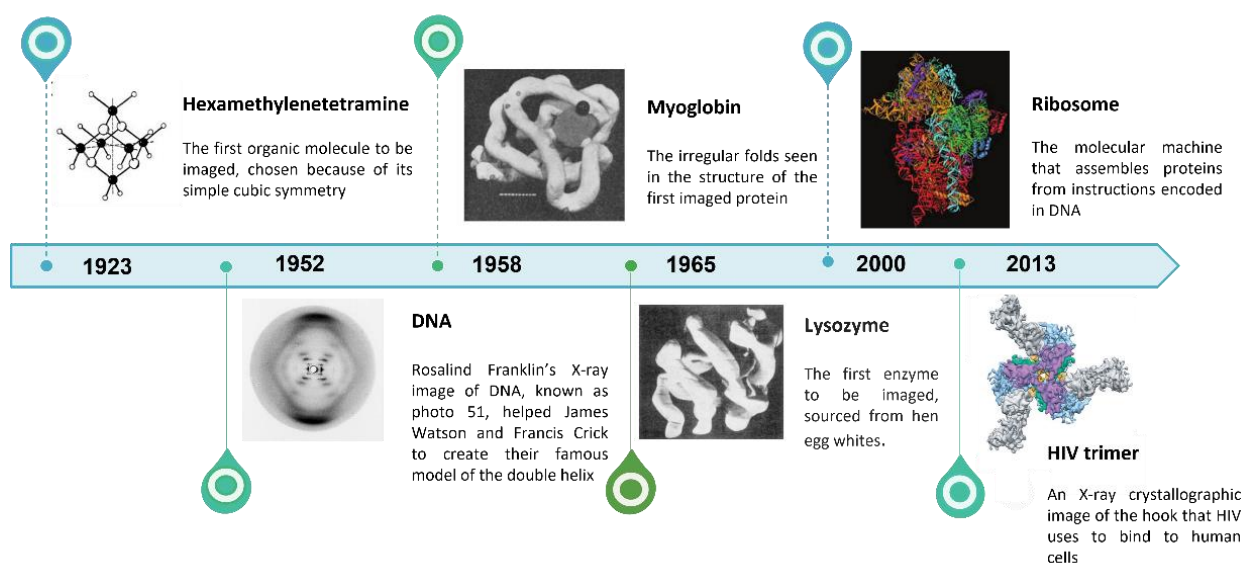


Figure 3-4. Some of the most important discoveries highlighted in the history of X-ray crystallography.

3.1.3 X-ray crystallographic studies of protein-ligand interactions

As mentioned above, advances in resolution and technology have allowed to study not only the protein structures, but also their interactions with small molecules. One of the earliest examples of the use of X-ray crystallography to study protein-ligand interactions is the determination of the structure of insulin bound to zinc ions, reported in 1969.^[12] Since then, multiple crystal structures of protein-small molecules complexes were obtained. For instance, the mechanisms of action of commonly used aspirin (PDB ID: 5F19) or atorvastatin (PDB ID: 1HWK) , as well as recently approved kinase inhibitor imatinib (PDB ID: 1IEP) or monoclonal antibody adalimumab (PDB ID: 3WD5) were elucidated by X-ray crystallography. Since around 30 years ago, X-ray crystallography has also found application as a screening tool for fragment-based drug discovery (FBDD). A few compounds derived from FBDD are already approved for clinical use (e.g. vemurafenib used for the treatment of late-stage melanoma or venetoclax used to treat leukemia), while many others are undergoing clinical trials.^[5] Nowadays, advances in X-ray crystallography techniques have made it possible to study protein-ligand interactions at an even higher level of detail. The Protein Data Bank (PDB) contains tens of thousands crystal structures of ligand-protein complexes.^[13] The number of high-resolution structures is constantly growing, allowing to gain a deeper understanding of the molecular basis of small molecules mechanism of actions and protein functions.

Usually, obtaining the crystal structure of a protein-ligand complex involves several steps. The first step is the purification of the protein of interest and preparing it for crystallization. This requires significant efforts and resources as not every protein can be easily obtained and crystallized. The most common method for setting up crystallization experiments is vapor diffusion using hanging or sitting drops. Once the crystallization conditions of the protein are established, the ligand is either soaked or co-crystallized. Soaking involves incubating preformed crystals of either the ligand-free protein (the apoenzyme form) or co-crystals of a previously bound ligand with a new ligand. In its turn, co-crystallization involves incubating the protein with excess ligand to form a complex prior to setting up the crystallization experiments. The success of soaking depends on several factors, including the stability of the protein-ligand complex and the quality of the protein crystals. Sometimes co-crystallization experiments fail to produce crystals. In such cases, the seeding technique can be used. A previously obtained crystal of good quality, is used as a starting point to decouple nucleation and initiate the growth of a new larger crystal. Homogeneous seeding techniques include microseeding, streak seeding, and macroseeding.^[2]

Appropriate crystals are then stabilized and protected using a cryoprotectant such as glycerol or ethylene glycol. Once treated with the cryoprotectant, the crystals are placed in

a cryoloop and rapidly frozen in liquid nitrogen. The main reason for cooling the crystals is to reduce the damage caused by X-rays during data collection, which is caused by radiation-induced chemical changes or by heating of the crystal. By cooling the crystals, the mobility of the atoms in the crystal lattice is reduced, which can help to preserve the crystal structure and improve the quality of the X-ray diffraction data. X-ray diffraction data of the protein-ligands crystals are collected from the crystal using e.g. a synchrotron X-ray source. Usually, the X-ray beam remains fixed while the crystal is rotated in small increments, at a defined angular speed. The total length of time that a crystal is exposed to the X-ray beam can vary, ranging from a few seconds to several minutes, depending on the intensity of the X-ray source. Details of data collection and the amount of data needed depend on the characteristics of the crystal, such as its cell size and symmetry. Data processing nowadays is usually done using software programs like XDS or HKL-2000.^[14,15] In the majority of cases when the structure of a related protein is already known, the molecular replacement (MR) method is used to determine the crystal structure. MR resolves the phase problem by providing initial estimates for the phases of a new structure by applying a rotation and a translation function to find the correct position of the search model in the unit cell. If a model of an isomorphous crystal is available, the structures can directly be determined using the difference Fourier method and the phases of the model in the absence of ligands and solvent molecules as starting point for refinement. After a first cycle of rigid body and restrained refinement, the initial electron density maps are inspected for the presence of positive difference density delineating the shape of a ligand bound to a binding site. The model is then further improved to obtain the final structure through iterative cycles of model building and refinements. Finally, the accuracy of the structure is validated using various techniques, such as R-factor analysis and comparison with other experimental data, to ensure that the structure is correct and biologically meaningful. Besides MR, other methods to obtain the structure of a protein-ligand complex, include direct methods which use a statistical analysis of the intensities of the reflections in the diffraction pattern to determine the electron density map; isomorphous replacement which uses crystals of similar proteins with different heavy atoms (such as mercury or platinum) to solve the phase problem or multi-wavelength anomalous diffraction (MAD) which uses the differences in the

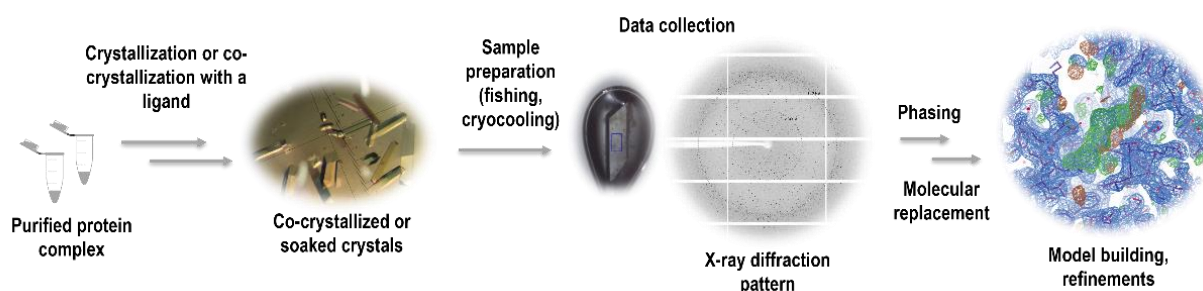


Figure 3-5. General workflow for structural determination of protein-ligand complex by X-ray crystallography by molecular replacement.

scattering properties of different heavy atoms in the crystal to solve the phase problem.^[16]

However, since the development of AlphaFold^[47], the latter methods have become obsolete to solve the phase problem of proteins of known folds. A general workflow for a structural determination of protein-ligand interactions by X-ray crystallography is depicted in Figure 3-5.

Over the past two decades, X-ray crystallography has undergone several important advances. First of all, advances in sample preparation, data collection, and refinement methods have led to an increase in the number of high-resolution protein-ligand complex structures. High-resolution structures (1.5–2 Å) provide very detailed information on the interactions between the protein and ligand, including hydrogen bonding and van der Waals interactions. At the same time, development of robotic crystallization screening systems and data collection methods enabled the high-throughput crystallography, routinely used in the pharmaceutical sector.^[5] Other challenges, including the data collection under the cryogenic conditions or structural characterisation of transient protein-ligand complexes, have also been addressed. Thus, at many synchrotrons (e.g. SLS at the PSI or Diamond Light Source in the UK) it is now possible to collect the X-ray diffraction data at room temperature, using *in situ* crystal data collection, without the need for additional sample treatment such as cryocooling (reviewed in^[17]). Serial-crystallography allows to collect data from many tiny crystals, useful for small and challenging samples, such as membrane proteins and some viruses.^[18] It is also possible to collect the data from a crystal over time, allowing changes in the crystal structure to be observed as a function of time (time-resolved crystallography). This approach can be used to study protein-ligand binding or enzymatic reactions, which occur on a time scale of milliseconds to seconds.^[19,20]

3.1.4 Other methods to study protein-ligand interactions: comparisons with X-ray crystallography

Apart of X-ray crystallography, protein-ligand interactions can be monitored and characterized by a range of biophysical techniques. NMR and Cryo-EM are another structural techniques that are commonly used. Furthermore, a panel of biophysical techniques includes isothermal titration calorimetry (ITC), fluorescence-based thermal denaturation/differential scanning fluorimetry (DSF) and fluorescence polarization (FP) assays, surface plasmon resonance (SPR)^[21] or grating-coupled interferometry (GCI).^[22]

NMR can primarily provide information about the mode of binding, and the conformational changes that occur upon binding. In case of low-affinity ligands, it also allows to measure the K_d . In the NMR experiments, the binding of a ligand to a protein is studied by monitoring changes in the NMR spectrum of the protein (protein-observed NMR) or a ligand (ligand-observed NMR). Specifically, NMR spectra of the protein and the ligand are compared in their free and bound states. The experiments can be performed on isotopically labelled (¹³C, ¹⁵N, ²H) protein samples, however 2D spectra (COSY, HSQC, NOESY) are often necessary to assign the signals and understand the changes in the protein structure. In case of ligand-

observed NMR experiments, less protein is required, and simple 1D ^1H spectra (using such methods as WaterLOGSY or Saturation Transfer Difference (STD) or 2D $1\text{H}-1\text{H}$ NOESY are often sufficient.^[3] ^{19}F NMR spectra can also be used to monitor the ligand-binding to protein.^[23] As of recently, NMR experiments have also found application in drug discovery fragment-based screens.^[24]

Cryo-EM involves imaging the sample in a thin layer of vitreous ice under cryogenic conditions using an electron microscope. The sample is flash-frozen to preserve its native state and prevent radiation damage. Multiple images are collected from different angles, which are then aligned and merged to generate a 3D reconstruction of the macromolecule. This technique allows to determine the structures of large and complex macromolecular assemblies that are difficult to crystallize or too dynamic for X-ray crystallography. In the last years, the resolution of cryo-EM and its application to study protein-ligands interactions has been increasing, however often it is not sufficient to see the detailed chemical environment of the ligand.^[48]

ITC can be used to determine the affinity, stoichiometry, and thermodynamics of binding interactions between molecules. In ITC, a small amount of one molecule is added to a solution containing the other molecule, and the heat released or absorbed is measured. It is particularly useful for determining the binding constants of weakly interacting molecules.^[25]

Fluorescence polarization assays involve labelling of one molecule with a fluorescent dye and measuring the degree of polarization of the emitted light as the molecule rotates in solution. When the labelled molecule binds to a larger molecule, such as a protein or nucleic acid, the rotational motion is restricted, resulting in a change in the degree of polarization. It is a fast and sensitive method for detecting and quantifying binding interactions.^[26]

DSF, also known as Thermal Shift Assay (TSA), is a technique used to study the thermal stability and folding of proteins. It is a fast and convenient method for identifying ligands or conditions that can stabilize or destabilize a protein and is widely used in drug discovery. DSF involves monitoring the change in fluorescence of a dye that binds to exposed hydrophobic regions of a protein as the temperature is increased. As the protein denatures, the dye is released and the fluorescence decreases. Hence, it is possible to determine the level of denaturation by observing the fluorescent signal.^[21]

SPR is used to study molecular interactions in real-time, without the need for labelling. It involves immobilization of one molecule on a surface and flowing the other molecule over the surface. As the second molecule binds to the immobilized molecule, the refractive index of the surface changes, resulting in a change in the angle of reflected light. By monitoring this change in real-time, the kinetics and affinity of the interaction can be determined.^[27]

Similarly to SPR, GCI is a label-free optical biosensing technique which involves the use of a diffraction grating to generate an evanescent wave that interacts with biomolecules immobilized on the grating surface. The interaction of the evanescent wave with the biomolecules causes a shift in the wavelength of the reflected light, which can be measured

Table 3-1. Summary of parameters of different techniques used to study protein/ligand interactions (modified from ²¹).

Technique	Advantages	Disadvantages
X-ray crystallography	<ul style="list-style-type: none"> • Intermediate throughput • Can rapidly identify binding site and ligand binding mode • Can directly identify ligand-induced conformational changes 	<ul style="list-style-type: none"> • Requires expensive X-ray sources (in-house, access to synchrotrons) • Crystal packing may occlude binding site • High occupancy of the ligand binding site required
Cryo-EM	<ul style="list-style-type: none"> • Can visualize macromolecules in their native state without the need for crystallization • Adapted for structure determination of very large protein complexes 	<ul style="list-style-type: none"> • Expensive equipment • Low throughput • Challenging sample preparation
DSF	<ul style="list-style-type: none"> • High throughput • Applicable to most target proteins • Direct binding assay 	<ul style="list-style-type: none"> • Prone to false positives and false negatives • Material intensive • Across-plate variability
FP	<ul style="list-style-type: none"> • High throughput • Applicable to most target proteins • Competition binding assay 	<ul style="list-style-type: none"> • Prone to false positives and artifactual effects • Requires labelling of known ligand
NMR (ligand-observed)	<ul style="list-style-type: none"> • Intermediate throughput • Applicable to most target proteins (>10 kDa) • Provides quality control 	<ul style="list-style-type: none"> • Prone to false positives due to compound aggregation or nonspecific effects
NMR (protein-observed)	<ul style="list-style-type: none"> • Intermediate throughput • Can identify binding site (need peak assignment) • Can measure Kd from ligand titrations 	<ul style="list-style-type: none"> • Limited to small (<30 kDa) and soluble target proteins • Requires expensive isotope labelling of target proteins • Material intensive
ITC	<ul style="list-style-type: none"> • Direct/competition binding assays • Applicable to most target proteins • High information content (Kd, ΔH, ΔS and n) 	<ul style="list-style-type: none"> • Low throughput • Material intensive • Requires large heat changes upon binding for reliable measurements
SPR	<ul style="list-style-type: none"> • Label-free detection and ease of automation • Applicable to most target proteins • Direct/competition binding assays • Low material consumption • High information content • (Kd, kon, koff and n) 	<ul style="list-style-type: none"> • Requires immobilization of one of the binding partners to a surface • Prone to artifacts due to compound aggregation or nonspecific effects • Requires time-consuming assay optimization

and used to determine the amount and rate of binding of the analyte to the surface.^[28]

Each biophysical and structural technique described has advantages and disadvantages depending on the sensitivity, material consumption, difficulty of sample preparation and the

Table 3-2. Summary of parameters of different techniques used to study protein/ligand interactions (adapted from ²¹)

Technique	Screening throughput	Material consumption	Covalent immobilization	Detectable K_d range	Binding site information
X-ray crystallography	Low	Intermediate	None	Up to ligand solubility	Excellent
NMR	Intermediate	Intermediate	None	Low nM—10 mM	Good
DSF	High	Intermediate	None	Up to 5 mM	None
FP	High	Low	None	Down to K_d of probe	Limited to competition
ITC	Low	High	None	Low nM—5 mM	Limited to competition
SPR	Intermediate	Low	Required	pM—2 mM	Limited to competition

information obtained. For instance, DSF and FP are very useful for high-throughput screening for promising ligands, while SPR allows to measure real-time quantitative binding affinities and kinetics of the ligand-protein binding. However, they provide none to limited information about the binding site and mechanism of action of the studied ligands, which can be obtained by X-ray crystallography or NMR. NMR is a solution-based technique, which can provide information about dynamic behaviour and weak interactions, while X-ray crystallography is a solid-based technique, which requires the protein to be crystallized: a task that can be challenging to reach for some proteins and ligands.^[21] The comparison of different techniques based on their parameters and applications are presented in Tables 3-1 and 3-2, respectively.

Overall, the choice of technique depends on the specific research question and the properties of the protein and ligand being studied. Often a combination of techniques is needed to obtain a comprehensive data. If we consider our protein of interest, tubulin, such techniques as ITC, FP or SPR can certainly be useful to biophysically characterize the interactions with ligands and their affinities. Ligand-based NMR experiments in solution could be useful to obtain additional structural information or in some cases determine the ligand affinities.^[29] However, to obtain high-resolution structural information of protein-ligands interactions, X-ray crystallography remains the technique of choice, considering the availability of robust tubulin crystallization systems. The detailed information on tubulin crystallization and X-ray crystallography of MTAs, including experimental data, is described in Sections 3.2 and 3.3.

3.2 TUBULIN CRYSTALLIZATION

3.2.1 INTRODUCTION

In 1998, Nogales et al. used electron crystallography on taxol-stabilized zinc-induced tubulin sheets to obtain the first near-atomic resolution (3.7 Å) structure of tubulin. This provided the first tubulin model and allowed to identify tubulin domains and the taxol binding site on β -tubulin. However, in the two-dimensional zinc-induced sheets tubulin was arranged in antiparallel way.^[30] A few years later, using a combination of scanning transmission electron microscopy and digital image processing, a stathmin complex consisting of two longitudinally aligned α/β -tubulin heterodimers in a kinked protofilament-like structure was suggested.^[31] Shortly after, in 2000, a first X-ray structure of a GDP-tubulin complex with a stathmin-like domain SLD of the neural protein RB3 was published, termed T₂R. It is worth noting that soluble tubulin cannot be crystallized due to its dynamic propensity to polymerization. RB3 can sequester tubulin by stabilizing it in its tetrameric form. It forms a complex with tubulin in a curved conformation, preventing the incorporation of tubulin into microtubules.^[32] The T₂R structure was used to elucidate the tubulin interactions with some ligands, including colchicine, podophyllotoxin or vinblastine.^[33,34] The resolution of most T₂R structures reached around 4 Å^[35] and therefore could not always provide a detailed structural insight into the ligand binding pose. Higher-resolution structures (2.0 – 2.5 Å, best resolution of 1.8 Å^[36]) were then obtained, by using the subtilisin treated tubulin to remove the C-terminal tails prior to the complex assembly^[49] or adding the enzyme tubulin tyrosine ligase (TTL) to the T₂R complex (Figure 3-6A).^[37] In the T₂R-TTL system, the TTL protein is bound to both the α 1- and β 1-tubulin subunits at the RB3-capped end of the tetramer. This system has become the most common tubulin crystallization setup, and has been used to solve most tubulin-ligands structures.^[35] Moreover, it has recently been used to perform a crystallographic fragment screening and a comprehensive analysis of binding sites on tubulin^[38] (discussed in Chapter 1.3). T₂R-TTL is characterized by both its high accessibility of binding sites for most tubulin ligands and the presence of an inter-tubulin dimer interface. At the same time an alternative tubulin crystallization system, TD₁, was developed (Figure 3-6B). It consists of one $\alpha\beta$ -tubulin dimer and the designed ankyrin repeat protein (DARPin) D1, which was selected for its high-affinity binding to β -tubulin.^[39] It is the second most frequently used high-resolution tubulin crystallization system to investigate tubulin-ligands interactions.^[35] It allows to achieve even higher resolution compared to the T₂R-TTL (routinely 2.0 Å, best resolution of 1.5 Å^[40]), due to which it has also found application in room temperature serial crystallography experiments.^[41] The two crystal systems differ in symmetry and space group. T₂R-TTL belongs to the space group 19 and TD1 to space group 4. Due to the absence of inter-tubulin dimer interface and a more compact crystal packing, not all MTAs binding sites are accessible in TD1. For this reason, co-crystallization is preferred in case of TD1 while T₂R-TTL is commonly used both in soaking and co-crystallization experiments. Further differences include the origin of tubulin that can be

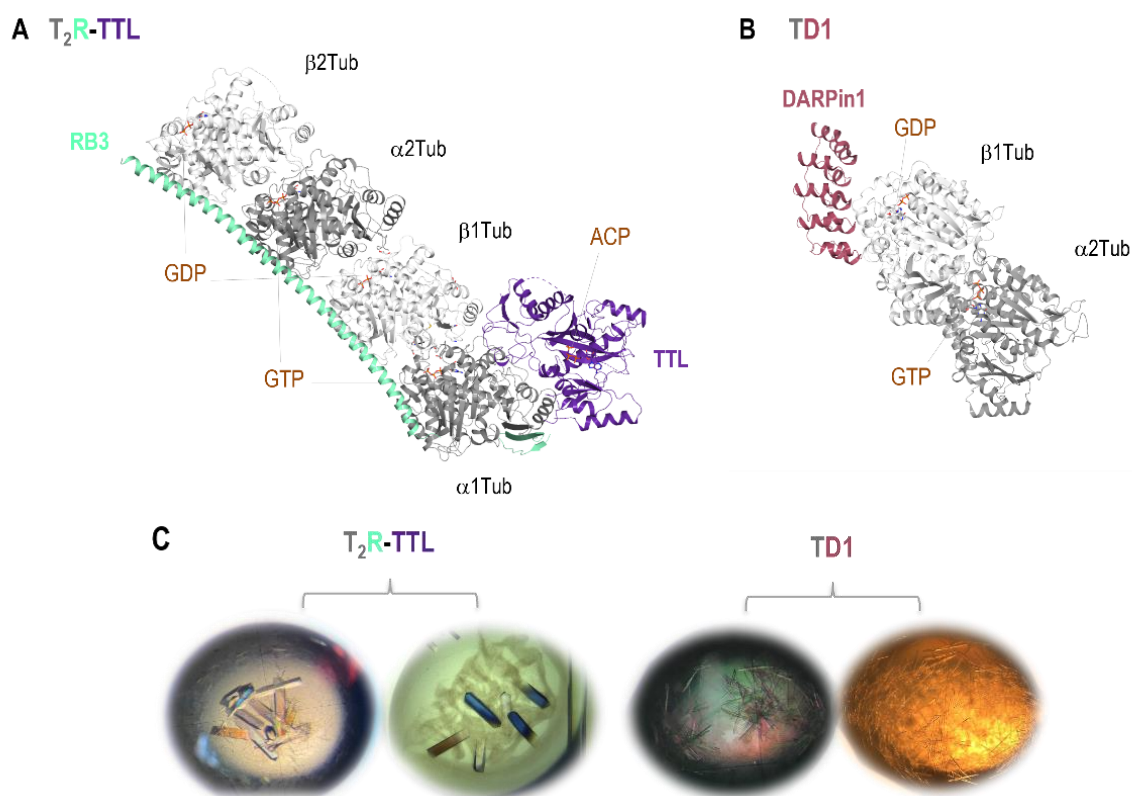


Figure 3-6. Tubulin crystallization systems (A) T_2R -TTL (PDIB ID: 5LXT) and (B) TD1 (PDB ID: 6S8K), shown in ribbon representation, α - and β -tubulin are coloured in dark and light grey, respectively. The SLD/RB3 protein is coloured in light green, the TTL in dark violet, DARPin in dark red. The nucleotides GDP, GTP and ACP are shown in sticks representation. (C) Representative images of tubulin crystals obtained with T_2R -TTL and TD1 crystallization systems.

used. Both the T_2R -TTL system have so far been used with mammalian $\alpha\beta$ -tubulin of bovine, human or recombinant origin. Moreover, the TD1 system was recently used with *Tetrahymena thermophila* $\alpha\beta$ -tubulin (Tt-TD1). The latter is used to specifically study the protein-ligands interactions of compounds with antiparasitic/antimalaria properties, which would target the protozoan tubulin but not the mammalian one.^[42]

Additionally, tubulin-TOG1 and tubulin- α Rep crystallization systems are available, used for the study of protein-protein interactions.^[43,44]

3.2.2 MATERIALS AND METHODS

3.2.2.1 T₂R-TTL crystallization complex

Protein preparation

T₂R-TTL complex is composed of two dimers of mammalian $\alpha\beta$ -tubulin, the rat stathmin-like protein RB3 and the chicken TTL protein. Lyophilized calf brain tubulin is purchased from the Centro de Investigaciones Biologicas Margarita Salas (Microtubule Stabilizing Agent Group), CSIC, Madrid Spain. This calf brain tubulin is purified as described.^[45] RB3 and TTL are expressed and purified from bacteria *Escherichia coli* (Figure 3-7). In case of RB3, three

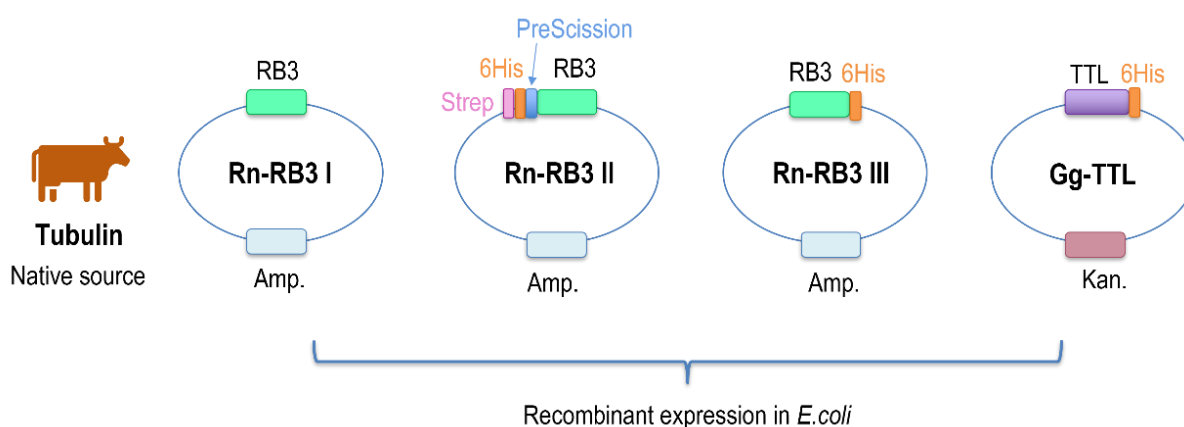


Figure 3-7. Sources of proteins needed for the preparation of T₂R-TTL crystallization complex. For RB3 and TTL, schematic plasmid map constructs for the recombinant protein expression in *E. coli* are depicted. Relevant plasmid resistance genes and purification or expression tags are indicated (Amp. = ampicillin, light blue; Kan. = kanamycin – dark pink; 6Hix = hexahistidine, orange; Strep-tag in pink, PreScission protease cleavage site in blue).

different purification procedures can be used depending on the chosen plasmid construct. Thus, standard procedure plasmid encoding for the rat stathmin-like domain of *Rattus norvegicus* RB3 in a pET3d vector is used (Rn-RB3 I).^[42] Modified procedures include the use of N-terminal (Rn-RB3 II, PSPCm7 vector) or C-terminal (Rn-RB3 III, NSKn1 vector)

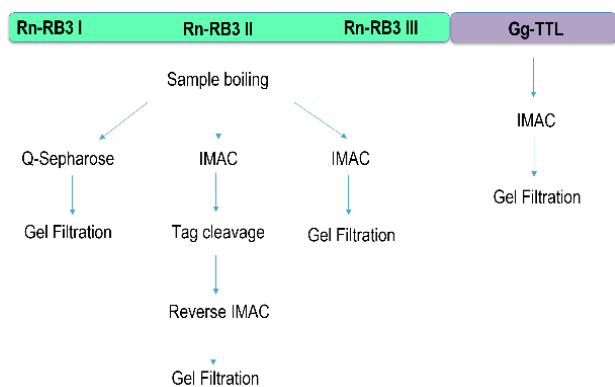


Figure 3-8. Purification schemes for the RB3 and TTL.

polyhistidine purification tags (HisTags). The constructs were cloned by Anne-Catherine Abel. In the case of Rn-RB3 II, removal of the N-terminal His-tag is needed as the tag interferes with the formation of the complex, while the C-terminal His-tagged Rn-RB3 III can be used without cleavage. Similarly, TTL with the C-terminal His tag Gg-TTL is used for crystallization.

Purification schemes for all constructs are depicted in Figure 3-8.

Expression and purification of Rn-RB3 I

Protein & Culture Information

Expression strain	BL21 DE3
Plasmid	Standard plasmid pET3d
MW	17 kDa
Extinction coefficient (for ml/mg)	0.09
Medium	LB
Antibiotic (1:1000)	Amp
Volume overnight preculture	100 mL
Volume expression culture	6 L

Purification buffers

Buffer A

Tris/HCl pH 8.0	20 mM	
EGTA	1 mM	
DTT	2 mM	added directly before use

Buffer B

Tris/HCl pH 8.0	20 mM	
EGTA	1 mM	
NaCl	1M	
DTT	2 mM	added directly before use

SEC Buffer

HEPES pH 7.2	10 mM	
NaCl	150 mM	
DTT	2 mM	added directly before use

Used columns/ programs

IEX	Q Sepharose Anion exchange	Manual run, gradient 0-50% B in 20 CV
SEC	Superdex 75 16/60	Standard SEC 1 sample

*the columns were purchased from Cytiva Life Sciences

Procedure:

1. On ice, 0.5 μ L of the plasmid encoding RB3 were added to 10 μ L of chemically competent *E.coli* BL21 (DE3) cells, purchased from New England Biolabs, and incubated for 10 min.
2. The cells were heat-shocked at 42 °C for 15 s, then incubated on ice for 10 min. 100 μ L of SOC medium was added and incubated for 2 h at 37 °C by shaking at 180 rpm.
3. The cells were transferred on an LB agar plate supplemented with ampicillin and the plate was incubated at 37 °C overnight.
4. The cells were suspended in 2 mL of LB medium on the plate and the suspension was transferred to 200 mL LB medium supplemented with 200 μ L of ampicillin stock solution. The cells were incubated for 1 h at 37 °C while shaking at 180 rpm.
5. 6 L of LB medium supplemented with 1 mL ampicillin stock solution in 2 L Erlenmeyer flasks were prepared.
6. The LB medium was inoculated with 10 mL preculture per 1 L cell medium and the cells were incubated at 37 °C while shaking at 180 rpm. The optical density at λ ¼ 600 nm (OD600) of the cell suspension was measured and once an OD600 reached 0.6, the cells were induced with IPTG (0.5 mM final concentration, 500 μ l of 1M stock per 1L of bacterial culture) and the culture was incubated for 4 h at 37 °C while shaking at 180 rpm.
7. The cells were harvested by centrifugation using ThermoFisher BIOS 16 3@ 4000 rpm, 15'@ 4 °C and resuspended in 10 mL RB3 lysis buffer (Buffer A + DNase and Protease inhibitors purchased from Roche) per 1 L of cell culture.
8. The cells were lysed on ice with an ultrasonic cell disruptor, with 2 s on 2 s off pulses for 10 min.
9. The lysate was centrifuged at 15 000 rpm, 4°C for 20 min.
10. The supernatant was boiled for 15 min.
11. The boiled lysate was centrifuged at 15 000 rpm, 4°C for 20 min and diluted to 200 ml with Buffer A.
12. The supernatant was applied to a Q Sepharose column on an FPLC AKTA® Purifier system. The column was washed with 20 column volumes (CVs) of RB3 anion-binding buffer.
13. RB3 protein was eluted over 20 CVs with a linear gradient to of 0-50% RB3 anion-elution buffer (Buffer B).
14. The eluted fractions were analysed on SDS-PAGE, the fractions containing RB3 were pulled, and concentrated to 5 mL using a 3 kDa cut-off concentrator.
15. The pooled RB3 was applied to a Superdex 75 16/60 column and eluted with RB3 SEC buffer.

16. The eluted fractions were analysed on SDS-PAGE, the fractions containing RB3 were pooled, concentrated to ~20 mg/mL RB3 using a 3 kDa cut-off concentrator. On average, 14 mg of purified protein were obtained, and subsequently flash-frozen in 20 μ L aliquots and stored at 80 °C.

Expression and purification of Rn-RB3 II

Protein & Culture Information

Expression strain	BL21 DE3
Plasmid	His-strep-rnRB3, PSPCm7 vector
MW	20.3 kDa (17 kDa after cleavage)
Extinction coefficient (for ml/mg)	0.34 (0.09 after cleavage)
Medium	LB
Antibiotic (1:1000)	Kan
Volume overnight preculture	100 mL
Volume expression culture	12 L

Purification buffers

<u>Buffer A</u>	
Tris/HCl pH 8.0	20 mM
NaCl	500 mM
Beta-mercaptoethanol	2 mM
<u>Buffer B</u>	
Tris/HCl pH 8.0	20 mM
imidazole	500 mM
NaCl	150 mM

SEC Buffer

SEC buffer as reported above for Rn-RB3 I was used.

Used columns/ programs

IMAC	IMAC HisTrap™ [®]	4% B wash, 40% B elution
SEC	Superdex 75 16/60	Standard SEC 1 sample

*the columns were purchased from Cytiva Life Sciences

Procedure:

Steps 1-11 as reported for Rn-RB3 I were done.

12. The supernatant was applied to an IMAC HisTrap™[®] column on an FPLC AKTA™[®] Purifier system. The column was washed with 4% of RB3 Buffer B.

13. RB3 protein was eluted with 40% of Buffer B.
14. The eluted fractions were analysed, pooled, and digested with PreScission protease (PSC) overnight at 4°C (250 µL of 1 mg/mL solution).
15. A reverse IMAC was done, and the washed-out protein was analyzed on SDS-PAGE and concentrated to 5 mL using a 3 kDa cut-off concentrator for an injection on a size-exclusion column (SEC). The elution of the reverse IMAC was collected to check for the presence of uncleaved RB3.
16. The pooled RB3 was applied to a Superdex 75 16/60 column and eluted with RB3 SEC buffer.
17. The eluted fractions were first analyzed on SDS-PAGE. the fractions containing RB3 were pooled and concentrated to ~20 mg/mL RB3 using a 3 kDa cut-off concentrator. On average, 49,3 mg of purified RB3 were obtained, and subsequently flash-frozen in 20 µL aliquots and stored at 80 °C.

Expression and purification of Rn-RB3 III

Protein & Culture Information

Expression strain	BL21 DE3
Plasmid	rnRB3_strep_His, NSKn1 vector
MW	17.6 kDa
Extinction coefficient (for ml/mg)	0.08
Medium	LB
Antibiotic (1:1000)	Kan
Volume overnight preculture	100 mL
Volume expression culture	12 L

Purification buffers

Purification buffers as reported above for Rn-RB3 II were used.

Used columns/ programs

IMAC	HisTrapTM®	4% B wash, 40% B elution
SEC	Superdex 75 16/60	Standard SEC 1 sample

*the columns were purchased from Cytiva Life Sciences

Procedure:

Steps 1-13 as reported for Rn-RB3 II were done.

14. The eluted fractions were analyzed on SDS-PAGE. Fractions containing RB3-His were pooled and concentrated to 5 mL using a 3 kDa cut-off concentrator for an injection on a gelfiltration column.
15. The pooled RB3 was applied to a Superdex 75 16/60 column and eluted with RB3 SEC buffer.

16. The eluted fractions were analyzed on SDS-PAGE, the fractions containing RB3 were pooled, concentrated to ~20 mg/mL RB3 using a 3 kDa cut-off concentrator. 92 mg were obtained, they were flash-freezed in 20 μ L aliquots and stored at 80 °C.

Expression and purification of Gg-TTL

Protein & Culture Information

Expression strain	BL21 DE3
Plasmid	TTL plasmid C-ter 6*His
MW	43,49 kDa
Extinction coefficient (for ml/mg)	1.226
Medium	LB
Antibiotic (1:1000)	Kan
Volume overnight preculture	100 mL
Volume expression culture	6 L

Purification buffers

Buffer A

Tris/HCl pH 7,5	50 mM	
NaCl	500 mM	
Imidazole	20 mM	
10% glycerol		
Beta-mercaptoethanol	5 mM	added directly before use

Buffer B

Tris/HCl pH 7,5	50 mM	
NaCl	250 mM	
Imidazole	500 mM	
10% glycerol		
Beta-mercaptoethanol	5 mM	added directly before use

SEC Buffer

Bis-Tris propane pH 6,5	50 mM	
NaCl	200 mM	
MgCl ₂	2,5 mM	
1% glycerol		
DTT	2 mM	added directly before use

Used columns/ programs

IMAC	HisTrap™ [®] 5 ml	5 ml HisTrap OB30 CB 4B 20 CV 40B 10 CV
------	----------------------------	---

*the columns were purchased from Cytiva Life Sciences

Procedure:

1. On ice, 0.5 μ L of the plasmid encoding TTL was added to 10 μ L of chemically competent *E.coli* BL21 (DE3) cells and incubated for 10 min.
2. The cells were heat-shocked at 42 °C for 15 s, then incubated on ice for 10 min. 100 μ L of SOC medium was added and incubated for 2 h at 37°C by shaking at 180 rpm.
3. The cells were transferred on an LB agar plate supplemented with kanamycin and the plate was incubated at 37 °C overnight.
4. The cells were suspended in 2 mL of LB medium on the plate and the suspension was transferred to 200 mL LB medium supplemented with 200 μ L of kanamycin stock solution.
5. The cells were incubated for 1 h at 37 °C while shaking at 180 rpm.
6. 6L of LB medium supplemented with 1 mL kanamycin stock solution in a 2 L Erlenmeyer flask were prepared.
7. The medium was inoculated with 10 mL preculture per 1 L of cell medium, and the cells were incubated at 37 °C while shaking at 180 rpm. The optical density at λ 600 nm (OD600) of the cell suspension was measured and once an OD600 reached 0.6, the cell suspension was cooled to 20 °C for 30 min, then the cells were induced with IPTG (0.5 mM final concentration, 500 μ l of 1M stock per 1L of bacteria) and the culture was incubated for overnight at 20 °C while shaking at 180 rpm.
8. The cells were harvested by centrifugation using ThermoFisher BIOS 16 3@ 4000 rpm, 15'@ 4 °C and resuspended in 10 mL TTL lysis buffer (Buffer A + DNase and Protease inhibitors) per 1 L of cell culture.
9. The cells were lysed on ice with an ultrasonic cell disruptor, with 2 s on 2 s off pulses for 10 min.
10. The lysate was centrifuges at 15 000 rpm, 4°C for 30 min.
11. The supernatant was applied to a Ni-NTA column on an FPLC AKTA Purifier system.
12. The column was washed with 30 CVs of TTL IMAC-binding buffer, and then washed with 20 CVs of 4% TTL IMAC-elution buffer.
13. TTL protein was eluted over 10 CVs with TTL IMAC-elution buffer (Buffer B).
14. The eluted fractions were analysed on SDS-PAGE, the fractions containing TTL were pooled and concentrated to 5 mL using a 10 kDa cut-off concentrator.
15. The pooled RB3 was applied to a Superdex 200 16/60 column and the protein was eluted the protein with TTL SEC buffer.
16. The eluted fractions were analysed on SDS-PAGE, the fractions containing TTL were pooled and concentrated to \sim 20 mg/mL RB3 using a 10 kDa cut-off concentrator. On average, 31 mg of purified TTL were obtained, and were subsequently flash-frozen in 15, 30 and 50 μ L aliquots and stored at -80 °C.

Analysis of protein purity by 12% or 15% SDS-PAGE The protein purity was analysed by 12% or 15% SDS-PAGE. The example gels are depicted in Figure 3-9.

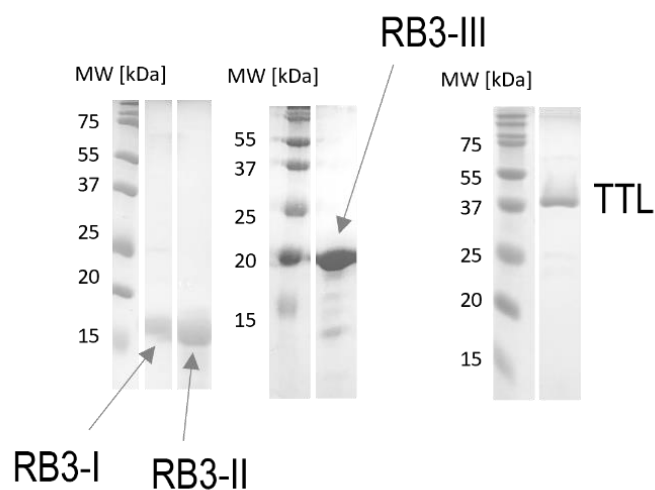


Figure 3-9. Coomassie stained SDS-PAGE illustrating the purity of proteins.

Complex formation

The T₂R-TTL complex can be formed either by using tubulin subjected to a polymerization-depolymerization cycle prior to complex assembly (which lowers the occurrence of β 3 tubulin) or without the cycling step (higher β 3 tubulin occurrence).

Complex formation using tubulin pol/depol purification:

Buffers

Polymerization Buffer	50 mM MES-KOH pH 6.8 0.5 mM EGTA 0.4 mM GTP (added directly before use) 6 mM MgCl ₂ 33% glycerol
Depolymerization Buffer	80 mM Pipes-KOH pH 6.8 0.5 mM EGTA 2 mM GDP (added directly before use) 1 mM MgCl ₂ 2 mM CaCl ₂
PD-10 Buffer	15 mM Pipes-KOH pH 6.8 0.3 mM MgCl ₂ 0.2 mM EGTA 0.1 mM GDP (added directly before use)

Procedure:

1. 10 mg of tubulin were resuspended at 10 mg/mL in polymerization buffer on ice. Then each 1 mL containing 10 mg was transferred into a separate centrifugation tube and centrifuged for 15' @ 50 000 x rpm (MLA-130 rotor was used). After centrifugation, white aggerates were observed.
2. The supernatant was transferred to a fresh centrifuge tube and incubated for 20 minutes at 37 °C.
3. After incubation, the solution turned turbid. The sample was centrifuged for 20 minutes at 70 000 x rpm (MLA-130). A white pellet of microtubules was observed after centrifugation.
4. The supernatant was removed and 1 mL of depolymerization buffer was added on top of each pellet. For easier resuspension, the pellets were incubated 20 minutes on ice with the buffer before pipetting up and down.
5. A desalting column (PD10 column) was equilibrated in the 4°C room with PD10 buffer, tubulin was loaded onto the column in maximum 2.5 mL fractions.
6. The tubulin was eluted and the fractions containing tubulin were determined with a UV-Vis spectrophotometer.
7. The fractions were pooled, and the molar amount of tubulin was determined.
8. A six-fold molar excess of RB3 was added to tubulin on ice and gently mixed by pipetting.
9. 0.6 times the molar tubulin quantity of TTL was added on ice and gently mixed by pipetting.
10. The complex was concentrated to 15-20 mg/ml at 4° C.
11. Nucleotides and reducing agent were then added (10 mM DTT, 0.1 mM GDP, 1 mM ACP).
12. The crystallization complex was flash-frozen in 14 and 28 µL aliquots and stored at -80 °C.

Complex formation without tubulin pol/depol purification:

PD 10 buffer

PD10 buffer was prepared and used as as reported above.

Procedure:

1. On ice PD10 buffer was added to lyophilized tubulin (about 10-20mg of protein and ~200-300uL buffer).
2. The tubulin was incubated for 20 minutes on ice (every 5 minutes mixed gently without pipetting)
3. A desalting column (PD10 column) was equilibrated in the 4°C room with PD10 buffer, tubulin was loaded onto the column in maximum 2.5 mL fractions.
4. The tubulin was eluted and the fractions containing tubulin were determined with a UV-Vis spectrophotometer.

5. The fractions were pooled, and spun down to remove aggregates at 50'000 rpm using a TLA120 rotor for 10min at 4°C.
6. The supernatant was recovered, and the molar amount of tubulin was determined.
7. A six-fold molar excess of RB3 was added to tubulin on ice and gently mixed by pipetting.
8. 0.6 times the molar tubulin quantity of TTL was added on ice and gently mixed by pipetting.
9. The complex was concentrated to 15-20 mg/ml at 4° C.
10. Nucleotides and reducing agent were added (10 mM DTT, 0.1 mM GDP, 1 mM ACP).
11. The crystallization complex was flash-frozen in 14 and 28 μ L aliquots and stored at -80 °C.

A representative analysis of the T₂R-TTL complex on a 12 % SDS-PAGE is shown below (Figure 3-10).

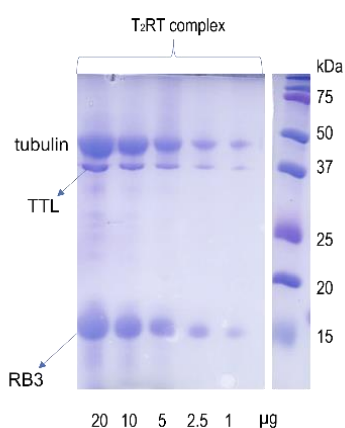


Figure 3-10. Coomassie stained SDS-PAGE illustrating the purity of formed T₂R-TTL complex

Crystallization

Solutions for crystallization

40% Glycerol	40% (v/v) glycerol in ddH ₂ O.
50% PEG	50% (w/v) PEG4000 scales in ddH ₂ O.
1M MES	19.5 g of 2-(N-morpholino)ethanesulfonic acid dissolved in 100 mL ddH ₂ O.
1 M imidazole	6.8 g imidazole dissolved in 100 mL ddH ₂ O
T ₂ R-TTL crystallization buffer pH 6.5	55.5 mL of 1 M MES mixed 44.5 mL of 1 M imidazole

Divalent ions:	300 mM CaCl ₂ , 300 mM MgCl ₂ : 30 mL of 1 M CaCl ₂ and 30 mL of 1 M MgCl ₂ ; filled up to 100 mL with ddH ₂ O.
250 mM L-tyrosine	2.26 g of L-tyrosine dissolved in 50 mL 1 M HCl.

Screening and crystallization procedure: The freshly prepared complex was screened to find the optimum conditions for crystallization. A 96-well plate with T₂R-TTL crystallization screen was prepared using a Formulator[®] Crystallography Screen Builder. Each plate contained 100 μL of T₂R-TTL crystallization buffer, 100 μL divalent ions, and 20 μL L-tyrosine. PEG4000 was distributed in a horizontal gradient from 1-12%, and glycerol in a vertical gradient of 2-16%, to find the appropriate window for crystallization (Figure 3-10). The wells were filled up with

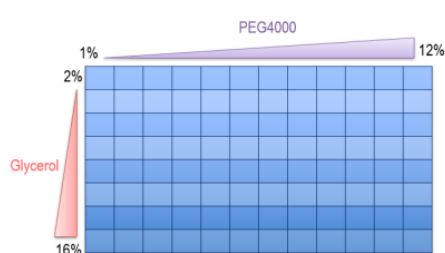


Figure 3-10. Schematic representation of a 96-well plate for the T₂RT-TTL crystallization

ddH₂O to 1 mL and the screen could be stored at 4° C or at room temperature. Commonly, a Mosquito[®] crystallization robot was used to dispense the prepared solutions for screening. Thus, the screen was aliquoted into a 96-well sitting-drop crystallization plate by pipetting 0.2 μL of T₂R-TTL complex followed by 0.2 μL reservoir solution into the well. Crystal growth was monitored for a few consecutive days and the best conditions were selected. Once the conditions were established, the needed amounts of crystals

were commonly set up manually using hanging drop crystallization plates and a drop volume up to 2 μL for easier handling. Occasionally, sitting drop crystallization plates were used or microbatch crystallization method. The bigger crystals could also be prepared using

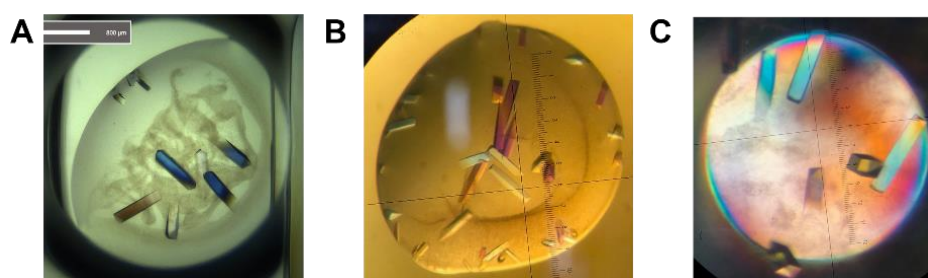


Figure 3-11. Examples of crystals obtained with the T₂R-TTL complex. The crystals were set up using the hanging drop method (A) with the complex formed after tubulin polymerization/depolymerization cycles; (B) with the complex formed without tubulin polymerization/depolymerization cycles; (C) T₂R-TTL complex crystals set up using microbatch crystallization under a layer of oil.

Mosquito® crystallization robot (up to 1+1 µl protein/reservoir drops). Crystal seeding was applied when needed. Examples of differently obtained T₂R-TTL crystals are shown in Figure 3-11.

3.2.3 REFERENCES

- [1] C. M. Dobson, *Annu. Rev. Biochem.* **2019**, *88*, 25–33.
- [2] A. P. Turnbull, P. Emsley, *Methods Mol. Biol.* **2013**, *1008*, DOI 10.1007/978-1-62703-398-5_17.
- [3] O. Cala, F. Guillière, I. Krimm, *Anal. Bioanal. Chem.* **2014**, *406*, DOI 10.1007/s00216-013-6931-0.
- [4] J. H. Van Drie, L. Tong, *Bioorganic Med. Chem. Lett.* **2020**, *30*, DOI 10.1016/j.bmcl.2020.127524.
- [5] L. Maveyraud, L. Mourey, *Molecules* **2020**, *25*, DOI 10.3390/molecules25051030.
- [6] Jan Drenth, in *Princ. Protein X-Ray Crystallogr.*, Springer Science, New York, USA, **2007**, p. 21.
- [7] J. M. Thomas, *Nature* **2012**, *491*, DOI 10.1038/491186a.
- [8] Jan Drenth, in *Princ. Protein X-Ray Crystallogr.*, Springer Science, New York, USA, **2007**, pp. 14–15.
- [9] N. Jones, *Nature* **2014**, *505*, DOI 10.1038/505602a.
- [10] and A. W. A. Dodson, E.J., *Protein Crystallography: A Consise Guide*, Wiley-Blackwell, **2012**.
- [11] K. Hasegawa, *Rigaku J.* **2012**, *28*, 14–18.
- [12] M. J. Adams, T. L. Blundell, E. J. Dodson, G. G. Dodson, M. Vijayan, E. N. Baker, M. M. Harding, D. C. Hodgkin, B. Rimmer, S. Sheat, *Nature* **1969**, *224*, DOI 10.1038/224491a0.
- [13] “PDB: <https://www.rcsb.org/stats/growth/growth-xray>,” **n.d.**
- [14] W. Kabsch, *Acta Crystallogr. Sect. D Biol. Crystallogr.* **2010**, *66*, 125–132.
- [15] Z. Otwinowski, W. Minor, *Methods Enzym.* **1997**, *276*.
- [16] R. A. Palmer, H. Niwa, in *Biochem. Soc. Trans.*, **2003**.
- [17] M. A. Hough, F. Prisch, J. A. R. Worrall, *Front. Mol. Biosci.* **2023**, *10*, 1–6.
- [18] L. Zhu, X. Chen, E. E. Abola, L. Jing, W. Liu, *Trends Pharmacol. Sci.* **2020**, *41*, DOI 10.1016/j.tips.2020.08.009.
- [19] M. Schmidt, H. Ihee, R. Pahl, V. Srajer, *Methods Mol. Biol.* **2005**, *305*, DOI 10.1385/1-59259-912-5:115.
- [20] J. M. Martin-Garcia, *Crystals* **2021**, *11*, DOI 10.3390/cryst11050521.
- [21] A. Ciulli, *Methods Mol. Biol.* **2013**, *1008*, DOI 10.1007/978-1-62703-398-5_13.
- [22] Ö. Kartal, F. Andres, M. P. Lai, R. Nehme, K. Cottier, *SLAS Discov.* **2021**, *26*, DOI 10.1177/24725552211013827.
- [23] C. R. Buchholz, W. C. K. Pomerantz, *RSC Chem. Biol.* **2021**, *2*, DOI 10.1039/d1cb00085c.
- [24] M. J. Harner, A. O. Frank, S. W. Fesik, *J. Biomol. NMR* **2013**, *56*, DOI 10.1007/s10858-013-9740-z.
- [25] L. Damian, *Methods Mol. Biol.* **2013**, *1008*, DOI 10.1007/978-1-62703-398-5_4.
- [26] A. M. Rossi, C. W. Taylor, *Nat. Protoc.* **2011**, *6*, DOI 10.1038/nprot.2011.305.
- [27] S. G. Patching, *Biochim. Biophys. Acta - Biomembr.* **2014**, *1838*, DOI 10.1016/j.bbamem.2013.04.028.
- [28] D. Patko, K. Cottier, A. Hamori, R. Horvath, *Opt. Express* **2012**, *20*, DOI 10.1364/oe.20.023162.
- [29] M. J. Clément, P. Savarin, E. Adjadj, A. Sobel, F. Toma, P. A. Curmi, *Probing Interactions of Tubulin with Small Molecules, Peptides, and Protein Fragments by Solution Nuclear Magnetic Resonance*, **2010**.
- [30] E. Nogales, S. G. Wolf, K. H. Downing, *Nature* **1998**, *391*, 199–203.
- [31] M. O. Steinmetz, R. A. Kammerer, W. Jahnke, K. N. Goldie, A. Lustig, J. Van Oostrum, *EMBO J.* **2000**, *19*, DOI 10.1093/emboj/19.4.572.
- [32] B. Gigant, P. A. Curmi, C. Martin-Barbey, E. Charbaut, S. Lachkar, L. Lebeau, S. Siavoshian, A. Sobel, M. Knossow, *Cell* **2000**, *102*, DOI 10.1016/S0092-8674(00)00069-6.
- [33] R. B. G. Ravelli, B. Gigant, P. A. Curmi, I. Jourdain, S. Lachkar, A. Sobel, M. Knossow, *Nature* **2004**, DOI 10.1038/nature02393.
- [34] B. Gigant, C. Wang, R. B. G. Ravelli, F. Roussi, M. O. Steinmetz, P. A. Curmi, A. Sobel, M. Knossow, *Nature* **2005**, *435*, DOI 10.1038/nature03566.
- [35] M. O. Steinmetz, A. E. Prota, *Trends Cell Biol.* **2018**, *28*, 776–792.
- [36] A. E. Prota, K. Bargsten, D. Zurwerra, J. J. Field, J. F. Díaz, K. H. Altmann, M. O. Steinmetz, *Science (80-)*. **2013**, *339*, 587–590.
- [37] A. E. Prota, M. M. Magiera, M. Kuijpers, K. Bargsten, D. Frey, M. Wieser, R. Jaussi, C. C. Hoogenraad, R. A. Kammerer, C. Janke, M. O. Steinmetz, *J. Cell Biol.* **2013**, *200*, 259–270.
- [38] T. Mühlethaler, D. Gioia, A. E. Prota, M. E. Sharpe, A. Cavalli, M. O. Steinmetz, *Angew. Chemie - Int. Ed.* **2021**, *60*, 13331–13342.
- [39] L. Pecqueur, C. Duellberg, B. Dreier, Q. Jiang, C. Wang, A. Plückthun, T. Surrey, B. Gigant, M. Knossow,

- Proc. Natl. Acad. Sci. U. S. A.* **2012**, *109*, 12011–12016.
- [40] G. La Sala, N. Olieric, A. Sharma, F. Viti, F. de Asis Balaguer Perez, L. Huang, J. R. Tonra, G. K. Lloyd, S. Decherchi, J. F. Díaz, M. O. Steinmetz, A. Cavalli, *Chem* **2019**, *5*, DOI 10.1016/j.chempr.2019.08.022.
- [41] T. Weinert, N. Olieric, R. Cheng, S. Brünle, D. James, D. Ozerov, D. Gashi, L. Vera, M. Marsh, K. Jaeger, F. Dworkowski, E. Panepucci, S. Basu, P. Skopintsev, A. S. Doré, T. Geng, R. M. Cooke, M. Liang, A. E. Prota, V. Panneels, P. Nogly, U. Ermler, G. Schertler, M. Hennig, M. O. Steinmetz, M. Wang, J. Standfuss, *Nat. Commun.* **2017**, *8*, DOI 10.1038/s41467-017-00630-4.
- [42] N. Gaillard, A. Sharma, I. Abbaali, T. Liu, F. Shilliday, A. D. Cook, V. Ehrhard, M. Banger, A. J. Roberts, C. A. Moores, N. Morrisette, M. O. Steinmetz, *EMBO Mol. Med.* **2021**, *13*, DOI 10.15252/emmm.202013818.
- [43] V. Campanacci, A. Urvoas, T. Consolati, S. Cantos-Fernandes, M. Aumont-Nicaise, M. Valerio-Lepiniec, T. Surrey, P. Minard, B. Gigant, *Structure* **2019**, *27*, DOI 10.1016/j.str.2018.12.001.
- [44] P. Ayaz, X. Ye, P. Huddleston, C. A. Brautigam, L. M. Rice, *Science (80-.)*. **2012**, *337*, DOI 10.1126/science.1221698.
- [45] E. Dráberová, V. Sulimenko, T. Sulimenko, K. J. Böhm, P. Dráber, *Anal. Biochem.* **2010**, *397*, 67–72.
- [46] J. Hutchings, G. Zanetti, *Biochem. Soc. Trans.* **2018**, *46*, DOI 10.1042/BST20170351.
- [47] John Jumper, Richard Evans, Alexander Pritzel, Tim Green, Michael Figurnov, Olaf Ronneberger, Kathryn Tunyasuvunakool, Russ Bates, Augustin Žídek, Anna Potapenko et al., *Nature*. **2021**, *596*, 583–589.
- [48] Renaud, JP., Chari, A., Ciferri, C. et al. *Nat Rev Drug Discov* **2018**, *17*, 471–492
- [49] Nawrotek A., Knossow M., Gigant B. *J. Mol. Biol.* **2011**, *412*, 35–42

3.3 X-RAY CRYSTALLOGRAPHY STRUCTURE DETERMINATION OF TUBULIN-MTAs COMPLEXES

In this section, the determination of MTAs-tubulin crystal structures and the subsequent structural analysis is described. When available, biochemical data is also included. Subchapter **3.3.1-3.3.3** includes the projects regarding the **colchicine site ligands**: the training projects (3.3.1-3.3.2) and the TubInTrain-derived project comprising crystallographic screening and the identification of an isotype-specific ligand (3.3.3). The most extensive subchapter **3.3.5** focuses on **rationally designed novel Todalam analogues**. The overview on the structural data of the project and the crystal structures of the bound ligands are shown and discussed here. The chemistry part of this project is previously discussed in section 2.4.

3.3.1 SuFEx SULFONATE MIMICS COMBRETASTATIN-A4

Abstract: A SuFEx click chemistry has been applied to synthesize biologically active sulfonate analogs of combretastatin-A4. Seven of the derivatives have been evaluated, and their crystal structures in complex with tubulin have been determined to 2.3 – 2.8 Å resolution. Furthermore, they were evaluated in a competition assay with MTC, and their affinities towards tubulin have been determined. Overall, this shows the first successful application of SuFEx derivatives as MTAs.

Declaration of contribution: This project has emerged as a collaboration with John Moses lab, Cold Spring Harbor Laboratory. It was my first training project during my secondment in at the Paul Scherrer Institute. With the compounds emerged from this work, I have gained my first experience in crystallization, data collection and structure determination on the compounds emerged from this work. I have performed soaking experiments and collected data for four compounds of the series. The data for the other three compounds were provided by Dr. Andrea Prota. Subsequently, I have determined the crystal structures of the whole series of these compounds, and prepared the figures and interpretation described below, and determined their binding affinities by MTC competition assays. Anne-Catherine Abel assisted me on the practical level in the initial phases of the training, and Dr. Andrea Prota guided the whole training process. Furthermore, I performed the MTC competition assays of these compounds, in order to determine their binding affinities.

3.3.1.1 INTRODUCTION

Recently, the catalytic sulfur (VI) fluoride exchange (SuFEx) click chemistry reaction has been described by Moses lab.^[1] This approach has been applied to synthesize a library of sulfonate mimics of CA-4, allowing to obtain a library of derivatives in a high-throughput fashion (performing the synthesis in a 96-well plate). In this way, 82 products were identified and upon the evaluation of their activity in cell viability experiments and tubulin assembly assay, seven compounds were chosen for the X-ray crystallography experiments with tubulin. All the synthesized compounds maintain the trimethoxyphenyl ring of CA-4 but possess a sulfonyl moiety in place of the CA-4 double bond. Ring B of the CA-4 has been modified and replaced with differently substituted phenyl groups (P17, P37, P71), substituted indole (P45, P50), naphthalene (P111) or biphenyl (P113) (Figure 3-13).

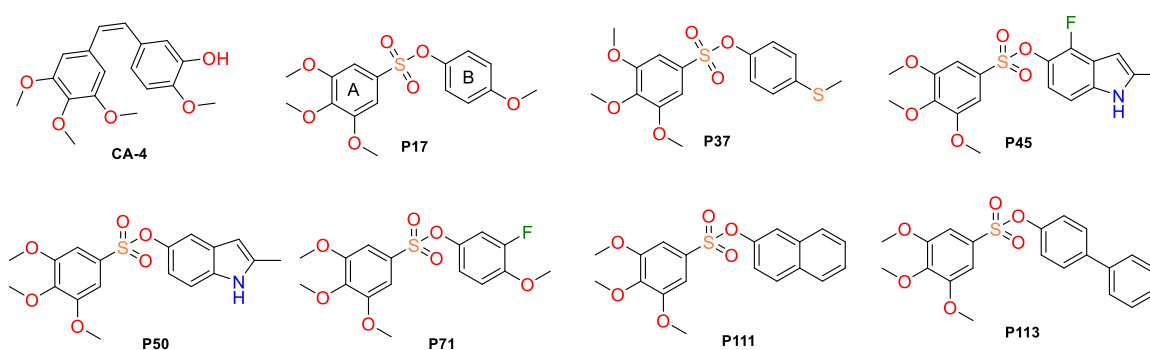


Figure 3-13. Chemical structures of CA-4 and the sulfonate CA-4 analogues.

3.3.1.2 RESULTS AND DISCUSSION

Structural description

To elucidate the tubulin-binding mode of the seven selected CA-4 mimetics upon binding to tubulin, we performed X-ray crystallography experiments. To obtain the tubulin crystals, the T₂R-TTL complex was used, formed by a protein complex composed of two bovine brain $\alpha\beta$ -tubulin heterodimers, the rat stathmin-like protein RB3, and the chicken TTL (discussed in Section 3.2) All seven compounds were soaked into the T₂R-TTL crystals, and their corresponding structures were determined in 2.3 – 2.8 Å resolution range (Table 3-3).

Table 3-3. The resolution of the obtained sulfonate CA-4 analogues-tubulin crystal structures.

Compound	P17	P37	P45	P50	P71	P111	P113
Resolution (Å)	2.6	2.67	2.78	2.57	2.28	2.79	2.25

The ligands bind to the colchicine site of tubulin, which is formed by residues of strands β S8, β S9, and β S10, loop β T7, and helices β H7 and β H8 of β -tubulin, and loop α T5 of α -tubulin. Similarly to CA-4 and other colchicine site ligands, the binding of the studied compounds

induces a conformational change of the β T7 loop, therefore preventing the curved-to-straight transition in tubulin and inhibiting tubulin polymerization (mechanism of action of colchicine site ligands is discussed in Section 1.3.3).

For all seven ligands, a similar binding mode was observed, closely resembling the one of parent CA-4. The trimethoxyphenyl moiety of compounds **P17-P113** occupies a hydrophobic pocket shaped by the side chains of β Tyr202, β Cys241, β Leu242, β Leu248, β Ala250, β Ile318, β Ala354, and β Ile378. The sulfonate group forms the hydrogen bonds with the β Asp251 and β Leu255. For compounds **P71**, **P17** and **P37** the second ring B fits into a predominantly hydrophobic pocket is shaped by β Asn258, β Met259, β Thr314, β Ala316, β Lys352, α Thr179 and α Val181. Interestingly, for ligand **P17** the α T5 loop is flipped down (Figure 3-14).

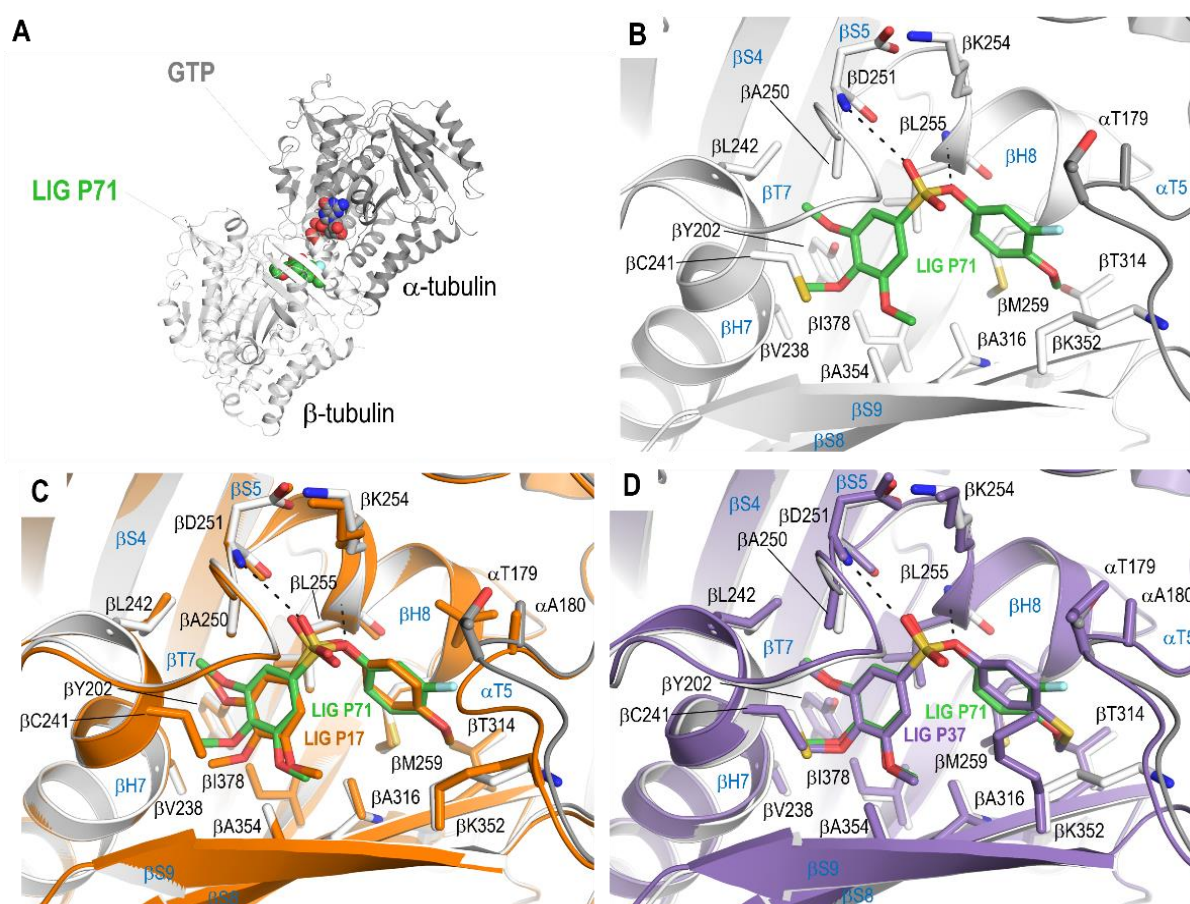


Figure 3-14. X-ray crystal structures of the tubulin-P71, tubulin-P17 and tubulin-P37 complexes. (A) Overall view of the tubulin-P71 complex structure. The β -tubulin and α -tubulin chains are in white and dark grey ribbon representation, respectively. The tubulin-bound ligand **P71** and the GTP molecule are represented as spheres. (B) Close-up view of the interaction network observed between **P71** (green) and tubulin (white/gray). Interacting residues of tubulin are shown in stick representation and are labeled. Oxygen and nitrogen atoms are colored in red and blue, respectively; carbon atoms are in green (**P71**) or white/gray (tubulin). Hydrogen bonds are depicted as black dashed lines. Secondary structural elements of tubulin are labeled in blue. (C) The same close-up view as in (B) with the superimposed tubulin-P17 (orange) structure. (D) The same close-up view as in (B) with the superimposed tubulin-P37 (violet) structure.

Identical binding mode is observed for the compounds with a bulky ring B (Figure 3-15). Only in case of **P113**, the trimethoxy groups of ring A are adapt differently, with p-methoxy pointing down towards the sidechain of Ile378. Overall, the conformations of interacting residues remain unchanged for all ligands, with the only exception being of the β Lys352 sidechain, which is quite flexible and adopts different conformations depending on the nature of the ligand.

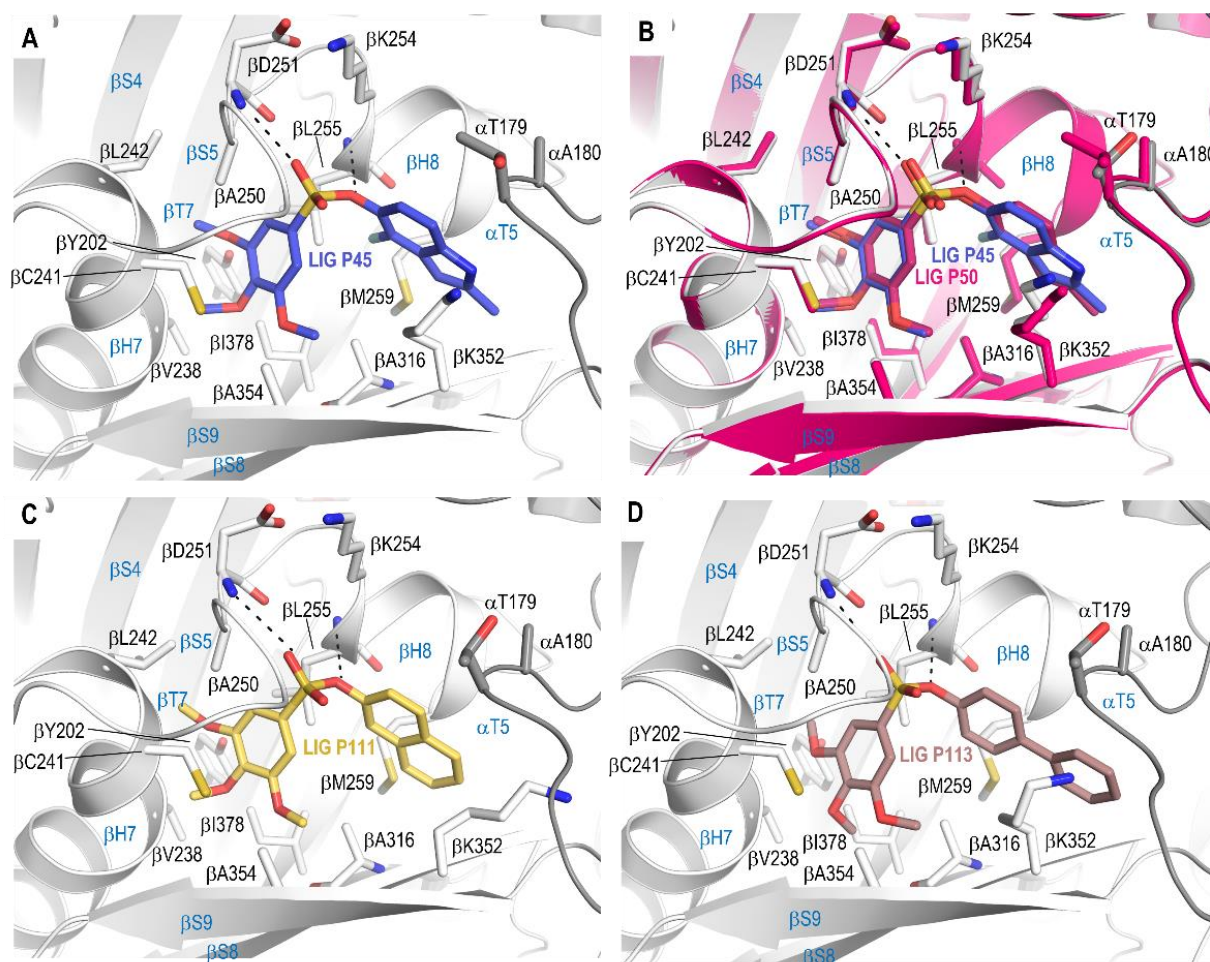


Figure 3-15. X-ray crystal structures of the tubulin-P45, tubulin-P50, tubulin-P111 and tubulin-P113 complexes. (A) Close-up view of the interaction network observed between **P45** (intense blue) and tubulin (white/gray). (B) Close-up view as in (A) with the superimposed tubulin-P50 (pink) structure. (C) Close-up view of the interaction network observed between **P111** (yellow) and tubulin (white/gray). (D) Close-up view of the interaction network observed between **P113** (light brown) and tubulin (white/gray). For all panels, the same representation style as in Fig.1-14 is applied.

To compare the binding mode of this compound class to that of tubulin-CA-4 (PDB ID 5LYJ; Figure 3-16A) and tubulin-colchicine (PDB ID 4O2B; Figure 3-16B), the relevant superpositions were done using the structure of tubulin-P71. As expected, the conformational changes and the poses adapted by the ligands are very similar to that of CA-4. However, compared to colchicine, the α T5 loop is not perturbed in the studied structures (with the exception of tubulin-P17). Furthermore, differences can be

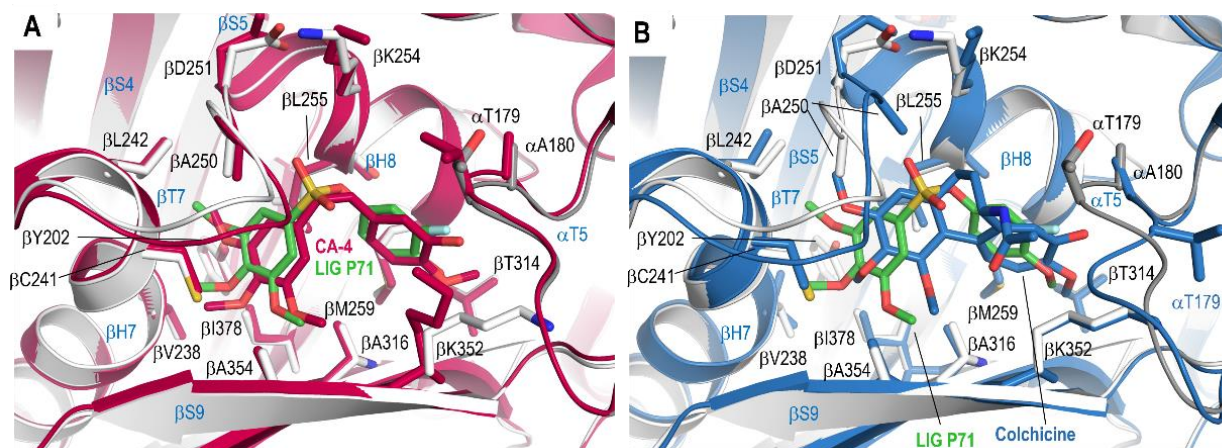


Figure 3-16. Structural superimpositions of tubulin-P71 (green/grey) and (A) tubulin-CA-4 (dark pink; PDB ID 5LYJ), (B) tubulin-colchicine (blue; PDB ID 4O2B). For all panels, the same representation style as in Fig.3-14 is applied. All structures were superimposed onto their β 1-tubulin chains.

noticed in the Asn249-Ala251 segment of the β T7 loop which adapts a slightly different conformation.

Biochemical evaluation

Competition assay with MTC

To further test the interaction of compounds **P17-P113** (Figure 3-13) with tubulin and determine their binding affinities, an MTC competition assay was performed. MTC, 2-methoxy-5-(2,3,4-trimethoxyphenyl)-2,4,6-cycloheptatrien-1-one (Figure 3-17), is the

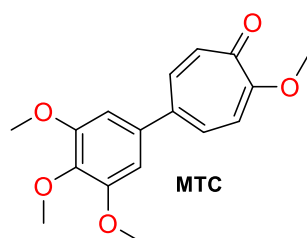


Figure 3-17. Chemical structure of MTC

fluorescent colchicine analogue, which forms a complex with tubulin with a peak of emission maximum at 421 nm (the maximum can slightly vary from 421 to 423) upon excitation at 350 nm. The UV absorbance spectrum of these compounds, followed by their ability to displace MTC in different concentrations (0.1 μ M to 40 μ M), were assessed. All compounds **P17-P113** could displace the MTC probe, confirming once again their binding to the colchicine pocket of tubulin, and their binding constants were calculated (Table 3-4).

Table 3-4. Binding affinities determined for the compounds **P17-P113**.

Compound	Nocodazole	P17	P37	P45	P50	P71	P111	P113
Kd (M^{-1})	2.0×10^6	2.65×10^6	2.7×10^6	3.0×10^6	1.7×10^6	1.82×10^6	1.4×10^6	1.34×10^6

Nocodazole was used as a control and the determined affinity was in the range with of the one previously described in the literature ($2.5 \times 10^6 M^{-1}$).^[2]

3.3.1.3 EXPERIMENTAL SECTION

Proteins and Compounds

The production of the stathmin-like domain of RB3 and chicken TTL in bacteria, as well as the reconstitution of the T₂R-TTL complex was done as described in Section 3.2. Compounds P17-P113 and MTC were provided by the John Moses lab.

Crystallization, data collection, and structure determination

Crystals of T₂R-TTL were grown by the vapor-diffusion method following the established protocols by Prota et al.^[3,4] The complex crystallized over night at 20 °C in the conditions listed below (Table 3-5). The crystals were soaked for 5 hours at 20°C in reservoir solutions containing 5 mM for of each of the compounds received (Figure 3-13). The crystals were transferred consecutively into cryo-protectant solutions I and II, before flash-freezing in liquid nitrogen and subsequent data collection.

Table 3-5. Crystallization condition and cryo-protectant solution composition

Crystallization buffer 1	PEG 4K (4 %), glycerol (9 %), MgCl ₂ (30 mM), CaCl ₂ (30 mM), tyrosine (5 mM), MES/Imidazole pH 6.5 (100 mM)
Crystallization buffer 2	PEG 4K (4 %), glycerol (10%), MgCl ₂ (30 mM), CaCl ₂ (30 mM), tyrosine (5 mM), MES/Imidazole pH 6.5 (100 mM)
Cryo-solution I	PEG 4K (10 %), glycerol (16%), MgCl ₂ (30 mM), CaCl ₂ (30 mM), tyrosine (5 mM), MES/Imidazole pH 6.5 (100 mM)
Cryo-solution II	PEG 4K (10 %), glycerol (20%), MgCl ₂ (30 mM), CaCl ₂ (30 mM), tyrosine (5 mM), MES/Imidazole pH 6.5 (100 mM)

Native data were collected at 100K at beamline X06SA of the Swiss Light Source (Paul Scherrer Institut, Villigen PSI, Switzerland). Data were processed and merged with XDS.^[5] The T₂R-TTL structures were determined using the difference Fourier method using the phases of a T₂R-TTL complex in the absence of ligands and solvent molecules as starting point for refinement (PDB ID 5LXT). Initial refinement included 10 cycles of rigid body and restrained refinement in Refmac^[6], followed by further refinement cycles in Phenix^[7]. The resulting models were further improved through iterative model rebuilding in Coot^[8] and refinement in Phenix. The quality of the structures was assessed with MolProbity.^[9]

Chains in the T₂R-TTL complex were defined as follows: chain A, α 1-tubulin; chain B, β 1-tubulin; chain C, α 2-tubulin; chain D, β 2-tubulin; chain E, RB3; chain F, TTL. Structure visualization, molecular editing and figure preparation were performed with the PyMOL molecular graphics system (The PyMOL Molecular Graphics System, Version 2.5.2 Schrödinger, LLC).

Competition assay with MTC

Lyophilized tubulin was suspended on ice in 10 mM NaPi with 0.1 mM GTP as a buffer. Tubulin was spun down using MLA 120 rotor at 50,000rpm at 4°C to remove the aggregates (10-20 min). Then, the emission spectra of each compound separately were measured to determine the background emission. The excitation wavelength was chosen based on the UV absorbance spectra of the MTC and the studied compounds (**P17-P113** and nocodazole as a control),). 350 nm was the maximum value of the MTC absorbance where the other compounds presented no to minimum (in case of compounds **P111**, **P113** and nocodazole) absorbance.

10 µM of tubulin and 10 µM of MTC were mixed in a buffer and left in on ice for 10 min, then the fluorescence intensity of the complex was measured. The compounds were then added to 150 µl of the complex (appropriate for the cuvette) in triplicates in concentrations of 0.1 µM, 0.5 µM, 1 µM, 2.5 µM, 5 µM, 10 µM, 15 µM, 20 µM, 30 µM, and 40 µM. 15 min incubation was done for each sample, after which they were measured using a Cary Eclipse spectrophotometer. Emission maximum values at 421 nm were used to calculate the displacement ratios with the help of the Prism software. The formula used for the calculation: $\log EC_{50} = \log(10^{\log K_i} \cdot (1 + \text{HotNM} / \text{HotKdNM}))$ $Y = (\text{Top} - \text{Bottom}) / (1 + 10^{(X - \log EC_{50})}) + \text{Bottom}$, where X is a logmolar concentration of a measured ligand and Y is a percentage of binding.

3.3.2 STILBENE_DERIVED COLCHICINE SITE BINDERS

Abstract: A set of promising tubulin binders for glioblastoma treatment has been identified by Rokit Pharma. To support their development and to elucidate their binding site, the compounds were submitted for X-ray crystallography experiments. The crystal structures of two compounds, termed **TUB-001** and **TUB-119**, were determined to 2.1 and 2.0 Å resolution, respectively. The structural data is presented here. Additional details of the project itself are not revealed due to data protection.

Declaration of contribution: This project has emerged within the collaboration with Rokit Pharma and has served as the second training project during secondment. I have prepared the T₂R-TTL complex and performed soaking experiments for the received compounds. Data collection and structure refinements were done by Dr. Andrea Prota. Furthermore, I prepared the final images and drafted the final report of structural data, further elaborated by Dr. Andrea Prota and Prof. Michel Steinmetz.

3.3.2.1 RESULTS AND DISCUSSION

Structural description

To obtain a detailed description of how the eight selected TUB compounds (Fig. 3-19, 3-21A) interact with tubulin, we performed X-ray crystallography experiments. To this aim, the T₂R-TTL crystallization system was used, which is formed by a protein complex composed of two bovine brain $\alpha\beta$ -tubulin heterodimers, the rat stathmin-like protein RB3, and the chicken tubulin tyrosine ligase (TTL). Using this approach, only **TUB-001** and **TUB-119** were found to be bound to T₂R-TTL and their corresponding complex structures were determined to 2.1 and 2.0 Å resolution, respectively.

Both ligands bind to the colchicine site of tubulin, which is formed by residues of strands β S8, β S9, and β S10, loop β T7, and helices β H7 and β H8 of β -tubulin, and loop α T5 of α -tubulin. One of the main features observed upon ligand binding is a conformational change of the β T7 loop, which is necessary to form the space allowing colchicine-site ligands to bind. In their bound states, the ligands prevent the rearrangement of secondary structural elements that occur during the curved-to-straight conformational change in the $\alpha\beta$ -tubulin heterodimer upon its assembly into microtubules. Such mechanism of action can be observed for both tubulin-**TUB-001** and tubulin-**TUB-119** complexes, suggesting that, similarly to other known colchicine-site ligands, **TUB-001** and **TUB-119** destabilize microtubules by preventing the curved-to-straight conformational transition in tubulin.

For both ligands, we observed an identical binding mode. In both the tubulin-**TUB-001** and tubulin-**TUB-119** complexes, the stilbene core of the ligands adapts the *trans* configuration. The prenylated-methoxyphenol substituted ring A is buried in the pocket that is shaped by the side chains of β Leu248, β Ala250, β Asp251, β Lys254, and β Leu255. It forms hydrogen bonds to the main chain amide of β Asp251 and to two water molecules connecting both main chain carbonyls of β Leu248 and α Thr179, and the side chain of α Asn101. The prenyl moieties of both the compounds establish hydrophobic contacts to the side chains of β Cys241, β Ala316, β Ile318, and β Ala354. Furthermore, the 3'-methoxy-4'-hydroxy substituted ring B of both compounds and their linking alkenes are stacked between the side chains of β Lys352, β Asn258, and α Val181, and are further stabilized by mixed hydrophobic and polar contacts to β Met259, β Thr314, β Asn349, and the α T5 loop residues α Ser178, α Thr179, and α Val181. Finally, the 4'-hydroxy groups of ring B form one hydrogen bond to the main chain carbonyl of β Asn349 and on water-mediated hydrogen bond to α Ser178 (Figure 3-19C, 3-19D).

To compare the distinct binding mode of this compound class to that of other colchicine-site ligands, we inspected their superimpositions onto the tubulin-colchicine (PDB ID 4O2B; Figure 3-20A), tubulin-combretastatin A4 (CA-4; PDB ID 5LYJ; Figure 3-20B), and tubulin-

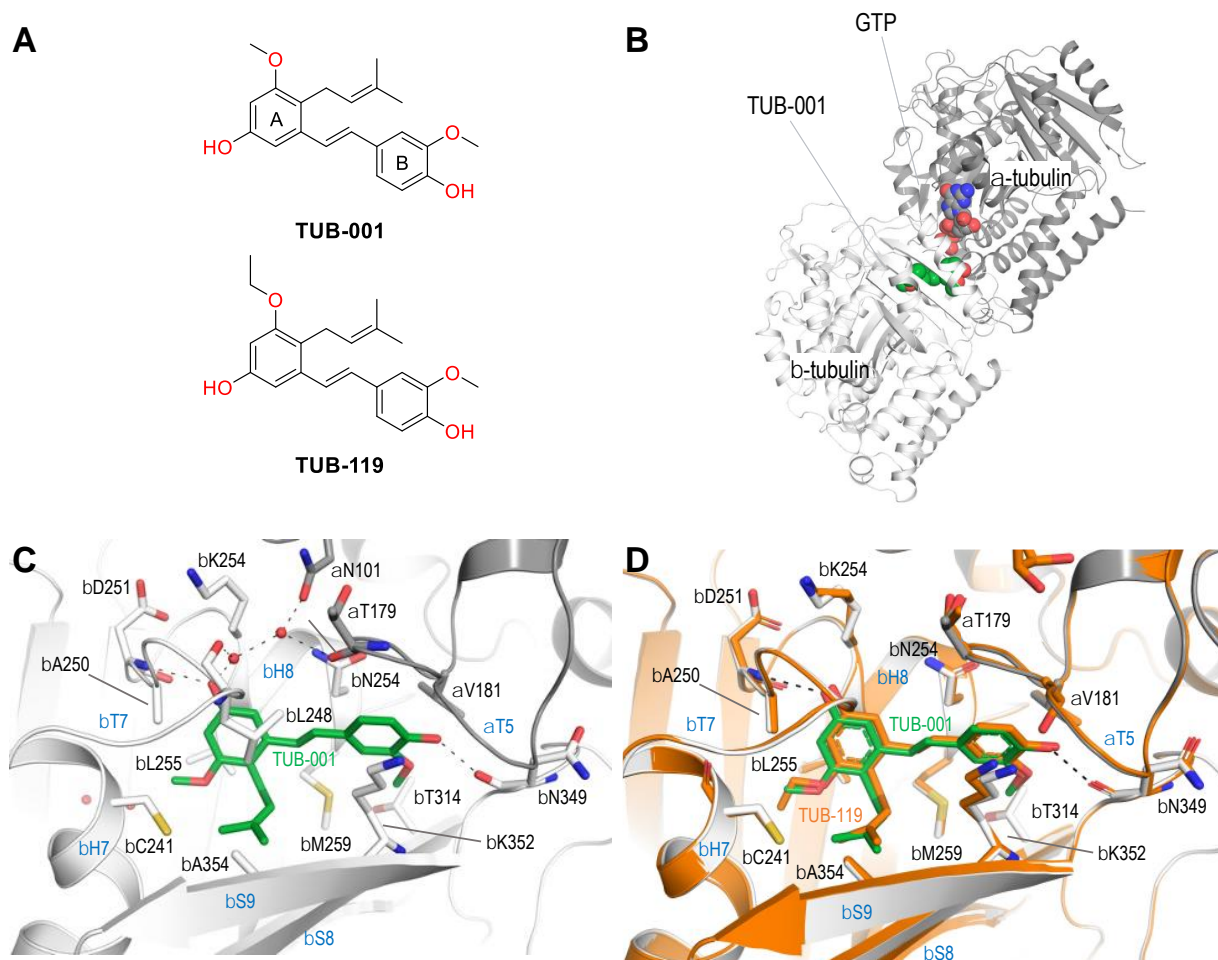


Figure 3-19. X-ray crystal structures of the tubulin-TUB-001 and tubulin-TUB-119 complexes. **(A)** Chemical structures of compounds **TUB-001** and **TUB-119**. **(B)** Overall view of the tubulin-TUB-001 complex structure. The β -tubulin and α -tubulin chains are in white and dark grey ribbon representation, respectively. The tubulin-bound ligand TUB-001 and the GTP molecule are represented as spheres. **(C)** Close-up view of the interaction network observed between **TUB-001** (green) and tubulin (white/gray). Interacting residues of tubulin are shown in stick representation and are labeled. Oxygen and nitrogen atoms are colored in red and blue, respectively; carbon atoms are in green (**TUB-001**) or white/gray (tubulin). Key interacting water molecules are represented as red spheres. Hydrogen bonds are depicted as black dashed lines. Secondary structural elements of tubulin are labeled in blue. **(D)** The same close-up view as in (C) with the superimposed **TUB-119** (orange) structure.

plinabulin (PDB ID 6S8K; Figure 3-20DF) structures. Compared to colchicine, the α T5 loop is not perturbed in the tubulin-TUB structures, which is flipped out in the colchicine structure to avoid clashes with the colchicine molecule. Moreover, minor rearrangements are observed in the β Asn249- β Ala250 segment of the β T7 loop thereby adapting a slightly different conformation. In the case of CA-4, the conformational changes observed in the site are quite similar; however, the ligands adopt substantially different poses. In the case of the TUBs, the prenylated-methoxyphenol substituted ring A is shifted, allowing the prenyl moiety to fit in the place that is otherwise occupied by the trimethoxy-substituted ring of CA-4. Interestingly, while CA-4 is only able to bind in the *cis* configuration, both TUBs are bound in the *trans* configuration. Overall, although the ligands occupy similar space as the

colchicine and the CA-4 molecules (Zone 1 of the colchicine site;), the TUB scaffold is bound in a different, unique way. On the contrary, the plinabulin molecule occupies a different zone of the site (Zone 2), thereby only slightly overlapping its substituted imidazole ring with the isoprenyl moiety of the TUBs. Of note, in both TUB crystal structures, two water molecules occupy the space that is otherwise filled by plinabulin. The observed structural differences could be exploited to introduce further TUB scaffold modifications in the meta position of the prenylated phenol moieties of to potentially improve the pharmacological profile and potency of this compound class.

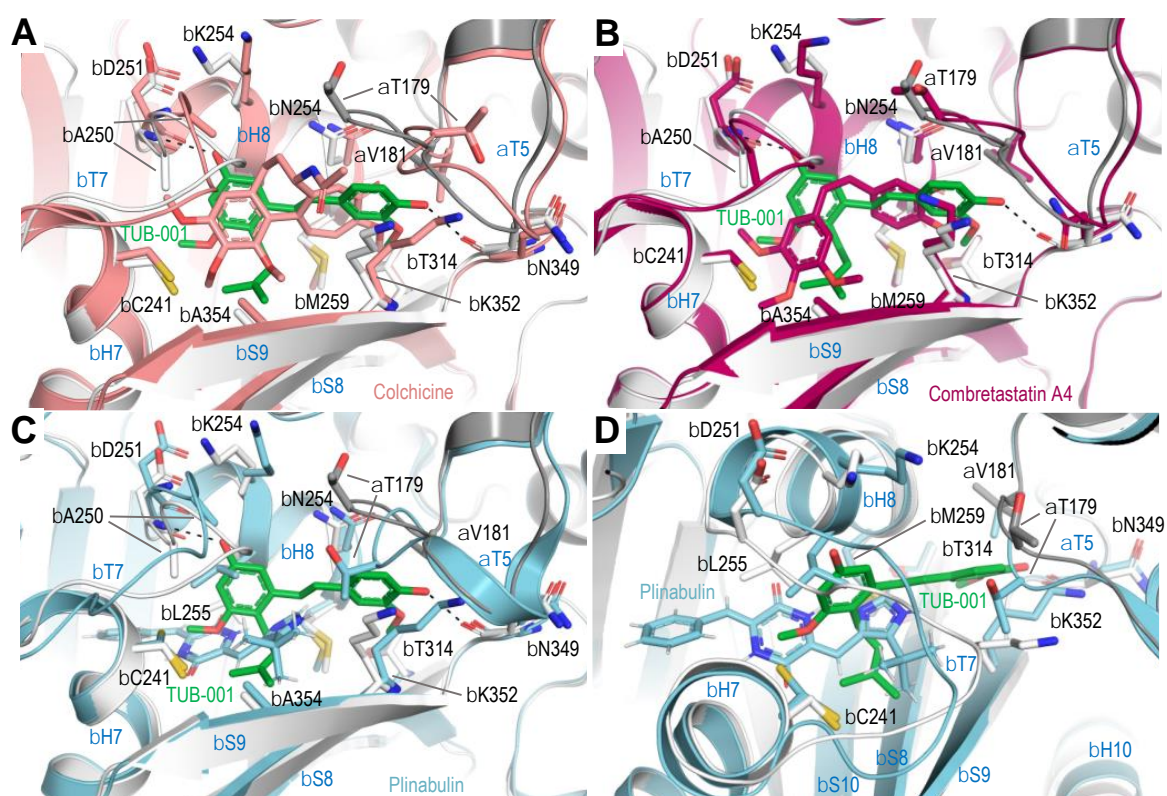


Figure 3-20. Comparison of the TUB-001 tubulin-binding pose to selected colchicine-site targeting agents. Structural superimpositions of tubulin-TUB-001 (green/grey) and (A) tubulin-colchicine (salmon; PDB ID 4O2B; rmsd of 0.32 Å over 364 C α -atoms), (B) tubulin-combretastatin (purple; PDB ID 5LYJ; rmsd of 0.25 Å over 359 C α -atoms). (C) and (D) Superimposition of tubulin-TUB-001 (green/white/grey) and tubulin-plinabulin (cyan; PDB ID 6S8K; rmsd of 0.36 Å over 363 C α -atoms) in two different orientations. For all panels, the same representation style as in Fig.3-19 is applied. All structures were superimposed onto their β 1-tubulin chains.

Modeling

To obtain insight into why only TUB-001 and TUB-119 bound to our T₂R-TTL crystal system, we modeled the other six TUB variants 143, 146, 148, 149, 168, and 170 into the colchicine site individually, using the binding pose of the bound compound TUB-001 as a starting point.

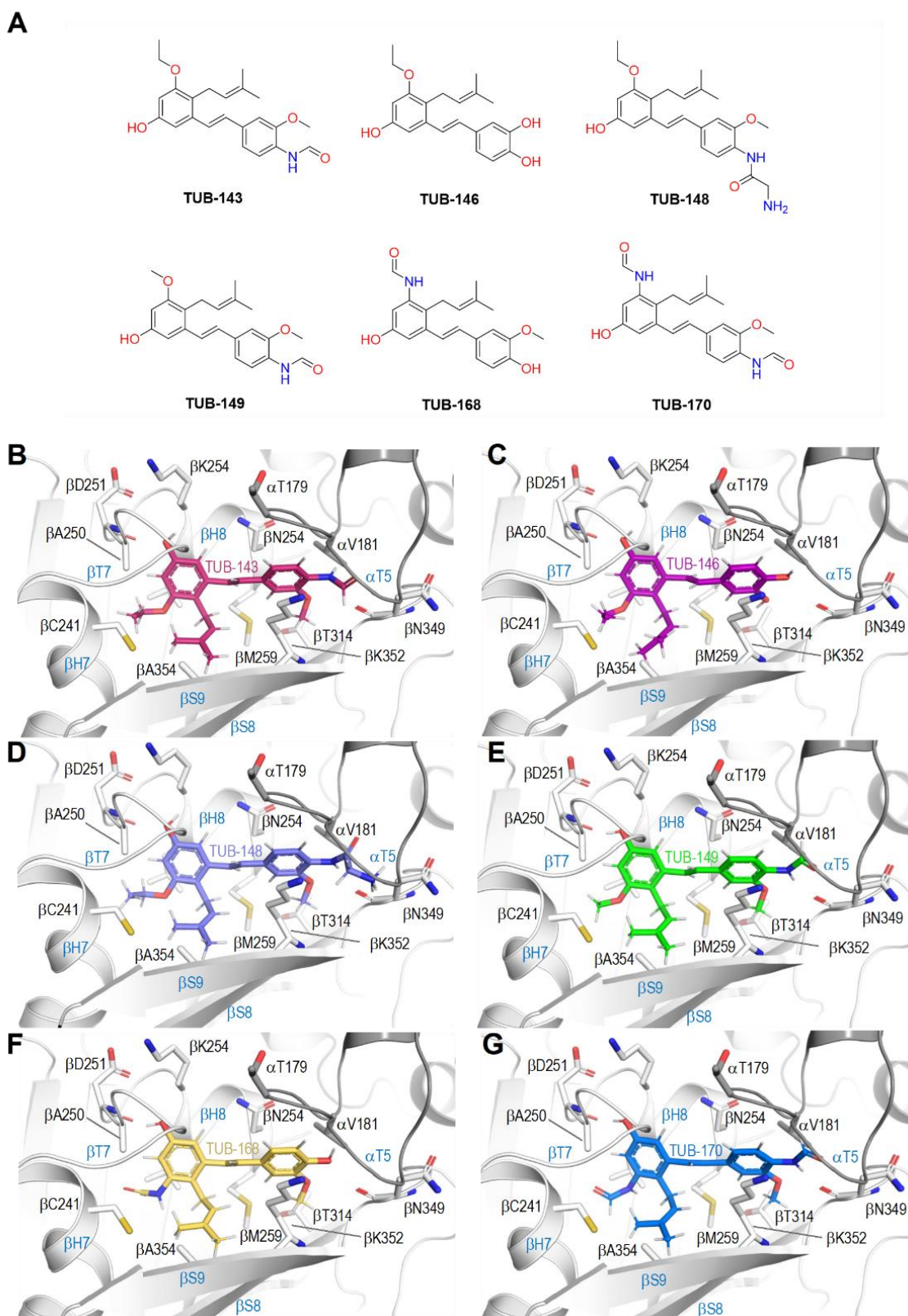


Figure 3-21. Compounds modeled into the crystal structure of T₂R-TTL-TUB-001 complex. (A) Chemical structures of the modeled TUB-compounds. **(B)** TUB-143, warm pink; **(C)** TUB-146, purple; **(D)** TUB-148, slate; **(E)** TUB-149, green; **(F)** TUB-168, orange-yellow; **(G)** TUB-170, marine. The α -tubulin and β -tubulin chains are in white and dark grey ribbon representation, respectively. The same representation style as in Fig.3-19 is applied.

The molecules were first minimized by using the MAB all atom force field in Moloc^[10] and then fitted into the binding site by relaxing all residues within 5 Å distance. The major differences between the crystal structures and the modeled ligands were observed in the formamide moieties of **TUB-143**, **TUB-149**, and **TUB-170** and in the 2-aminoacetamide of **TUB-148**, as opposed to the free hydroxyl groups of compounds **TUB-001** and **TUB-119**.

Based on the modeled structures, we evaluated the space needed to fit these groups, which seems appropriate for all the compounds. Although in the case of compound 148 the distance between the 2-aminoacetamide and β Asn349 is very close and could lead to potential clashes in the structure, minor rearrangements of the α T5 loop might be sufficient to accommodate the ligand. In the case of **TUB-168** and **TUB-170**, we assessed the space needed for the formamide groups in meta position and could not observe any steric hinderance that wouldn't allow these moieties to fit. Overall, based on the observations from the modeled structures, we did not find chemical or structural features that could prevent binding, suggesting that the lack of observed binding in the crystals is likely due to other factors such as, e.g., compound solubility.

3.3.2.2 EXPERIMENTAL SECTION

Proteins and Compounds

The production of the stathmin-like domain of RB3 and chicken TTL in bacteria, as well as the reconstitution of the T₂R-TTL complex was done as described in Section 3.2. The compounds were provided by Rokit Pharma.

Crystallization, data collection, and structure determination

Crystals of T₂R-TTL were grown by the vapor-diffusion method following the established protocols by Prota et al.^[3,4] The complex crystallized over night at 20 °C in the conditions listed below (Table 3-6). The crystals were soaked for 6 hours at 20°C in reservoir solutions containing 5 mM of each of the compounds received (Figures 3-19A, 3-21A). The crystals were transferred consecutively into cryo-protectant solutions I and II, before flash-freezing in liquid nitrogen and subsequent data collection.

Table 3-6. Crystallization condition and cryo-protectant solution composition

Crystallization buffer 1	PEG 4K (3 %), glycerol (10 %), MgCl ₂ (30 mM), CaCl ₂ (30 mM), tyrosine (5 mM), MES/Imidazole pH 6.5 (100 mM)
Crystallization buffer 2	PEG 4K (3 %), glycerol (11%), MgCl ₂ (30 mM), CaCl ₂ (30 mM), tyrosine (5 mM), MES/Imidazole pH 6.5 (100 mM)
Cryo-solution I	PEG 4K (10 %), glycerol (16%), MgCl ₂ (30 mM), CaCl ₂ (30 mM), tyrosine (5 mM), MES/Imidazole pH 6.5 (100 mM)
Cryo-solution II	PEG 4K (10 %), glycerol (20%), MgCl ₂ (30 mM), CaCl ₂ (30 mM), tyrosine (5 mM), MES/Imidazole pH 6.5 (100 mM)

Native data were collected at 100K at beamline X06DA of the Swiss Light Source (Paul Scherrer Institut, Villigen PSI, Switzerland). Data were processed and merged with XDS.^[5] The T₂R-TTL structures were determined using the difference Fourier method using the phases of a T₂R-TTL complex in the absence of ligands and solvent molecules as starting point for refinement (PDB ID 5LXT). The positioning of the ligands within the T₂R-TTL complex and ligand electron densities are shown in Figure 3-22. Initial refinement included 10 cycles of rigid body and restrained refinement, followed by further refinement cycles in Refmac.^[6] The resulting models were further improved through iterative model rebuilding in Coot^[8] and refinement in Phenix.^[7] The quality of the structures was assessed with MolProbity.^[9]

Chains in the T₂R-TTL complex were defined as follows: chain A, α 1-tubulin; chain B, β 1-tubulin; chain C, α 2-tubulin; chain D, β 2-tubulin; chain E, RB3; chain F, TTL (Figure SXA3-22). Structure visualization, molecular editing and figure preparation were performed with the PyMOL molecular graphics system (The PyMOL Molecular Graphics System, Version 2.5.2 Schrödinger, LLC).

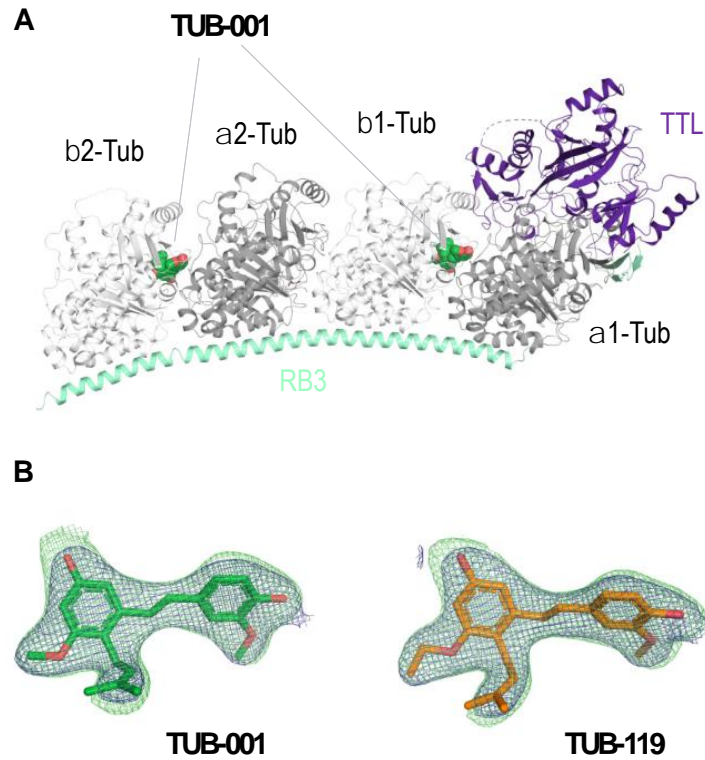


Figure 3-22. The T_2R -TTL-TUB-001 complex and ligand details. **(A)** Overall view of the T_2R -TTL-TUB-001 complex structure. The α -tubulin and β -tubulin chains are in white and grey, TTL is in rubidium, and RB3 is in samarium ribbon representation, respectively. The two bound TUB-001 molecules are represented as green spheres, respectively. **(B)** Electron-density maps of both the TUB-001 and TUB-119 ligands bound to tubulin in their corresponding T_2R -TTL complexes. The SigmaA-weighted $2mFo - DFc$ (deep blue mesh) and $mFo - DFc$ (lime mesh) omit maps are contoured at $+1.0\sigma$ and $+3.0\sigma$, respectively. The map calculations excluded the atoms of the TUB ligands.

3.3.3 CHALCONE 251 SELECTIVELY TARGETING β III TUBULIN ISOTYPE

Abstract: Based on computational screening of Enamine compound libraries for novel tubulin binders, a total of 68 were submitted for crystallographic and biochemical evaluation. As a result, a promising hit was identified, termed “**251**”. This chalcone was found to bind to the colchicine site of tubulin, specifically targeting the tubulin β III isotype. The crystal structure, relevant structural comparisons with other colchicine site binders possessing a similar binding mode and biochemical data demonstrating the compound specificity are described. β III isotype is the most prevalent tubulin-isotype in the brain. It is known to be highly expressed in neuronal or neuroplastic tumors and upregulated by different types of cancer cells, leading to drug resistance to MTAs commonly used in chemotherapy. Therefore, **251** or derivatives thereof could have a potential application in the treatment of gliomas and other types of tumors or as a probe to provide insights into the dynamics of neuronal microtubules.

Declaration of contribution:

This project was performed within the WP-1 activities of TubInTrain project aimed on identification of novel tubulin binders. Computational studies were performed by Maxim Shevelev, group of Prof. Varnek, Laboratory of Chemoinformatics at the University of Starsbourg, France. As a result, 68 compounds were selected for crystallographic and biochemical screening. My work included the preparation of T₂R-TTL complex and its crystallization, followed by soaking and co-crystallization experiments of those molecules, data collection and refinements. In total, I collected over 300 datasets in the resolution range between 2.1 and 3.0 Å. Subsequently, I identified **251** as a hit and determined its crystal structure in complex with tubulin. Final refinements and data analysis were done with the help of Dr. Andrea Prota. The biochemical characterization was done by the group of J. Fernando Díaz, Centro de Investigaciones Biológicas Margarita Salas, Madrid, Spain. MTC assay and tubulin assembly experiments were done by Ahmed Soliman, while cell viability assays were done by Francesca Bonato. Furthermore, molecular dynamics simulations are performed by Anne-Catherine Abel, group under the guidance of Prof. Pieraccini, at University of Milan.

3.3.3.1 INTRODUCTION

Although a great number of diverse tubulin binders are currently known (reviewed in Chapter 1), compounds of new scaffolds and new properties could still greatly contribute to the class of MTAs. Nowadays, efficient mining of the chemical space by computational and crystallographic screening can easily yield promising hits in a high-throughput fashion. For this purpose, compounds can be screened from readily available databases and selected screening libraries, such as e.g. Enamine.^[11,12] With that in mind, using pharmacophore-based screening of known tubulin-binding sites, the computational screening of Enamine library was performed by Maxim Shevelev. Sixty-eight compounds were selected for X-ray crystallography evaluation of potential tubulin binders using the established T₂R-TTL crystallization system.^[4] To comprehensively assess the compounds, they were also screened for activity on tubulin polymerization. As a result, a hit compound, numbered “**251**”, was identified. Initially, it was found to bind to the colchicine site on tubulin and exert destabilizing effect on tubulin assembly.

It is commonly known that multiple α - and β -tubulin genes encode different $\alpha\beta$ -tubulin isotypes that are expressed by human cells. The upregulation of certain tubulin isotypes by cancer cells, notably β III-tubulin, underlies a well-known mechanism of drug resistance to commonly used MTAs, e.g. paclitaxel.^[13,14] Therefore, a ligand selectively targeting β III-tubulin could overcome the resistance and improve the specificity of tubulin binders as cancer therapeutics. To develop such isotype-selective ligands, a thorough understanding of the distinct structural and kinetic characteristics of tubulin binders to various β -tubulin isotypes is needed. The peculiar behavior of our hit in soaking and crystallization experiments and its unusual kinetic interplay in a competition assay experiments with MTC made us investigate selective binding of this compound to one of the tubulin isotypes, specifically β III-tubulin.

To characterize the binding of **251**, we aimed to obtain its crystal structure with tubulin and perform the comparisons with other colchicine site-drugs, to help identify specific binding properties associated with targeting of certain tubulin isotypes. Based on the structural data, molecular dynamic simulations are performed to further elucidate the mechanism behind the ligand selectivity. Furthermore, we envisioned a comprehensive biochemical characterization, including cell viability assays both β III-overexpressed and P-gp resistant cell lines.

It is also worth noting that β III-tubulin is abundant in the brain, compared to systemic organs and tissues, and its expression is associated with neuronal differentiation and decreased cell proliferation. Therefore, a β III-specific ligand could eventually find application as a probe to study the neuronal microtubules, highly relevant in the context of work performed within TubInTrain.

3.3.3.2 RESULTS AND DISCUSSION

Structural description

The selected 68 compounds were screened by X-ray crystallography using soaking and co-crystallization experiments with the T₂R-TTL crystallization system (described in Section 3.2). The T₂R-TTL crystallization setup was chosen as most binding sites are accessible in this system. Using this approach, compound **251** (Figure 3-23A) was identified as a hit. Eventually, its crystal structure was determined to 2.0 Å resolution.

Initial screens were performed in both short-/long-term soaking and co-crystallization experiments using the T₂R-TTL complex prepared with previously polymerized/depolymerized tubulin. Although a clear perturbation of the colchicine site highlighting a bound ligand was detected, the data did not allow to obtain a well-defined ligand density needed for the correct modelling of the compound in the crystal structure. The best-defined electron density delineating the bound ligand **251** with high occupancy was obtained with a T₂R-TTL crystallization complex assembled without additional tubulin polymerization/depolymerization cycles. The final crystal structure of **251** in complex with tubulin was obtained with just 2h soaks. Careful analysis of the electron density in the site suggested that the compound selectively binds to β III-tubulin, which would also explain its peculiar behavior. It is worth noting, that tubulin polymerization/depolymerization experiments lead to changes in the isotype ratios of tubulin, and such treated tubulin has a much lower β III-isotype content. Therefore, ligand **251** was modelled in the β III-tubulin structure, which is characterized by the presence of β Ser241 and β Val318 in the colchicine site, in place of β Cys241 and β Ile318 of β II-tubulin (Figure 3-10D).

251 binds to the colchicine site of tubulin, formed by residues of the strands β S8, β S9, and β S10, the loop β T7, and the helices β H7 and β H8 of β -tubulin, and the loop α T5 of α -tubulin. Differently to the colchicine analogues described in Section 3.3.1 and 3.3.2, which occupy zone I and II of the colchicine site, **251** occupies zones II and III, which are located mostly on β -tubulin. Upon the binding of the ligand, the β T7 loop undergoes a conformational change, while the α T5 loop remains in a “closed” conformation. The binding mode of **251** suggests that, similarly to other colchicine site binders, it destabilizes microtubules by preventing the curved-to-straight conformational transition in tubulin. The 5-pyridine moiety of the ligand (ring A in Figure 3-23A) is buried in the pocket shaped by the side chains of β Ile4, β Tyr52, β Gln136, β Asn167, β Phe169, β Glu200, β Val238, β Thr239, β Leu242, and β Leu252. Furthermore, the pyridine nitrogen N1 establishes a hydrogen bond with the carboxamide hydrogen of the β Asn167. The α , β -unsaturated carbonyl system characteristic for chalcones forms hydrophobic interactions with β Tyr202 and is further stabilized by a hydrogen bond formed between the C8-carbonyl of the ligand and the side chain of β Glu200. The data in the literature has already demonstrated that the latter likely exists as a carboxylic acid rather than as a carboxylate and can therefore engage in a hydrogen bonding interaction. The

methylpyrazole moiety (ring B in Figure 3-23A) is sandwiched between the side chains of β Leu255 and β Ile378, and further surrounded by β Met259, β Val238, and β Ser241, with which it establishes a third hydrogen bond. Finally, the fluorophenyl moiety (ring C in Figure 3-23A) is stabilized by hydrophobic contacts to β Leu248, β Lys352, β Ala316, the main chain carbonyl of β Thr317, β Val318, the backbone atoms of β Val353, β Ala354, and to the α T5 loop residue α Thr179 (Figure 3-23D).

To compare the distinct binding mode of **251** to that of other colchicine-site ligands, we inspected their superimpositions onto the colchicine site ligands occupying similar space: tubulin-TUB075 (PDB ID 6FKJ; Figure 3-23E), tubulin-TN16 (PDB ID 3HKD; Figure 3-23F), and tubulin-plinabulin (PDB ID 6S8L; Figure 3-23G).

A great overlap can be observed between 251 and TUB-075 molecules, and both β T7 and α T5 loops adapt a similar conformation. The 5-pyridine and 5-phenyl moieties of 251, and TUB075, respectively, establish similar interactions. Similarly, the rings of the fluorophenyl (**251**) and the 2-ethoxy aniline moiety (TUB075) perfectly superimpose in both structures and establish hydrophobic interactions. Furthermore, the chalcone carbonyl of 251 establishes a hydrogen bond with the β Glu200, as also observed for the C3 carbonyl of TUB075 cyclohexanedione. Very similar structural features are observed in case of TN16 and plinabulin, with hydrophobic moieties connected by a pyrrolidinedione (TN16) or a diketopiperazine (plinabulin) able to establish hydrogen bonds with β Glu200 and β Cys241 (or β Ser241). In the case of TUB075 and TN16, the compounds do not present any isotype specificity. However, plinabulin is known to preferentially interact with β II- compared to β III-tubulin^[15], in contrast to **251**. Both crystal structures of plinabulin with β II and β III tubulin complexes are available, and the β III-tubulin-plinabulin structure has been used for comparison. While all the compared structures establish similar interactions and can be described by a common pharmacophore model, the crucial difference that can be spotted is that in the case of TUB075, TN16 and plinabulin the central rings establish the hydrogen bonds, while in the case of 251 it is the chalcone carbonyl. In fact, the central ring B of 251 is shifted towards the β Ser241 and β Val318, and the methylpyrazole N2 nitrogen engages in a hydrogen bond interaction with β Ser241 by occupying the same space as both the C1 carbonyls and the aliphatic moieties of all three TUB075, TN16 and plinabulin. The latter are less bulky in this section of the molecule compared to the methylpyrazole of 251, suggesting that **251** preferentially binds to an isotype possessing more space (β Val318 instead of β Ile318) in this position to avoid clashes. To deeper investigate the possible protonation states within the binding site and evaluate the stability of **251** within the pocket, the molecular dynamics simulations of **251**-tubulin complex are currently being performed by Anne-Catherine Abel, under the guidance of Prof. Pieraccini at the University of Milan.

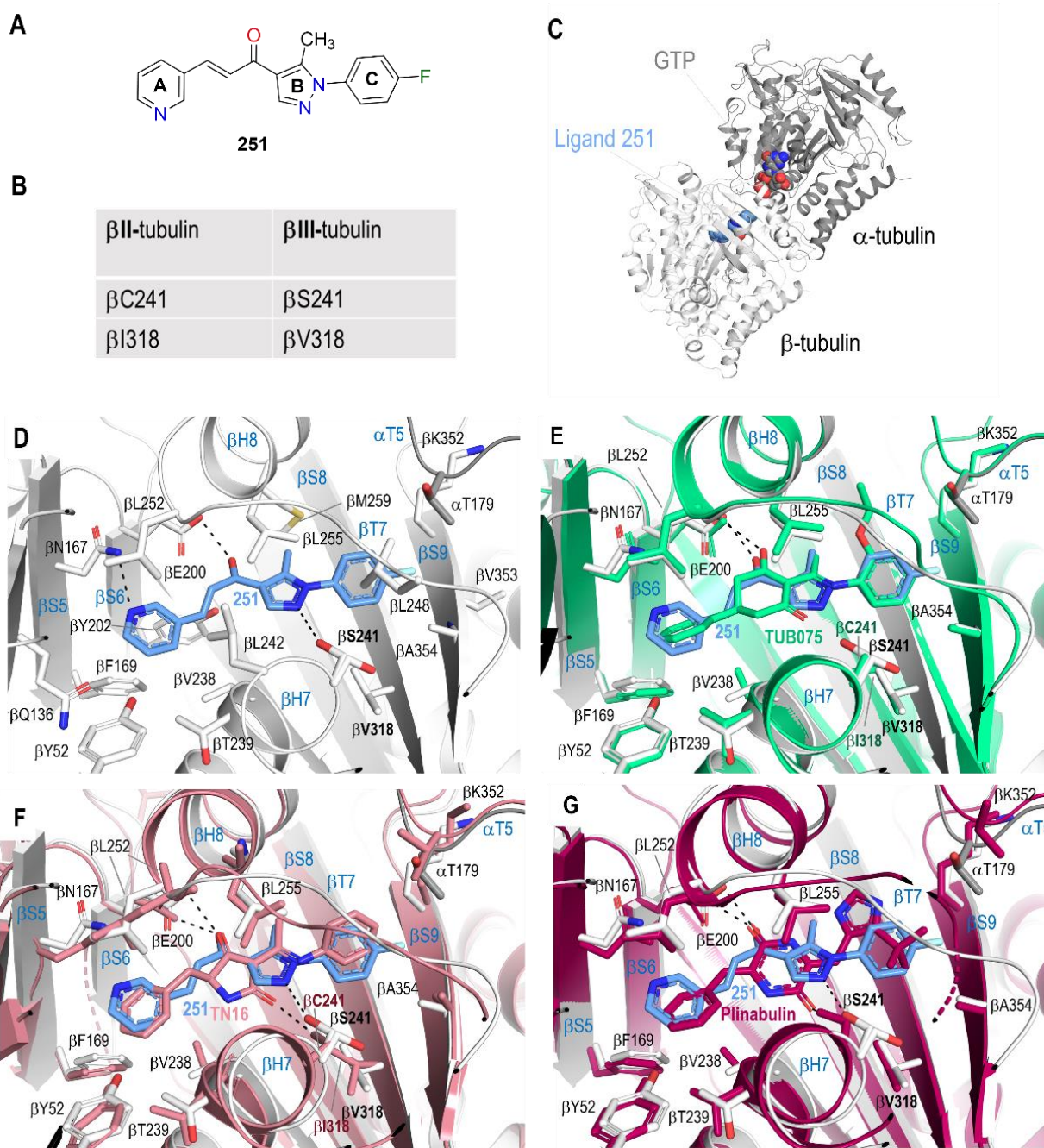


Figure 3-23. Crystal structure of the tubulin-251 complex. (A) Chemical structure of **251**; (B) Main differences in the colchicine site between β II- and β III-tubulin isotypes; (C) Overall view of the T_2R -TTL-251 complex structure. The α -tubulin and β -tubulin chains are in dark and light grey ribbon representation, respectively. The tubulin bound **251** and the GTP molecules are represented as spheres; (D) Close-up view of the interaction network observed between **251** (blue) and tubulin (white/grey). Interacting residues of tubulin are shown in stick representation and are labelled. Oxygen and nitrogen atoms are coloured in red and blue, respectively; carbon atoms are blue (**251**) or white/grey (tubulin). Hydrogen bonds are depicted as black dashed lines. Secondary structural elements of tubulin are labelled in blue. (E-G) Superimpositions of the tubulin-**251** and (E) tubulin-TUB075 (green; PDB ID:6FKJ; rmsd of 0.193 Å over 373 C α -atoms), (F) tubulin-TN16 (light pink; PDB ID: 3HKD; rmsd of 0.530 over 371 C α -atoms), (G) tubulin-plinabulin (lawrencium; PDB ID:6S8L; rmsd of 0.386 Å over 356 C α -atoms) complex structures in the same orientation and representation as in panel (D). All structures were superimposed onto their β 1-tubulin chains.

Biochemical evaluation

The biochemical characterization was done by in the group of J. Fernando Díaz, Centro de Investigaciones Biológicas Margarita Salas, Madrid, Spain, by Ahmed Soliman and Francesca Bonato.

Polymerization assay

To investigate the effect of compound **251** on tubulin assembly dynamics in vitro, we performed duplicated polymerization assays in aqueous GAB buffer (10 mM NaPi, 30% glycerol, 1 mM EGTA, 6 mM MgCl₂, 1 mM GTP, pH 6.7). The assembly time-course of 25 μM tubulin in the presence of 27.5 μM of the tested compound was monitored in a

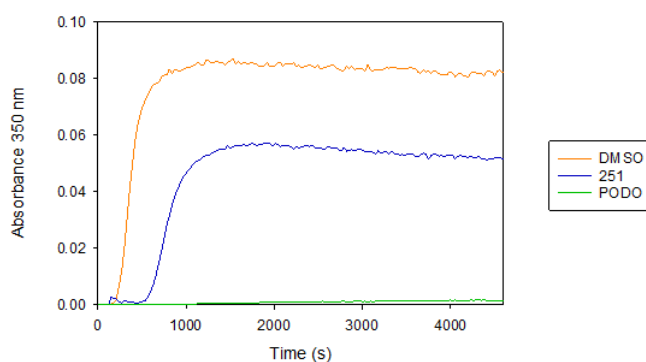


Figure 3-24. Inhibition of tubulin assembly by compound **251**. All experiments were performed as duplicates of two independent experiments.

ThermoFisher Appliskan plate reader, measuring the absorbance at 355 nm for at least 4600s at 37 °C. The increase of the solution's turbidity mirrors the formation of microtubules or other types of tubulin aggregates. Tubulin with DMSO (vehicle) and 27.5 μM podophyllotoxin (reference destabilizer) were used as controls. The polymerization curves obtained are reported below.

For strong polymerization inhibitors such as podophyllotoxin, no increase in absorbance is observed. Compound **251** behaves as a moderate inhibitor of tubulin assembly: the polymerization curve is characterized by a decrease in the slope and in the plateau of the curve, as well as in a longer lag time which indicates fewer nucleation events occurring in solution.

Cell viability assays

The toxicity of compound **251** was then evaluated in five different cell lines: human non-small cell lung cancer A549, human cervical carcinomas HeLa and HeLaβIII (multidrug-resistant overexpressing βIII tubulin isotype), and human cervical carcinomas Kb3.1 and KbVb (multidrug-resistant overexpressing P-glycoprotein). All five cell lines were cultured at

37°C in Dulbecco's modified Eagle medium (DMEM) supplemented with 10% fetal calf serum, 2 mM L-glutamine, 1 mM sodium pyruvate, 40 µg mL⁻¹ gentamycin, 100 IU mL⁻¹ penicillin and 100 µg mL⁻¹ streptomycin in a 5% CO₂ air atmosphere. Antiproliferation assays were performed as described.^[16] DMSO was used as vehicle for all compounds, where less than 0.5% was employed in the assay. Mebendazole and podophyllotoxin were used as reference colchicine-site binders.

As reported in Table 3-7, compound **251** showed IC₅₀ values in the micromolar range. Interestingly, the IC₅₀ values in the resistant cell lines were lower than the ones in the reference cell lines.

Table 3-7. IC ₅₀ of selected colchicine site binders in A549, HeLa, HeLaβIII, Kb3.1 and KbVb cell lines. ^[a]							
Cmpd	IC ₅₀ [nM]	IC ₅₀ [nM]	IC ₅₀ [nM]	R/S	IC ₅₀ [nM]	IC ₅₀ [nM]	R/S
	A549	HeLa	HeLaβIII		Kb3.1	KbVb	
Mebendazole	390 ± 30	180 ± 20	300 ± 20	2	560 ± 50	460 ± 30	0.8
Podophyllotoxin	14.3 ± 0.5	11 ± 1	9.0 ± 0.8	0.8	13.3 ± 0.8	22 ± 2	2
251	13800 ± 600	7700 ± 900	3400 ± 600	0.5	12300 ± 700	7400 ± 800	0.6

[a] Data are the mean ± SEM values of three independent experiments with duplicates in each one.

3.3.3.3 EXPERIMENTAL SECTION

Proteins and Compounds

The production of the stathmin-like domain of RB3 and chicken TTL in bacteria, as well as the reconstitution of the T₂R-TTL complex was done as described in Section 3.2. Compound **251** was purchased from **Enamine**.

Crystallization, data collection, and structure determination

Crystals of T₂R-TTL were grown by the vapor-diffusion method following the established protocols by Prota et al.^[3,4] The complex crystallized over night at 20 °C in the conditions listed below (Table 3-8). The crystals were soaked for 2 hours at 20°C in reservoir solutions containing 5 mM of **251**. The crystals were transferred consecutively into cryo-protectant solutions I and II, before flash-freezing in liquid nitrogen and subsequent data collection.

Table 3-8. Crystallization condition and cryo-protectant solution composition

Crystallization buffer 1	PEG 4K (4 %), glycerol (11 %), MgCl ₂ (30 mM), CaCl ₂ (30 mM), tyrosine (5 mM), MES/Imidazole pH 6.5 (100 mM)
Crystallization buffer 2	PEG 4K (4 %), glycerol (11%), MgCl ₂ (30 mM), CaCl ₂ (30 mM), tyrosine (5 mM), MES/Imidazole pH 6.5 (100 mM)
Cryo-solution I	PEG 4K (10 %), glycerol (16%), MgCl ₂ (30 mM), CaCl ₂ (30 mM), tyrosine (5 mM), MES/Imidazole pH 6.5 (100 mM)
Cryo-solution II	PEG 4K (10 %), glycerol (20%), MgCl ₂ (30 mM), CaCl ₂ (30 mM), tyrosine (5 mM), MES/Imidazole pH 6.5 (100 mM)

Native data were collected at 100K at beamline X06DA of the Swiss Light Source (Paul Scherrer Institut, Villigen PSI, Switzerland). Data were processed and merged with XDS.^[5] The T₂R-TTL structures were determined using the difference Fourier method using the phases of a T₂R-TTL complex in the absence of ligands and solvent molecules as starting point for refinement (PDB ID 5LXT). Initial refinement included 10 cycles of rigid body and restrained refinement, followed by further refinement cycles in Refmac.^[6] The resulting models were further improved through iterative model rebuilding in Coot^[8] and refinement in Phenix.^[7] The quality of the structures was assessed with MolProbity.^[9]

Chains in the T₂R-TTL complex were defined as follows: chain A, α 1-tubulin; chain B, β 1-tubulin; chain C, α 2-tubulin; chain D, β 2-tubulin; chain E, RB3; chain F, TTL (Figure SXA). Structure visualization, molecular editing and figure preparation were performed with the PyMOL molecular graphics system (The PyMOL Molecular Graphics System, Version 2.5.2 Schrödinger, LLC).

3.3.1 REFERENCES

- [1] C. J. Smedley, J. A. Homer, T. L. Gialelis, A. S. Barrow, R. A. Koelln, J. E. Moses, *Angew. Chemie - Int. Ed.* **2022**, *61*, e202112375.
- [2] J. Head, L. L. Y. Lee, D. J. Field, J. C. Lee, *J. Biol. Chem.* **1985**, *260*, DOI 10.1016/s0021-9258(17)39148-2.
- [3] A. E. Prota, K. Bargsten, D. Zurwerra, J. J. Field, J. F. Díaz, K. H. Altmann, M. O. Steinmetz, *Science (80-.)*. **2013**, *339*, DOI 10.1126/science.1230582.
- [4] A. E. Prota, M. M. Magiera, M. Kuijpers, K. Bargsten, D. Frey, M. Wieser, R. Jaussi, C. C. Hoogenraad, R. A. Kammerer, C. Janke, M. O. Steinmetz, *J. Cell Biol.* **2013**, *200*, 259–270.
- [5] W. Kabsch, *Acta Crystallogr. Sect. D Biol. Crystallogr.* **2010**, *66*, 125–132.
- [6] G. N. Murshudov, P. Skubák, A. A. Lebedev, N. S. Pannu, R. A. Steiner, R. A. Nicholls, M. D. Winn, F. Long, A. A. Vagin, *Acta Crystallogr. Sect. D Biol. Crystallogr.* **2011**, *67*, 355–367.
- [7] P. D. Adams, P. V. Afonine, G. Bunkóczi, V. B. Chen, I. W. Davis, N. Echols, J. J. Headd, L. W. Hung, G. J. Kapral, R. W. Grosse-Kunstleve, A. J. McCoy, N. W. Moriarty, R. Oeffner, R. J. Read, D. C. Richardson, J. S. Richardson, T. C. Terwilliger, P. H. Zwart, *Acta Crystallogr. Sect. D Biol. Crystallogr.* **2010**, *66*, 213–221.
- [8] P. Emsley, K. Cowtan, *Acta Crystallogr. Sect. D Biol. Crystallogr.* **2004**, *60*, DOI 10.1107/S0907444904019158.
- [9] I. W. Davis, L. W. Murray, J. S. Richardson, D. C. Richardson, *Nucleic Acids Res.* **2004**, *32*, W615-619.
- [10] P. A. Karplus, K. Diederichs, *Science (80-.)*. **2012**, *336*, DOI 10.1126/science.1218231.
- [11] L. Maveyraud, L. Mourey, *Molecules* **2020**, *25*, DOI 10.3390/molecules25051030.
- [12] D. M. Volochnyuk, S. V. Ryabukhin, Y. S. Moroz, O. Savych, A. Chuprina, D. Horvath, Y. Zabolotna, A. Varnek, D. B. Judd, *Drug Discov. Today* **2019**, *24*, DOI 10.1016/j.drudis.2018.10.016.
- [13] M. Kavallaris, *Nat. Rev. Cancer* **2010**, *10*, DOI 10.1038/nrc2803.
- [14] A. L. Parker, W. S. Teo, J. A. McCarroll, M. Kavallaris, *Int. J. Mol. Sci.* **2017**, *18*, DOI 10.3390/ijms18071434.
- [15] G. La Sala, N. Olieric, A. Sharma, F. Viti, F. de Asis Balaguer Perez, L. Huang, J. R. Tonra, G. K. Lloyd, S. Decherchi, J. F. Díaz, M. O. Steinmetz, A. Cavalli, *Chem* **2019**, *5*, DOI 10.1016/j.chempr.2019.08.022.
- [16] R. M. Buey, I. Barasoain, E. Jackson, A. Meyer, P. Giannakakou, I. Paterson, S. Mooberry, J. M. Andreu, J. F. Díaz, *Chem. Biol.* **2005**, *12*, 1269–1279.

3.3.2 RATIONALLY DESIGNED NOVEL TODALAM ANALOGUES: TOWARDS SITE_SPECIFIC CYSTEINE TARGETING (structural part)

Declaration of contribution: The structural part of the Todalam project has been one of the most extensive activities performed during the secondment period. My work included the preparation of the T₂R-TTL complex and its crystallization, followed by soaking and co-crystallization experiments of over seventy potential Todalam binders, which emerged out of the 1st series of screening/design., Furthermore, my work comprised data collection, refinements and subsequent analysis and figure preparation. Final corrections of the crystal structures and data analysis were done with the help of Dr. Andrea Prota.

3.3.2.1 INTRODUCTION TO THE STRUCTURAL PART

The general introduction and aims of the project have been outlined in Section 2.4. As mentioned, over forty synthesized molecules of the 1st series Todalam analogues have been submitted for X-ray crystallography experiments. In parallel, the computational groups performed the virtual screening of the commercially available libraries, and another thirty commercially available compounds have been identified, characterized by some additional scaffold modifications. As a result, sixty-five compounds representing eight scaffold modifications have been submitted for X-ray crystallography screening, represented in Figure 3-25. Other five compounds include representatives of different structures, which cannot be categorized into any of the scaffolds depicted above.

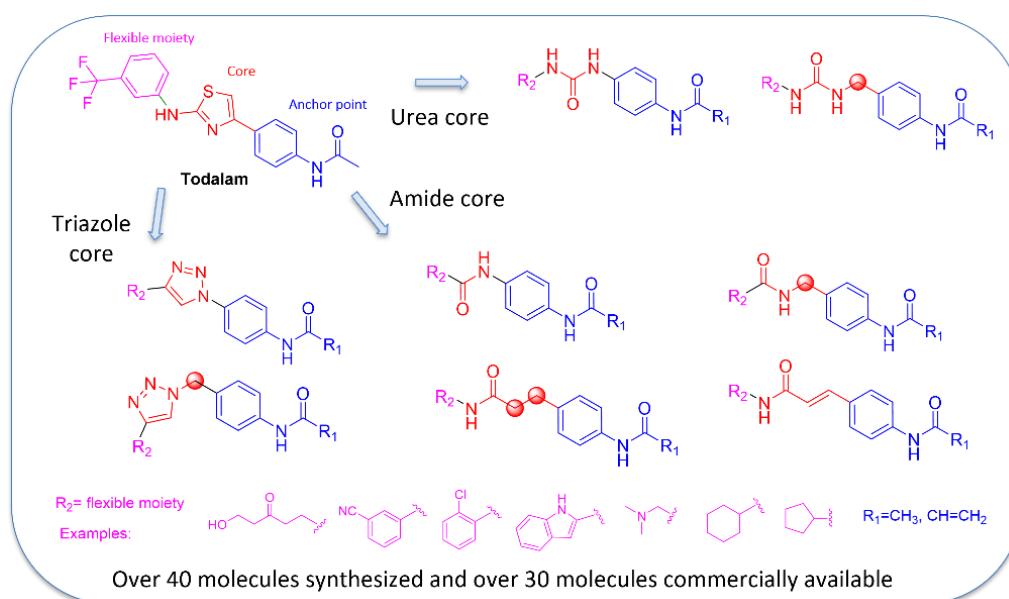


Figure 3-25. Summary of the compounds' scaffolds submitted for X-ray crystallography experiments.

3.3.2.2 RESULTS AND DISCUSSION

Structural description

All of the compounds emerged from the 1st series of Todalam analogues were soaked into the T₂R-TTL crystals. Eighteen of the studied compounds were well-defined in the binding site, and their corresponding structures were determined in to a resolution range of 2.1 – 2.8 Å resolution range. Additionally, the binding of the compounds **91** and **95** could be detected, however it was not possible to deduct the positioning of the those ligands based on the obtained electron densities. The co-soaking with vinblastine was then applied, and the structures of those compounds were successfully determined.

All of the identified hits bind to the Todalam site of tubulin at the interdimer interface (Figure 3-26) and shaped by the sheets S4, S5 and helix H8 of α -tubulin, and the T3 loop and H11' of β -tubulin. From the structural point of view, the Todalam site can be divided into the three zones, corresponding with the division of the ligands into the three main moieties of anchoring point (zone A), core fragment (zone B) and flexible moiety (Zone C). The detailed description of the binding modes of the hits obtained for each of the scaffolds is discussed below.

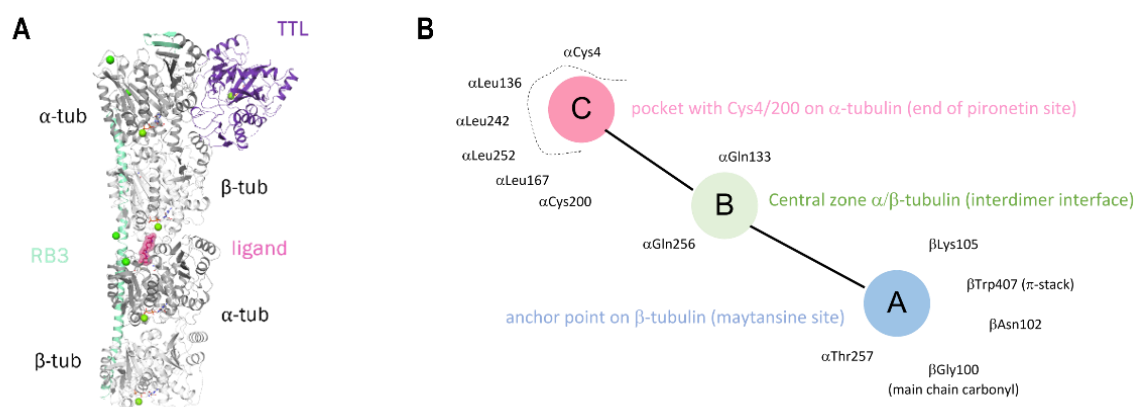


Figure 3-26. (A) Location of the Todalam site ligand in the T₂R-TTL complex structure. The β -tubulin and α -tubulin chains are in white and grey, TTL is in rubidium, and RB3 is in samarium ribbon representation, respectively. The Todalam site ligand is represented as pink spheres. (B) The structural division of the Todalam site into the three zones.

▪ Urea derivatives

The crystal structures of six urea derivatives have been determined (Figure 3-27, **80-85**).

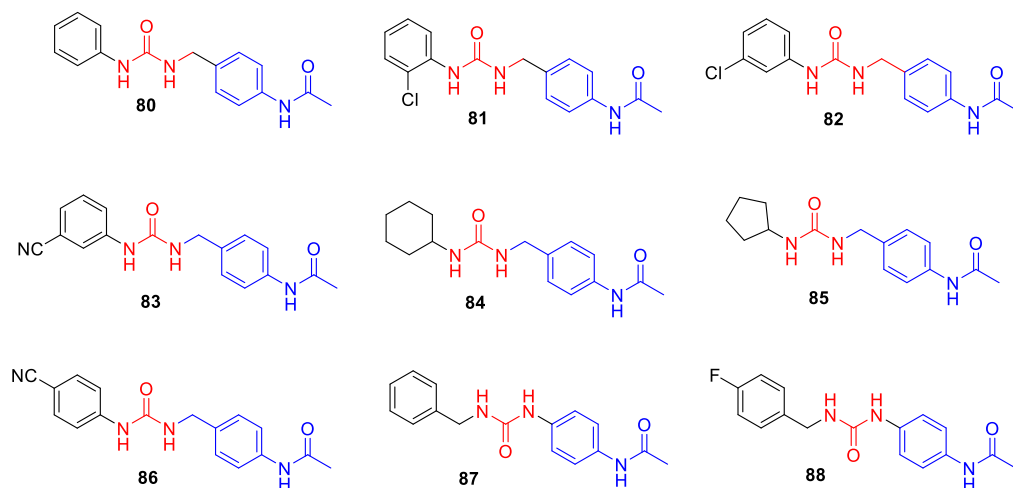


Figure 3-27. Chemical structures of the urea derivatives: **80-85** represent the structures of the bound molecules, while 66-68 are the examples of unbound (**86, 88**) or poorly defined (**87**) urea derivatives.

The chemical structures of the obtained hits are depicted in Figure 3-27, and the resolutions of their crystal structures in complex with tubulin are listed in Table 3-8.

Table 3-8. The resolution of the obtained urea derivatives-tubulin crystal structures.

Compound	80	81	82	83	84	85
Resolution (Å)	2.4	2.1	2.2	2.5	2.5	2.3

As shown in Figure 3-28A on the example of unsubstituted urea derivative **80**, the acetanilide anchoring point of the compound occupies the above-mentioned zone A, shaped by the β T3 loop residues β G100 and β N102, and by the side chains of β K105, β W407 and α T257. Its amide moiety establishes two hydrogen bonds with β N102 and α T257, while the phenyl is further stabilized by a π -stacking interaction with the side chain of β W407. The core urea moiety is fully involved in interactions with α -tubulin at the central zone of the interdimer interface. It establishes three hydrogen bond interactions with α Q133, α Q256 and α S165. Finally, the phenyl occupies the hydrophobic pocket formed by the side chains of residues α C4, α F52, α L136, α L167, α L242, and α L252. The crystal structure of the urea derivative was then compared to that of the parent Todalam (Figure 3-28B). As shown, the space occupied by both compounds and their position is highly similar, with the acetanilide part of the compounds perfectly superimposed. The main differences can be noted in the core region, as the aminothiazole has been shown to establish only two hydrogen bonds with α Q256^[1], as opposed to the three hydrogen bonds established by urea. The positioning of the phenyl moieties of both compounds is highly similar as well, with a slight difference

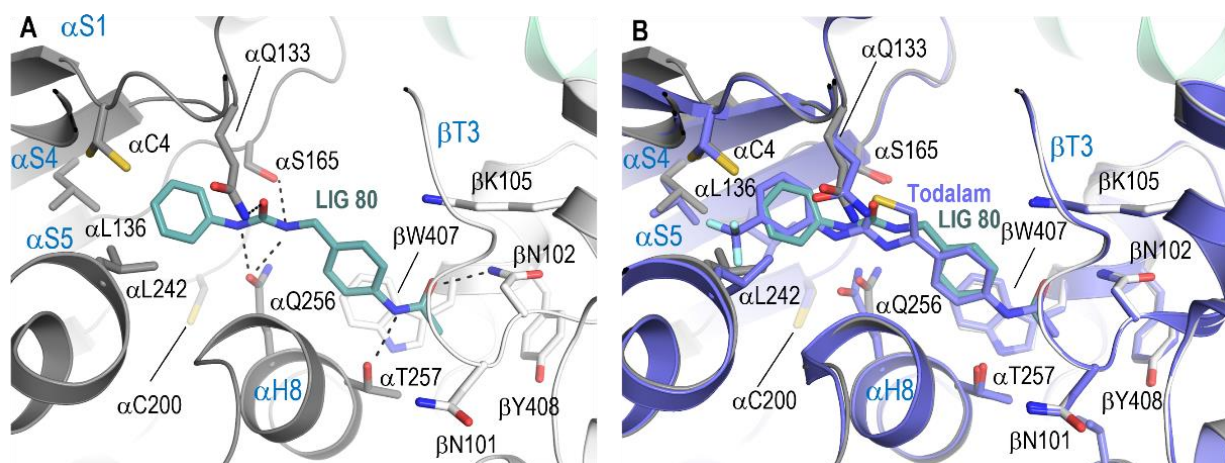


Figure 3-28. (A) Binding mode of compound **80** (greyish green) as seen in the crystal structure of the tubulin-**80** complex. The β -tubulin and α -tubulin chains are in white and dark grey ribbon representation, respectively. Interacting residues of tubulin are shown in stick representation and are labeled. Oxygen and nitrogen atoms are colored in red and blue, respectively; carbon atoms are in greyish green (**80**) or white/gray (tubulin). Hydrogen bonds are depicted as black dashed lines. Secondary structural elements of tubulin are labeled in blue. (B) The same close-up view as in (A) with the superimposed tubulin-Todalam (PDB ID: 5SB7, violet) structure.

in the conformation of the α L136 side chain, most likely shifted in order to fit the meta-CF₃ of Todalam.

Further modifications in the urea scaffolds could be analyzed by obtaining the crystal structures of compounds **81**, possessing an ortho-Cl substituent, as well as **82** and **83**, possessing meta-Cl and meta-CN substituents. Although these compounds accommodated in the pocket in same way as the unsubstituted urea **80**, some flexibility of the substituted rings could be noted. Interestingly, the meta-Cl substituent of **82** pointed towards the α C4,

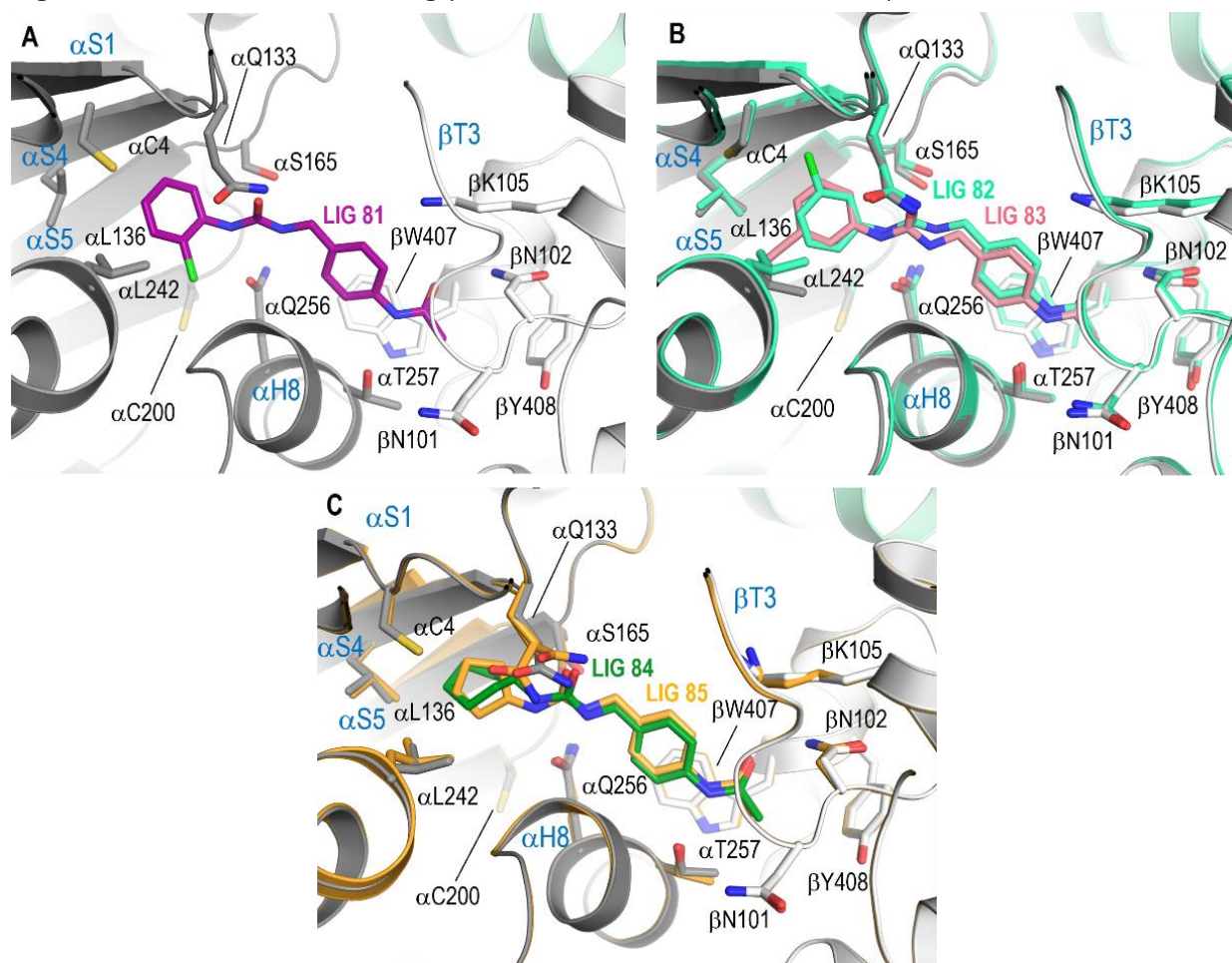


Figure 3-29. X-ray crystal structures of the tubulin-**81** (bright pink) (A), tubulin-**82** (cyan) and tubulin-**83** (pink) complexes (B), tubulin-**84** (green) and tubulin-**85** (yellow) complexes (C) in the same close-up view as in Figure 3-28. For all panels, the same representation style as in Fig.3-28 is applied.

while the bulkier meta-CN of **83** pointed towards the α L242 side chain. Similarly as in the case of Todalam meta-CF₃, the α L242 flips aside to fit the cyano group.

The crystal structures of the compounds **86-88**, which chemical structures are depicted in the Figure 3-27, could not be obtained. In particular, no electron density indicating ligand binding could be observed for compound **86** and **88**, while poorly-defined density could be observed for compound **87**. The only difference between the unbound and bound molecules is the presence of a para-substituent on the phenyl ring. This could imply that while meta-

and ortho-substitution do not interfere with the binding of the molecules, the para-substitution potentially leads to unfavourable clashes preventing the appropriate accommodation of the ligands in the pocket. Furthermore, the compounds in which urea moiety was directly attached to the core (such as e.g. **87**) were very poorly defined in the binding pocket, highlighting the importance of the interactions established by the core urea moiety. In case of ligand **87**, the distance between the urea nitrogens and the α Q133 and α Q256 exceeds 4 Å, likely preventing the formation of hydrogen bond interactions.

- Triazole derivatives

Sixteen different triazole derivatives have been tested, however only two crystal structures of compounds **49** and **50** were determined to (Figure 3-30).

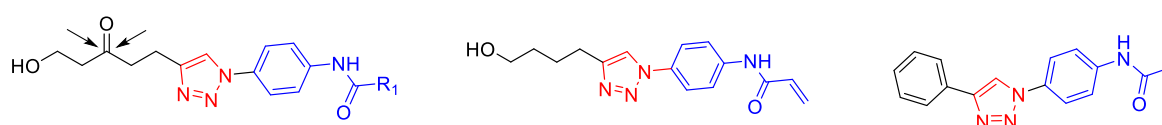


Figure 3-30. Chemical structures of the urea derivatives: **49-50** represent the structures of the bound molecules, while **89-90** are the examples of unbound triazole derivatives.

As shown in Figure 3-32, the binding mode of triazole derivatives closely resembles that of Todalam. The interactions of the acetanilide moiety remain unchanged with respect to

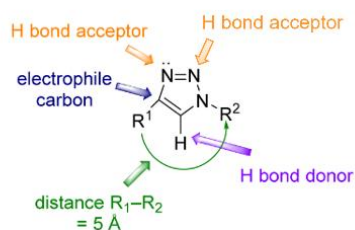


Figure 3-31. H-bond acceptor and donor of the triazole core.

Todalam and the urea derivatives, as it forms two hydrogen bonds with β N102 and α T257, and further establishes a π -stacking interaction with β W407. However, some differences can be noted in the core and in the flexible part of the triazole derivatives. In contrast to the urea, which possesses two H-donors (NH) and one H-acceptor (carbonyl), the triazole core can establish only two hydrogen bonds interactions (Figure 3-31), with α S165 and the side chain α Q256

(Figure 3-32). The lack of an additional hydrogen bond could partially contribute to the lower stability of the triazole derivatives in the binding site, as noted by the fact that many substituents cannot be tolerated. In fact, the bound compounds **49** and **50** are characterized by a 5C-aliphatic chain with an additional carbonyl. It is worth noting that the structurally very similar compound **89**, lacking the carbonyl moiety on the chain, was not bound in the crystal, suggesting the importance of the carbonyl for the binding. This structural data served as a foundation for the development of the warhead-bearing triazole derivatives described in Chapter 2.4. It is worth noting that unsuccessful results were obtained with the aromatic substituents (e.g. compound **90**). Intriguingly, the binding of this compound could not be observed in the crystal structure, while its destabilizing effect on tubulin polymerization was detected in the assembly assay. Overall, although less modifications can be tolerated in the case of the triazole scaffold, as compared to the urea one, it provides a

great advantage in terms of chemistry as triazole-containing compounds can be easily prepared by CuAAC click reaction.

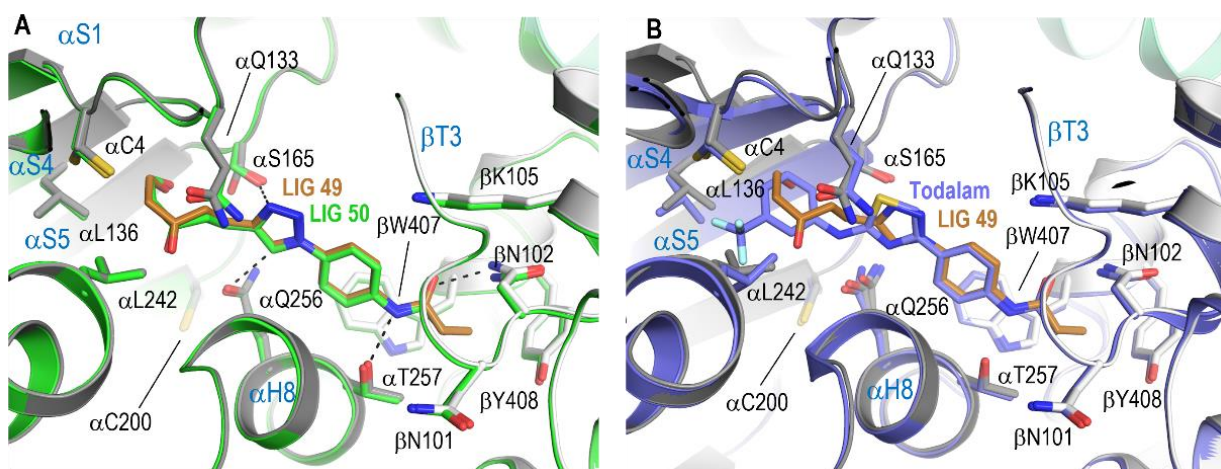


Figure 3-32. (A) Binding mode of compound **49** (copper) as seen in the crystal structure of the tubulin-**49** complex superimposed with the tubulin-**50** complex (green). The β -tubulin and α -tubulin chains are in white and dark grey (tubulin-**49**) and green (tubulin-**50**) ribbon representation, respectively. Interacting residues of tubulin are shown in stick representation and are labeled. Oxygen and nitrogen atoms are colored in red and blue, respectively. Hydrogen bonds are depicted as black dashed lines. Secondary structural elements of tubulin are labeled in blue. (B) The same close-up view as in (A) with the superimposed tubulin-Todalam (PDB ID: 5SB7, violet) structure. For all panels, the same representation style as in Fig.3-28 is applied.

- Amide derivatives

The library of amide derivatives which emerged from the virtual screening campaign represents the most structurally extensive set of compounds. Generally, the obtained hits can be divided into four categories based on the scaffold modifications. The first category is represented by compounds **91-92**, in which the amide moiety is directly attached to the acetanilide anchoring point. The second category is represented by compound **51**, which is characterized by the presence of one carbon atom in between the amide and the anchor point. Compounds **93-95** belong to the third category, and finally, derivatives of cinnamic acid **96-98** possessing a double bond in-between the amide moiety and the acetanilide are the members of the fourth category (Figure 3-33). Eight high-resolution crystal structures of tubulin-amide derivatives were determined.

For what concerns the first category of ligands, out of twelve compounds the binding was detected only for compound **91**. Moreover, initially the electron density of the bound ligand obtained within the standard soaking procedure did not allow to place the amide moiety of the ligand correctly. To relax the interdimer interface such to improve the occupancy of the ligand, we decided to apply the co-soaking in the presence of vinblastine. This approach was first reported by Mühlethaler et al.¹ where a much higher degree of perturbation of the

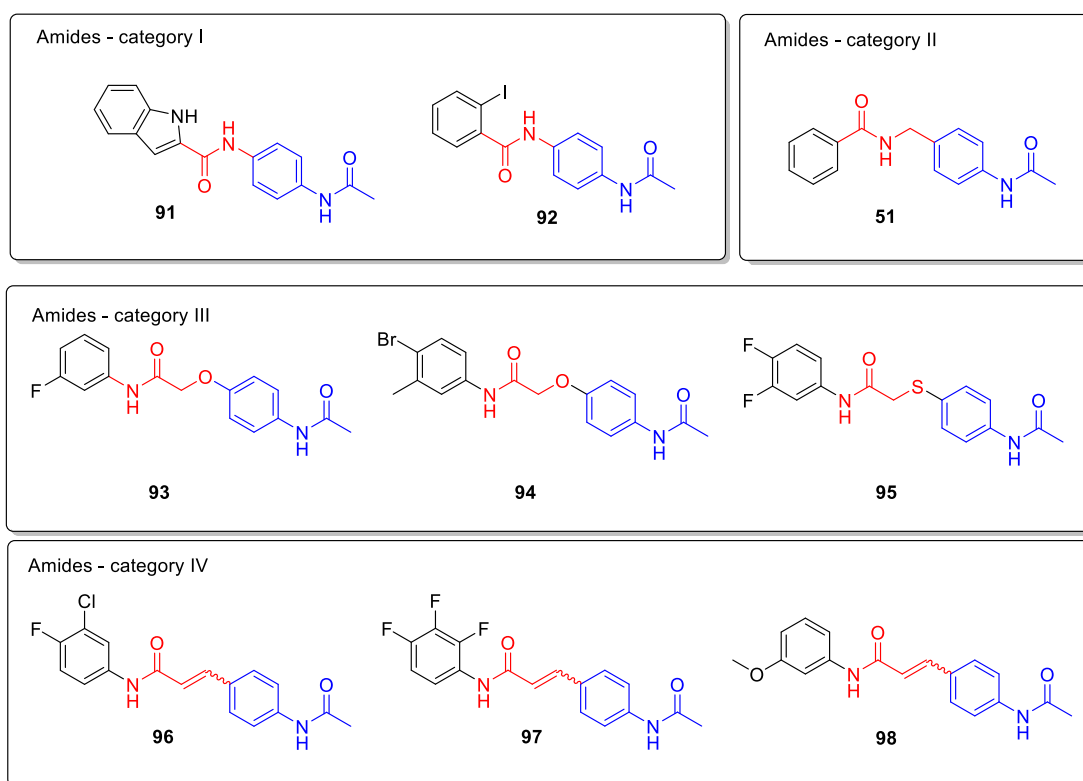


Figure 3-33. Chemical structures of the selected amide derivatives

Todalam site was observed in the Todalam-vinblastine-tubulin crystal structure, compared to the original Todalam-tubulin structure. This strategy was chosen considering the location of the vinblastine binding site and its mechanism of action. Since vinblastine acts as a wedge between the two tubulin dimers, its binding contributes to higher accessibility of the Todalam binding site. Thus, having applied this strategy to compound **91**, we successfully obtained its crystal structure in complex with tubulin in the presence of vinblastine (Figure 3-34). As depicted below, the binding mode of compound **91** is notably different from that of urea and triazole derivatives described. Even though the anchoring part of acetanilide maintains the identical interactions, the position of the amide moiety and the indole is greatly shifted. The amide of **91** establishes two water-mediated hydrogen bond interactions with the side chains of α Q133 and α Q256, while the nitrogen of the indole moiety establishes a hydrogen bond with α S165. It is worth noting that no binding was detected for any of the amide derivatives of the first group, lacking an additional NH-group (e.g. compound **92**), highlighting the importance of this hydrogen bond. For comparison, the crystal structure of **91** was superimposed to that of Todalam in the presence of vinblastine. (Figure 3-34C).

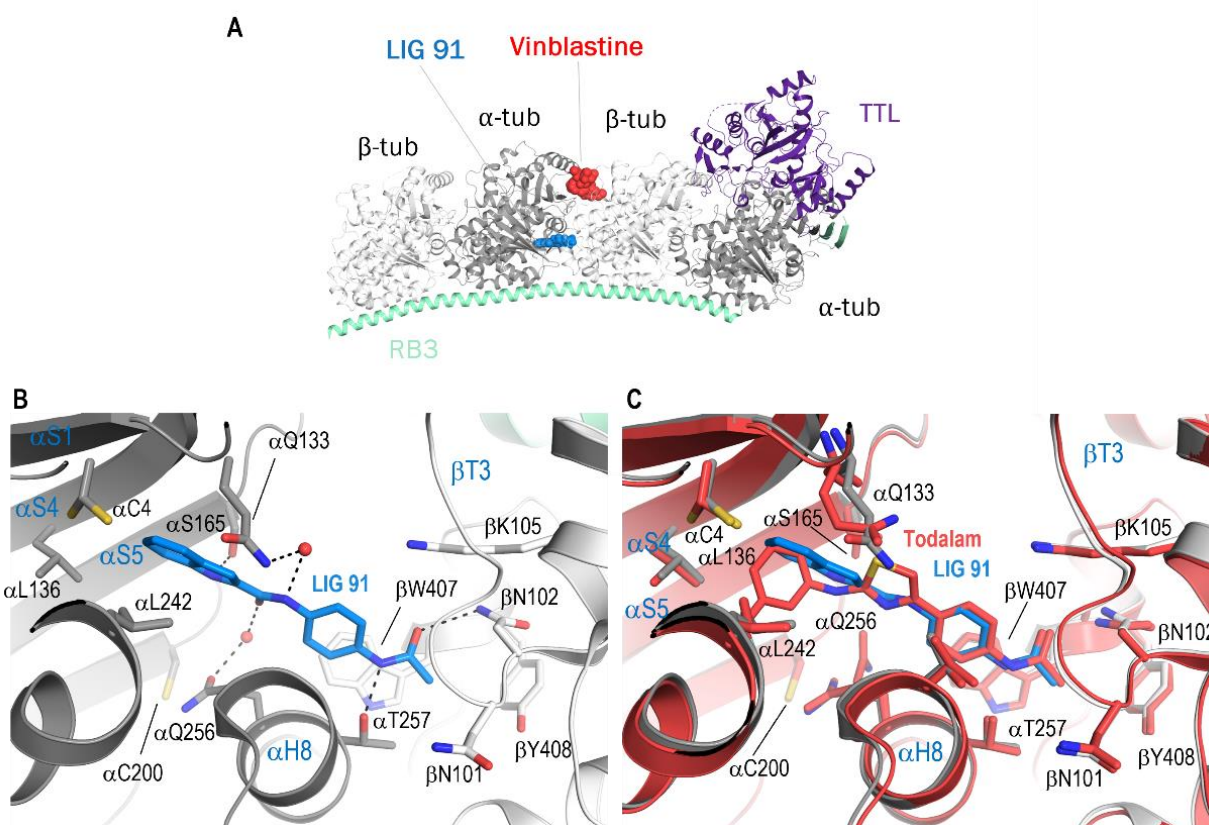


Figure 3-34. (A) Location of the compound **91** and vinblastine sites in the T_2R -TTL-**91**-vinblastine complex structure. Compound **91** and vinblastine are represented as blue and red spheres, respectively. (B) Binding mode of compound **91** (blue) as seen in the crystal structure of the tubulin-**91**-vinblastine complex. (C) The same close-up view as in (B) with the superimposed tubulin-Todalamin-vinblastine (PDB ID: 7Z7D, light red) structure. For all panels, the same representation style as in Fig. 3-28 is applied.

For what concerns the second category of amides, two compounds of this scaffold were

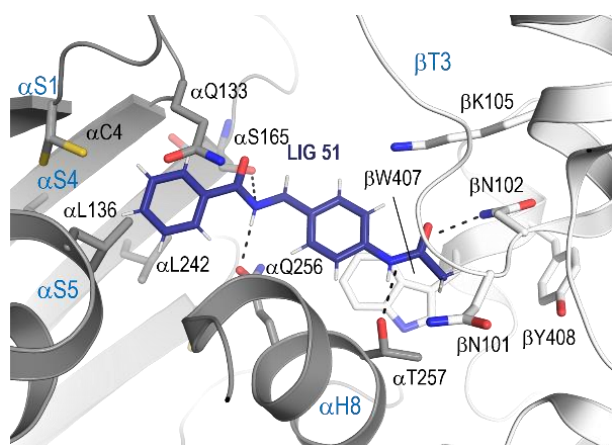


Figure 3-35. (A) Binding mode of compound **51** (dark violet) as seen in the crystal structure of the tubulin-**51** complex. The same representation style as in Fig. 3-28 is applied.

evaluated, out of which only the crystal structure of compound **51** was obtained. As shown in Figure 3-35, it accommodates in the pocket similarly to the urea derivatives, with the NH- of the amide establishing the hydrogen bond interactions with $\alpha Q256$ and $\alpha S165$ and the carbonyl with the $\alpha Q133$. Importantly, the shorter analogue of compound **51** lacking the extra carbon bond between the anchoring moiety and the amide was not bound, while the longer analogues and urea derivatives occupy more space in the pocket, making it difficult to introduce further modifications in the flexible moiety

due to the limited space. As a result, compound **51** presented an optimum compromise between favorable binding and susceptibility to further optimization, and therefore its scaffold was chosen as the starting point for the design of warhead-bearing amide derivatives (discussed in Section 2.4).

The third series of amide derivatives is characterized by a presence of additional heteroatoms (O, S) in the amide chain. The crystal structures of compounds of **93** and **94** were obtained by standard soaking procedure. The acetanilide moiety remains unchanged with respect to the urea and triazole scaffolds, while the core moiety of the two compounds establishes two hydrogen bonds with α Q256 and α Q133. Interestingly, the aliphatic amide of **93** and **94** adopts a ring like shape, similar to that of thiazole of Todalam and triazole of **49-50**. As expected, the substituted phenyls, buried in the pocket formed by the side chains of residues α C4, α F52, α L136, α L167, α L242, and α L252, are characterized by the most

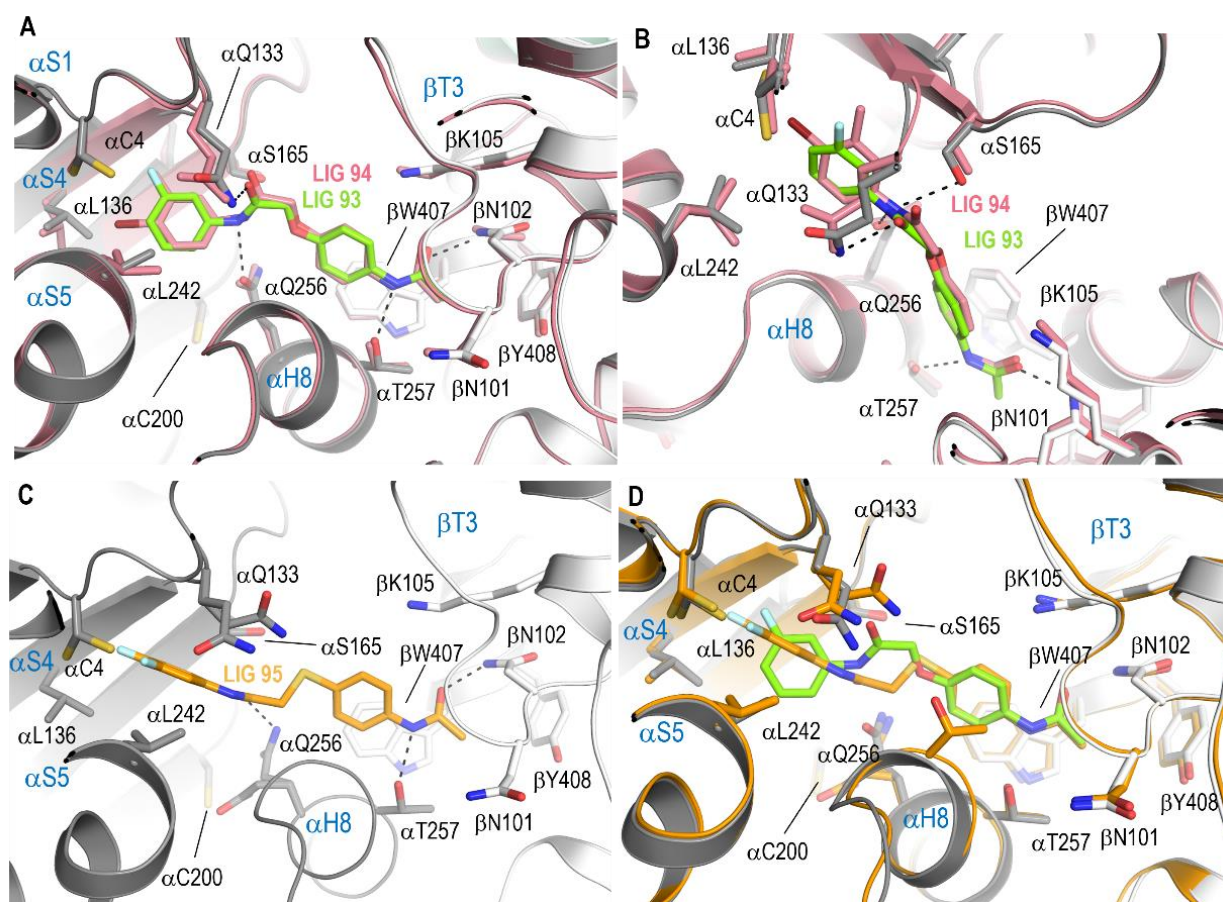


Figure 3-36. (A, B) Binding mode of compound **93** (light green) as seen in the crystal structure of the tubulin-**93** complex superimposed with the tubulin-**94** complex (light pink). The β -tubulin and α -tubulin chains are in white and dark grey (tubulin-**93**) and light pink (tubulin-**94**) ribbon representation, respectively. Interacting residues of tubulin are shown in stick representation and are labeled. Oxygen and nitrogen atoms are colored in red and blue, respectively. Hydrogen bonds are depicted as black dashed lines. Secondary structural elements of tubulin are labeled in blue. (C) The same close-up view as in (A) of the tubulin-**95**-vinblastine crystal structure. (D) Superimposition of tubulin-**93** and tubulin-**95**-vinblastine crystal structures. For all panels, the same representation style as in Fig.3-28 is applied.

flexibility (Figure 3-36A-B). It is worth noting that while both meta-F/CH₃ and para-Br substituents on the phenyl ring were well-tolerated, the compounds possessing a bulkier para-substituent e.g. para-CN, were not bound in the crystal structure, a similar effect as observed in the case of urea derivatives. To our surprise, in case of compound **95**, structurally closely related to the compounds **93** and **94**, a less-defined density of the bound ligand was obtained, not allowing to determine the correct placement of the amide carbonyl. To overcome this issue, co-soaking in the presence of vinblastine was performed, and the crystal structure of tubulin-**95**-vinblastine was obtained. As previously noted in case of compound **91**, the pose of the ligand is significantly shifted and higher perturbation in the site is observed. Both α Q256 and α Q133 which establish key interactions with the developed scaffolds, can adopt two different confirmations, and only one confirmation of α Q256 is able to establish the hydrogen bond with the amidic NH- (Figure 3-36C). The differences in the binding modes of ligands **93** and **95** are highlighted in the Figure 3-36D. It is worth noting that although great differences are noted in the core and flexible part of the ligand, the pose of anchoring moiety of both ligands remains unchanged.

Finally, the crystal structures of amide derivatives **96-98** were determined. The double bond of compounds **96-98** can exist in both cis- and trans- configurations, as they were purchased as a mixture of stereoisomers (Figure 3-33). However, only the *trans* configuration can be observed in the crystal structures of the three studied ligands, adapting a similar pose to the above-described **51**.

To conclude, all the developed scaffolds possessing either urea, amide or triazole can well accommodate in the pocket. The key interactions of all structures are established by the anchoring point, which establishes two hydrogen bonds, and the core moiety, which depending on its nature is able to establish two to four hydrogen bond interactions. Importantly, both aliphatic and aromatic substituents in the flexible chain were well-tolerated. The phenyl rings possessing additional substituents in meta- and para- position can adapt in the pocket, while some of a bit bulkier para- substituents (e.g. cyano) prevent the binding of the molecules. Altogether, this data provided a solid foundation for the design of warhead-bearing compounds with the developed scaffolds.

3.3.5.3 EXPERIMENTAL SECTION

The complex formation, crystallization, data processing and refinements were done as described in Section 3.3.3.3. The standard soaking procedure involved soaking of the compounds at 5mM final concentration in reservoir solutions for 5-6 hours at 20°C. Alternatively, compounds were soaked overnight. The co-soaking experiments in the presence of vinblastine included soaking of the Todalam site ligand at 5 mM and vinblastine at 1 mM final concentration in reservoir solutions, for 1-2 hours at 20°C. Prolonged soaking in the presence of vinblastine led to the destruction of crystals and/or lack of diffraction.

3.3.1 REFERENCES

- [1] T. Mühlethaler, L. Milanos, J. A. Ortega, T. B. Blum, D. Gioia, B. Roy, A. E. Prota, A. Cavalli, M. O. Steinmetz, *Angew. Chemie - Int. Ed.* **2022**, *61*, e202204052.

CONCLUSIONS AND FUTURE PERSPECTIVES

Tubulin is one of the most important types of proteins in a living cell. After many years of tubulin and microtubules research, small molecules which are able to target them still remain of high interest.

This thesis was aimed at the development of new tubulin binders, with a focus on chemical synthesis and structural biology aspects. “Can other, different from Todalam scaffolds, be developed to target this novel site?” or “How can the nature of the ester chain of maytansinoids influence their biological properties?” Here, those questions are addressed demonstrating that many advances can be done using a wide range of structurally diverse tubulin binders.

Thus, the project focused on the maytansinol functionalization not only allowed to explore the chemistry of a complex natural product maytansinol and the influence of the introduced modifications on its binding mode and activity but set out foundation for the development of maytansinoid-bearing specific protein degraders or ADCs with different types of linkers. The second project which included the synthetic efforts towards the total synthesis of glycybridin B gives a chance to identify a new tubulin binder, but also represents an exciting challenge from the synthetic point of view. In fact, other trials to perform the alfa-hydroxylation reaction are currently performed in our research group. Furthermore, great attention has been paid to the covalent targeting strategy, highlighted in the work done for the pironetin and Todalam analogues. Those two projects show the utility of two completely different approaches which complement each other. The design of pironetin analogues strongly relied on the simplification of the pironetin structure, and a more elaborated synthetic pathway was applied comparing to the Todalam site binders. In case of the latter, a highly rational design strategy was implemented, strongly depending on the structural data and computational studies. At the same time, the synthesis of the Todalam analogues relied on the cost- and time-efficiency, as a large amount of the planned molecules could be prepared in a relatively short time. A great deal of positive results was obtained in the development of Todalam site ligands. Over twenty new Todalam site binders were identified, including the potential covalent binders. Further studies to evaluate hit compounds will be done to confirm their ability to covalently target tubulin.

It is worth noting that we didn't plan to develop tubulin binders as therapeutics but approached them as chemical probes that could be helpful to explore the field of microtubule-targeting agents and eventually to understand the role of microtubules with respect to neurodegenerative diseases. The effect of the most promising compounds derived from the described projects on neuronal cells will be studied at the University of Osnabrück. The studies of the maytansinoids are currently ongoing, and the selected Todalam site binders will be submitted for such experiments.

Apart from the mentioned projects, Chapter 3 also provides an overview on the tubulin crystallization and X-ray crystallography as a technique to study tubulin-compounds interactions. Two training projects are included, one of which was born from a collaboration with a company, proving once again the high interest in the development of tubulin binders. Another interesting project included the crystallographic screening of the set of compounds identified within the virtual screening, yielding an isotype-specific ligand 251. The development of the isotype-specific ligands is highly relevant in the era of target therapies, as it allows to specifically target certain types of cells and diseases. Further studies on compound 251 will be done, to better understand the specificity of its interaction with the neuronal β 3-tubulin.

To conclude, this thesis represented a set of different approaches which can be applied to develop microtubule-targeting agents, and the work discussed herein yielded a great number of novel tubulin binders and provided a foundation for their further studies. Moreover, it highlighted the importance of the multidisciplinary work in research.

ACKNOWLEDGEMENTS

My PhD journey has been a great experience in both personal and professional ways, and I would like to express my gratitude to the people who made it so.

First of all, I would like to thank my supervisor Prof. Daniele Passarella for giving me the possibility to join his research group and the TubInTrain project in the first place. I was very lucky to have you as my supervisor in this journey and I am grateful for your support and guidance during these years. You have always done your best and succeeded in creating an amazing working environment in Passalab and have done the same as a coordinator in TubInTrain. Thank you for encouraging me to learn and acquire new competences, and to actively collaborate with others. I really appreciate the way in which you always motivated us students to share our ideas and our research, to attend conferences and congresses and to interact, also outside the lab. You have opened up for me an amazing world of natural products chemistry which I hope will continue to thrive in the group!

Next, I would like to thank Dr. Andrea Prota, my co-supervisor from Paul Scherrer Institut. Thank you for introducing me to structural biology and taking all those hours of your time to explain me the concepts of X-ray crystallography. I have learnt a lot from you, and I really appreciate the support you gave me, and the fruitful discussions we had. Thank you for giving me a warm welcome, for ensuring that my stay in Switzerland went smoothly, and for organizing the Raclette evening and my Farewell party, it was a lot of fun! I would also like to thank you for your dedication as a WP-1 coordinator, without which it wouldn't be possible to get the results we managed to achieve.

Many thanks to Prof. Michel Steinmetz for letting me join his lab, for finding time to discuss with me my research and for always being supportive and giving constructive feedback. It was a pleasure to work with you and your team.

I would like to thank Juan Ignacio Padrón Peña for agreeing to be a part of my Doctoral Committee as an external expert.

I would also like to express my gratitude to other members of my Doctoral Committee, Prof. Stefano Pieraccini and Prof. Jan Pieter Abrahams.

Furthermore, I would like to acknowledge Prof. Constantinos Athanassopoulos and Prof. Markus Kalesse for their time and effort to evaluate and approve this thesis.

I would like to thank my TubInTrain colleagues and friends. Thank you Helena, Maxim, Annie, Kali, Davide, Nicolò, Josine, Francesca, Simone, Ahmed, Milo and Sai. It was great to be a part of the TubInTrain network together with you, and we created great memories together

during our meetings in Favignana, Strasbourg, Madrid and Barcelona. I would like to particularly thank the WP-1 members Helena, Annie, Francesca and Maxim for the productive collaborations! Special thanks to the initial Milano team of Helena, Josine and Kali with whom we shared the lockdown and post-lockdown experiences in 2020, and the 2023 Milano team joined also by Annie and Milo. We had a lot of fun together during the aperitivo times! I would also like to thank the TubInTrain project manager Benedetta for organizing the TubInTrain events, handling often tricky administrative and bureaucratic issues of the project, and sharing with us the morning coffees, the scientific meetings and treating us to dinner.

Thanks to the Passalab members Alice, Paolo, Martina, Antonia, Arianna, Valerio, Andrea, Miriam, to the former Passalab members Elisa, Eleonora and Paola and to all the Bachelor and Master students we had over the years. It was a pleasure working with you!

I would like to particularly thank Antonia and Eleonora for my first year in Passalab. Antonia, you have been a great companion to me during my first period in Passalab, always willing to help and to pass to me your knowledge. It was really a pleasure to share the office and the lab with you, I still remember the evenings we passed there taking an Italian course or discussing the chemistry during the coffees. Eleonora, I would like to thank you for your sincerity, willingness to help and advice you gave me.

I would also like to especially thank Alice and Paolo with whom I shared the office during my last months in Passalab. I really enjoyed working and discussing with you! Our trips together in Rimini and in Ischia have been truly exciting and memorable. I wish both of you great successes with continuation of the tubulin binders projects.

Martina, Andrea, Arianna and Valerio, it was great spending time with you and sharing lunch times together. Thanks for your positive attitude, dedication to research and creating a nice atmosphere in the lab.

I would also like to thank my labmates from Steinmetz lab Annie, Valentin, Mateusz, Natacha, Ashwani, Thorsten, Sandro and Matteo. A huge thanks for giving me a warm welcome and introducing me to the Swiss culture, and for our countless scientific discussions during lunch. I must admit that hiking and discussing science during our retreat in the Swiss mountains was absolutely beautiful and unforgettable experience.

Annie, thank you for taking your time to show me everything around in the lab and to instruct me on my first experiences of protein expression or crystal fishing. We have spent many hours working together, have had many interesting discussions and many memorable and fun moments and trips, e.g., our stay in Heidelberg! I really enjoyed working with you.

Valentin, thank you for your kindness and eagerness to help. Mateusz, it was nice to have you in the team and to have the ability to discuss the differences in Polish and Swiss cultures. Natacha and Ashwani, you both are great scientists, and it was a pleasure to interact with you!

I would like to thank my family for the love, support, and encouragement they gave me, and especially my parents for their upbringing. Thank you for all!

Finally, I would like to enormously thank my boyfriend, Dario. You have been by my side during all the best and worst moments of this journey, starting from the times of drafting the application papers, to moving to Milan and then to Switzerland and back, taking countless hours of trains to come to visit me or cooking dinner for me when I was finishing the thesis after work. And much much more...This success wouldn't have been possible without your support, and I cannot describe how grateful I am for it.

Curriculum vitae

Name: **Zlata Boiarska**

Date of birth: 13/07/1996

Email address: zlata.boiarska@outlook.com

○ EDUCATION

03/2020 - 05/2023	Ph.D. Program in Chemistry – University of Milan, Italy Dissertation title: Microtubule-targeting agents: synthesis and structural determination of their interactions
03/2020 - 07/2023	Ph.D. Program in Biochemistry – University of Basel, Switzerland, and Paul Scherrer Institut, Villigen, Switzerland (via co-tutelle agreement).
09/2013 - 04/2019	Master's degree in Pharmacy, Jagiellonian University, Krakow, Poland. Title master's thesis: Imidazopyridines as potential ligands of central nervous system receptors Rector's Scholarship for the best students 2016/2017; 2017/2018
02/2018 - 06/2018	Erasmus Trainee – University of Groningen, Netherlands Research project: Synthesis of the 14-3-3/p53 PPI stabilizers using MCR chemistry.

○ PROFESSIONAL EXPERIENCE

03/2023 - current	Junior Research Scientist – Medicinal Chemistry Unit, IRBM, Pomezia (Rome), Italy
03/2020 - 02/2023	Early Stage Researcher (PhD student) within the Marie Curie European Joint Doctorate "TubInTrain" – research group of Prof. Daniele Passarella, Department of Chemistry, University of Milan, Italy.
07/2021 – 07/2022	Visiting PhD student - one-year secondment at Paul Scherrer Institut, Villigen, Switzerland, at the group of Prof. Michel Steinmetz, Laboratory of Biomolecular Research, Switzerland.
06/2022 - 07/2022	Trainee – LeadXpro company. Part-time internship in the computational team
04/2019 - 11/2019	Pharmacist – community pharmacy «Apteka Sloneczna», Krakow, Poland
09/2019 – 03/2019	Pre-registration pharmacist – «Apteka prywatna S.C», Krakow, Poland

○ **Language skills**

Polish – native/bilingual

Russian – native/bilingual

English – fluent

Italian – fluent

German - basic

○ **Publications**

<https://www.researchgate.net/profile/Zlata-Boiarska>

ORCID 0000-0003-1235-5717

A co-author of 6 scientific publications, first author of 3 of them (as of March 2024).

○ **Other skills**

- Teamwork, problem-solving, accuracy and attention to detail, critical thinking